2022

Development of a state-of-the-art atomic de-excitation package in Geant4, for use in space, environment, and bio-medical sciences

Samer Bakr

UNIVERSITY
OF WOLLONGONG
AUSTRALIA

Development of a state-of-the-art atomic de-excitation package in Geant4, for use in space, environment, and bio-medical sciences.

Samer Bakr

This thesis is presented as part of the requirements for the conferral of the degree:

Doctor of Philosophy

Supervisor:
Associate Professor Susanna Guatelli

Co-supervisor:
Professor Anatoly Rosenfeld
Associate supervisors:
Professor David D. Cohen
Professor Rainer Siegele

The University of Wollongong
School of Physics, Centre for Medical Radiation Physics

August, 2022

This research has been conducted with the support of an Australian Government Research Training Program Scholarship.

Declaration

I, *Samer Bakr*, declare that this thesis is submitted in partial fulfilment of the requirements for the conferral of the degree *Doctor of Philosophy*, from the University of Wollongong, is wholly my own work unless otherwise referenced or acknowledged. This document has not been submitted for qualifications at any other academic institution.

Samer Bakr

May 7, 2023

Abstract

The goal of this project is to further develop, improve and validate the Geant4 physics component modelling atomic de-excitation. Geant4 is one of the most used general-purpose Monte Carlo codes for modelling the interactions of particles in matter used in radiation physics, in applications spanning from high energy physics to space, environment and bio-medical sciences. This project is motivated by the ongoing effort to improve the physics model of Geant4, to meet the requirements of a very diverse user community.

Geant4 is capable of simulating the radiative (X-ray) and non-radiative (Auger electron) relaxation processes of singly ionised atoms. The first release of an atomic de-excitation module is dated in 1999 and further improved. The Low Energy Electromagnetic package's first release included a basic functional implementation of X-ray fluorescence emission, which was initially associated with parameterized model implementations of the photoelectric and electron impact ionisation processes. It was then extended to describe Auger electron emission.

In this thesis, I developed a state-of-the-art X-ray fluorescence data library in Geant4, calculated using the Hartree-Fock method, which is widely recognised as a more realistic model than the Hartree-Slater model used in the default Geant4 data libraries (based on the EADL, developed at Lawrence Livermore National Laboratory, California, US). In addition, I implemented in Geant4 PIXE ionisation cross sections for proton and α particles calculated by Cohen et al. based on ECPSSR method. The new Geant4 data libraries, called here *G4–ANSTO*, have been released for the first time in Geant4 11.0, in December 2021.

I validated the new data libraries against my experimental results performed at ANSTO, Luca Heights, NSW, Australia, in terms of fluorescence X-ray yields per incident proton, α and carbon ion. I benchmarked the new *G4–ANSTO* libraries against the pre-existing, default Geant4 data libraries used for atomic de-excitation. For all studied samples, from low to high atomic number Z materials, most lines were observed to be significantly higher when using the *G4–ANSTO* approach with the exception of the L_l line. The study showed that the Geant4-calculated X-ray emission spectra and the ANSTO experimental

measurements were in a reasonably good agreement.

Auger emitting radioisotopes are of particular interest in targeted radiotherapy because, once internalised in tumour cells, they may give dose to radiation-sensitive targets while causing minimal damage to surrounding cells. Thus, I benchmarked for the first time the emission of Auger electrons deriving from multiple radioisotopes decays calculated by means of Geant4 against other theoretical approaches and available experimental results. When comparing Geant4 to other theoretical approaches, an overall good agreement, usually within few percent in terms of Auger electron energies, was found between Geant4 and other theoretical approaches. In terms of emission yields, a good agreement (within 3%) was found for vacancies in the K shell. In the case of vacancies in the L and M shells, the level of agreement was worse (within 15%). Overall, the total number of the Auger electron emitted per radioactive decay was found significantly higher in Geant4.

Finally, as part of the benchmarking and validation of the novel Geant4 atomic de-excitation package, I examined the impact of a recently included X-ray fluorescence data library, *fluor_ANSTO*, on the Auger electrons emission yield. Therefore, the Auger electron spectra and the total Auger electron yield for several radionuclides generated by the *G4–ANSTO* and the *G4–default* data libraries were compared to one another. The comparison reveals that the results produced by both data libraries are just barely different. However, *fluor_ANSTO* data library exhibits slightly lower Auger electron yields than the *G4–default* data library, which is understandable given that the *fluor_ANSTO* data library shows a greater X-ray fluorescence yield than the *G4–default* data library. Furthermore, because the sum of the X-ray fluorescence and of the Auger electron emission yield is one, the results are consistent with the prediction.

In summary, in this work, which takes place within the Geant4 Collaboration, I implemented a new atomic de-excitation package in Geant4, which is based on a more accurate theoretical approach. I validated it against experimental measurements and provided to the Geant4 User community for the first time in Geant4 11.0.

Acknowledgements

To begin, I would like to express my heartfelt appreciation to the University of Wollongong and Prof Susanna Guatelli for awarding me the PhD scholarship; without this scholarship, the work presented in my thesis would not have been possible.

Further, I am grateful to Prof Susanna Guatelli, my primary supervisor, whose expertise was invaluable in formulating the research questions and methodology. Her insightful feedback pushed me to sharpen my thinking and brought my work to a higher level. I would like to thank her for being patience, supportive, and for guiding me through this journey. Her high standards have made me better in what I do.

I would like to express my gratitude to my co-supervisor, Distinguished Prof Anatoly Rosenfeld, for his encouragement, direction, and support during this research. I would like to thank my co-supervisor, Distinguished Prof David D. Cohen, for his patience, advice, constructive talks, and excellent explanations, which helped me gain a better understanding and broaden my knowledge. Special thank you and appreciation to Prof Rainer Siegele, my co-supervisor, to assist in any way he could throughout the research project. I had great times discussing with him and absorbing from his knowledge. I also would like to say thank you to my colleague Dr David Bolst, for his assistance with Geant4 and the University's clusters.

In addition, I would like to thank my parents for their encouragement, wise counsel and sympathetic ear. Their love, support, and unwavering belief in me has kept my spirits and motivation high during this journey. Finally, I would like to thank my best friend and wife Salaam for her love and constant support, for all the late nights and early mornings.

Publications

List of peer-reviewed publications:

- **S. Bakr**, D.D. Cohen, R. Siegele, S. Incerti, V. Ivanchenko, A. Mantero, A. Rosenfeld, S. Guatelli, (2022) **"Validation of the Geant4 PIXE component for incident carbon ions"**, *Journal of Nucl. Instruments Methods Phys. Res. Sect. B Beam Interact. with Mater. Atoms,* vol 532, 2022, pp. 38-46.
`https://doi.org/10.1016/j.nimb.2022.10.010`

- **S. Bakr**, D.D. Cohen, R. Siegele, J. W. Archer, S. Incerti, V. Ivanchenko, A. Mantero, A. Rosenfeld, S. Guatelli, (2021) **"Geant4 X-ray fluorescence with updated libraries"**, *Nuclear Instruments and Methods in Physics Research Section B: Beam Interactions with Materials and Atoms,* vol. 507, 2021, pp. 11-19.
`https://doi.org/10.1016/j.nimb.2021.09.009`

- **S. Bakr**, T. Kibedi, B. Tee, D. Bolst, M. Vos, M. Alotiby, L. Desorgher, D. H. Wright, A. Mantero, A. Rosenfeld, V. Ivanchenko, S. Incerti, S. Guatelli, (2021) **"A benchmarking study of Geant4 for Auger electrons emitted by medical radioisotopes"**, *Journal of Applied Radiation and Isotopes* May 2021, 174.
`https://doi.org/10.1016/j.apradiso.2021.109777`

- E.Engels, **S. Bakr**, D. Bolst, D. Sakata, N. Li, P. Lazarakis, S. J. McMahon, V. Ivanchenko, A. Rosenfeld, S. Incerti, I. Kyriakou, D. Emfietzoglou, M. L. F. Lerch, M. Tehei, S. Corde and S. Guatelli, (2020) **"Advances in modelling gold nanoparticle radiosensitization using new Geant4-DNA physics models"**, *Physics in Medicine and Biology*, November 2020, 174.
`https://doi.org/10.1088/1361-6560/abb7c2`

- V. Ivanchenko, A. Bagulya, **S. Bakr**, M. Bandieramonte, D. Bernard, M. Bordage, J. Brown, H. Burkhardt, P. Dondero, V. Grichine, S. Guatelli, I. Hrivnacova, S.

Incerti, O. Kadri, D. Konstantinov, I. Kyriakou, M. Maire, A. Mantero, J. Ramos-Mendez, M. Novak, L. Pandola, D. Sakata, D. Sawkey, I. Semeniouk, W. G. Shin,N. H. Tran, and L. Urban on behalf of the Geant4 Collaboration, (2020), **"Geant4 electromagnetic physics progress"**, *EPJ Web of Conferences*.
https://doi.org/10.1051/epjconf/202024502009

- V. Ivanchenko, A. Bagulya, **S. Bakr**, M. Bandieramonte, D. Bernard, M. Bordage, J. Brown, H. Burkhardt, P. Dondero, S. Elles, V. Grichine, S. Guatelli, F. Hariri, A. Howard, S. Incerti, S. Yung Jun, O. Kadri, I. Kyriakou, M. Maire, A. Mantero, M. Novak, D. Sawkey, I. Semeniouk, A. Sokolov, and L. Urban on behalf of the Geant4 Collaboration, (2019), **"Progress of Geant4 electromagnetic physics developments and applications"**, *EPJ Web of Conferences*.
https://doi.org/10.1051/epjconf/202024502009

- **S. Bakr**, D.D. Cohen, R. Siegele, S. Incerti, V. Ivanchenko, A. Mantero, A. Rosenfeld, S. Guatelli, (2018) **"Latest Geant4 developments for PIXE applications"**, *Journal of Nucl. Instruments Methods Phys. Res. Sect. B Beam Interact. with Mater. Atoms,* vol. 436, no. October, pp. 285–291.
https://doi.org/10.1016/j.nimb.2018.10.004

List of Conferences

Abstracts and presentations:

- **Ion Beam Analysis** conference 2021, (Online)
- **26th Geant4 Collaboration** meeting 2021, (Online)
- **25th Geant4 Collaboration** meeting 2020, (Online)
- **Ion Beam Analysis** conference 2019, (Antibes, France)
- **24th Geant4 Collaboration** meeting 2019, (Jefferson Lab, New York, USA)
- **NSTLI seminars** 2019, (Australia's Nuclear Science and Technology Organization (ANSTO), Sydney, Australia)
- **Heavy Ion Accelerator** Symposium 2018, (Australian National University, Canberra, Australia)
- **Third Geant4 International User** conference 2018, (Bordeaux, France)
- **MedPhys 2017**, (University of Sydney, Sydney, Australia),
- **Geant4 User Workshop** 2017, (Sege Hotel, Wollongong, Australia),
- **22th Geant4 Collaboration** meeting 2017, (University of Wollongong, Wollongong, Australia)
- **Innovation in Radiation Applications** 2017, (University of Wollongong, Wollongong, Australia)

List of Acronyms and Abbreviations

- **A, a**

  ANSTO - Australia's Nuclear Science and Technology Organisation.

  ANU - Australian National University.

  ARC - Australian Research Council.

- **C, c**

  CAS - Centre for Accelerator Science.

  CK - Coster-Kronig.

  CPU - Central Processing Unit.

- **E, e**

  EADL - Evaluated Atomic Data Library.

  EC - Electron Capture.

  ECPSSR - the energy loss (E) and Coulomb deflection (C) of the projectile and the perturbed-stationary state (PSS) and relativistic (R) nature of the target's inner shell.

  EMS - Electron Momentum Spectrometer.

  ENSDF - Evaluated Nuclear Structure Data File.

- **I, i**

  IC - Internal Conversion

  ICRP - International Commission on Radiological Protection.

  IUPAC - International Union of Pure and Applied Chemistry.

- **J, j**

  JINR - Joint Institute for Nuclear Research.

- **M, m**

  MDL - Minimum Detection Limit.

  MSL - Mars Science Laboratory.

- **N, n**

  NCRIS - National Collaborative Research Infrastructure Strategies.

- **P, p**

  PIXE - Particle Induced X-ray Emission.

  PWBA - Plane Wave Born Approximation.

- **Q, q**

  QED - Quantum Electrodynamics.

Contents

Chapter 1

Introduction

1.1 Vision of the Project

The aim of this project is to develop a state-of-the-art atomic de-excitation package in Geant4, called here (*G4–ANSTO*), to improve the modelling of this physical phenomenon, of interest for applications spanning from space and environmental sciences to bio-medical applications. The Geant4 simulation toolkit [1] is one of the most used general purpose Monte Carlo codes in the world for radiation physics applications, demonstrated by the fact that the first paper describing Geant4 [1] is the most cited publication in the Nuclear Science and Technology category, as defined by Journal Citations Reports, with currently more than 16,000 citations (Scopus, accessed on 07/05/2022).

In particular, I improved the existing ionisation cross sections of incident proton and α particles, and the X-ray fluorescence radiation yield data libraries in Geant4, based on the recommendations of D. D. Cohen and R. Siegele, two top international leading experts in experimental PIXE and associated theoretical modelling. I implemented and benchmarked the new data libraries, called here *G4–ANSTO*, with respect to already available Geant4 models (*G4–default*) and I validated them against my experimental measurements performed at ANSTO, Luca Heights, NSW, Australia.

For completeness, as part of the benchmarking of the novel *G4–ANSTO* atomic de-excitation package, I examined the impact of the data libraries on the Auger electrons emission yield. Finally, I benchmarked for the first time the emission of Auger electrons deriving from multiple radioisotopes decays calculated by means of Geant4 against other theoretical approaches and available experimental results.

1.2 Motivation

The ongoing effort to improve the physics model and broaden the dataset options available in Geant4, to meet the requirements of a very diverse user community, inspired this project. Despite the availability of a set of ionisation cross sections and atomic relaxation datasets (see section 2.5.5), one of the goals of the *Electromagnetic Physics Working Group* of the Geant4 Collaboration is to update the current Geant4 physics component with state-of-the-art physics models, to be able to appropriately address the needs of the Geant4 user community, in a variety of domains, including environmental physics, geology, archaeology, space and bio-medical sciences.

The Geant4 Monte Carlo Toolkit's prediction of atomic vacancy generation and relaxation process, both of which are responsible for fluorescence X-ray and Auger electrons' emission, will be improved as a result of this research.

1.3 Thesis Outline

The focus of this thesis is to develop and validate a state-of-the-art Geant4 atomic de-excitation package, which is based on the recommendations of D. D. Cohen and R. Siegele [2], and which is a self-consistent, accurate, and robust recommended approach.

Chapter 2 of this thesis is a review of the literature on atomic de-excitation and existing physics modelling approaches to describe it. The *G4–ANSTO* has been validated against experimental measurements performed at ANSTO, therefore the PIXE technique is also described in chapter 2. Finally, this chapter provides a brief description of the Geant4 Monte Carlo toolkit, as well as a description of how the atomic de-excitation is modelled in Geant4.

Chapter 3 describes the inclusion of a state-of-the-art proton and α particle shell ionisation cross section library based on ECPSSR approach as calculated by Cohen et al. [2]. The new ionisation cross sections have been released in Geant4 11.0.

The fluorescence X-ray spectra obtained by the *ECPSSR_ANSTO* set of cross sections and, alternatively, the currently available sets of Geant4 PIXE cross sections have been compared. Moreover, a comparison with experimental data obtained at ANSTO has been performed.

Chapter 4 reports the results of the development of Geant4 of a new data-driven library, called in this thesis *fluor_ANSTO*, that can be used in any Geant4 application that requires

X-ray fluorescence to be described. These probabilities for Hartree-Fock X-ray fluorescence transitions were included into *fluor_ANSTO*. Additionally, I compared Geant4 results obtained using *fluor_ANSTO* and the pre-existing Geant4 default one (*G4–default*) to experimental data. The new data libraries have been released in Geant4 11.0.

Chapter 5 presents the experimental work that I performed at ANSTO on ANTARES tandem accelerator utilising the heavy ion microprobe beamline employing carbon ions in order to conduct further validation tests for the new approach *G4–ANSTO*.

Chapter 6 demonstrates the use of carbon ions to compare the fluorescence X-ray spectra obtained by the *G4–ANSTO* model with the *G4–default* model. These two approaches were compared to recently performed experimental observations at ANSTO heavy ion microprobe beamline.

Chapter 7 benchmarks the modelling of the emission of Auger electrons in Geant4 deriving from the decay of some radionuclides against existing theoretical approaches. The simulation results are compared to experimental measurements as well. This is the first time that the Geant4 atomic de-excitation package has been compared to other theoretical models and experimental data for Auger electron emission yields.

Chapter 8 investigates the influence of the *fluor_ANSTO* X-ray fluorescence data library on the Auger electrons emission yield. In this project, I mainly validated the *fluor_ANSTO* for modelling X-ray fluorescence, however Geant4 users may adopt the *fluor_ANSTO* to study Auger electron emission (e.g., in nanomedicine [3]). Therefore, I analysed the spectra of the Auger electrons produced with *fluor_ANSTO*, for completeness. This is crucial when developing a software tool for a diverse scientific community.

Chapter 9 presents the general conclusions and recommendations deriving from the results of this project.

Chapter 2

Literature Review

This chapter offers a concise description of the major relevant physical concepts developed by previous theorists and researchers up to the time this thesis topic was begun. These key concepts are examined in further detail in the various topical chapters of this thesis. Here, a general review of atomic de-excitation and physical interactions involved in Particle Induced X-ray Emission (PIXE) has been provided. I also briefly describe PIXE's various analytical applications to highlight the significance of this analytical technique. Then, quick overview is provided of the Geant4 Monte Carlo toolkit, which is the simulation code used in this thesis. Two general properties of PIXE modelling are discussed: the physics of PIXE technique and PIXE atomic excitation and de-excitation mechanisms in Monte Carlo codes.

2.1 Introduction

When light ions, such as protons or α particles from an accelerator, interact with an atom in the target material, many reactions may occur. Interactions between ions with an electron cloud of a target atom frequently result in ionisation (electron ejection) and subsequent photon emission. Other outer electron transitions will fill the vacancies left by electrons ejected from the K or L shell by the Coulomb interaction of the incident ion, and an X-ray photon or Auger electron is produced which carries the excess energy. The X-ray energies of K, L, and M shells fall into discrete bands, making each target's X-ray signature unique [4].

Particle Induced X-ray Emission, or PIXE, was a technique firstly suggested by Johansson and Campbell in 1970 [5]. This technique is focused on collecting the X-rays produced by an accelerator ion beam irradiation of the target sample [4]. The energy of the released X-ray is characteristic of the bombarded atom, and the number of characteristic X-rays generated is proportional to the elemental concentration [6–10]. X-rays

emerging from the transitions involving vacancies in the M shell have generally low energies $(1-3\ keV)$, L shell X-rays have intermediate energies $(1-20\ keV)$, and K shell X-rays have high energies $(1-30\ keV)$ [4]. Therefore, a typical PIXE detection system can work throughout the whole X-ray energy range of $1-40\ keV$, allowing it to detect X-rays arising from transitions involving vacancies in the K, L, or M shells. It is possible to conduct analysis on metals, ceramics, and all other kinds of substances using this process. The exceptional sensitivity of PIXE compared to other X-ray analytical techniques is due to the lack of background radiation in the X-ray range above a few keV [4].

Depending on the element, energy, and total charge of incident particles, X-ray filters, and quality of the X-ray detector, PIXE sensitivities range from 1/100 ppm. Some X-rays cannot be detected because they are absorbed by the detector's window atmosphere or by the filter [11] .

PIXE gained popularity in the mid-1970s as a result of Johansson and Johansson's [12] excellent analysis of PIXE's analytical applications. Johansson et al. [13] demonstrated in 1970 that a mixture of X-ray excitation by protons and detection by a Si(Li) detector was a stable multi-elemental research approach with strong sensitivity. The PIXE popularity did not begin until the commercial Si(Li) detector was released in the late 1970s and early 1980s. Since then, several articles on methodology and implementations have been published.

PIXE is now available all around the world, with several accelerator labs running their own analytical equipment. Currently, more than 100 laboratories in more than 30 countries use the PIXE technique [4]. These accelerators operate with terminal voltages ranging from 1 to 5 MV (2 to 3 MV in general), utilising mainly protons as bombardment particles for various target material analyses. PIXE is a novel and powerful tool for multi-element non-destructive trace element analysis of small samples [6–10].

Since 1964, Australia's Nuclear Science and Technology Organisation (ANSTO) has operated accelerators. The ANSTO Centre for Accelerator Science is a world-class facility for ion beam analysis and accelerator mass spectrometry. The Centre is renowned globally for the superiority of its operations and excellent expertise [11]. It attracts users from all around the world, including those in academia, publicly-funded research institutions, private industry, and Government. The Centre for Accelerator Science offers users access to a range of technologies in one place that may be used for air pollution investigations, isotopic dating, climate science, material modification and characterisation, nuclear detector characterisation, radiation damage studies, forensic science and microbiological and life sciences studies [11].

Among several ion-beam technologies, PIXE is without a doubt the most popular [14, 15], due to its multi-element nature and suitability for analysing trace elements with medium and high atomic numbers in a matrix composed of light elements [5]. To achieve a sufficient level of precision for signal and background estimates [14], simulation of a PIXE experiment is particularly advantageous, given that the method requires a particle accelerator operated by experienced personnel as well as a complex system of detectors and associated techniques. Monte Carlo radiation physics simulation codes are ideally suited for PIXE modelling because they can reproduce the stochastic behaviour of the emission process. Modelling of the PIXE process comprises modelling both atomic ionisation and de-excitation [14]. The PIXE package in the Geant4 simulation toolkit is the subject of investigation in this thesis [16, 17].

2.2 De-excitation of Atoms

When an atom is ionised, an electron from an atomic shell that is knocked-out, causing the atom to be out of equilibrium. An electron from an upper shell usually falls into the inner shell in a very short period of time ($\sim 10^{-15}$ s), to fill the vacancy. When an electron from the outer shell moves to occupy a vacancy in an inner shell, it loses a specific, discrete amount of energy [18, 19].

In an ion-atom collision, the leftover energy from the collision is removed either in a radiative form (X-ray fluorescence), or in a non-radiative form (Auger electron emission).

2.2.1 Radiative Transition

Radiative transitions result in emission of photons which comprise "characteristic radiation", since the wavelength λ or energy $h\nu$ of the emitted photon are characteristic of the element from which the photon arises. This happens because the atomic binding energies, and therefore their associated energy differences, are unique to the atomic species. The term "fluorescent radiation" is used as an alternative to describe these characteristic photons. The complete set of photons arising from radiative transitions from a given atom is referred to as the "line spectrum" of that atom type [20].

2.2.2 Non-radiative Transition

Non-radiative transitions are a different channel of atomic de-excitation where Auger electrons are emitted. Electrons may undergo transitions that supposedly violate the selection rules for production of characteristic radiation; in such a case, the energy dif-

ference is rapidly transferred to other orbital electrons which are ejected from the atom as Auger electrons, Coster-Kronig electrons or super Coster-Kronig electrons, as shown schematically in figure 2.1. They have a higher probability in low Z materials [20].

The kinetic energy of these electrons is given by the energy released through the primary electronic transition minus the binding energy of the emitted Auger electron. In the Coster-Kronig effect the transition energy is transferred to an electron in another shell and the emitted electron is called a Coster-Kronig electron [20]. Super Coster-Kronig electrons result when an electron from a higher shell obtains and then releases the energy difference between the higher and a lower shell with an electron vacancy (see figure 2.1).

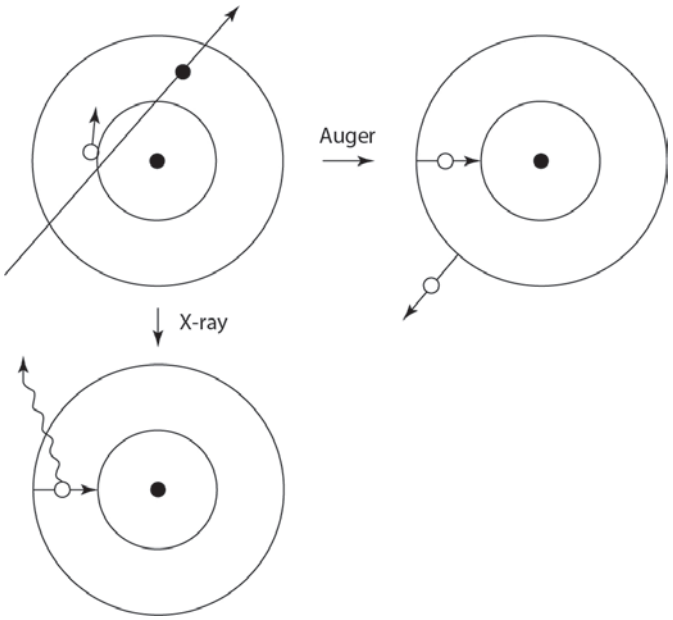

Figure 2.1: The interaction between an ion and an electron from an inner shell and the emission of an Auger electron and X-ray characteristic photon. Courtesy of ([21])

Figure 2.1 depicts the atomic de-excitation and release of X-ray characteristic photons and Auger electrons. Its energy is determined by the difference between both binding energies of the first and second shells in the atom [19]. In this case (see figure 2.2), the photon energy is equal to $B_K - B_L$.

For example, L-shell Auger electron energy is:

$$T = (B_K - B_L) - B_L = B_K - 2B_L \tag{2.1}$$

2.2.3 Radiative and Non-radiative Transitions Notation

For **radiative transition**, the *Siegbahn* notation system has been used in this thesis.

The traditional *Siegbahn* notation labels the electron sub-shells extending from the nucleus with the symbols K, L_1, L_2, L_3, M_1, and so on (decreasing in binding energy). The K shell has no sub-shells, the L shell has three sub-shells, labelled L_i $(i = 1\ to\ 3)$,

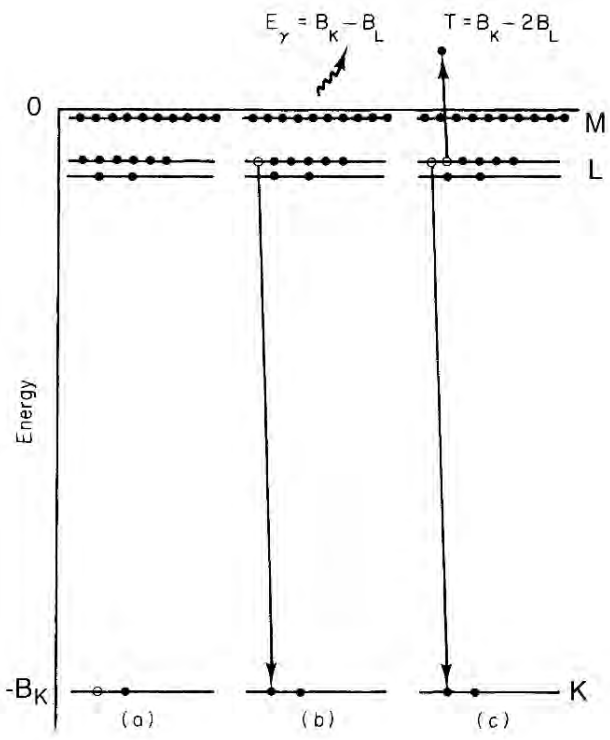

Figure 2.2: There are two competing processes for de-exciting an atom with a vacancy in the K shell. (a) Shows an atom with a vacancy in K shell. (b) An electron transferring from the L shell to the K shell, emitting a photon. (c) An electron has been transferred from the L shell to the K shell. Its released energy is picked up by another electron in the L shell. This electron is referred to as an Auger electron. Courtesy of ([19])

Table 2.1: Labelling of different K and L X-ray transitions to represent electron transitions.

K X-ray Lines	**L X-ray Lines**	
$K_{\alpha 1}\ (K-L_{III})$	$L_l\ (L_{III}-M_I)$	$L_{\gamma 1}\ (L_{II}-N_{IV})$
$K_{\alpha 2}\ (K-L_{II})$	$L_{\alpha 1,2}\ (L_{III}-M_{IV,V})$	$L_{\gamma 2}\ (L_I-N_{II})$
$K_{\beta 1}\ (K-M_{III})$	$L_{\beta 1}\ (L_{II}-M_{IV})$	$L_{\gamma 3}\ (L_I-N_{III})$
$K_{\beta 2}\ (K-N_{II,III})$	$L_{\beta 2}\ (L_{III}-N_V)$	$L_{\gamma 4}\ (L_I-O_{III})$
$K_{\beta 3}\ (K-M_{II})$	$L_{\beta 3}\ (L_I-M_{III})$	$L_{\gamma 6}\ (L_{II}-O_{IV})$

the M shell has five sub-shells, labelled M_i $(i = 1\ to\ 5)$ and the N shell has seven sub-shells labelled N_i $(i = 1\ to\ 7)$ (see figure 2.3). These letters are used to identify the electron transitions that create the characteristic X-ray lines. The electron sub-shells are labelled using the three quantum numbers n, l, and j, in spectroscopic notation. The principal quantum number $n = 1, 2, 3$ ... corresponds to the major shells K, L, M... The letters s, p, d, f, ... are used to denote sub-shells with orbital angular momentum $l = 0, 1, 2, 3$ ... , respectively, and the quantum number $j = 1 + s$, where $s = 0$ or $1/2$ is the standard electron spin number. Allowable electron transitions have $\Delta n > 0$, $\Delta l = \pm 1$ and $\Delta j = 0, \pm 1$; transfers without these values occur with a very low probability and are referred to as forbidden transitions.

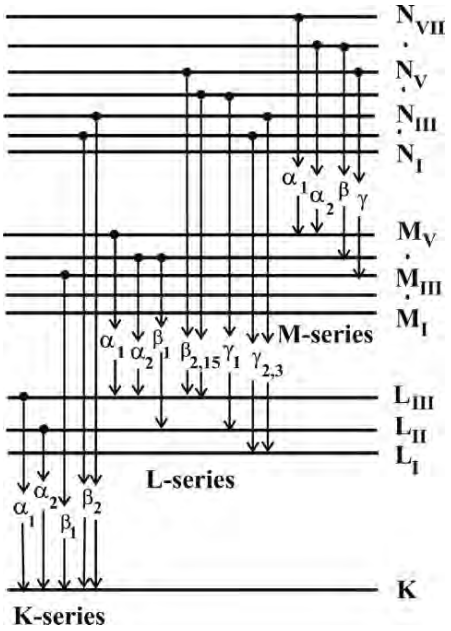

Figure 2.3: Diagram of energy levels for K, L, M and N sub/shells. Courtesy of ([22])

Figure 2.3 depicts the allowed X-ray fluorescences for initial vacancies in the target atom's K and L sub/shells. It should be noted that L_1 $(2s_{1/2})$ sub-shell electrons cannot fill the vacancy in the K shell $(1s_{1/2})$ since their angular momentum would need to be modified during the quantum transformation [22]. Using traditional *Siegbahn* notation, they are known as K_α, K_β, L_α, L_β and L_γ X-ray transitions, depending on which shell the original vacancy occurred in (see table 2.1). Table 2.1 displays the X-ray transitions that occur when there is a vacancy in the K or L sub/shells.

Alternatively, non-radiative transitions are commonly identified by *IUPAC* notation system. Consider a transition in which an electron in the L_2 sub-shell fills an initial vacancy in the K shell. A KL_2L_3 Auger electron will appear if the energy released is transferred to an electron in the L_3 sub-shell which is ejected. KYZ, likewise, refers to an electron released from the Z shell [23, 24]. The situation is compounded further by the fact that non-radiative transitions can occur between sub-shells, affecting the number

of vacancies in each sub-shell. These are known as *Coster–Kronig* transitions, and they are accompanied by the emission of an electron. For instance, a vacancy in a L_1 sub-shell may be filled by an electron from L_3 sub-shell, with release of an electron from the M shell. Moreover, a super-Coster–Kronig transition may occur, involving electrons from the same shell, such as a vacancy in the M_1 shell being filled by an electron from the M_2 shell and an electron from the M_4 shell being ejected [19].

2.2.4 Radiative and Non-radiative Yields

To an observer it appears to be random whether the atom de-excites by releasing a photon or an Auger electron after creating a vacancy. This happens for all vacancies but here I will focus on the K shell [19]. An atom in an excited state implies a vacancy in one of its sub/shells. The excited state's associated lifetime τ is related to the level width Γ by $\Gamma.\tau = \hbar$ where $\hbar$ is the reduced Planck's constant. The excited state's total decay rate A is the inverse of its lifespan $A = \tau^{-1}$ or $\Gamma = A.\hbar$. If different decay processes from the excited state are considered to be independent, the level width is equal to the sum of the radiative width, Γ_R the Auger width, Γ_A and the Coster-Kronig width, Γ_{CK}: [23]

$$\Gamma = \Gamma_R + \Gamma_A + \Gamma_{CK} \tag{2.2}$$

Yields for the different processes are given as follows;
Fluorescence yield:

$$\omega_R = \frac{\Gamma_R}{\Gamma} \tag{2.3}$$

Auger yield:

$$\omega_A = \frac{\Gamma_A}{\Gamma} \tag{2.4}$$

Coster-Kronig yield:

$$\omega_{CK} = \frac{\Gamma_{CK}}{\Gamma} \tag{2.5}$$

All three, of a sub/shell for the same initial vacancy distribution, add up to one: [23]

$$\omega_R + \omega_A + \omega_{CK} = 1 \tag{2.6}$$

If a vacancy is in a K shell, the previous relation will be modified as follow:

$$\omega_R^K + \omega_A^K = 1 \tag{2.7}$$

Figure 2.4 depicts the relationship between Auger electron yields and X-ray fluorescence yields as a function of atomic number. The Auger electron yield is found to have higher probability in low Z materials, whereas the X-ray fluorescence yield is found to

be higher in high Z materials (see figure 2.4).

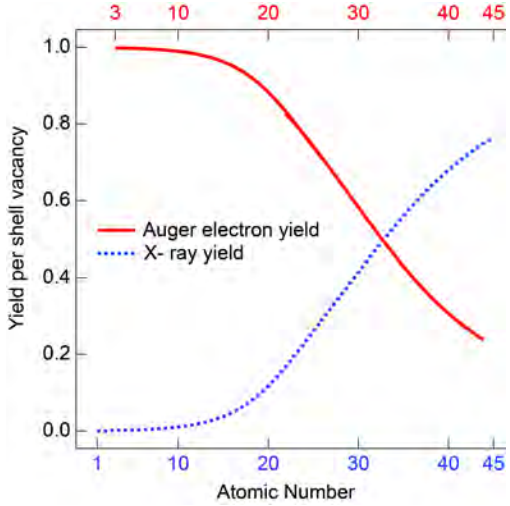

Figure 2.4: The Auger electron and X-ray fluorescence yields with respect to atomic number of the target material. Courtesy of ([25])

For a vacancy in the L or higher shells, the fluorescence yield for each sub-shell must be considered. Although the average fluorescence yields $\bar{\omega}_R^L, \bar{\omega}_R^M$ and so on may be defined for each shell, these are not a fundamental property of the atom, since the values are dependent on the vacancy distribution in the sub-shells [19]. $\omega_R^K, \bar{\omega}_R^L$ and $\bar{\omega}_R^M$ values as a function of Z are shown in figure 2.5.

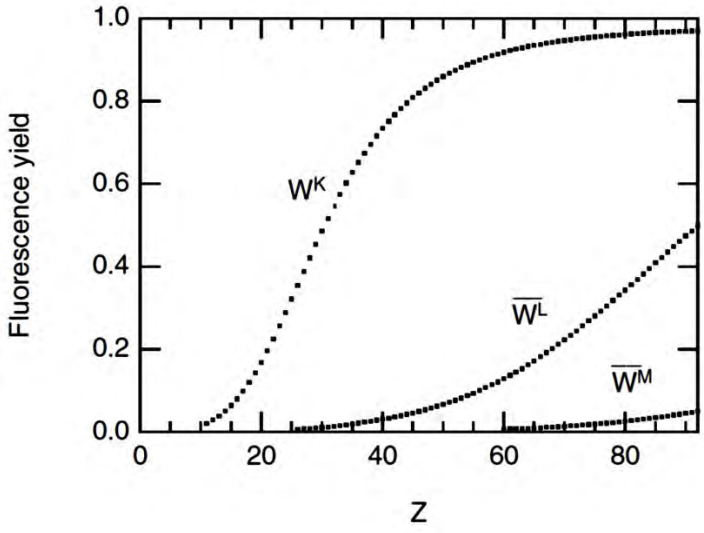

Figure 2.5: Fluorescence yields for vacancies in the K, L, and M shells as a function of atomic number Z . Table 8 in Hubbell et al. [26] provides the points. Courtesy of ([19])

Non-radiative transitions are significantly more essential for the L shell (where the fluorescence yield is much smaller) than for the K shell, as can be seen in figure 2.5. Non-radiative transitions are practically the sole process for higher shells [19]. The fluorescence yield depends on two factors; the atomic number Z_2 of the target and its initial

charge state, and is independent of the projectile atomic number Z_1 and its incident energy E_1. For light ions incident on heavy targets, i.e. $(\frac{Z1}{Z2}) << 1$. It has usually been thought that the yield of light ion fluorescence in heavy atoms is independent of the charge state of the target atom, and neutral atom fluorescence yield figures can be used [27]. Because there are additional decay mechanisms and more than one sub-shell in studies of L shell ionisation, the relationships between observed X-ray intensities and theory become more complicated [27].

2.2.5 Transition Probability

As previously stated, a vacancy in a certain sub/shell can be filled by various transitions from higher sub-shells. To calculate the probability of a certain transition i occurring, we must know the ratio of the partial radiative width, $\Gamma_R^S(i)$, for that transition relative to the total radiative width, Γ_R^S of that sub-shell s. The relative X-ray emission rate for the transition i in the sub-shell s is defined as:

$$C_R^S(i) = \frac{\Gamma_R^S(i)}{\Gamma_R^S} \tag{2.8}$$

The emission rates of lines within a sub-shell are critical in quantitative X-ray analysis for identifying the elements [27]. The probability of a specific transition is equal to the emission rate of that line multiplied by the fluorescence yield of the sub/shell:

$$P_R^S(i) = \frac{\Gamma_R^S(i)}{\Gamma_R^S}.\omega_R^S = C_R^S(i).\omega_R^S \tag{2.9}$$

2.2.6 PIXE: Ionisation and X-ray Production Cross Sections

The interaction cross section σ quantifies the probability of a specific type of interaction. The cross section is the effective area exposed to incoming ions at each interaction location (atom or nucleus) and is measured in centimetres per atom or barns per atom, where 1 barn = 10^{-24} cm^2. Comparing the total X-ray production cross section, σ^x, to the theoretically calculated total ionisation cross sections, σ^i, includes calculating the radiative probability that an initial vacancy will decay and emit an X-ray. The number of photons released when vacancies in the shell are filled, divided by the number of primary vacancies N in the shell, represents the fluorescence yield of the shell. A K shell has only one sub-shell, and the fluorescence yield is stated as ω_κ. The total K shell X-ray production cross section is linked to the K shell ionisation cross section σ_k^i, by the shell fluorescence yield ω_κ by:

$$\sigma_k^x = \omega_\kappa.\sigma_k^i \tag{2.10}$$

Where ω_K falls between 0 and 1 [27]. There are three and five sub-shells for the L and M shells respectively and the fluorescence yields are written as ω_i, where $i = L_1, L_2, L_3$ or M_1, M_2, M_3, M_4, M_5 for the L and M shells, respectively [27]. Bambynek et al. [28] and Krause [29] review the physics of atomic de-excitations and present theoretical and experimental data for the fundamental parameters [19]. A more recent review of the fundamental parameters of atomic de-excitation is provided by Hubbell et al. [26].

2.3 PIXE Applications

Particle Induced X-ray Emission (PIXE) technology is suitable for geological, environmental, biological, art, and archaeological investigations. PIXE technique has been applied by collaborations of scientists from various fields to estimate the concentrations of micro- and macro-elements in a given sample. This technique provides fast, non-destructive analysis of test materials in the form of solids, powders, filter substrates, and liquids [22]. PIXE has a variety of analytical applications. The following sections provide an overview of different types of applications, although it is not intended to be a complete list of every possible application of the technique. The goal is only to highlight the unique analytical features of PIXE that are especially relevant in each of the primary applications of interest for the subject of this thesis [21].

2.3.1 Environmental Pollution Studies

The first PIXE articles featured studies of aerosols caught by filter papers collecting these minute particles from the atmosphere, and similar work is still being done at a rapid rate today [4]. Many countries and international organisations have become more worried in recent years about the steady deterioration of environmental quality caused by a variety of industrial, man-made, and natural contaminants [30]. Many studies have been conducted using PIXE to inform understanding on occupational health, atmospheric visibility, acid rain, soil erosion, and environmental impacts [4]. Environmental quality investigations have revealed that, due to the small sample sizes that are commonly available and the low toxicity levels that are frequently involved, there is a need for highly sensitive multi-elemental analysis procedures that can be applied to air, water, soil, and biological samples [30].

The PIXE technique has proven to be well adapted to this sort of broad range analysis, encompassing almost the full element spectrum while needing just micrograms of total material [30]. Several laboratories across the world have conducted studies of airborne pollution using PIXE and similar methods, and the results clearly indicate its utility in

environmental sciences [30].

2.3.2 Applications in Earth and Planetary Sciences

The geo-sciences, as well as related industrial operations (prospecting, mining, beneficiation, and so on), have a high demand for elemental analysis. Simultaneously, the criteria for analytical techniques are rather high, and geological samples are usually complicated - they can be composed of a variety of minerals and have an inhomogeneous structure. They often contain a matrix of major elements, as well as a significant number of minor and trace elements, including commercially important metals. An analytical approach must be multi-element capable in order to be effective for geological applications. Trace element concentrations in minerals are significant in geological process analyses. The elemental profile may reveal information about the mineral origin and the connections between various geological structures. Trace elements can also be used as a guidance in the search for precious minerals [5].

The amount of material to be analysed in many geological applications is extremely vast. A single mining or prospecting firm, for example, may produce bore cores with a total length of tens of kilometres every year. As a result, a large throughput is required for the analytical system to be employed. In this regard, it is important to recognise that not only the actual analysis but also the sample preparation must be considered. A technique that allows for immediate analysis without the need for time-consuming preparatory steps offers a significant benefit. As a result, it can be confidently stated that elemental analysis in geology and mineralogy requires a rapid, multi-elemental, and moderately sensitive approach that requires just a minimal amount of sample preparation. The combination of these criteria makes PIXE a highly effective tool for utilisation in this particular application area, alongside Alpha-particle X-ray Spectrometers (APXS) and other X-ray emission techniques [5, 31].

Since its landing on Mars in August 2012, the Curiosity Rover carrying the Mars Science Laboratory (MSL) has been utilising its equipment to examine the geology of Gale Crater. This location was chosen in part because orbital observations showed the presence of sedimentary layers in a central mound, perhaps recording the evolution of the regional Martian environment from warm and wet to cold and dry. Among the numerous accomplishments since Curiosity's landing are the discoveries that an ancient lake existed in the crater with a pH that might have supported microbial life. One of the techniques used for elemental analysis of rocks and unconsolidated material is PIXE [32].

2.3.3 Bio-medical Applications

The nature of biological materials, where light components (undetectable by PIXE) constitute the dominating matrix, is the primary reason for PIXE's phenomenal success in biomedical applications. This supports achieving the greatest outcomes in terms of MDLs for higher-Z elements. Because of this trace-element capability, valuable information on physiological and pathological processes in biomedicine may be obtained from PIXE [21]. The multi-element nature of the analysis and the tiny sample sizes are two more strengths of PIXE in this context [4].

The second aspect of PIXE that is significant in biomedical applications is its high spatial resolution, which allows for high-definition mapping of trace-element distributions in tissues. When a microbeam is employed, the intracellular distribution of trace elements may be observed, and in certain cases, μ-PIXE is regarded as a superior technique [4, 30, 33].

PIXE has traditionally been employed in biomedicine to detect trace amounts of transition and heavier elements in tissues. The detection of lighter elements, such as aluminium, potassium, and calcium, has lately attracted scientists' curiosity. Alternative methods sometimes struggle to identify low concentration levels of these elements, which are well within PIXE's analytical capabilities, especially when working with small tissue samples or at the cellular level [21].

2.3.4 Applications in Art and Archaeology

Archaeologists are most interested in having a solid understanding of the composition of archaeological artefacts in terms of major and trace elements. The composition of metal artefacts provides information on ancient technological knowledge and aids in the distinguishing of prehistoric cultural traditions [22].

PIXE targets in the form of thin samples are frequently challenging to produce. Thick samples of the specimens of interest may be utilised in these instances. A thick piece of tissue, bone, rock, or archaeological sample, for example, can be mounted and irradiated directly, either in vacuum or in a non-vacuum facility, with no pre-treatment or other preparation required [30]. The establishment of a dedicated accelerator in the Laboratoire de Recherche des Musees de France, in the basement of the Louvre Museum in Paris, demonstrates the relevance of PIXE measurements in this domain. This accelerator has made a major contribution towards a better understanding of the materials and processes employed in the past for the analysis of works of art, among other things, by relying heavily on PIXE analyses [21].

2.4 Monte Carlo Simulations

A Monte Carlo method is a set of mathematical approaches based on random number generation that are used to simulate values of stochastic variables, given its their cumulative distribution functions [34]. Monte Carlo simulations are a type of investigation tool utilised in many fields of scientific research and industrial development, and they are recognised as "the gold standard" for characterizing particle movement inside a medium [35, 36].

2.4.1 Geant4

Geant4 (GEometryANd Tracking) [1, 37, 38] is a widely used Monte Carlo toolkit that evolved in 1994 from a CERN-based research project to replace the previous Monte Carlo code, Geant3, which was released in 1974 [39]. Geant4's initial public release was in 1998, and it was written in C++ to take advantage of the object-oriented technology. Geant4 differs from several other regularly-used general purpose Monte Carlo codes, such as FLUKA [40], MCNP [41], and PHITS [42], which are FORTRAN-based platforms [37, 43].

Geant4 is a software toolkit for simulating a particle passage through matter. It has been widely used in a number of studies and projects, including high energy physics, astrophysics and space science, medical physics, and radiation protection. Its functionality and modelling capabilities are being expanded, while its performance is being simultaneously improved [37]. The Geant4 simulation toolkit [1] includes extensive detector and physics modelling capabilities integrated in a flexible package [38].

Geant4 includes a comprehensive set of features such as tracking, geometry, physics models, and hits. The physics processes encompass a wide span, including electromagnetic, hadronic, and optical processes, as well as a huge collection of data on long-lived particles, materials, and elements, over a wide energy range spanning from eV in some cases to TeV in others. It was developed and built to clearly reveal the physics models being used, to handle complicated geometries, and to allow for easy customization for best use in a variety of applications [1].

Because Geant4 is a "toolkit", a user cannot simply "run" it "out of the box", but must instead create an application based on the Geant4 kernel. A user application must provide at least a description of the experimental setup in which primary particles are created and tracked while interacting with the target. Secondary particles that emerge from the interactions in the experimental setup are also tracked. The presence of three classes, *DetectorConstruction*, *PrimaryGeneratorAction*, and *PhysicsList*, are the minimal need for

a Geant4 application [43].

Furthermore, Geant4 offers interfaces that allow users to engage with their application and save their findings. The toolkit includes visualisation drivers and interfaces, graphical user interfaces, and a flexible framework for persistency [37].

A worldwide collaboration of over 100 scientists from various cooperating institutions, High Energy Physics projects, and universities designed and developed Geant4. In terms of the size and extent of the code, as well as the number of participants, the Geant4 Collaboration is considered one of the largest and most ambitious projects of its kind. It has proven that robust software engineering practises and object-oriented technology can be used successfully to develop a coherent and maintainable software product, even when dealing with the fast-changing and open-ended needs of physics research [1]. Major modifications to the toolkit have been made in recent years to suit the demands of the user community and to efficiently use the increased computing power made accessible by technological developments [38].

2.5 Atomic De-excitation in Geant4

Since 1999, an atomic de-excitation module has been provided in Geant4 and has been extensively verified [44–46]. Models for the formation of vacancies in atomic shells and the consequent emission of fluorescence X-rays and Auger electrons are also included [16]. This feature was first made available in December 2011 (version 9.5) for both the "Low energy" and "Standard" electromagnetic physics processes of Geant4 through the development of a unified general interface to handle atomic de-excitation [46–48].

2.5.1 Electromagnetic Sub-packages

The standard electromagnetic package [1, 37] simulates electromagnetic interactions between particles with energies ranging from 1 keV to 10 PeV. It is used to model particle interactions of interested for CERN's Large Hadron Collider experiments and other high-energy physics research. This package is also utilised in a variety of different application fields, including medical and space science [46].

This package contains models for ionisation, bremsstrahlung, photoelectric effect, Compton scattering, gamma conversion, and many other electromagnetic processes. The Geant4 toolkit structure allows for alternative methods when many models with varying levels of accuracy and CPU efficiency of simulation coexist for each physical process. The electromagnetic sub-package "Low energy" [37] offers an alternate set of models that extends

Geant4's usefulness at lower energy levels (by default down to 100 eV) [46].

2.5.2 Geant4 Data Libraries

The Geant4 unified interface for atomic de-excitation is capable of simulating both Auger electron and X-ray fluorescence emission (in this context, Coster–Kronig electrons are also referred to as "Auger electrons" and are treated similarly by the de-excitation interface). This interface makes use of atomic de-excitation data from the Livermore Evaluated Atomic Data Library (EADL) [48, 49].

This evaluated data library includes a collection of physical parameters for elements with atomic numbers ranging from 6 to 100, including electron binding energies for all sub-shells and the probabilities of radiative and non-radiative transitions between sub-shells [44].

In *EADL*, the energies of relaxation products are computed as the difference between the binding energies of the shells participating in the transition, as derived from Scofield's theoretical calculation [50]. The probabilities for radiative transitions are derived from Scofield-Hartree–Slater calculations [50], whereas the probabilities for non-radiative transitions are derived from Dirac–Hartree–Slater calculations by Chen et al. [51] with Hubbell corrections [46, 52].

The Geant4 Atomic De-excitation package can only deal with singly ionised atoms; this property corresponds to the conditions under which the *EADL* data were generated and does not represent a limitation on electromagnetic processes that generate no more than one initial vacancy. All of the assumptions that underpin the *EADL* calculations also hold true for the Geant4 relaxation model that is based on them: for example, the binding energies of an ionised atom are considered to be the same as those of a neutral atom in the Geant4 model (no systematic theoretical or experimental compilations of the binding energies of ionised atoms are available) [44].

2.5.3 Files' Structure in Geant4 Libraries

The *EADL* library data is kept in external data files; their location in the file system is transparent to the software implementation, and their use in the physics algorithms is independent of the data file format. In comparison to the original *EADL* data library, the data file system is designed with higher granularity of data files: binding energy data, radiative and non-radiative transition probabilities are held in independent files for each

element of the periodic table.

This design enables data to evolve with significant flexibility and independence from the code that handles it. Updated values derived from more recent data compilations or even from individual significant measurements may be used transparently as alternate sources of data for the data driven simulation model without requiring any adjustment to the software implementation [44].

2.5.4 PIXE in Geant4

Ionisation by incident protons or secondary electrons, for example, causes vacancies in the target atomic electronic structures. According to the related ionisation cross section, this process samples the element and shell from which the electron is emitted [49].

An electron from an outer shell, together with the emission of an X-ray photon, fills this vacancy in Geant4. This emission line's energy is unique to the emitting atom. The two Geant4 electromagnetic physics sub-categories provide comprehensive sets of physics processes and models that are easily accessible to users through periodically tested and updated "physics constructors", as suggested by both Geant4 electromagnetic physics working groups [49].

These constructors hold a list of particles and processes that allow for complete particle transport through matter utilising only electromagnetic interactions. They're based on a variety of different physics models [49].

The component's interface is defined by the *G4AtomicDeexcitation* class, which is responsible for driving the relaxation process from a given vacancy and returning the resultant secondary products. Through the *G4AtomicDeexcitation* interface, all Geant4 processes that create a vacancy in an atom connect with the Atomic De-excitation component [44]. *G4teoCrossSection* and *G4empCrossSection* are the classes that implement the interface to PIXE ionisation cross sections [46]. The atomic de-excitation simulation in Geant4 is divided into two stages: [16]

1. primary process, such as photoelectric effect, Compton scattering, or ionisation, creates a vacancy. On the basis of the cross section of the provided process, the sub/shell where the vacancy is generated by a process is sampled. An additional PIXE cross section is employed for the ionisation process [16].

2. Starting with the vacancy generated by the main process, the relaxation cascade

is initiated. Based on the corresponding transition probabilities, fluorescence X-rays, Auger electrons, or Coster-Kronig transitions are created by radiative and non-radiative transitions, and the resulting secondary electrons or X-rays are further tracked by Geant4 [16].

If the energy of the relaxation products (fluorescence photons, Auger and Coster-Kronig electrons) exceeds the production threshold, they are emitted; otherwise, an equivalent energy is converted into a local energy deposit. A Geant4 user application may be used to establish secondary production thresholds [44].

2.5.5 Ionisation Cross Sections Models

To simulate PIXE, Geant4 ionisation processes were essential to calculate the ionised sub/shells, for which values of atomic shell ionisation cross sections are required. Only the ionisation processes of the "Low energy" sub-package employed PIXE. The very first attempts to calculate ionised shells depended on Gryzinski cross sectional semi-classical calculations [53], which were ultimately replaced by another model, detailed in ref [54], created to replicate the collection of experimental data from Paul and Sacher. However, this model does not produce the expected outcomes, limiting its applicability [46].

In Geant4, there are presently three different PIXE cross sections data sets to generate a vacancy in a shell: [16]

1. The first collection of shell cross sections, called the *"Empirical"* set by Ben Abdelouahed [14], is the default Geant4 set for PIXE simulation in the "Standard" and "Low energy" sub-categories. It includes the empirical set produced by Paul, Sacher, and Bolik [55, 56] for incident protons and α particles, as well as the empirical set created by Orlic, Saw, and Tang [57] for incident protons [49]. These works were chosen based on their scientific value and success [46]. All of the original works' limitations and assumptions apply precisely to their corresponding Geant4 implementation. The Orlic et al. model for protons is applicable throughout an energy range of 0.1 to 10 MeV, and the atomic numbers for which the model provides all L sub-shells values (L_1, L_2, and L_3) correspond to Z values ranging from 41 to 92 [46].

2. The second set of cross sections, known as the *ECPSSR_FormFactor* set, is based on a polynomial approximation to universal ionisation cross sections of K, L, and a selection of M shells calculated from *ECPSSR* theory for incident proton and α particles.

Table 2.2: Summary of the characteristics of the ionisation cross sections that were employed in this work.

Geant4 name of cross section set (abbreviation)	Shells	Particles	Elements	Energy Range	Refs.
Empirical (Empirical)	K, L	Protons and α particles for K shells; protons for L shells	Z = 6–92 for K shells and protons; Z = 6–92 for K shells and α particles; Z = 41–92 for L shells and protons	Depends on Z	[55–57]
ECPSSR_FormFactor (FormFactor)	K, L, M	Protons and α particles	Z = 6–92 (K, L), Z = 62–92 (M)	0.1–100 MeV (K, L shells) 0.1–10 MeV (M shells)	[58, 59]
ECPSSR_Analytical (Analytical)	K, L	Protons and α particles	Z = 6–93 (K, L)	$\sim$ 0.1 MeV up to $\sim$ 1 GeV (depends on Z)	[14, 46]

Taborda and colleagues recently developed the *ECPSSR_FormFactor* set using the Basbas method, and it is detailed in [58, 59]. This set includes the 0.1–100 MeV range for K and L shells, as well as the 0.1–10 MeV range for M shells [49]. The *ECPSSR* theory is presently the most widely accepted theory in the scientific community for reproducing shell ionisation cross section values. As a result, *ECPSSR* is regarded as the best option for K and L sub/shells cross sectional calculations in Geant4. It was implemented in two types of models: analytical models and interpolated models [46]

3. *ECPSSR_Analytical* is the third set, which is based on an implementation of the *ECPSSR* theory proposed by Ben Abdelouahed for the description of K and L sub/shells ionisation for incident protons and α particles (see more information in [14, 46]) and it has a wider energy range applicability than the first two sets. It is utilised by default when the other sets' energy boundaries are exceeded [49].

Furthermore, in Geant4, any ion other than proton or α may be simulated by applying speed and charge scaling to proton Plane Wave Born Approximation *(PWBA)* ionisation cross section data sets. This approximation, however, is not realistic for slow heavy ions, where the Coulomb correction terms, which the *PWBA* ignores, can become extremely important [16, 60, 61].
The scaling relation is:

$$\sigma_h(E) = Q^2 \cdot \sigma_p(E \cdot \frac{M_p}{M_h}) \tag{2.11}$$

Where E is the incident particle's kinetic energy, M_h is its mass, Q^2 is the square of the effective electric charge [62] in electron charge units, and M_p is the proton mass. Shell ionisation cross sections for electron and positron are already included in the "Low energy" sub-package ionisation models, which sample shell vacancies [46].

Table 2.2 provides an overview of the ionisation shell cross sections sets that are available for use in Geant4's "Standard" and "Low energy" electromagnetic physics construc-

tors for PIXE simulation with incoming protons and α particles. I specify which atomic shell these models apply to, which incoming particles (protons and/or α particles) were used, which atomic element interacted, and the incidence energy range applicability. For completeness, full references are also included. The abbreviation is used in the first column to name the sets of shell ionisation cross sections and is provided in parenthesis [49].

The values of the shell cross sections can be obtained with relative ease in any Geant4 user application: first, the shell cross sections set must be selected using the *SetPIXECrossSectionModel* method of the universal atomic de-excitation interface presented in [46], passing as an argument the name of the set as given in column 1 of table 2.2. Then, for a given incident particle, atomic target element, atomic shell, and incident kinetic energy, the *GetShellIonisationCrossSectionPerAtom* method gives the cross sections values [49].

2.5.6 X-ray Fluorescence Models

The Atomic Relaxation component of Geant4 [44, 46], handling the emission of X-rays and Auger/Coster-Kronig electrons, is based on *EADL* [63], which provides the atomic electron binding energies and the radiative (fluorescence) and non-radiative (Auger and Coster–Kronig electrons) transition probabilities. The tabulated data are used to calculate the X-ray fluorescence lines [46] for Geant4 applications, whenever the atomic de-excitation has to be considered by the model. Validation studies of the G4-PIXE Package such as Pia et al. 2011 [64] and Guatelli et al. 2007 [44] showed that the *EADL* can reproduce the X-ray lines originating from K and L shell transitions within an accuracy of a few percent when compared to the experimental dataset by Deslattes et al. 2003 [65]. Hartree-Slater (HS) methods [66], were used to calculate the radiative transition probabilities reported in *EADL*. However, following the work of Campbell et al. [67, 68] Cohen et al. [2] recommended the Hartree-Fock approach [50] rather than the Hartree-Slater model [66].

A user of the Atomic Relaxation component of Geant4 may enable and disable fluorescence, Auger electron emission, and PIXE ionisation cross sections using macro commands, either for the entire simulated set-up geometry, or for selected sections of the sample geometry (using *G4Regionobjects*) [37, 46].

Chapter 3

ANSTO Ionisation Cross Sections

I revised the existing G4-PIXE based on the recommendations of D. D. Cohen and R. Siegele, international leaders in experimental PIXE and associated theoretical modelling.

This chapter is a modified version of the published work:
S. Bakr, D.D. Cohen, R. Siegele, S. Incerti, V. Ivanchenko, A. Mantero, A. Rosenfeld, S. Guatelli, (2018) **"Latest Geant4 developments for PIXE applications"**, *Journal of Nucl. Instruments Methods Phys. Res. Sect. B Beam Interact. with Mater. Atoms,* vol. 436, no. October, pp. 285–291.

https://doi.org/10.1016/j.nimb.2018.10.004

This work presented at the **Ion Beam Analysis** conference 2019, (Antibes, France), **24th Geant4 Collaboration** meeting 2019, (Jefferson Lab, New York, USA), **NSTLI seminars** 2019, (Australia's Nuclear Science and Technology Organization (ANSTO), Sydney, Australia), **Heavy Ion Accelerator** Symposium 2018, (Australian National University, Canberra, Australia), **Third Geant4 International User** conference 2018, (Bordeaux, France), **MedPhys 2017**, (University of Sydney, Sydney, Australia), **Geant4 User Workshop** 2017, (Sege Hotel, Wollongong, Australia), **Geant4 Collaboration** meeting 2017, (University of Wollongong, Wollongong, Australia) and **Innovation in Radiation Applications** 2017, (University of Wollongong, Wollongong, Australia).

3.1 Abstract

I describe the recent inclusion in Geant4 of state-of-the-art proton and α particle shell ionisation cross sections based on the ECPSSR approach as calculated by Cohen et al., called here *ECPSSR_ANSTO*. The new ionisation cross sections have been integrated into Geant4. I present a comparison of the fluorescence X-ray spectra generated by the

Table 3.1: Projectile kinetic energy and target element ranges of the *ECPSSR_ANSTO* cross sections for incident protons and α particles.

	Kinetic Energy	Target elements		
	K, L, M	K	L	M
Proton	0.2-5.2 MeV	6-92	25-92	60-92
α particle	0.2-20.2 MeV			

ECPSSR_ANSTO set of cross sections and, alternatively, the currently available sets of Geant4 PIXE cross sections. The comparisons are performed for a large set of sample materials spanning a broad range of atomic numbers. The two alternative PIXE cross sections approaches (Geant4 and ANSTO) have been compared to existing experimental measurements performed at ANSTO with gold, tantalum and cerium targets of interest for nanomedicine applications. The results show that, while the alternative approaches produce equivalent results for vacancies generated in the K and L shell, differences are evident in the case of M shell vacancies. This work represents the next step in the effort to improve the Geant4 modelling of the atomic relaxation and provide recommended approaches to the Geant4 user community. This new Geant4 development is of interest for applications spanning from life and space to environmental science.

3.2 Introduction

Particle Induced X-ray Emission (PIXE) describes the physical phenomenon of charged particles, such as protons, α particles and heavier ions, incident on a target, which ionises some atoms by removing one or more inner shell electrons from the K, L, or M sub/shells. The shell vacancy is subsequently filled by an electron of an outer shell. This process is accompanied by the emission of characteristic X-rays or Auger electrons and Coster-Kronig transitions with energies corresponding to the difference in the binding energies of the involved atomic shells.

The Geant4 toolkit [1] includes analytical and data driven PIXE cross sections for electrons, protons and heavier charged particles [38]. This chapter describes the recent inclusion in Geant4 of PIXE cross section for proton and α particles, which are based on the-state-of-the-art recommendations documented in (Cohen, 2015) [2] (1985, 86 and 89) [60, 69, 70], as alternative to the already available other Geant4 PIXE cross sections.

The novel Geant4 *ECPSSR_ANSTO* approach provides the ionisation cross section of the K, L, and M shells for incident protons and α particles in the energy ranges displayed in table 3.1.

The advantage of the proposed cross sections is that they have been extensively validated against PIXE experimental measurements by many PIXE labs including the Australian Nuclear Science and Technology Organisation [2]. This project is motivated by the constant effort to improve the physics models of Geant4 by including available state of the art physics models.

This work benefits applications of Geant4 in environmental physics, geology, archaeology, space science and medical physics. It may also impact significantly novel application domains such as nanomedicine, where an accurate modelling of atomic relaxation is required [44]. Schlathölter et al. [71], comments that the underlying nano-scale mechanism of nano-particle enhancement in proton therapy remains poorly understood and therefore, it is important to accurately characterise the secondary radiation field produced by the protons when incident on high-Z nano-particles, including the characteristics X-rays and Auger electrons deriving from the atomic relaxation. Porcel E et al. [72, 73] have shown enhanced damage to DNA in the presence of Pt and Gd nano-particles irradiated by fast helium ions and carbon ions and comment that Auger electrons play a significant role in the production of indirect damage of the radiation in the biological medium, which needs to be quantified.

3.3 The Geant4 Atomic Relaxation

The Geant4 Atomic Relaxation approach includes models for the generation of vacancies in atomic shells and the subsequent emission of fluorescence X-rays and Auger electrons. The development of this model were firstly described in (Guatelli et al, 2007a), [44] and was then improved in the following years [46, 48]. In Geant4, atomic relaxation simulation is articulated through two stages:

1. The creation of a vacancy by a primary process e.g. photoelectric effect, Compton scattering and ionisation. The shell (or sub-shell) where the vacancy is created by a process is sampled on the basis of the cross section of the given process. For the ionisation process an additional PIXE cross section is used. At each simulation step of charged particle number of vacancies, their position in space and shell types are sampled according to the PIXE cross section.

2. The relaxation cascade is triggered, starting from the vacancy created by the primary process. Fluorescence X-ray, Auger electrons or Coster-Kronig transitions are generated through radiative and non-radiative transitions, based on the respective transition probabilities and produced secondary electrons or γ are further tracked by Geant4.

There are currently three alternative PIXE cross sections data sets in Geant4 to generate a vacancy in a shell:

- The *"Empirical"* set, where K and L sub/shells ionisation cross sections are based on empirical and semi-empirical compilations by Paul et al. and Orlic et al. [49].
- The *"ECPSSR_FormFactor"* set, based on a polynomial approximation of the ionisation cross sections of K, L and a selection of M shells calculated by Taborda et al. using Basbas method but with the *ECPSSR* theory for incident protons and α particles [49].
- The *"Analytical"* set, based on the *ECPSSR* theory adapted by Abdelouahed et al, [14] for the description of K and L shells ionisation for incident protons and α particles [49].

In addition, it has been possible in Geant4 to simulate any ion, other than proton or α particle, by applying speed and charge scaling to the proton Plane Wave Born Approximation (PWBA) ionisation cross section data sets. However, this approximation is not accurate for slow heavy ions where the Coulomb correction terms, ignored by the PWBA, can become very significant [60, 61].

3.4 Materials and Methods

The *ECPSSR* theory has been developed by Brandt and Lapicki for both K and L sub/shells ionisation by light ions $\frac{Z_1}{Z_2} < 0.3$, where Z_1 and Z_2 refer to the charges of the projectile and the target atom, respectively [61]. Cohen and Harrigan published *ECPSSR* K and L sub/shells ionisation cross sections for both protons and α particles bombardment for ion energies from 0.2 to 10 MeV and for a wide variety of target atoms, from carbon to curium. These tables supersede all previous tables of this type as they supply actual ionisation cross sections and do not rely on the scaling of some universal cross section function to obtain the required cross sections [2, 60, 69, 70].

Once included in the Geant4 toolkit, the *ECPSSR_ANSTO* cross sections have been compared directly to the alternative data sets already available in Geant4 to assess the level of agreement of the different approaches. The impact of the alternative ionisation cross section sets, *ECPSSR_ANSTO* and *ECPSSR_FormFactor*, has been quantified in terms of number of fluorescence X-rays generated per incident projectile.

Thirteen target materials (Al, Si, Fe, Zr, Te, Ce, Gd, Dy, Ta, W, Pt, Au, U) have been chosen, from low to high atomic number Z. Monochromatic beams of protons (1.00, 2.50,

3.00, 5.00 MeV) and α particles (5.00, 9.50, 15.00 MeV) are incident on 25 μm thick targets along the direction of the incident beam. The lateral sizes are 50 μm. The production threshold of secondary particles is ignored. The fluorescence X-rays have been counted once they are generated in the target. The default atomic relaxation library of Geant4, based on the Evaluated Atomic Data Library EADL [63], has been used to calculate the emission rates of the fluorescence X-ray, once the vacancy has been generated [49]. Two different versions of the *ECPSSR_FormFactor* have been considered in this work, which are included in *G4EMLOW 6.50* and *G4EMLOW 6.54* data libraries. The *G4EMLOW 6.50* and *G4EMLOW 6.54* are the Low Energy Electromagnetic data libraries, released with Geant4 10.3 and Geant4 10.4 beta versions, respectively. Note that the existing Geant4 PIXE *Empirical* and *Analytical* cross section sets [46] have not been considered in this work as they generate only K and L vacancies.

Finally, the Geant4 PIXE Package, with the *ECPSSR_ANSTO* cross sections, has been compared to experimental measurements performed at ANSTO using the 6 MV SIRIUS Tandem Accelerator. In this case, protons and α particles are incident on 25 nm thick cerium and tantalum and 100 nm thick gold targets along the direction of the incident beam, similarly to the ANSTO experimental setup. Using a 3.00 MeV proton beam, cerium, tantalum and gold targets are considered because of their possible application in High-Z nano-particle radio-enhancement in proton therapy [74, 75]. In addition, a tantalum target has been used for 10.00 MeV α particle beam. Relative fluorescence spectra are presented.

3.4.1 Experimental Setup

PIXE spectra were experimentally measured at the ANSTO heavy ion micro-probe beamline using 3.00 MeV proton and 10.00 MeV He^{+2} ion beams with currents varying between 0.5 and 2.5 nA. For X-ray detection, a 100 mm^2 high purity Ge detector with a solid angle of 90 msr was used. The detector has a 25 μm thick Be window. To prevent the scattered protons from entering the detector and to reduce the low energy X-ray yield from light elements such as the underlying Si in some of the samples, a 100 μm thick Mylar absorber (or filter) was placed in front of the detector.

The data were collected using the Data Acquisition System mpsys4 from Melbourne University together with a Canberra Model 2060 digital signal processor. The irradiated samples were 100 nm thick Au layer on silicon and 25 nm TaO layer on graphite. Additionally, a sample of CeO_2 embedded in a boron oxide pellet was used.

Since this study was a preliminary attempt to refine Geant4 X-ray emission spectra, I generated spot values from Geant4 calculations to compare against continuously measured experimental spectra, it was impractical to use Geant4 to define peaks of definite area. Hence, as a first approximation, matches were made only with peak heights, not peak areas. Clearly, it is desirable that later work should attempt to more finely model the entire energy range spanned by the experimentally observed X-ray emission.

3.5 Results and Discussion

3.5.1 Ionisation Cross Section Comparison

The proposed ANSTO ionisation cross sections have been calculated for all elements. As example figures 3.1 and 3.2 show the cross sections for a gold target against the kinetic energy of incident protons and α particles, respectively.

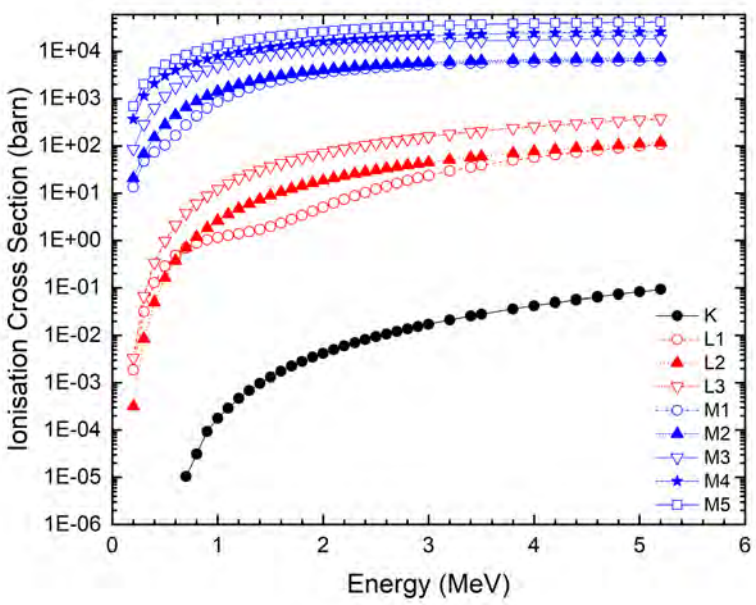

Figure 3.1: ANSTO proton ionisation cross sections for K, L, and M sub/shells for a gold target.

As expected, the cross sections increase with the vacancy being originated in the K, L, and M sub/shells.

The ionisation cross sections calculated by means of the *ECPSSR_FormFactor* with both *G4EMLOW 6.50* and *6.54* libraries and *ECPSSR_ANSTO* approaches were compared

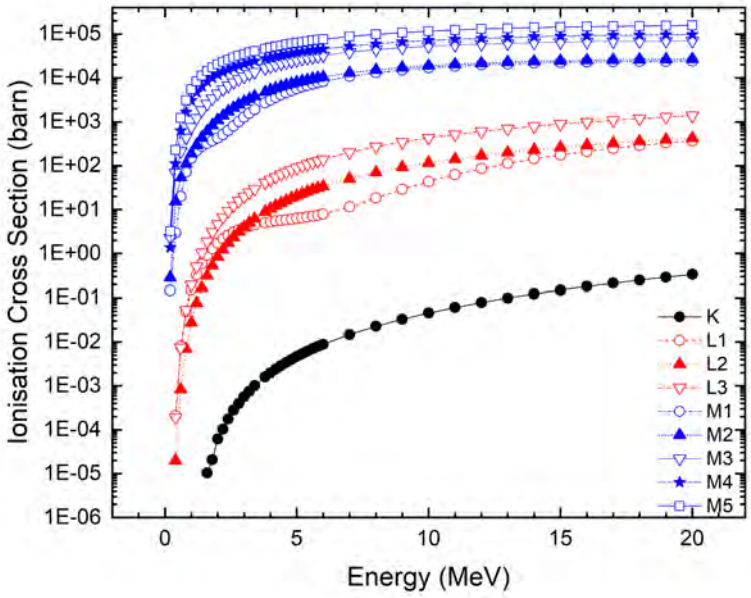

Figure 3.2: ANSTO α ionisation cross sections for K, L, and M sub/shells for a gold target.

for a set of different target materials. In this work, *G4EMLOW 6.50* and *6.54* ionisation cross sections libraries are called *ECPSSR_FormFactor v.6.50* and *v.6.54*, respectively.

Figures 3.3 to 3.7 show the ratio $R = \frac{\sigma_{ECPSSR\_FormFactor}}{\sigma_{ECPSSR\_ANSTO}}$, for K, L, and M shells and sub-shells with respect to the incident proton and α particle kinetic energy for low (silicon), medium (molybdenum) and high Z (gold) target materials. These figures illustrate how ANSTO's calculated ionisation cross sections behave in comparison to Geant4 *ECPSSR_FormFactor* ones.

It can be observed that in general, for the K shell, an agreement within 10% was observed for proton energies below 2.50 MeV for low Z target materials. Larger differences ($\sim$ 25%) are observed for high Z targets materials for proton energies below 1.50 MeV. Differences up to $\sim$ 10% are observed for incident α particles of kinetic energies higher than 15.00 MeV for low Z sample materials, while differences within $\sim$ 10% are observed for high Z sample materials for all considered incident α particle energies higher than 4.00 MeV.

For L sub-shells, the differences are less than 5% for all proton energies lower than 3.00 MeV, while they are less than 20% in the range 3–5.2 MeV for medium Z targets. For high Z materials differences, up to $\sim$ 10% are observed in the entire proton kinetic energy range. Differences between 10% and 20% are observed for medium and high Z

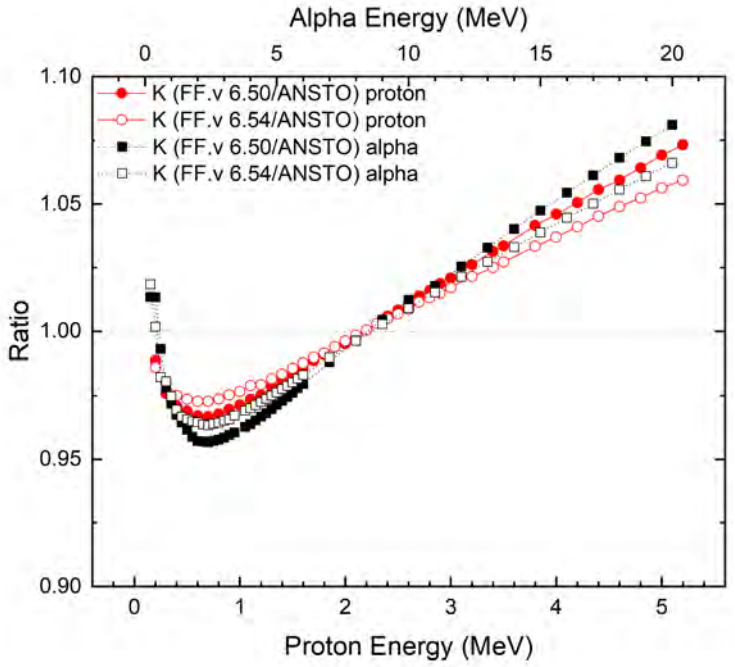

Figure 3.3: K shell ionisation cross section ratios for protons and α particles incident on a silicon target.

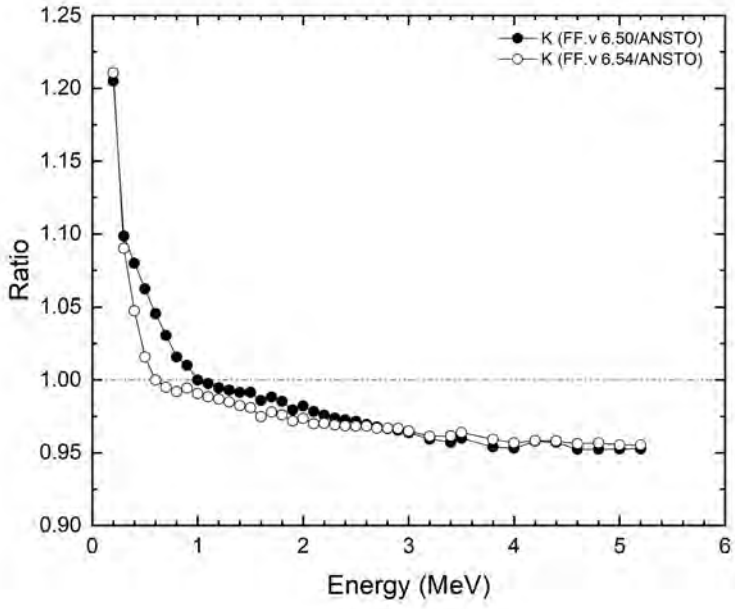

Figure 3.4: K shell ionisation cross section ratios for protons incident on a molybdenum target.

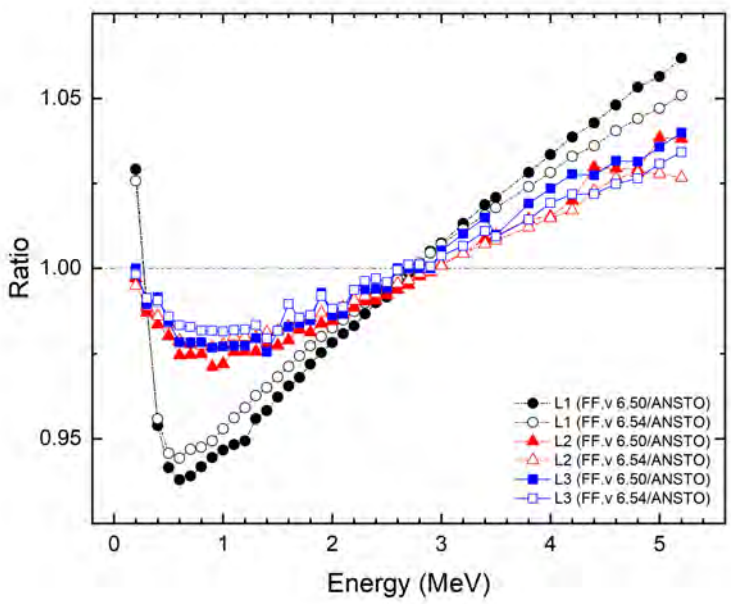

Figure 3.5: *L* sub-shells ionisation cross section ratios for protons incident on a molybdenum target.

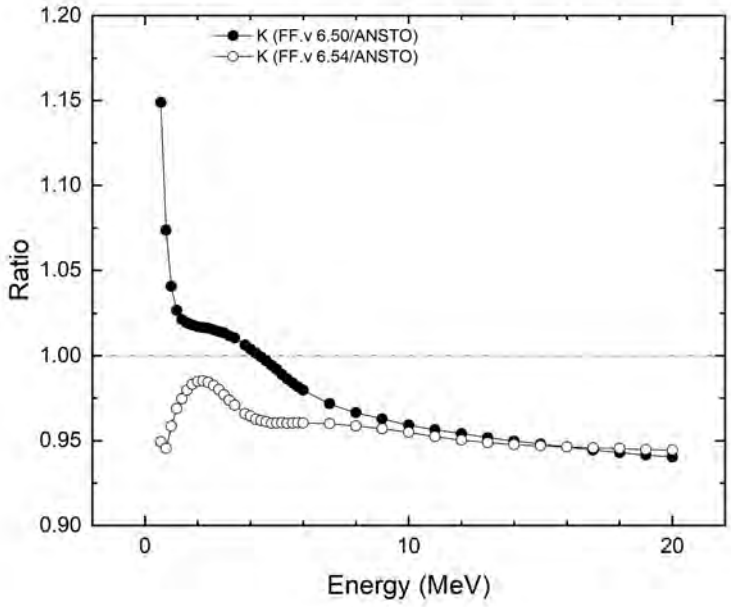

Figure 3.6: *K* shell ionisation cross section ratios for α particles incident on a molybdenum target.

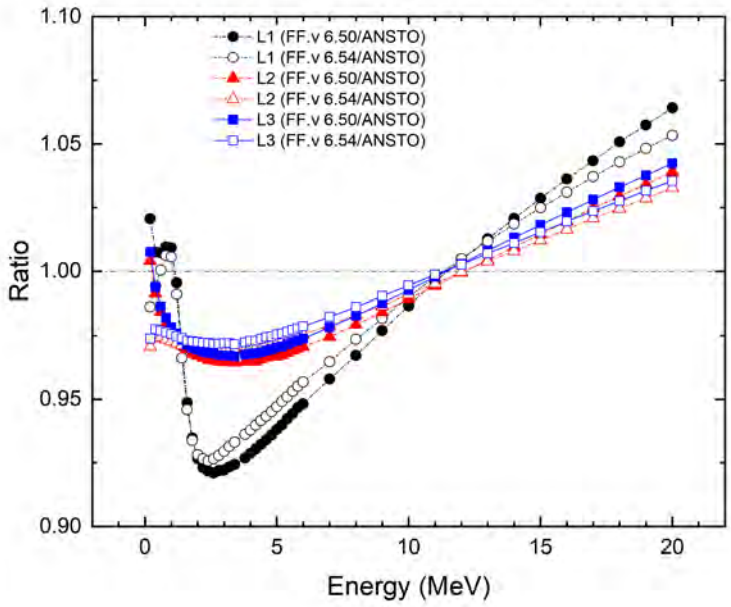

Figure 3.7: L sub-shells ionisation cross section ratios for α particles incident on a molybdenum target.

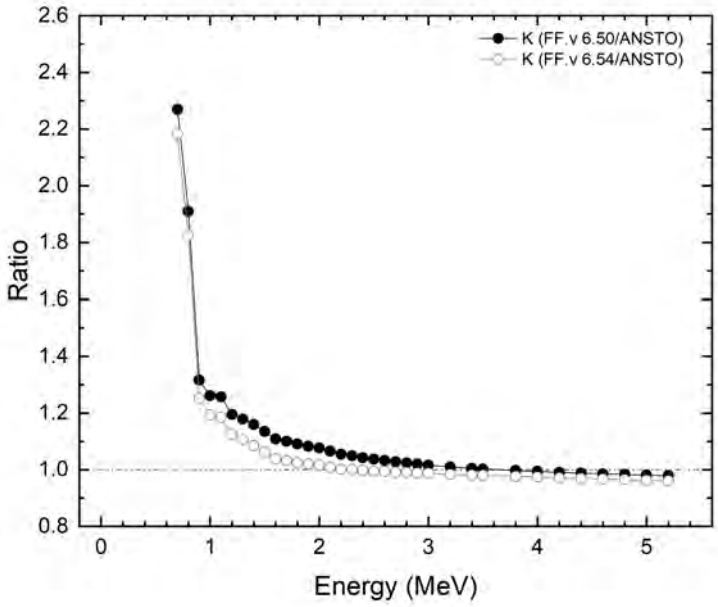

Figure 3.8: K shell ionisation cross section ratios for protons incident on a gold target.

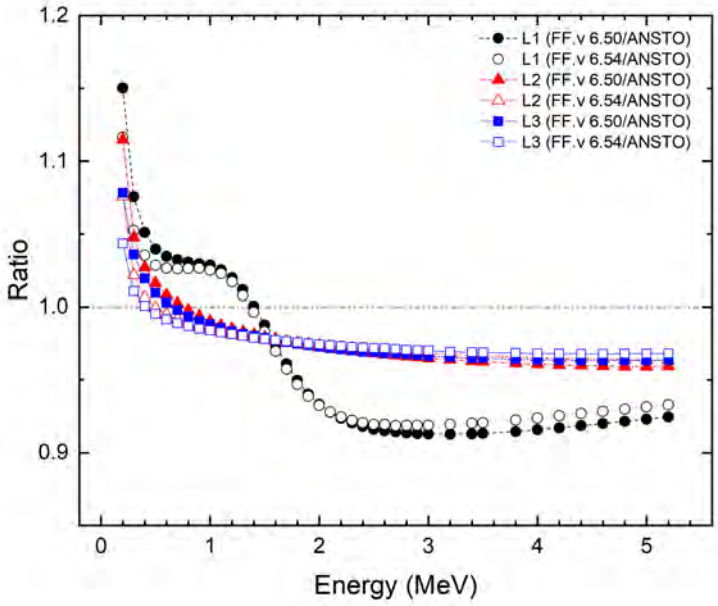

Figure 3.9: *L* sub-shells ionisation cross section ratios for protons incident on a gold target.

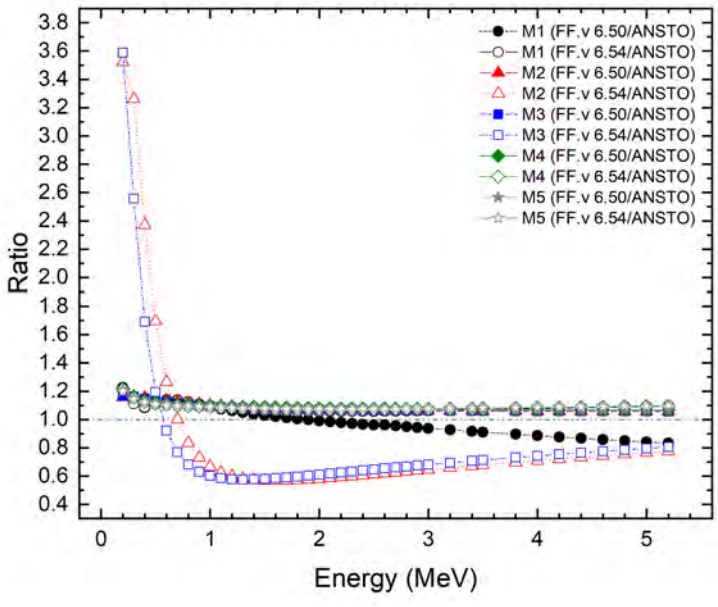

Figure 3.10: *M* sub-shells ionisation cross section ratios for protons incident on a gold target.

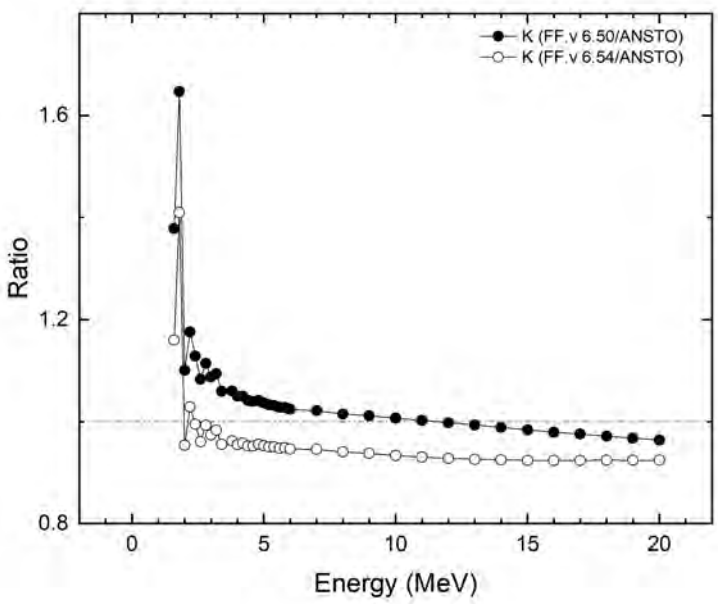

Figure 3.11: K shell ionisation cross section ratios for α particles incident on a gold target.

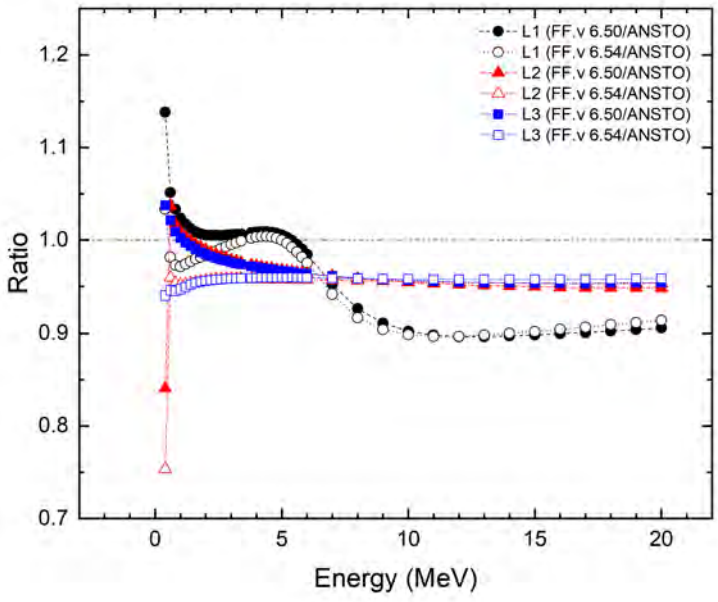

Figure 3.12: L sub-shells ionisation cross section ratios for α particles incident on a gold target.

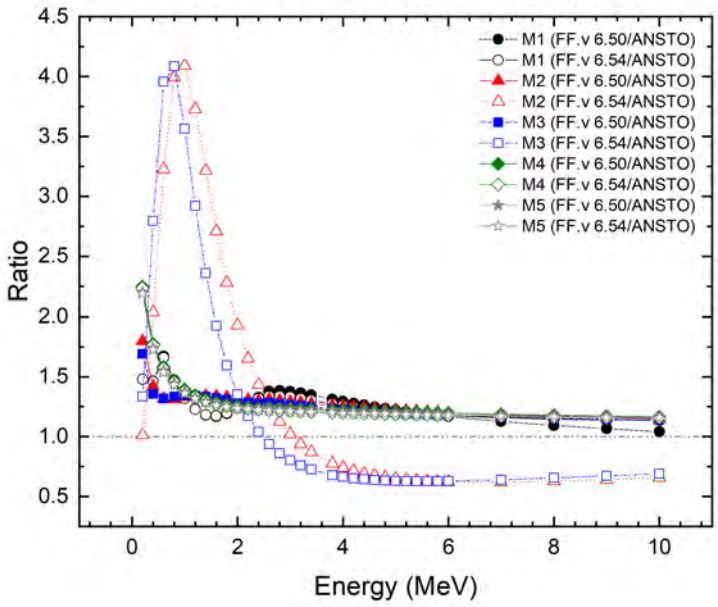

Figure 3.13: *M* sub-shells ionisation cross section ratios for α particles incident on a gold target.

targets, respectively, for the entire α particle energy range.

The *K* and *L* sub/shells ionisation cross sections of the *ECPSSR_FormFactor* model are closer to the *ECPSSR_ANSTO* when calculated by means of the Geant4 Low Energy EM library *6.54* version.

For *M* sub-shells, the differences between *ECPSSR_FormFactor v. 6.50* and *ECPSSR_ANSTO* are less than 20% for all proton energies less than 1 MeV, while they are less than 10% in the range 1–5.2 MeV, except for the M_1 sub-shell ionisation cross sections. In this case the differences are up to 40% for the entire proton energy range. Differences up to $\sim 25\%$ and $\sim 15\%$ have been found for α particles with energy 0.2–3 MeV and 3–10 MeV, respectively. In contrast, for M_2 and M_3 sub-shells, there are significant differences ($\sim 300\%$) for *ECPSSR_FormFactor v. 6.54* data sets when compared to *ECPSSR_FormFactor v. 6.50* and *ECPSSR_ANSTO*.

In general, it can be observed that differences are within $\sim 25\%$ for *ECPSSR_FormFactor v. 6.50* and *ECPSSR_ANSTO*. At lower energies, for both incident protons and α particles, the *ECPSSR_FormFactor* predicts consistently higher cross sections for all *K*, *L*, and *M* sub/shells. At higher energies and Z sample materials it seems that this trend inverts with the *ECPSSR_ANSTO* producing more ionisations for M_1 and *L* sub-shells.

3.5.2 Modelling X-ray Emission by Means of the *ECPSSR_ANSTO* Cross Sections

As an example of X-ray emission generated with the *ECPSSR_ANSTO* cross sections, figures 3.14 and 3.15 show the X-ray emission calculated in gold, deriving from vacancies in the L and M sub-shells generated by an incident 3.00 MeV proton and 9.50 MeV α particles, respectively. The results are compared for the *ECPSSR_FormFactor v. 6.50, v. 6.54* and *ECPSSR_ANSTO* data sets. The standard deviation of these results is less than 1.5%. No X-ray lines are shown for the Geant4 *Analytical* and *Empirical* approaches because they do not provide ionisation cross sections for the M sub-shells. It can be observed that the X-ray emission rates generated with the *ECPSSR_FormFactor* in the case of M sub-shells are higher than the ones generated with the *ECPSSR_ANSTO* cross sections. This reflects the fact that the *ECPSSR_FormFactor* cross section is higher than the *ECPSSR_ANSTO* one, as shown in figure 3.10. The emission rates of X-rays deriving from vacancies in the L sub-shells are almost identical (see figures 3.14 and 3.15).

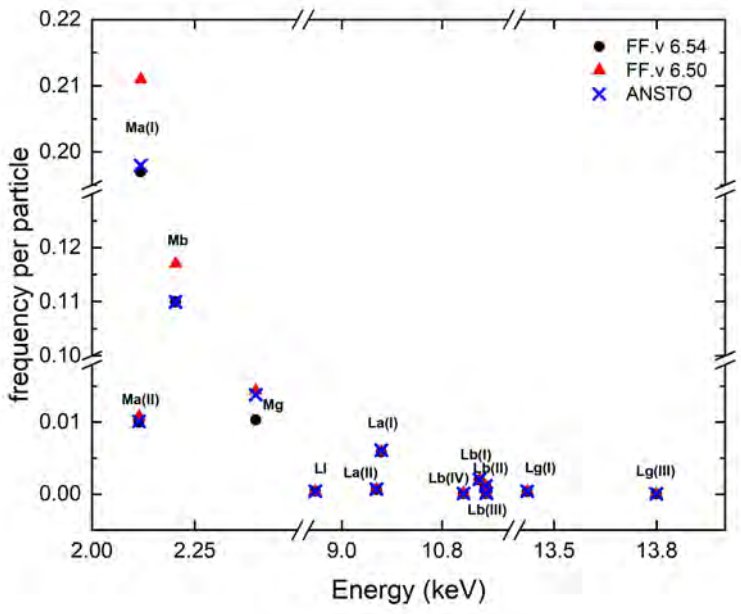

Figure 3.14: X-ray emission generated by 3.00 MeV incident protons incident on a gold target.

Tables 3.2 and 3.3 list the number of X-rays generated in a gold target per incident 3.00 MeV proton and 9.50 MeV α particle, respectively. For M-lines, it is clear that the frequency calculated via *ECPSSR_FormFactor* cross section is higher than the one calculated with the *ECPSSR_ANSTO* data set. For L-lines, the closest model to *ECPSSR_ANSTO* is the Geant4 Analytical model and the probabilities obtained with the *ECPSSR_FormFactor*

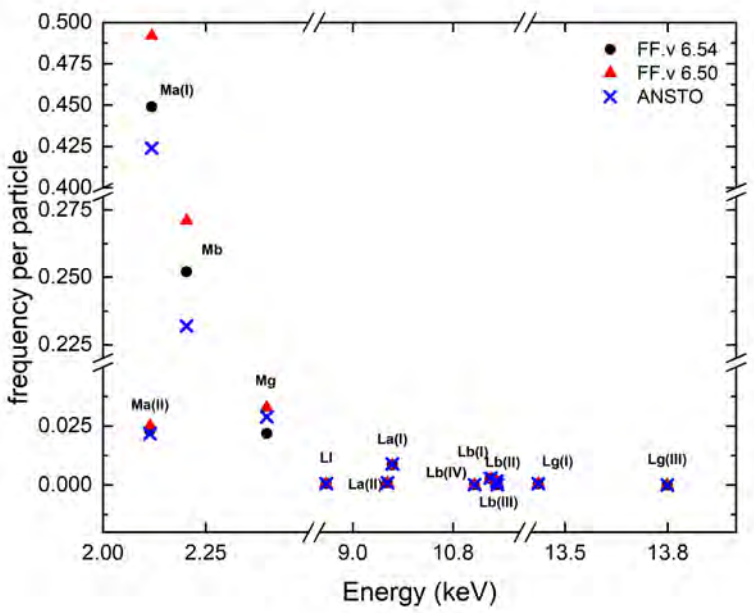

Figure 3.15: X-ray emission generated by 9.50 MeV α particles incident on a gold target.

and Empirical sets are lower than *ECPSSR_ANSTO*.

3.5.3 Validation of the Geant4 PIXE Package Against Experimental Measurements

The X-ray emissions calculated by the Geant4 PIXE Package with the *ECPSSR_ANSTO* and *ECPSSR_FormFactor* ionisation cross sections, have been compared against experimental spectra. Figures 3.16 to 3.19 show the comparison of the X-ray emission frequencies per incident particle, calculated by means of ANSTO and Form Factor cross sections, against experimental measurements. The Geant4 X-ray emissions have been normalized to the highest peak of the experimental spectra.

Results are shown for incident protons and α particles for the targets under study. It can be observed that the X-ray emission rates calculated with the *ECPSSR_ANSTO* cross sections are slightly higher than those generated using the *ECPSSR_FormFactor* (*v. 6.50, v. 6.54*), in agreement with figures 3.10 and 3.13.

The results show a good agreement between Geant4-calculated emission X-ray spectra and the experimental measurements. The *ECPSSR_ANSTO* and *ECPSSR_FormFactor* cross sections produce very similar results, because of their limited differences in the case of the L sub-shells. Bigger differences are expected when the vacancy is produced in the

Table 3.2: Number of X-rays generated in the gold target per incident 3.00 MeV proton, when adopting different cross sections approaches (*ECPSSR_ANSTO*, *ECPSSR_FormFactor*, *Analytical* and *Empirical*).

X-ray line	ANSTO	Form Factor v. 6.50	Form Factor v. 6.54	Analytical	Empirical
$M_{\alpha(II)}$	1.01×10^{-2}	1.08×10^{-2}	1.00×10^{-2}	4.36×10^{-5}	3.89×10^{-5}
$M_{\alpha(I)}$	1.98×10^{-1}	2.11×10^{-1}	1.97×10^{-1}	8.19×10^{-4}	7.77×10^{-4}
M_{β}	1.10×10^{-1}	1.17×10^{-1}	1.10×10^{-1}	4.17×10^{-4}	4.09×10^{-4}
M_{γ}	1.38×10^{-2}	1.44×10^{-2}	1.03×10^{-2}	5.47×10^{-5}	5.48×10^{-5}
L_{l}	3.97×10^{-4}	3.84×10^{-4}	3.91×10^{-4}	4.03×10^{-4}	3.85×10^{-4}
$L_{\alpha(II)}$	6.95×10^{-4}	6.72×10^{-4}	6.61×10^{-4}	7.00×10^{-4}	6.69×10^{-4}
$L_{\alpha(I)}$	6.12×10^{-3}	5.89×10^{-3}	5.88×10^{-3}	6.17×10^{-3}	5.84×10^{-3}
$L_{\beta(IV)}$	9.78×10^{-5}	9.30×10^{-5}	8.82×10^{-5}	1.02×10^{-4}	8.50×10^{-5}
$L_{\beta(I)}$	2.03×10^{-3}	1.95×10^{-3}	1.98×10^{-3}	2.04×10^{-3}	2.17×10^{-3}
$L_{\beta(II)}$	1.15×10^{-3}	1.09×10^{-3}	1.11×10^{-3}	1.16×10^{-3}	1.10×10^{-3}
$L_{\beta(III)}$	1.16×10^{-4}	1.01×10^{-4}	9.64×10^{-5}	1.14×10^{-4}	9.73×10^{-5}
$L_{\gamma(I)}$	4.03×10^{-4}	3.92×10^{-4}	3.84×10^{-4}	4.01×10^{-4}	4.30×10^{-4}
$L_{\gamma(III)}$	3.00×10^{-5}	2.99×10^{-5}	3.02×10^{-5}	3.04×10^{-5}	2.62×10^{-5}
$K_{\alpha(I)}$	1.38×10^{-6}	1.08×10^{-2}	2.00×10^{-6}	4.36×10^{-5}	3.89×10^{-5}

Table 3.3: Number of X-rays generated in the gold target per incident 9.50 MeV α, when adopting different cross sections approaches (*ECPSSR_ANSTO*, *ECPSSR_FormFactor*, *Analytical* and *Empirical*).

X-ray line	ANSTO	Form Factor v. 6.50	Form Factor v. 6.54	Analytical	Empirical
$M_{\alpha(II)}$	2.17×10^{-2}	2.52×10^{-2}	2.31×10^{-2}	5.83×10^{-5}	6.17×10^{-5}
$M_{\alpha(I)}$	4.24×10^{-1}	4.92×10^{-1}	4.49×10^{-1}	1.16×10^{-3}	1.16×10^{-3}
M_{β}	2.32×10^{-1}	2.71×10^{-1}	2.52×10^{-1}	5.83×10^{-4}	5.85×10^{-4}
M_{γ}	2.89×10^{-2}	3.28×10^{-2}	2.18×10^{-2}	7.90×10^{-5}	8.01×10^{-5}
L_{l}	5.84×10^{-4}	5.54×10^{-4}	5.57×10^{-4}	5.77×10^{-4}	5.75×10^{-4}
$L_{\alpha(II)}$	1.02×10^{-3}	9.62×10^{-4}	9.75×10^{-4}	1.01×10^{-3}	1.01×10^{-3}
$L_{\alpha(I)}$	8.93×10^{-3}	8.52×10^{-3}	8.48×10^{-3}	8.87×10^{-3}	8.88×10^{-3}
$L_{\beta(IV)}$	9.37×10^{-5}	8.46×10^{-5}	8.58×10^{-5}	9.54×10^{-5}	9.54×10^{-5}
$L_{\beta(I)}$	2.87×10^{-3}	2.75×10^{-3}	2.78×10^{-3}	2.84×10^{-3}	2.86×10^{-3}
$L_{\beta(II)}$	1.66×10^{-3}	1.59×10^{-3}	1.59×10^{-3}	1.66×10^{-3}	1.66×10^{-3}
$L_{\beta(III)}$	1.06×10^{-4}	9.79×10^{-5}	9.96×10^{-5}	1.07×10^{-4}	1.09×10^{-4}
$L_{\gamma(I)}$	5.72×10^{-4}	5.44×10^{-4}	5.38×10^{-4}	5.57×10^{-4}	5.63×10^{-4}
$L_{\gamma(III)}$	2.77×10^{-5}	2.78×10^{-5}	2.66×10^{-5}	2.98×10^{-5}	2.97×10^{-5}

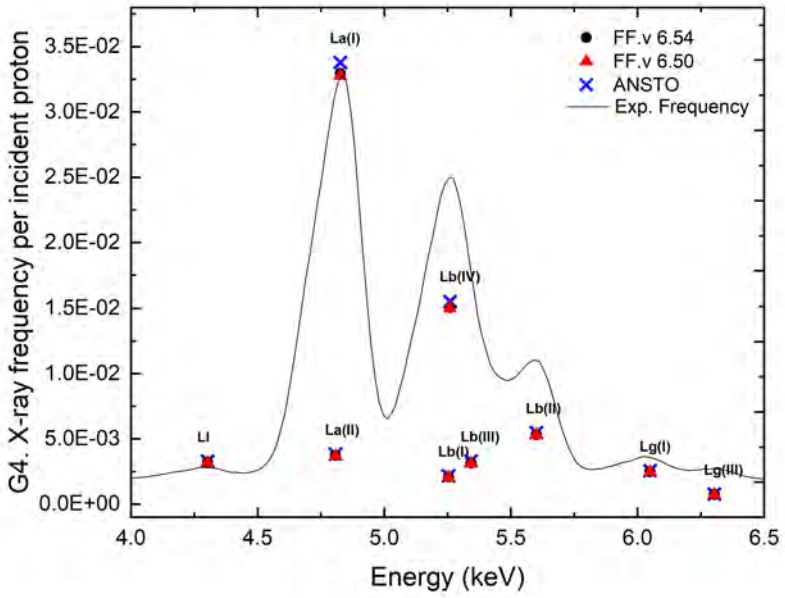

Figure 3.16: Geant4 Cerium X-ray emissions generated by a 3.00 MeV incident proton compared to the experimental spectrum.

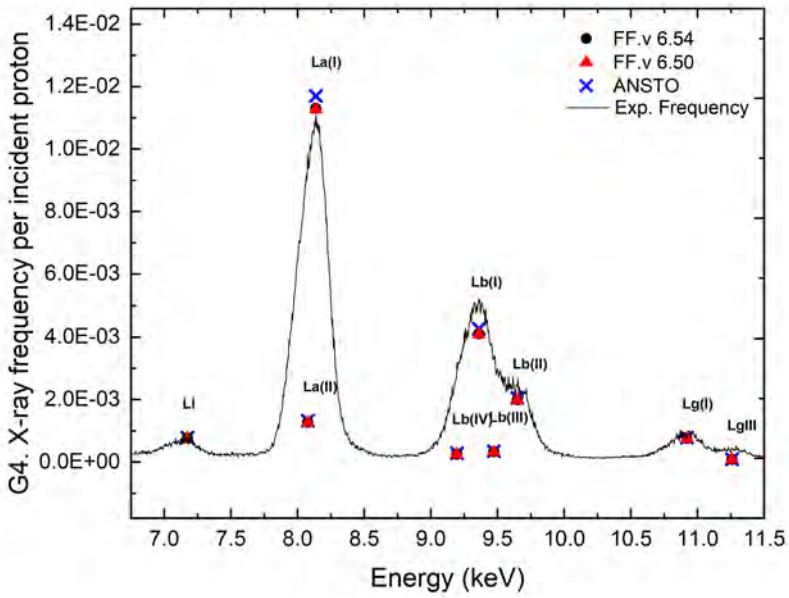

Figure 3.17: Geant4 tantalum X-ray emissions generated by a 3.00 MeV incident proton compared to the experimental spectrum.

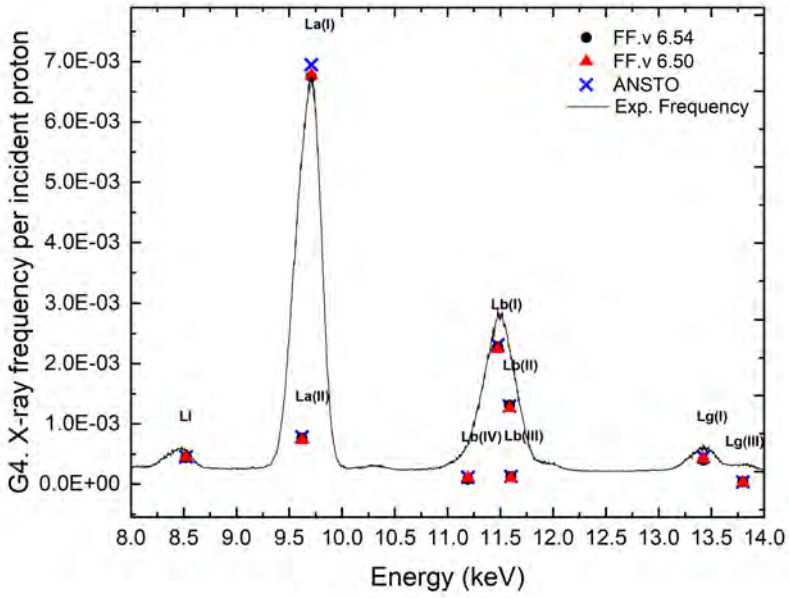

Figure 3.18: Geant4 gold X-ray emissions generated by a 3.00 MeV incident proton compared to the experimental spectrum.

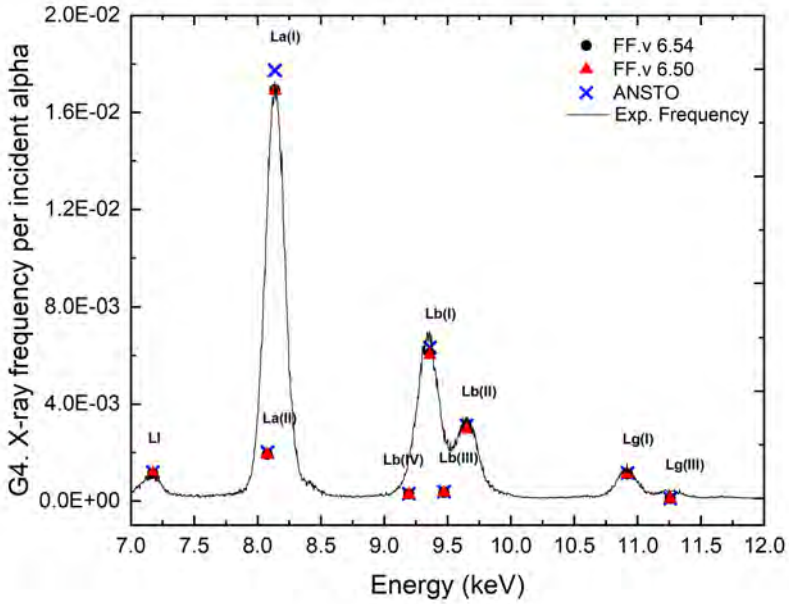

Figure 3.19: Geant4 tantalum X-ray emissions generated by a 10.00 MeV incident α compared to the experimental spectrum

M sub-shells.

3.6 Conclusion

ECPSSR_ANSTO cross sections for protons and α particles have been integrated in Geant4 for PIXE simulation. The *ECPSSR_FormFactor* and *ECPSSR_ANSTO* approaches can handle the M sub-shell relaxations. The two alternative sets, while providing more comparable results for K and L shells, show significant differences when modelling the M shell, which may have a significant impact in Geant4-based nanomedicine studies.

The larger differences between the model prediction and the measured experimental absorption cross sections for high-Z materials with occupied M sub-shells probably stems from their total atomic energies being comprised of nucleon and electron energies. Electron energies are typically small (from KeV down to 1/10 ths of eV), while nuclear interactions typically have energies of the order of MeV. Nonetheless, the total energy of the atomic species is influenced by both nuclear and electron processes. M-shell atoms will have many more subtly-nuanced possible interaction processes than atoms with only K and L shells occupied. The electron orbitals for M-shell species may be physically bigger (i.e., larger orbital radii) and there are more of them, which means that will tend to be more affected by the environment of the particular atom. The existing modelling for proton and α absorption may not have allowed for all the possible energy absorption and subsequent de-excitation mechanisms at work during absorption events in such bonded metallic samples and their substrates. Schlatholter et al. [71] and Porcel et al. [72, 73] have already noted that scattering mechanisms are poorly understood in high-Z number materials, and M-shell materials have the biggest Z numbers. Hence, further experimental data will always be necessary and valuable in this field.

For the future, it is recommended to validate the alternative sets of ionisation cross sections for this shell with accurate, reference experimental measurements, when available [76].

The novel cross sections, called *ECPSSR_ANSTO*, will be included in the public release of Geant4 and can be selected in a Geant4 user application by means of user interface commands on top of any electromagnetic physics configurations.

3.7 Acknowledgements

This project has been funded by the *Australian Research Council*, grant number ARC DP 170100967. The authors D. D. Cohen and R. Siegele would like to acknowledge *National Collaborative Research Infrastructure Strategy* (NCRIS) for funding of the *Centre*

for Accelerator Science (CAS) and to CAS staff for access to their ion beam analysis facilities.

Chapter 4

Geant4 X-ray Fluorescence with Updated Libraries

To get a unique complete *G4–ANSTO* approach based on the ANSTO calculations and recommendations of D. D. Cohen and R. Siegele, I integrated the *ANSTO HF* X-ray fluorescence yields, the second component of *G4–ANSTO* approach.

This chapter is a modified version of the published work:
S. Bakr, D.D. Cohen, R. Siegele, J. W. Archer, S. Incerti, V. Ivanchenko, A. Mantero, A. Rosenfeld, S. Guatelli, (2021) **"Geant4 X-ray fluorescence with updated libraries"**, *Nuclear Instruments and Methods in Physics Research Section B: Beam Interactions with Materials and Atoms,* vol. 507, 2021, pp. 11-19.
`https://doi.org/10.1016/j.nimb.2021.09.009`

This work presented at the **Ion Beam Analysis** conference 2021, (Online), **26th Geant4 Collaboration** meeting 2021, (Online), **25th Geant4 Collaboration** meeting 2020, (Online).

4.1 Abstract

I present the results concerning the development in Geant4 of a new data driven library, called here the *ANSTO HF* library. This X-ray fluorescence library is based on an approach of particular interest for PIXE simulation applications; however, it can be used in any Geant4 application where X-ray fluorescence needs to be described. The X-ray fluorescence transition probabilities were calculated within the Hartree-Fock (HF) approach, which is recognised to better reproduce PIXE experimental values compared with the Hartree-Slater approach, adopted in the current default Geant4 *EADL* data library. These HF X-ray fluorescence transition probabilities were integrated into a new Geant4 library

and will be released within Geant4 in the near future.

In this chapter, I compare the fluorescence X-ray spectra generated by the *ANSTO HF* library and by the currently available library (*EADL*-1991 [63]) within Geant4, for targets irradiated with protons and α particles with energies up to 10.00 MeV, a range of interest for PIXE applications. The comparisons were performed for a large set of sample materials spanning a broad range of target atomic numbers. These two approaches were compared to existing experimental measurements performed at the ANSTO heavy ion microprobe beamline using 2.00 MeV and 3.00 MeV proton and 10.00 MeV He^{+2} ion beams. This work represents a useful upgrade to the Geant4 atomic de-excitation package.

4.2 Introduction

Particle Induced X-ray Emission (PIXE) is a well-established non-destructive analytical technique to determine the elemental composition of a sample, with very broad applications ranging from archaeometry to zoology.

PIXE describes the phenomenon of charged particles, such as protons, α and heavier ions, interacting with matter. This includes the ionisation of atoms within the target by removing one or more electrons from the K, L, or M sub/shells, followed by atomic de-excitation. This shell vacancy is then filled by an electron from an outer shell with the subsequent emission of a characteristic X-ray. These fluorescence X-rays are then detected and used to determine the elemental composition of the irradiated target. The elements in a sample are identified by the energy of the emitted X-rays while their concentration is determined by the intensity of each specific X-ray line [77].

Geant4 [1] is a general-purpose Monte Carlo toolkit, describing particle interactions in matter in the energy range from a few eV to TeV. In the context of PIXE, Geant4 allows one to model the composition of both homogeneous and heterogeneous materials, gaseous samples for environmental applications, planetary samples for geological and space science studies. Like the PIXAN and GUPIX [78] packages, Geant4 models PIXE taking into account the absorption of emitted X-rays and the slowing down of the incident particle as it passes through a target.

The Geant4 Atomic Relaxation package includes models for the generation of vacancies in atomic shells and the subsequent emission of fluorescence X-rays and Auger electrons. The development of the Geant4 Atomic Relaxation Package was firstly documented in [44] and was more recently improved [46]. Two concepts are considered in the simu-

Table 4.1: Models and approaches in this comparison.

	G4–default	*G4–ANSTO*
Ionisation cross sections	*ECPSSR_FormFactor* [58, 59]	*ECPSSR_ANSTO* [16]
Transition probabilities	*EADL* (Hartree-Slater) [66]	*ANSTO HF* (Hartree-Fock) [50]

lation of atomic relaxation [44]:

- the creation of a vacancy by a primary process and
- the generation of the relaxation cascade.

The first one is handled by any Geant4 Electromagnetic Physics Package (including Standard, Livermore, Penelope, and Geant4-DNA models) which manages the primary interactions, e.g., the photoelectric effect, Compton scattering and ionisation; the second one is handled by the Atomic Relaxation package, which is used by all the primary processes generating a vacancy. The secondaries generated by the Atomic Relaxation are then passed to Geant4 tracking and managed as any other particle in the simulation.

Different ionisation cross sections for protons and α particles can be currently used in Geant4 to generate the vacancy in a shell, as described in [49]:

1. K and L shell ionisation cross sections based on empirical and semi-empirical compilations [55–57];
2. The so-called Form Factor set, based on an empirical polynomial approximation to the ionisation cross sections of K, L and a selection of M sub/shells calculated from the *ECPSSR* theory for incident protons and α particles [58, 59].
3. The third set, named *ECPSSR_Analytical*, is based on the *ECPSSR* theory [14] for the description of K and L sub/shells ionisation for incident protons and α particles [46];
4. the fourth set, called *ECPSSR_ANSTO* [16], based on the theoretical work of Brandt and Lapicki and documented in [2, 60, 69, 70].

In addition, the Atomic Relaxation Geant4 component [44, 46], handling the emission of X-rays and Auger/Coster-Kronig electrons, is based on the Evaluated Data Library *EADL* [63], which provides the atomic electron binding energies and the radiative (fluorescence) and non-radiative (Auger and Coster–Kronig electrons) transition probabilities. Such tabulated data are used to calculate the X-ray fluorescence lines [46] for Geant4

applications, where the modelling of atomic de-excitation is necessary. The radiative transition probabilities reported in the *EADL* were calculated according to Hartree-Slater (HS) methods [66], however following the work of Campbell et al. [67, 68] Cohen et al.[2] recommended the Hartree-Fock approach [50] rather than the Hartree-Slater model [66]. Validation studies of the G4-PIXE Package such as Guatelli et al. 2007 [44] and Pia et al. 2011 [64] showed that the *EADL* can reproduce the X-ray lines deriving from the K and L sub/shells transitions within few percentage accuracy when compared to a selected experimental dataset by Deslattes et al. 2003 [65]. However, such agreement may be significantly improved by using data libraries based on Hartree-Fock method [2].

This project is motivated by the ongoing effort to improve the physics model as well as providing the user with a broader range of dataset options in Geant4 [46]. Despite the availability of different ionisation cross sections and atomic relaxation data sets, there is the need to provide a range of options as well as a unique, accurate, self-consistent and robust recommended approach to the PIXE user community, within Geant4. This improvement also benefits applications of Geant4 in other domains, such as environmental physics, geology, archaeology, and space science.

4.3 Materials and Methods

The *ECPSSR* theory was developed by Brandt and Lapicki for both K and L shells ionisation by light ions $\frac{Z_1}{Z_2} < 0.3$, where Z_1 and Z_2 refer to the charges of the projectile and the target atom, respectively [61]. Cohen and Harrigan published *ECPSSR* K and L sub/shells ionisation cross sections for both protons and α particles bombardment for ion energies in the general PIXE range from 0.2 to 10.0 MeV and for a wide variety of target atoms, from carbon to curium [60, 69]. Their later publication included corrections to this dataset for the relativistic nature of the ions. This correction was not large for the MeV ions used in PIXE with energies between 1.00 MeV and 3.00 MeV.

In Geant4, atomic relaxation simulation is articulated through two stages:

1. The creation of a vacancy by a primary process e.g., photoelectric effect, Compton scattering and ionisation. The shell (or sub-shell) where the vacancy is created by a process is sampled based on the cross section of the given process.

2. For the ionisation process number and sub/shell of the vacancies are calculated according to the PIXE cross sections. Two ionisation cross section models were used in this work:

   (a) *ECPSSR_FormFactor* [58, 59] : based on a polynomial approximation of the ionisation cross sections of K, L and a selection of M sub/shells calculated

with the *ECPSSR* theory for incident protons and α particles. This approach is the most recent available Geant4 set.

(b) *ECPSSR_ANSTO* [16]: based on the *ECPSSR* approach of the ionisation cross sections of K, L, and M sub/shells as calculated by D. D. Cohen et al. [60] for incident protons and α particles. This approach was implemented in Geant4 and released in Geant4 in December 2021.

3. The relaxation cascade is triggered, starting from the vacancy created by the primary process. Fluorescence X-ray, Auger electrons or Coster-Kronig transitions are generated through radiative and non-radiative transitions, based on the respective transition probabilities. In the simulation, all secondary particles with energies greater than the cut energy of 10 eV are tracked. Two transition probability libraries were used in this work to generate the fluorescence X-rays:

   (a) *EADL* is the default library that is used in Geant4 to provide the transition probability and is based on Hartree-Slater approach [66].

   (b) a new fluorescence data library, called here *ANSTO HF*, from ANSTO calculations based on Hartree-Fock approach [50]. This was written analogously to the existing *EADL* Geant4 data library, for simplicity, transparency and to facilitate its integration in the *G4EMLOW* data library. Same binding energies of *EADL* (as in *G4EMLOW7.7*) were adopted in the *ANSTO HF* library.

Table 4.1 lists the approaches used in this work. Geant4 extended example TestEm5 and Geant4 10.05.p01 were used. The impact of the two fluorescence libraries, *ANSTO HF* and *EADL*, was quantified in terms of fluorescence X-ray yields per incident particle. Nine target materials (Si, Ti, Fe, Zn, Nb, Ru, Ce, Ta, Au) were chosen, from low to high atomic number Z materials.

When the particle's velocity matches the electron shell velocity, the chance of the K electron shell ionisation is maximised. For example, protons and α particles when incident on silicon need a kinetic energy of ~ 3 MeV and ~ 25 MeV, respectively, to achieve some degree of velocity matching [22]. This is strongly dependent on the target atomic number Z. Monoenergetic pencil beams of protons (2 and 3 MeV) and α particles (10 MeV) were considered as they are representative of some common PIXE applications where experimental data may be available for comparison with theory. These particles were incident on 25 μm thick targets along the direction of the incident beam.

The production threshold of secondary particles was ignored. The fluorescence X-rays were counted once they were generated in the target. Note that the existing Geant4 PIXE

Empirical and Analytical cross section sets [46] were not considered in this work as they generate only K and L vacancies.

Finally, the *G4–ANSTO* and *G4–default* (see table 4.1) were compared to experimental measurements performed at ANSTO using the 6 MV SIRIUS Tandem Accelerator [79]. The experimental spectra were normalised to the highest line of the *G4–ANSTO* X-ray emissions.

4.3.1 Experimental Setup

PIXE spectra were experimentally measured at the ANSTO heavy ion micro-probe beamline [79] using 2.00 and 3.00 MeV proton and 10.00 MeV He^{+2} ion beams with beam currents varying between 0.5 and 2.5 nA. For X-ray detection, a 100 mm^2 high purity Ge detector with a solid angle of 90 msr was used. The detector has a 25 μm thick Be window. To prevent the scattered protons from entering the detector and to reduce the low energy X-ray yield from light elements such as the underlying Si in some of the samples, a 100 μm thick Mylar absorber (or filter) was placed in front of the detector. The data were collected using the Data Acquisition System mpsys4 from Melbourne University together with a Canberra Model 2060 digital signal processor. The irradiated samples were: 1 mm silicon layer, 100 nm Au layer on silicon, 50 nm TiN layer on silicon, 50 nm ZnO layer on silicon, 25 nm Ta_2O_3 layer on graphite, 25 nm Ru oxide film on graphite, 45 nm Nb oxide film on graphite, Fe_2O_3 layer embedded in a boron oxide pellet, and a sample of CeO_2 embedded in a boron oxide pellet.

4.4 Results and Discussion

The following figures 4.1 to 4.7, 4.10 to 4.17, 4.20 to 4.26, 4.29 and 4.30 show the results of *G4–ANSTO* and *G4–default* approaches, with the X axis representing energy in keV and the Y axis representing X-ray frequency per incident particle. To compare *G4–ANSTO* to the experimental spectra, the *G4–ANSTO* data was convoluted with a Gaussian function. The reason behind calculating the Gaussian for *G4–ANSTO* is that there were different lines adjacent to each other and, therefore, their contribution was convoluted to produce the experimentally observed peaks.

In In these figures 4.1 to 4.7, 4.10 to 4.17, 4.20 to 4.26, 4.29 and 4.30, I simply calculated the Gaussian of *G4–ANSTO* and normalised it to the *G4–ANSTO* highest line to compare with the experimental data. Doing the same for the *G4–default* approach and plotting all the data and spectra on the same plot would deceive the readers and represent the Gaussian of both *G4–ANSTO* and *G4–default* to be nearly identical, as seen in fig-

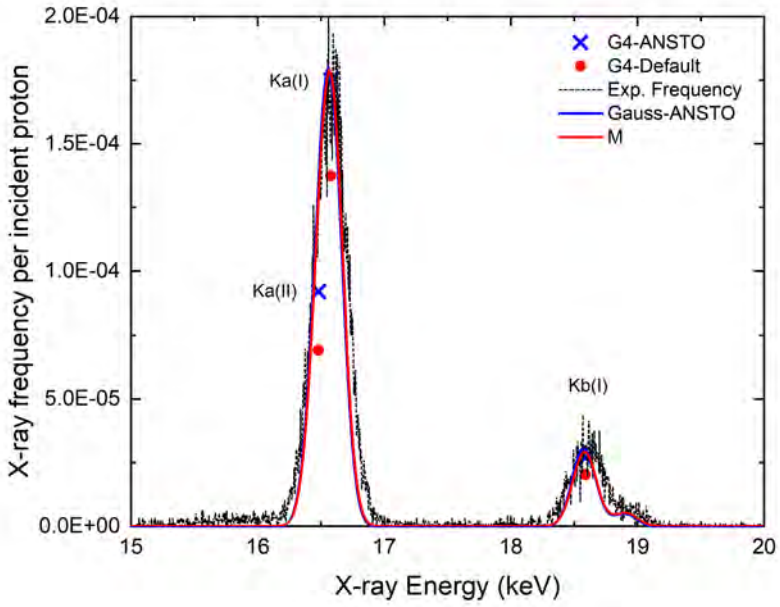

Figure 4.1: X-ray emission generated by 2.00 MeV incident protons on a niobium target, Z = 41.

ure 4.1.

Nonetheless, because the data libraries can be employed in a variety of applications ranging from space to environmental and healthcare applications, it is critical to demonstrate the absolute differences in X-ray emission yields produced with the two different data libraries.

4.4.1 Comparison of 2.00 MeV Incident Protons Results

Figures 4.2 to 4.11 compare the X-ray fluorescence yields obtained with *G4–default* and *G4–ANSTO* approaches, and experimental measurements. Figures 4.2 to 4.7 compare the X-ray emission frequencies (for the K shell) per incident particle generated by a 2.00 MeV proton on Si, Ti, Fe, Zn, Nb, and Ru samples. The Gaussian of *G4–ANSTO* results was calculated and compared with the experimental spectrum. The experimental spectra and the Gaussian of *G4–ANSTO* were normalised to the highest line of the *G4–ANSTO* X-ray emissions, in this case $K_{\alpha(I)}$. Figures 4.2 to 4.7 indicate that *G4–ANSTO* approach has higher X-ray emission rates (for $K_{\alpha(I)}$, $K_{\alpha(II)}$, and $K_{\beta(I)}$ X-ray lines) than the *G4–default* approach in all samples.

The ratio of *G4–ANSTO* to *G4–default* calculated X-ray yields of Nb and Ru derived primarily from vacancies in the K and L sub/shells produced by incident 2.00 MeV pro-

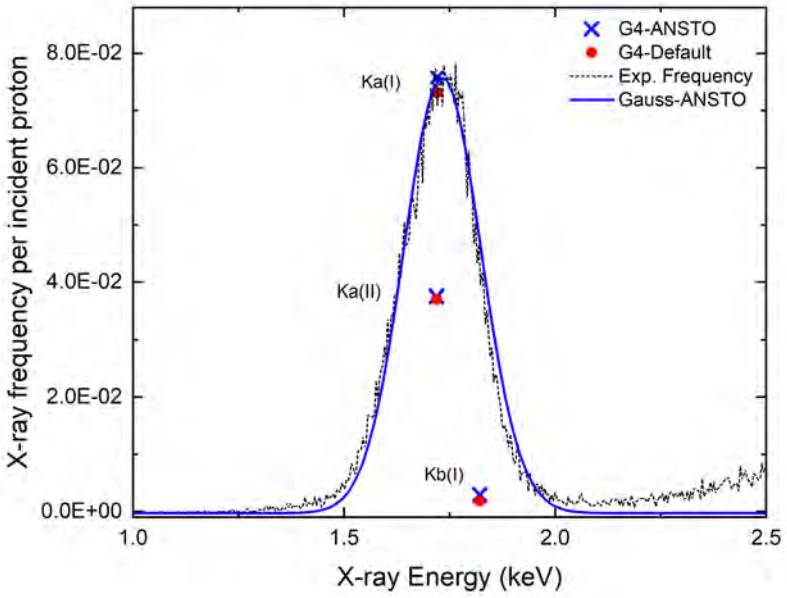

Figure 4.2: X-ray emission generated by 2.00 MeV incident protons on a silicon target, Z = 14.

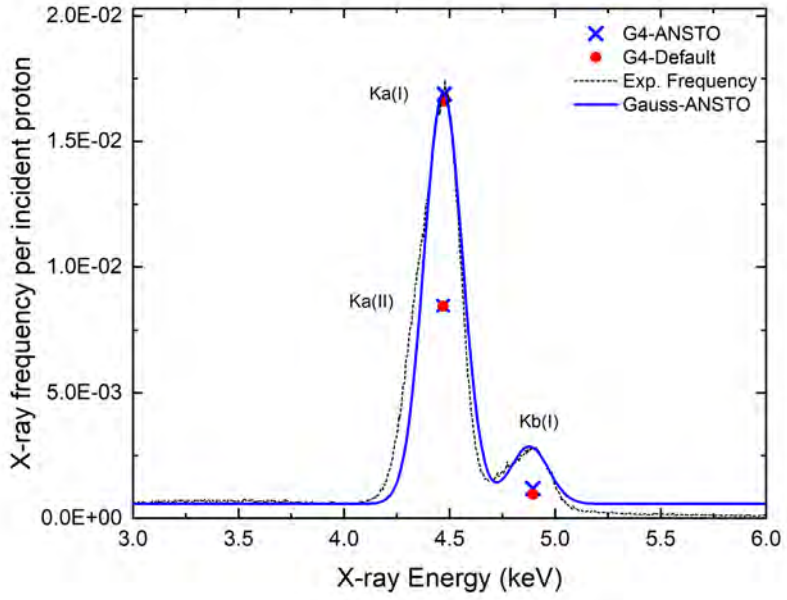

Figure 4.3: X-ray emission generated by 2.00 MeV incident protons on a titanium target, Z = 22.

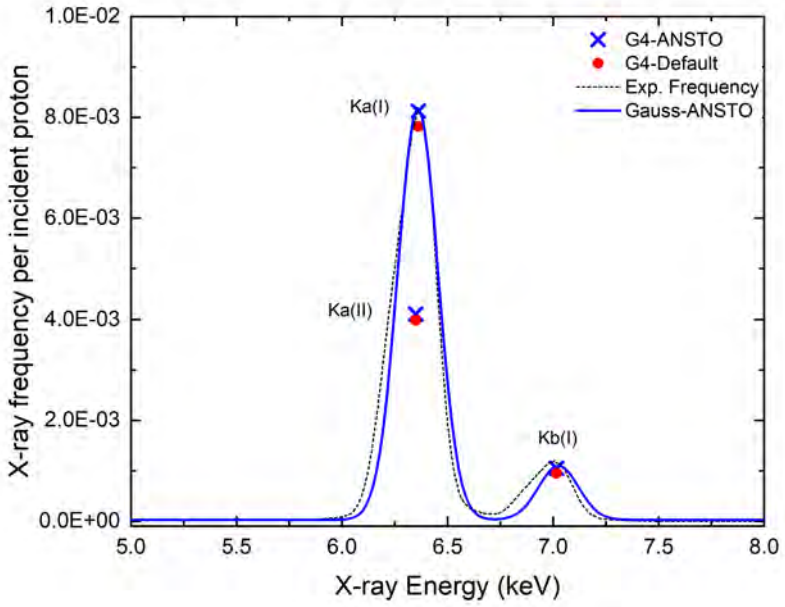

Figure 4.4: X-ray emission generated by 2.00 MeV incident protons on an iron target, Z = 26.

tons is shown in figures 4.8 and 4.9.

Figures 4.10 and 4.11 compare calculated X-ray yields to experimental spectra of Ce and Ta, which are driven primarily by vacancies in the L sub-shells created by incident 2.00 MeV protons.

The L sub-shells X-ray emissions for Nb (Z = 41) and Ru (Z = 44) samples were not obtained experimentally. Therefore, only the results of Geant4 simulation using the *G4–ANSTO* and *G4–default* approaches are shown in figures 4.8 and 4.9. The ratio of the lines generated by *G4–ANSTO* approach to the *G4–default* approach was displayed in figures 4.8 and 4.9. Most of Geant4 lines were found to be substantially higher in the *G4–ANSTO* approach for both samples (Nb and Ru). It can be noticed that most lines show no more $\sim$ 50% difference between *G4–ANSTO* and *G4–default* approaches, while it is around $\sim$ 100% difference for $L_{\gamma(I)}$ and $L_{\beta(II)}$ for Nb and Ru, respectively. Except the L_l line, the electron transition from $M_{(I)}$ sub-shell to $L_{(III)}$ sub-shell, in *G4–ANSTO* results is about $\sim$ 25% lower than in *G4–default* results.

Figures 4.10 and 4.11 depict the findings, which indicate a reasonable agreement between Geant4-calculated emission X-ray spectra and the experimental measurements. I found that the *G4–ANSTO* approach produces higher X-ray emission results than the *G4–default* one. The difference was particularly noticeable for the $L_{\alpha(I)}$ line. In addition,

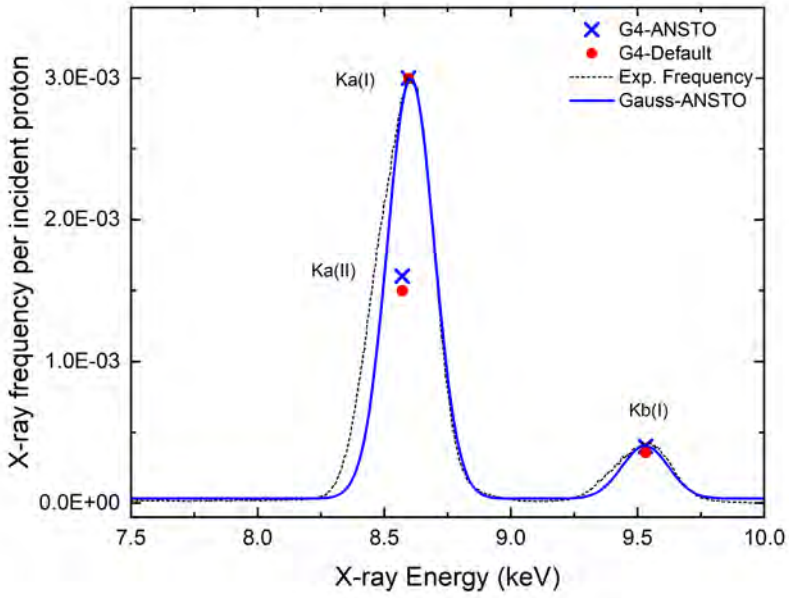

Figure 4.5: X-ray emission generated by 2.00 MeV incident protons on a zinc target, Z = 30.

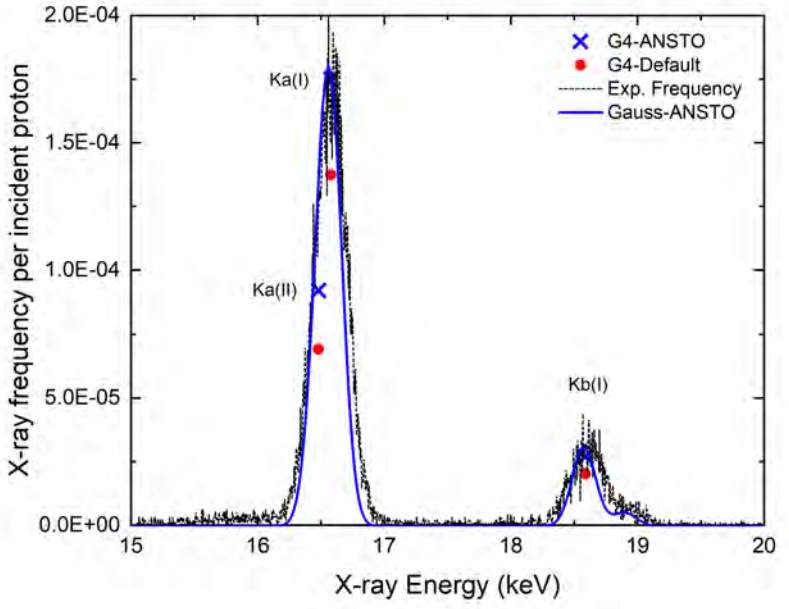

Figure 4.6: X-ray emission generated by 2.00 MeV incident protons on a niobium target, Z = 41.

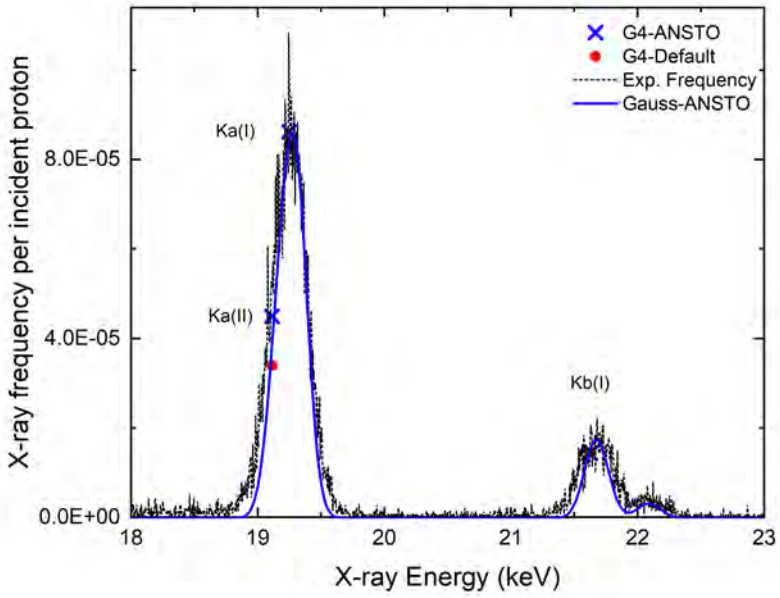

Figure 4.7: X-ray emission generated by 2.00 MeV incident protons on a ruthenium target, Z = 44.

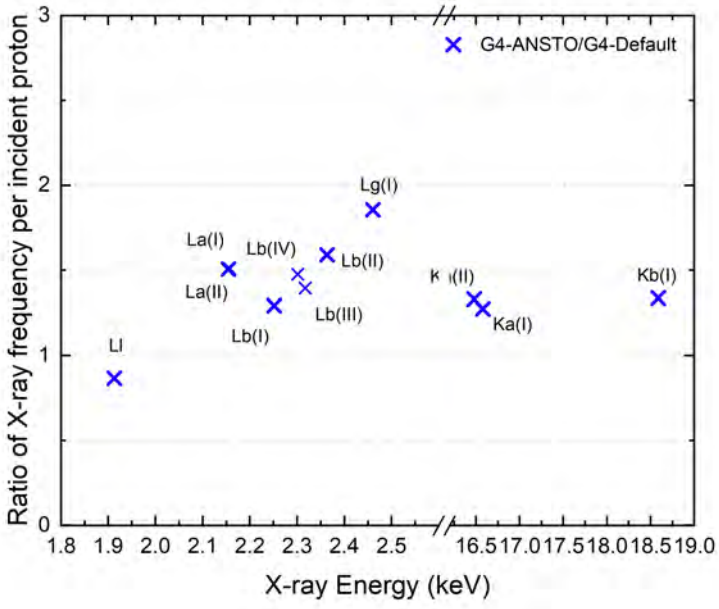

Figure 4.8: Ratio of X-ray emission generated by 2.00 MeV incident protons on a niobium target, Z = 41.

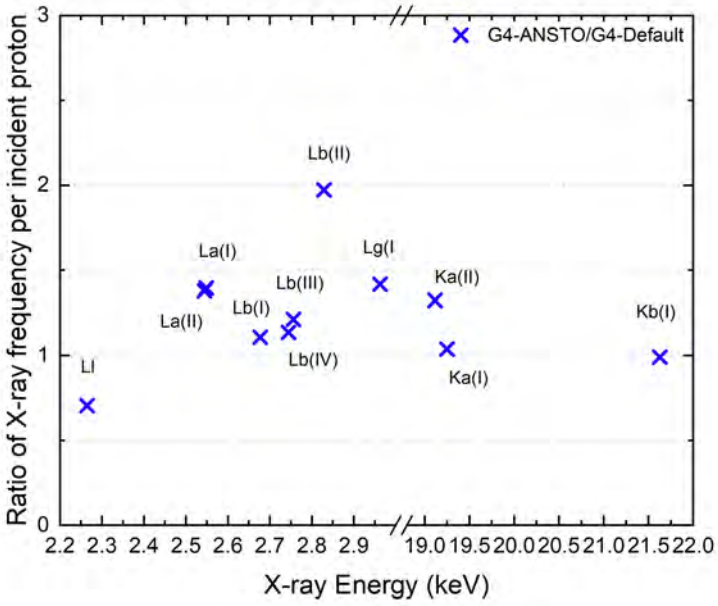

Figure 4.9: Ratio of X-ray emission generated by 2.00 MeV incident protons on a ruthenium target, Z = 44.

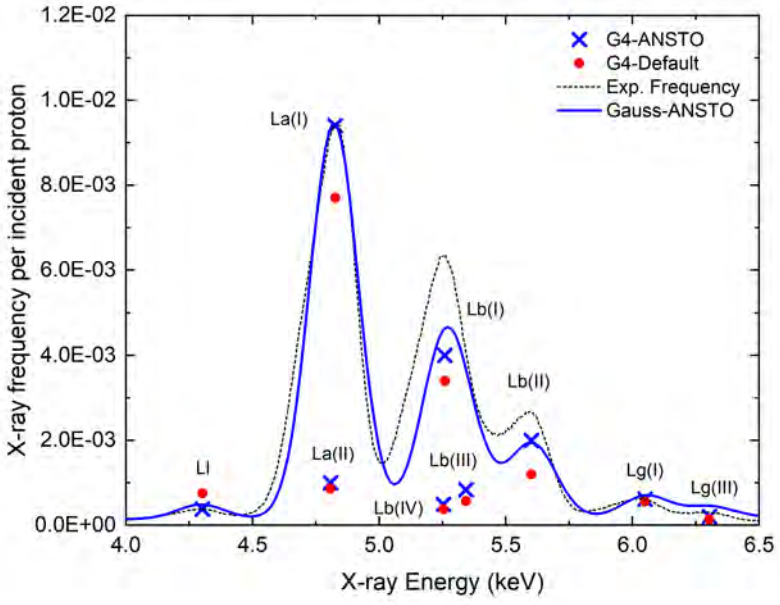

Figure 4.10: X-ray emission generated by 2.00 MeV incident protons on a cerium target, Z = 58.

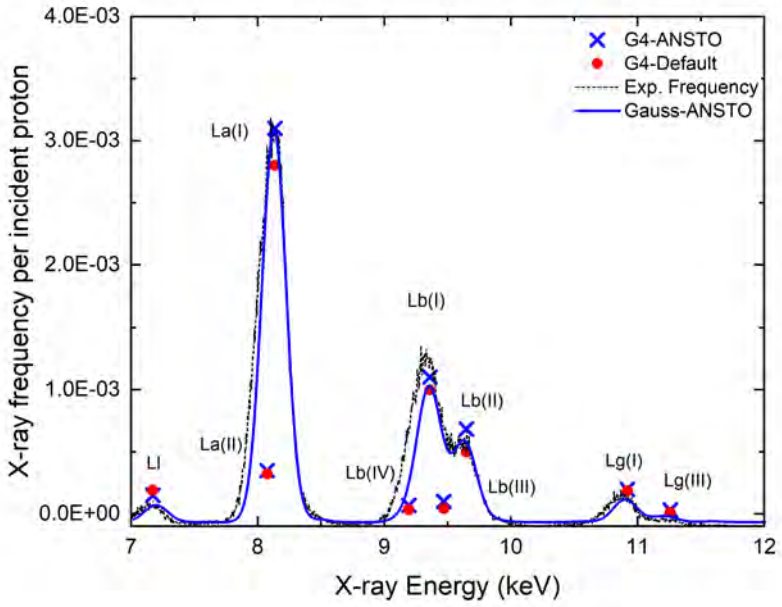

Figure 4.11: X-ray emission generated by 2.00 MeV incident protons on a tantalum target, Z = 73.

the lines ($L_{\beta(I)}$, $L_{\beta(II)}$, $L_{\beta(III)}$, $L_{\beta(IV)}$) calculated by means of both *G4–ANSTO* and *G4–default* approaches were lower than the experimental spectrum, which was attributable to the fact that these four lines were adjacent to each other and, therefore, their contribution was convoluted to produce the higher peaks observable in the experimental data. However, the Gaussian spectra of *G4–ANSTO* approach showed better results when compared to the experimental spectrum.

As shown in figures 4.10 and 4.11, the L_l line of cerium produced by the *G4–default* approach was higher than that generated by the *G4–ANSTO* one. The X-ray fluorescence databases of *G4–default* and *G4–ANSTO* approaches were compared to understand the reason for these variations in L_l X-ray yield and it was found that only the L_l X-ray line probability of transition was higher in *G4–default* when compared to *G4–ANSTO*.

4.4.2 Comparison of 3.00 MeV Incident Protons Results

Figures 4.12 to 4.17 compare calculated X-ray yields to experimental spectra of Si, Ti, Fe, Zn, Nb, and Ru derived primarily from vacancies in the K shell induced by incident 3.00 MeV protons.

Figures 4.18 and 4.19 depict the measured X-ray yields of Nb and Ru, which were primarily derived from vacancies in the L and K sub/shells induced by incident 3.00 MeV

protons.

Figures 4.20 to 4.22 compare calculated X-ray yields to experimental spectra of Ce, Ta, and Au, which were driven primarily by vacancies in the L sub-shells induced by incident 3.00 MeV protons.

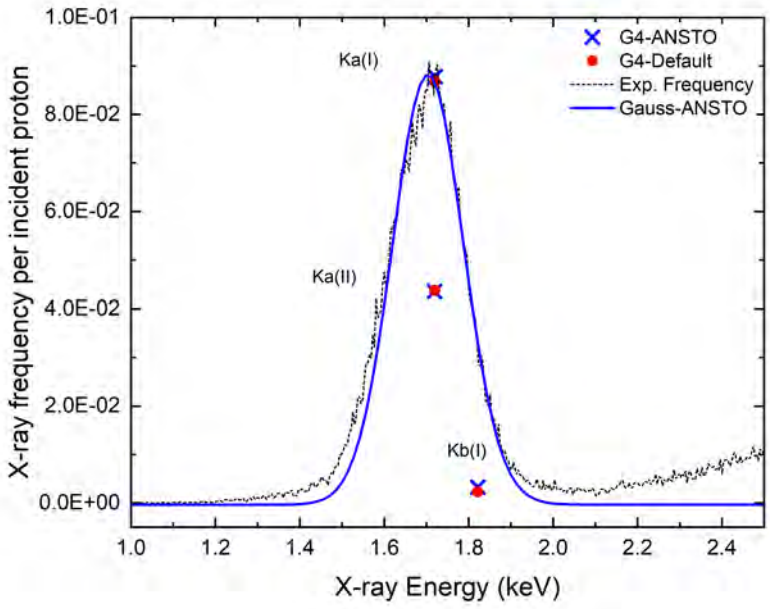

Figure 4.12: X-ray emission generated by 3.00 MeV incident protons on a silicon target, Z = 14.

Figures 4.12 to 4.22 provide a comparison of the *G4–ANSTO* and *G4–default* approaches' results. Figures 4.12 to 4.17 compare the calculated *G4–ANSTO* and *G4–default* X-ray emission frequencies (for the K shell) per incident particle, produced by a 3.00 MeV proton on Si, Ti, Fe, Zn, Nb, and Ru samples to experimental measurements. Additionally, the experimental spectrum was compared to the Gaussian of *G4–ANSTO* results. The experimental spectra and the Gaussian of *G4–ANSTO* were normalised to the highest line of the *G4–ANSTO* X-ray emissions, in this case $K_{\alpha(I)}$. Figures 4.12 to 4.17 show that the *G4–ANSTO* approach provides higher X-ray emission frequencies than the *G4–default* approach in all samples, except for $K_{\alpha(II)}$ X-ray line for Ru (see figure 4.17).

Since the L shell experimental spectra for these samples are not available, figures 4.18 and 4.19 only show the results of the Geant4 simulation, the ratio of lines generated by the *G4–ANSTO* approach to lines generated by the *G4–default* approach. It is worth noting that all lines show less than $\sim 50\%$ difference between *G4–ANSTO* and *G4–default* approaches, while $L_{\gamma(I)}$ and $L_{\beta(II)}$ for Nb and Ru, respectively, show about $\sim 100\%$ dif-

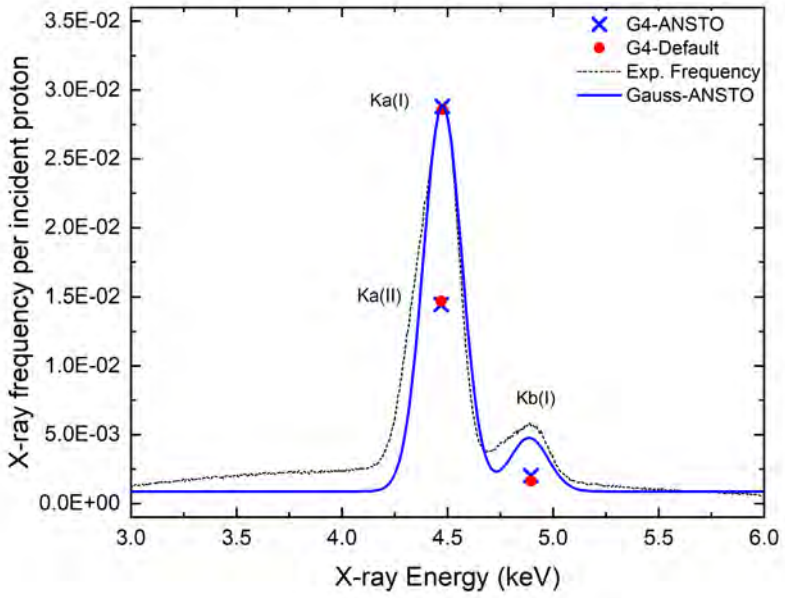

Figure 4.13: X-ray emission generated by 3.00 MeV incident protons on a titanium target, Z = 22.

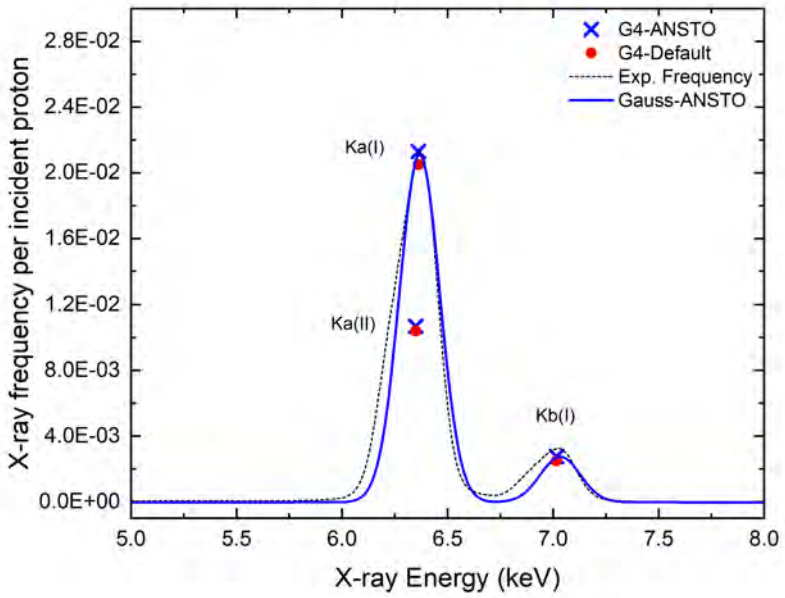

Figure 4.14: X-ray emission generated by 3.00 MeV incident protons on an iron target, Z = 26.

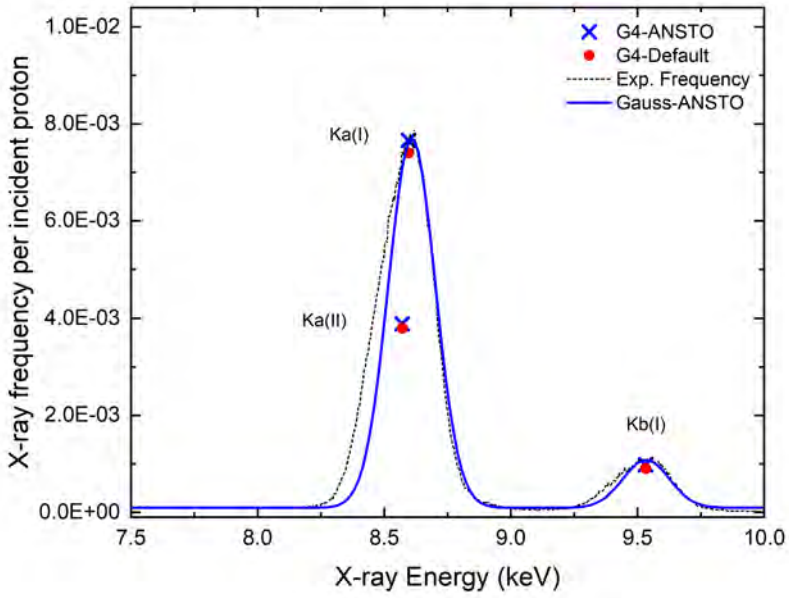

Figure 4.15: X-ray emission generated by 3.00 MeV incident protons on a zinc target, Z = 30.

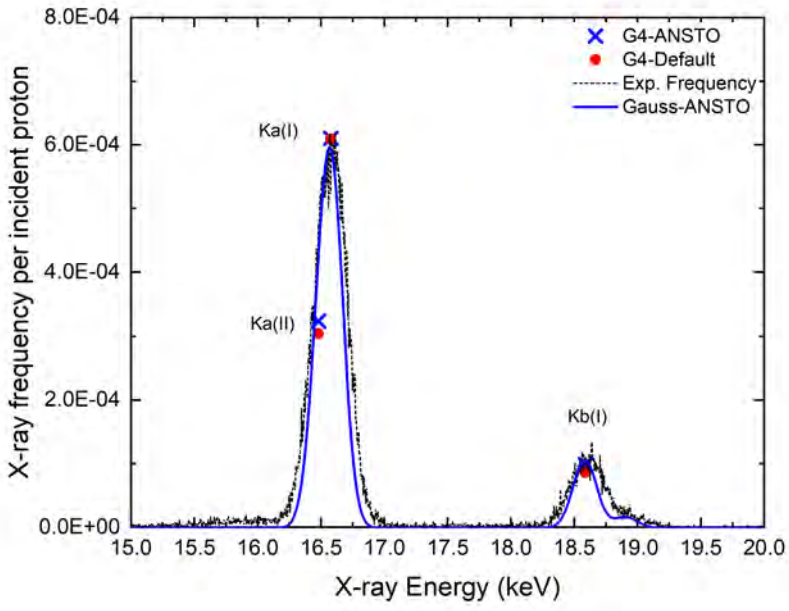

Figure 4.16: X-ray emission generated by 3.00 MeV incident protons on a niobium target, Z = 41.

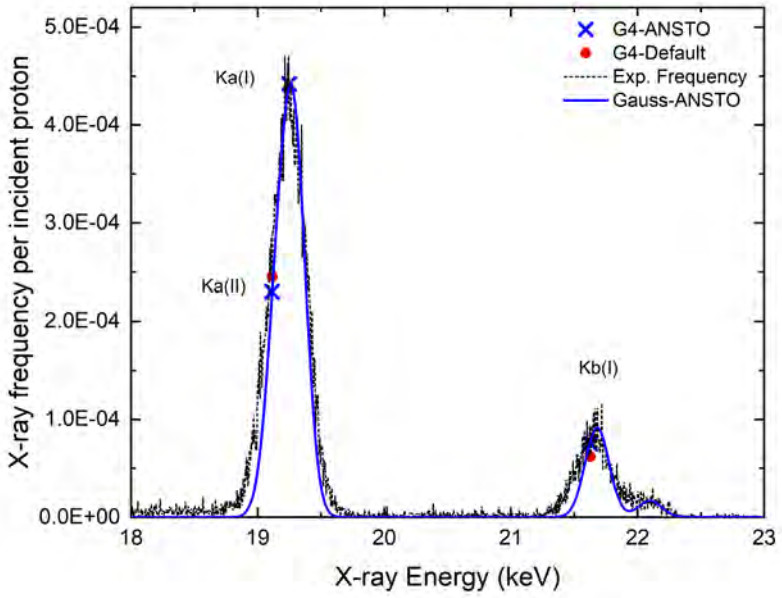

Figure 4.17: X-ray emission generated by 3.00 MeV incident protons on a ruthenium target, Z = 44.

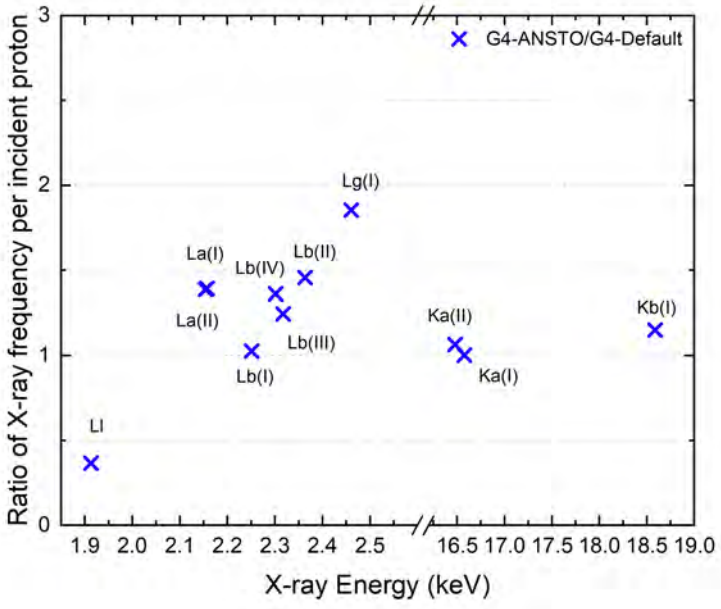

Figure 4.18: Ratio of X-ray emission generated by 3.00 MeV incident protons on a niobium target, Z = 41.

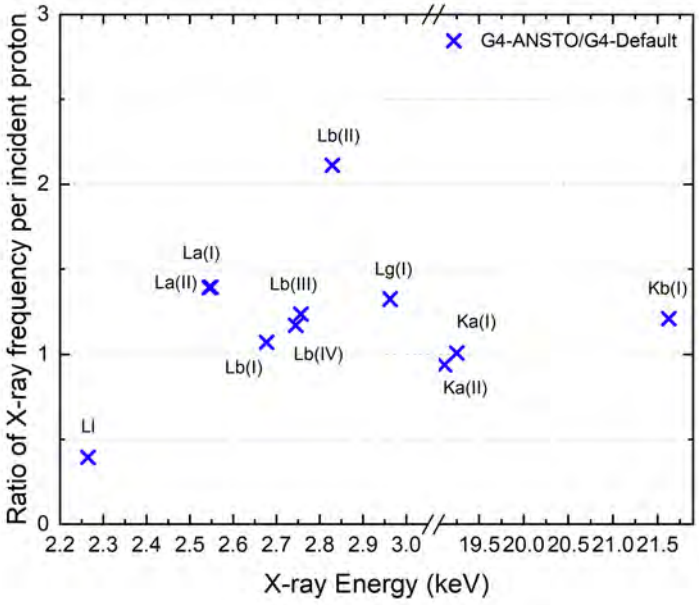

Figure 4.19: Ratio of X-ray emission generated by 3.00 MeV incident protons on a ruthenium target, Z = 44.

ference.

Figures 4.20 to 4.22 indicate that the Gaussian of *G4–ANSTO* emission X-ray spectra and the experimental measurements agreed reasonably well. The experimental spectrum and the Gaussian of *G4–ANSTO* were normalised to the highest line of the *G4–ANSTO* approach. I found that the *G4–ANSTO* approach produces higher X-ray emission results than the *G4–default* results. The differentiation was especially evident in the $L_{\alpha(I)}$ line. Figures 4.18 to 4.22 show that only the L_l X-ray yield is about $\sim 60\%$ higher in *G4–default* approach than in *G4–ANSTO* one since the probability of transition for the L_l X-ray line was higher in *G4–default* approach.

4.4.3 Comparison of 10.00 MeV Incident α Particles Results

Figures 4.23 to 4.26 compare calculated X-ray yields to experimental spectra of Ti, Zn, Nb, and Ru derived primarily from vacancies in the K shell induced by incident 10.00 MeV α particles.

Figures 4.27 and 4.28 depict the calculated X-ray yields of Nb and Ru, which result primarily from vacancies in the L and K shells induced by incident 10.00 MeV α particles.

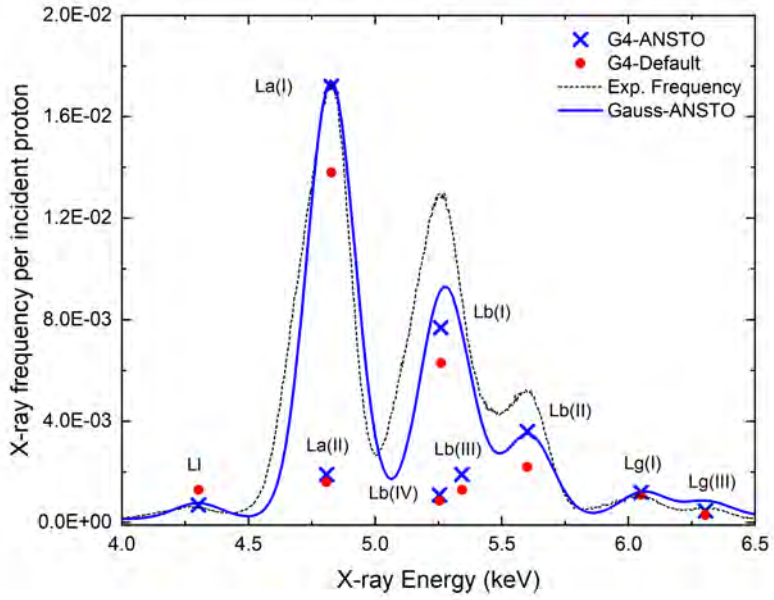

Figure 4.20: X-ray emission generated by 3.00 MeV incident protons on a cerium target, Z = 58.

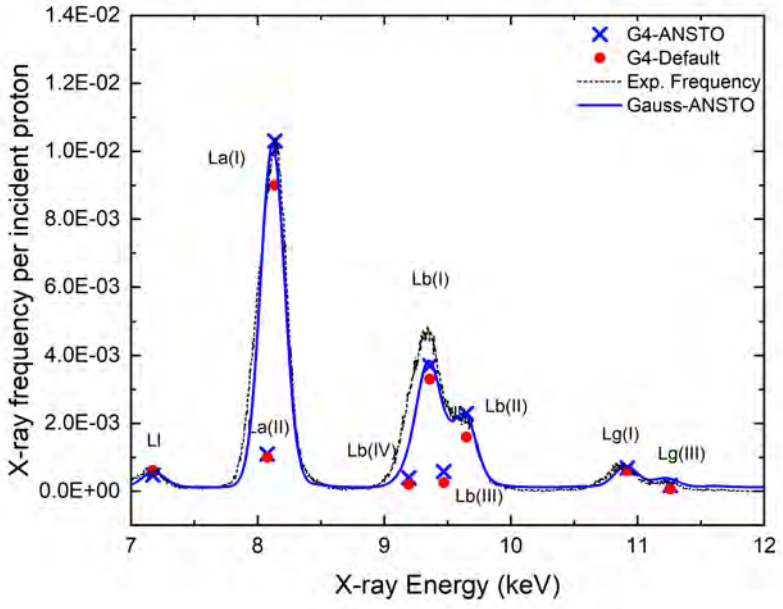

Figure 4.21: X-ray emission generated by 3.00 MeV incident protons on a tantalum target, Z = 73.

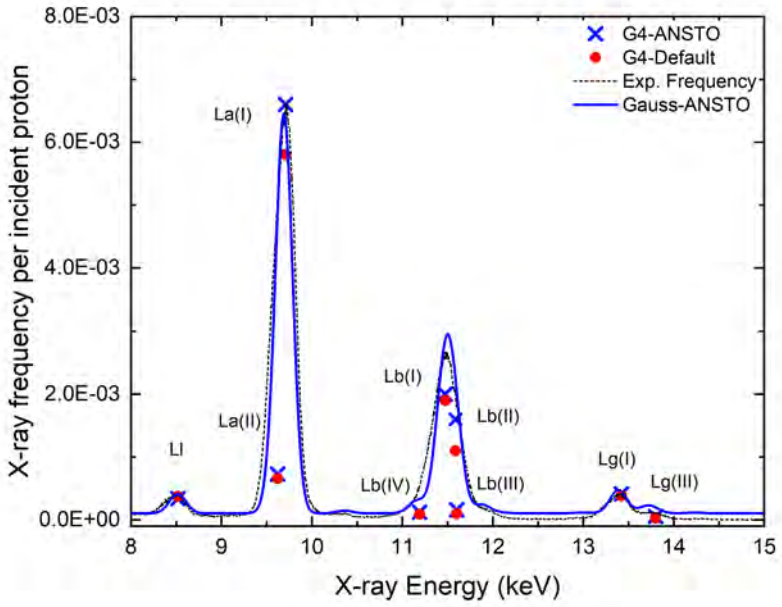

Figure 4.22: X-ray emission generated by 3.00 MeV incident protons on a gold target, Z = 79.

Figures 4.29 and 4.30 compare calculated X-ray yields to experimental Ta spectra derived primarily from vacancies in the L sub-shells induced by 10.00 MeV incident α particles.

Figures 4.23 to 4.30 compare the results of the *G4–ANSTO* and *G4–default* approaches. Figures 4.23 to 4.26 compares the X-ray emission frequencies (for the K shell), produced by 10.00 MeV α particles on Ti, Zn, Nb, and Ru samples, calculated using the *G4–ANSTO* and *G4–default* approaches to experimental measurements. The Gaussian of *G4–ANSTO* results were compared to the experimental spectrum. The experimental spectra and the Gaussian of *G4–ANSTO* were normalised to the highest line of *G4–ANSTO* approach, in this case $K_{\alpha(I)}$. Figures 4.23 to 4.26 show that the *G4–ANSTO* approach indicates about $\sim 5\%$ higher X-ray emission frequencies than the *G4–default* approach in all samples.

Figures 4.27 and 4.28 depict the L and K sub/shells X-ray emissions using the *G4–ANSTO* and *G4–default* approaches; the *G4–ANSTO* results were significantly higher than the *G4–default* results, a maximum of 50% difference for most lines, while $L_{\gamma(I)}$ and $L_{\beta(II)}$ for Nb and Ru, respectively, showed about $\sim 100\%$ difference. Besides the L_l line, which was $\sim 60\%$ lower using *G4–ANSTO* approach than *G4–default* approach.

Figures 4.29 and 4.30 depict the calculated Ta X-ray yields resulting primarily from vacancies in the L and M sub/shells induced by 10.00 MeV incident α particles. In figure 4.29, the Gaussian of *G4–ANSTO* X-ray emission results showed a reasonably good

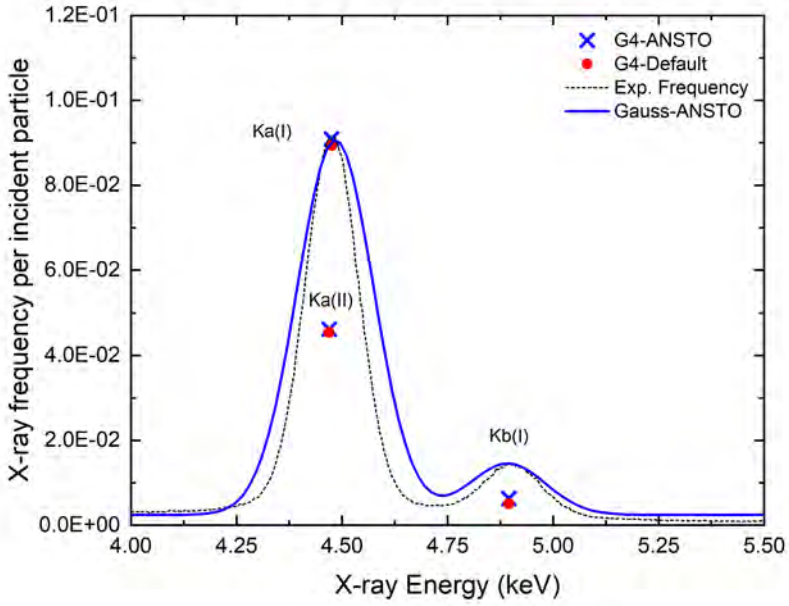

Figure 4.23: X-ray emission generated by 10.00 MeV incident α particles on a titanium target, Z=22.

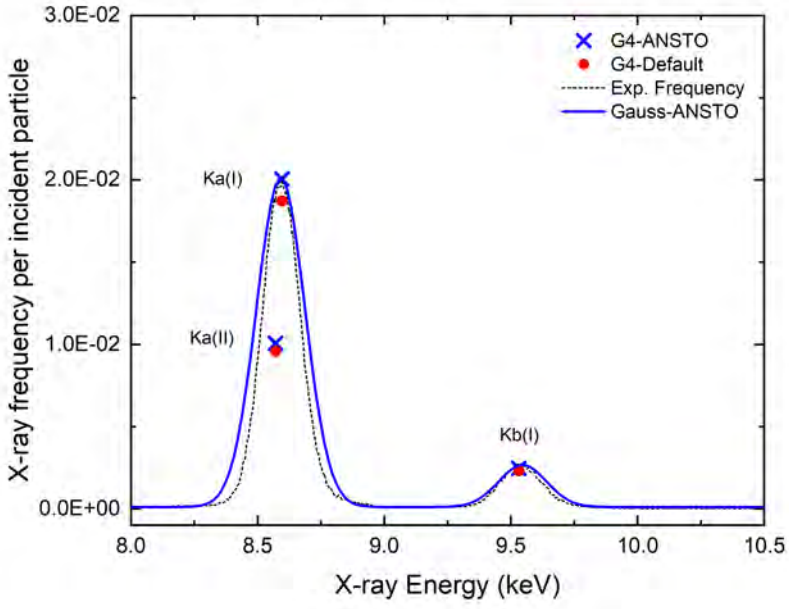

Figure 4.24: X-ray emission generated by 10.00 MeV incident α particles on a zinc target, Z=30.

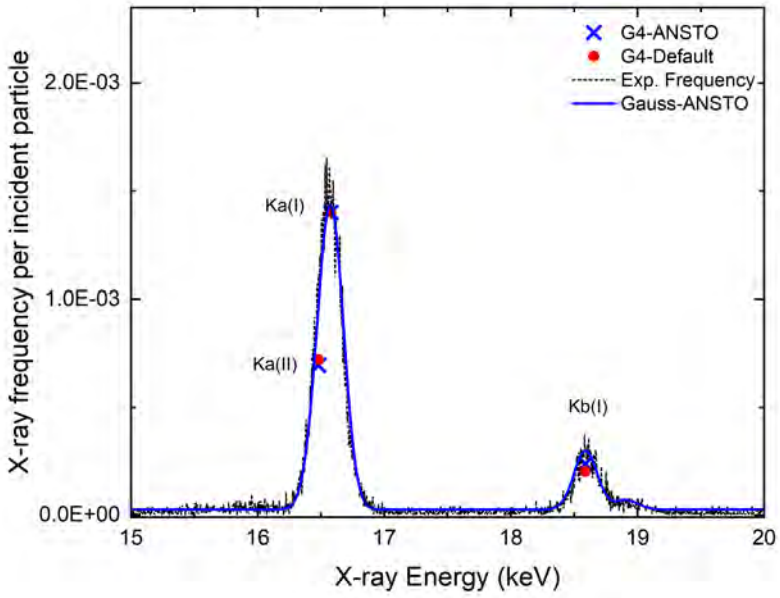

Figure 4.25: X-ray emission generated by 10.00 MeV incident α particles on a niobium target, Z=41.

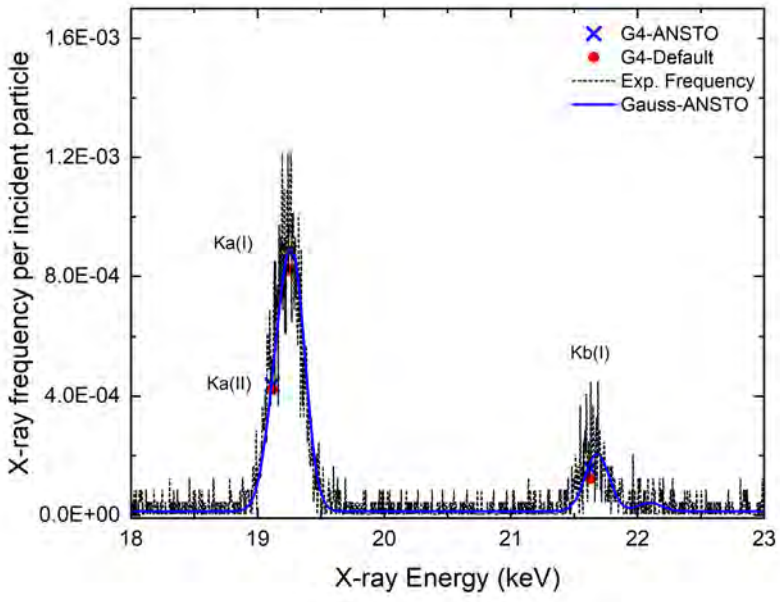

Figure 4.26: X-ray emission generated by 10.00 MeV incident α particles on a ruthenium target, Z=44.

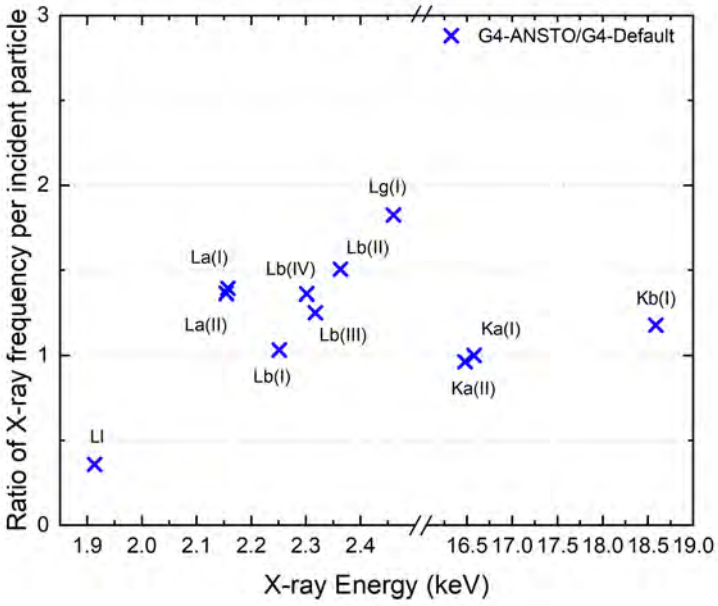

Figure 4.27: Ratio of X-ray emission generated by 10.00 MeV incident α particles on a niobium target, Z = 41.

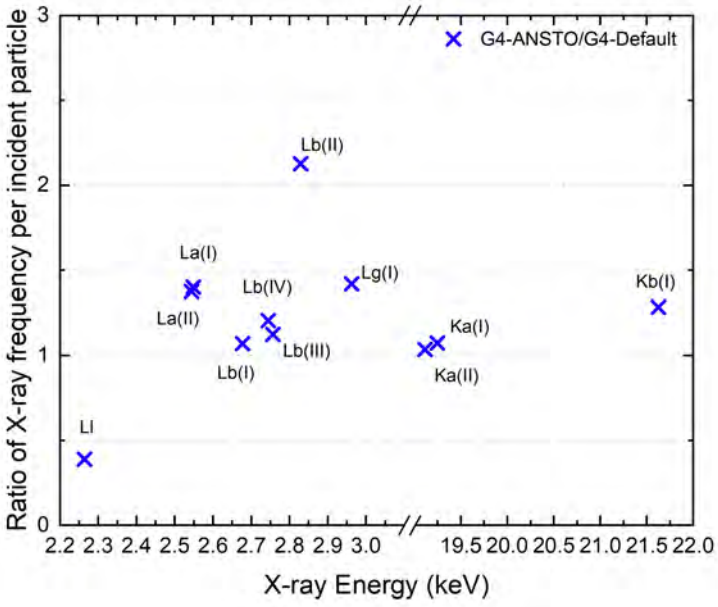

Figure 4.28: Ratio of X-ray emission generated by 10.00 MeV incident α particles on a ruthenium target, Z = 44.

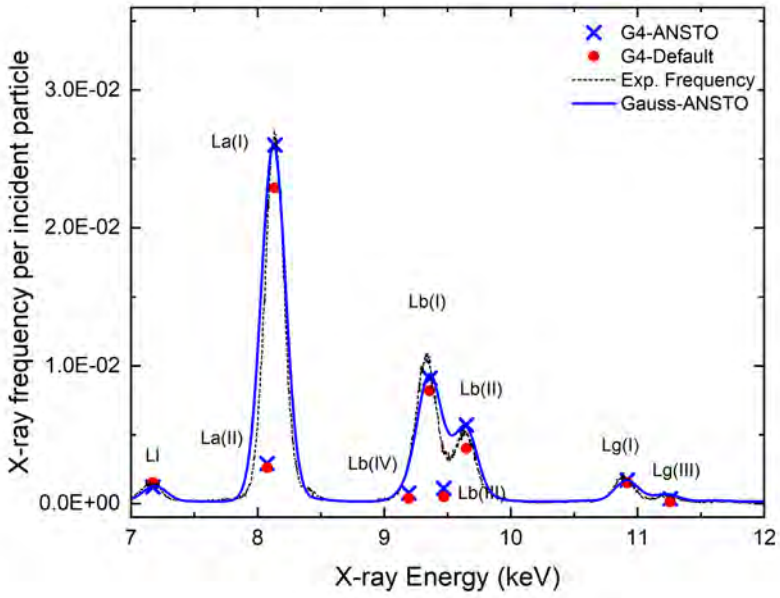

Figure 4.29: X-ray emission generated by 10.00 MeV incident α particles on a tantalum target, Z = 73.

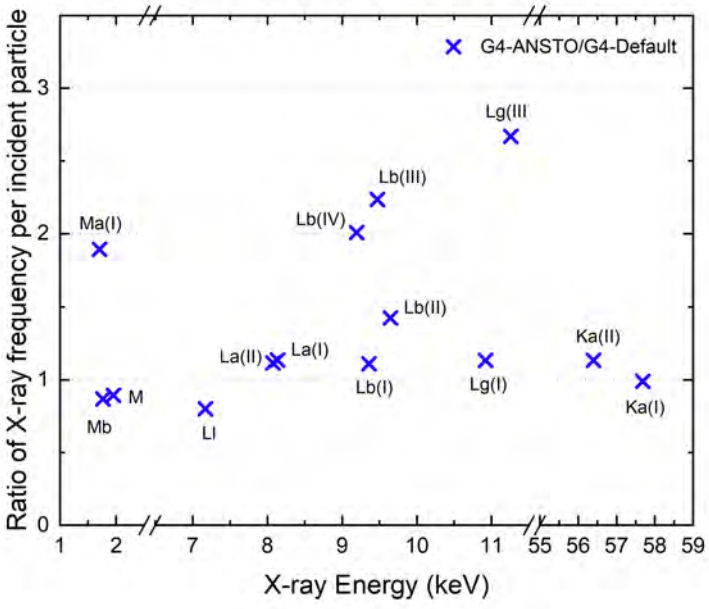

Figure 4.30: X-ray emission generated by 10.00 MeV incident α particles on a tantalum target, Z = 73.

agreement with the ANSTO experimental data. Figure 4.30, on the other hand, depicts the M and L sub/shells X-ray emissions for both the *G4–ANSTO* and *G4–default* approaches under consideration. Except for the L_l X-ray line, all *G4–ANSTO* X-ray lines created from vacancies in L sub-shells were higher (maximum of 100% besides of $L_{\beta(III)}$ and $L_{\gamma(III)}$ are about 150% higher) than the *G4–default* ones, due to the higher probability of transition in the *G4–default* approach, with the solely exception of the M_β and M_γ X-ray lines.

4.5 Conclusion

The *G4–ANSTO* approach, which includes the *ECPSSR_ANSTO* ionisation cross sections [16] and *ANSTO HF* fluorescence yield [50] libraries, was implemented in Geant4 and compared to *G4–default* approach. The *G4–default* approach includes the *ECPSSR_FormFactor* ionisation cross sections [58, 59] and *EADL* [66] fluorescence yield libraries. Geant4-calculated X-ray emission spectra using the *G4–ANSTO*, and the *G4–default* approaches were compared in terms of fluorescence X-ray yields per incident particle. Nine target materials (Si, Ti, Fe, Zn, Nb, Ru, Ce, Ta, Au) were under study, from low to high atomic number Z materials. Mono-energetic beams of protons (2.00 and 3.00 MeV) and α particles (10.00 MeV) were used.

For all samples, most lines were observed to be significantly higher when using the *G4–ANSTO* approach with the exception of the L_l line, corresponding to the electron transition from the $M_{(I)}$ sub-shell to the $L_{(III)}$ sub-shell. The study showed that the Geant4-calculated X-ray emission spectra and the ANSTO experimental measurements were in a reasonably good agreement. However, I am only analysing a few peaks with PIXE, but in reality, *G4–ANSTO* has significant differences with *G4–default* for other lines, which may be important in other application domains.

The novel *G4–ANSTO* X-ray fluorescence data libraries can be coupled with the *G4–ANSTO* cross sections [16] or with the Geant4 default cross sections, handling the generation of atomic vacancies (e.g., the photoelectric effect, Compton scattering and ionisation).

The *G4–ANSTO* approach will be included in the public release of Geant4 in the near future and will be usable by means of user interface commands on top of any electromagnetic physics configurations. The Geant4 PIXE user community will be able to use the *G4–ANSTO* libraries and models, which provide a unique, self-consistent, and stable recommended approach.

4.6 Acknowledgements

This work was funded by the *Australian Research Council*, grant number ARC DP 170100967. The authors would like to acknowledge the *Australian National Collaborative Research Infrastructure Strategy* (NCRIS) funding for accelerators and *Centre for Accelerator Science* staff for access to their ion beam analysis facilities.

Chapter 5

Carbon Ion Beam Experiments

This chapter describes experiments which I performed at ANSTO (Lucas Heights, NSW) to gain accurate X-ray emission data (PIXE) for the purpose of validating the novel Geant4 PIXE component.

Several experiments were conducted at ANSTO on the ANTARES tandem accelerator utilising the heavy ion microprobe beamline employing carbon ions (proton and α particles are previously discussed in chapter 4) in order to validate the novel Geant4 PIXE component. The remainder of this chapter presents the outcomes of our experiments at ANSTO.

5.1 Introduction

The carbon ion has gained significant popularity in PIXE applications across numerous laboratories globally and is considered a preferred ion for such purposes. In order to implement the novel PIXE approach within Geant4, it is necessary to ensure that the approach is compatible with the requirements of Geant4 users.

For a variety of significant reasons, medical uses of carbon ion beams are of special interest. Carbon ion carries more energy than photons, α particles and X-rays. Moreover, ions scatter less at the skin interface in biological soft matter and have better absorption coefficients than X-rays. Additionally, ionised nuclei may be easily produced and controlled. Furthermore, ions scatter less at the skin interface in biological soft matter and have better absorption coefficients than X-rays. Since biological matter is composed of water and carbon, any additional carbon atoms added by diagnostic equipment are less likely to cause a toxic reaction since they are already there [80].

The 10 MV ANTARES (Australian National Tandem Research Accelerator) accelerator delivers ion beams of energies from 5 to 100 MeV, depending on the ion species, with beam intensities up to a few microamperes [81]. Ion beams of almost every naturally-occurring isotope can be generated, devoid of interference from other isotopic species or molecular ions. ANTARES was launched in 1991 and has been improved on a regular basis since then [82].

A tandem accelerator's (heavy) ion beam is focused using a set of electromagnetic lenses. The "microprobe" is a beam that passes through a small rectangular aperture that is quite distant from the lens system in relation to the aperture size. The microprobe is basically an inverted microscope that employs an image probe consisting of a focused beam of accelerated ions with energies in MeV range [81]. The ion microbeam is characterised by the type, energy, and charge of the ions, as well as the microbeam current in a specified spot size region (which may also be referred to as the current density or the ion flux per area). A heavy ion microprobe is intended to focus ions much heavier than protons (e.g., ions from carbon, nitrogen, oxygen or even heavier atoms) which can form stable negative ions [82].

5.2 Materials and Methods

PIXE spectra were produced experimentally at the ANSTO heavy ion microprobe beamline using carbon ion beams of 1.00, 1.67, and 3.00 MeV/amu with currents varying from 0.5 to 2.5 nA. For X-ray detection, a 100 mm^2 high purity Ge detector with a solid acceptance angle of 90 msr (about 5.2^o) was used. The detector is equipped with a Be window that is 25 μm thick. A Canberra Model 2060 digital signal processor and the Melbourne University Data Acquisition System mpsys4 were used to collect the data [83]. There were eight research samples utilised in this study, all of which were designated as part of the International Atomic Energy Agency's Coordinated Research Project F11019.

The suite of targets for PIXE generation were a 1 mm silicon layer, a 50 nm TiN layer on silicon, a 50 nm ZnO layer on silicon, a 25 nm Ta_2O_3 layer on graphite, a 25 nm Ru oxide layer on graphite, a 45 nm Nb oxide layer on graphite, a Fe_2O_3 layer embedded in a boron oxide pellet, and a CeO_2 sample embedded in a boron oxide pellet. These were all successively individually exposed to the ion microprobe beams.

5.3 Results and Discussion

Figures 5.1 to 5.3 illustrate the experimental X-ray spectra originated by a carbon ion beam incident with energy 1.00, 1.67, and 3.00 MeV/amu, respectively, on Si, Ti, Fe, Zn, Nb, Ru, Ce, and Ta sample materials. Highlighted in red are the peaks of interest for later comparison with Geant4 simulation results (see chapter 6).

Figures 5.1a, 5.2a and 5.3a clearly show the Si $K_{\alpha 1}$ peak, which is the unique peak visible in the spectrum. Since the Ti sample was placed on a Si layer, I find $K_{\alpha 1}$ and $K_{\beta 1}$ peaks for Ti and $K_{\alpha 1}$ peaks for Si visible in the results of figures 5.1b, 5.2b and 5.3b. Only the $K_{\alpha 1}$ and $K_{\beta 1}$ peaks for Fe are visible in figures 5.1c, 5.2c and 5.3c. There was no significant contribution to X-ray intensity by the Boron (B) or oxygen (O) species. Because the Zn sample was also deposited on a Si layer, the Si $K_{\alpha 1}$ peak can be seen in figures 5.1d, 5.2d and 5.3d, along with the Zn $K_{\alpha 1}$ and $K_{\beta 1}$ peaks. The $L_{\alpha 1}$, $K_{\alpha 1}$, and $K_{\beta 1}$ peaks are depicted in figures 5.1e, 5.2e and 5.3e (for Nb) and figures 5.1f, 5.2f and 5.3f (for Ru). Figures 5.1g, 5.2g and 5.3g (for Ce) and figures 5.1h, 5.2h and 5.3h (for Ta) show the L_l, $L_{\alpha 1}$, $L_{\beta 1}$, $L_{\beta 2}$, $L_{\gamma 1}$, and $L_{\gamma 3}$ peaks.

5.4 Conclusion

A new Geant4 approach, called *G4–ANSTO*, has been recently added to the Geant4 user library. I performed experimental measurements to validate Geant4 and that is the first time that Geant4 PIXE has been validated for incident carbon ions. Several materials were utilised to generate the X-ray spectra at ANSTO utilising the ANTARES tandem accelerator. The heavy ion microprobe beamline, which employed carbon ions, was used to obtain the spectra, which will be compared later with the Geant4 simulated results. In all the spectra that were produced, there were very distinct characteristic X-ray intensity peaks which can be used for accurate elemental analysis. The precise validation of Geant4 simulation results incorporating these experimental data is covered in the next chapter.

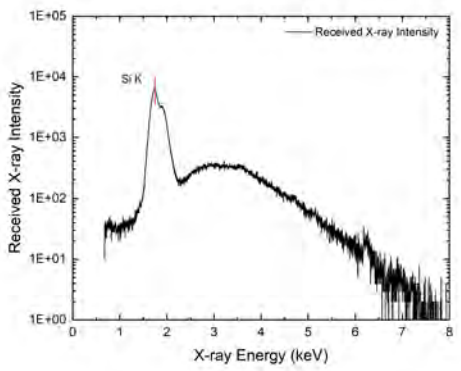

(a) Si

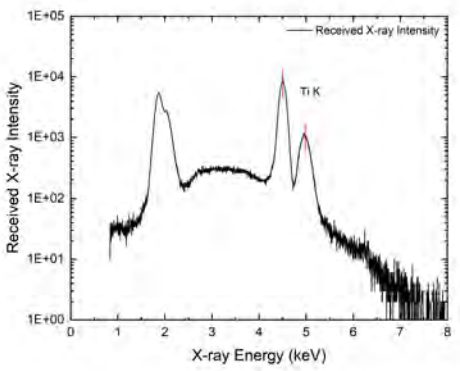

(b) Ti

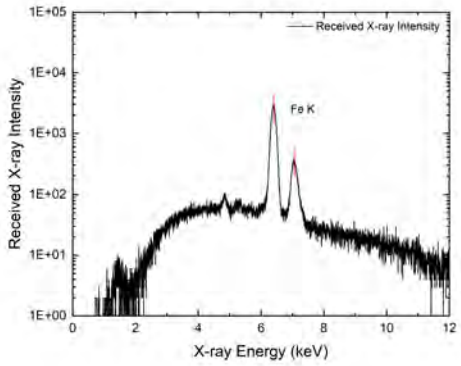

(c) Fe

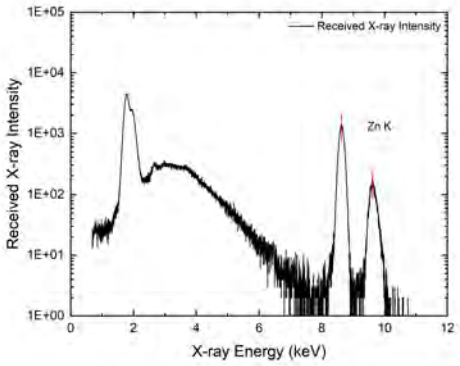

(d) Zn

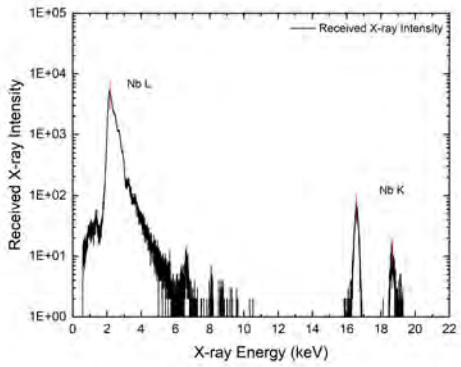

(e) Nb

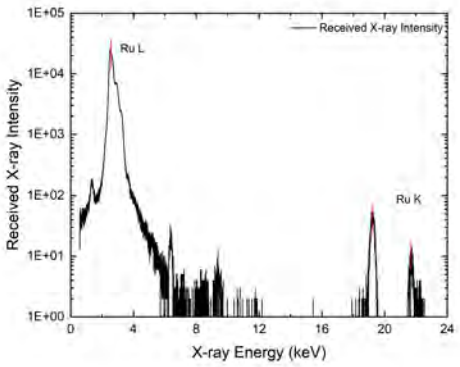

(f) Ru

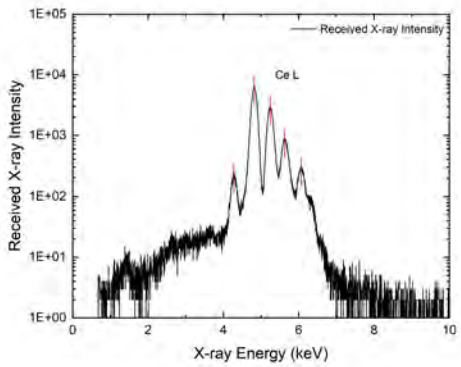

(g) Ce

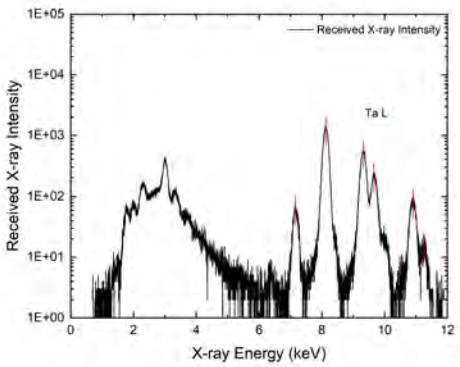

(h) Ta

Figure 5.1: X-ray frequency generated by 1.00 Mev/amu incident carbon ion on Si, Ti, Fe, Zn, Nb, Ru, Ce and Ta sample materials.

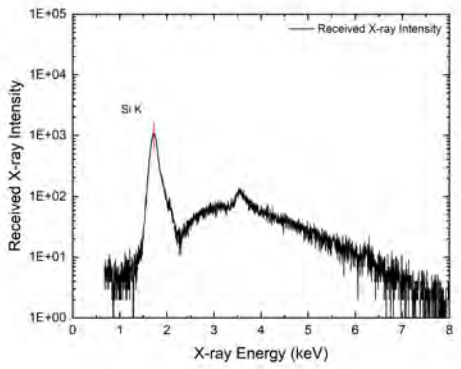

(a) Si

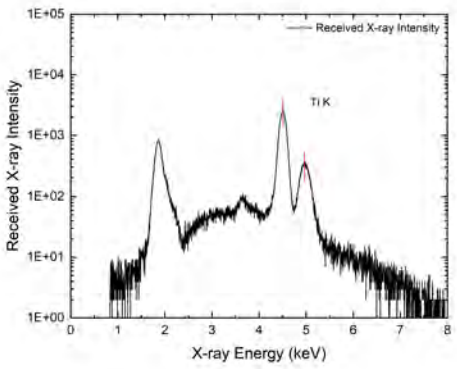

(b) Ti

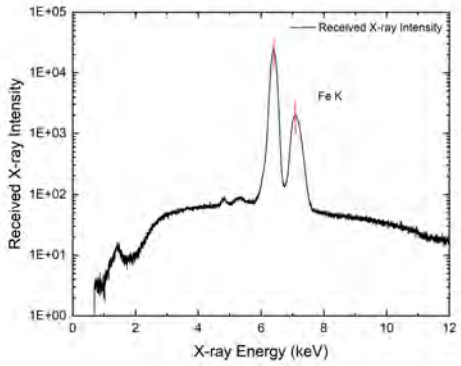

(c) Fe

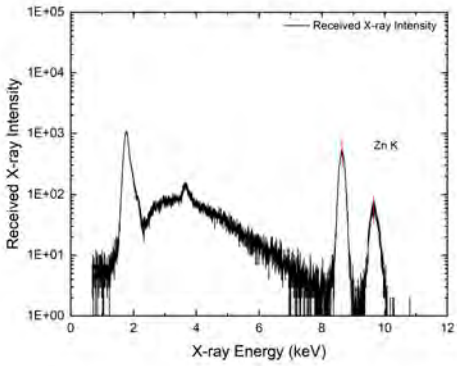

(d) Zn

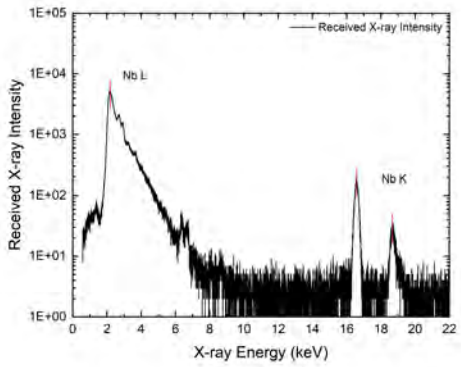

(e) Nb

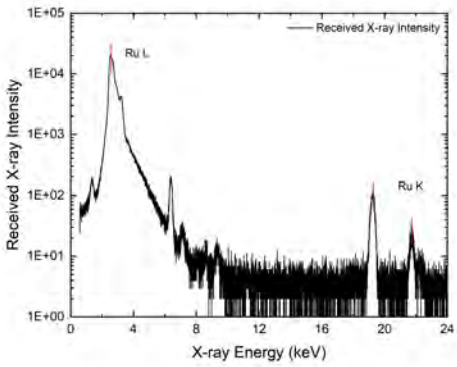

(f) Ru

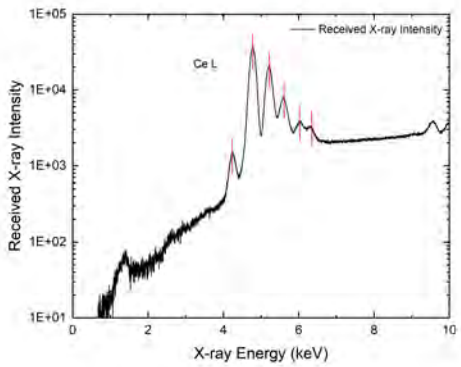

(g) Ce

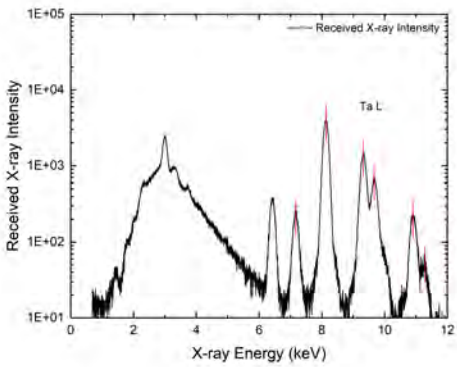

(h) Ta

Figure 5.2: X-ray frequency generated by 1.67 Mev/amu incident carbon ion on Si, Ti, Fe, Zn, Nb, Ru, Ce and Ta sample materials.

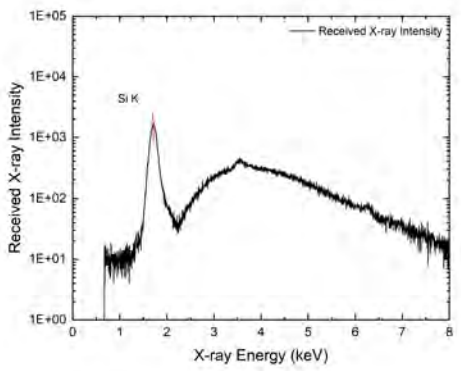

(a) Si

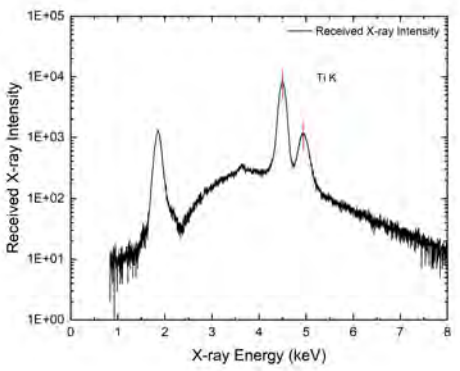

(b) Ti

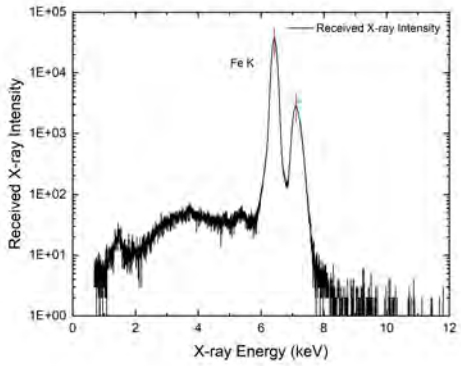

(c) Fe

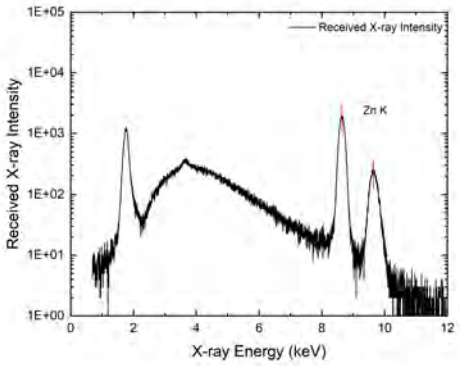

(d) Zn

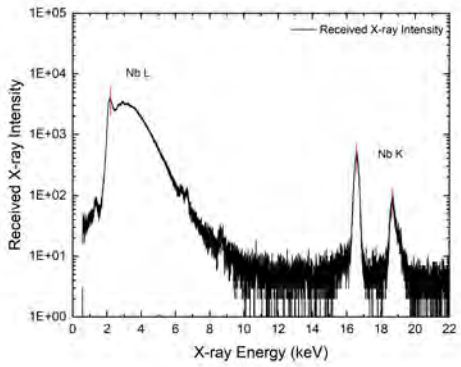

(e) Nb

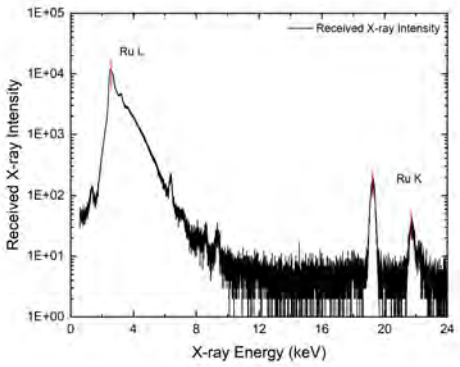

(f) Ru

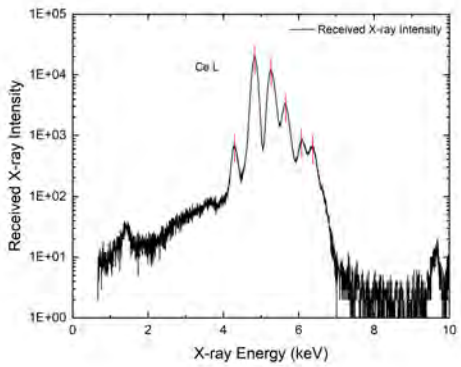

(g) Ce

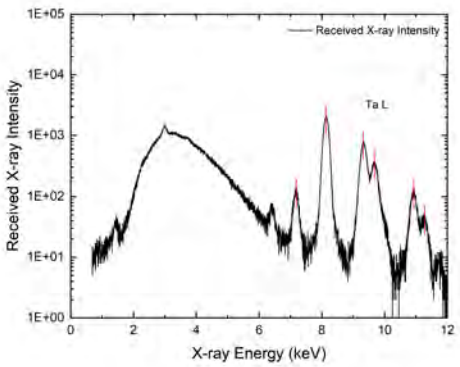

(h) Ta

Figure 5.3: X-ray frequency generated by 3.00 Mev/amu incident carbon ion on Si, Ti, Fe, Zn, Nb, Ru, Ce and Ta sample materials.

Chapter 6

Validation of the Geant4 PIXE Component

The spectra that I obtained (see chapter 5) using the heavy ion microprobe beamline, which used carbon ions, are compared with the Geant4 in this chapter.

This chapter is a modified version of the submitted work:
S. Bakr, D.D. Cohen, R. Siegele, S. Incerti, V. Ivanchenko, A. Mantero, A. Rosenfeld, S. Guatelli, (2022) **"Validation of the Geant4 PIXE component for incident carbon ions"**, *Journal of Nucl. Instruments Methods Phys. Res. Sect. B Beam Interact. with Mater. Atoms,*.

This work presented at the **Ion Beam Analysis** conference 2021, (Online), **26th Geant4 Collaboration** meeting 2021, (Online).

6.1 Abstract

The goal of this study is to experimentally validate PIXE modelling using the Geant4-ANSTO model "*G4–ANSTO*", distributed for the first time in Geant4 11.0, as well as the Geant4 default model ("*G4–default*"), for targets bombarded with carbon ions of energies up to 3 MeV/amu, an energy range of importance for PIXE applications. The experimental validation was performed using a variety of target materials, spanning a broad atomic number range. The reference experimental measurements were performed at the ANSTO heavy ion microprobe beamline ANTARES. To the authors' knowledge, this is the first benchmarking investigation for PIXE simulations in Geant4 utilising carbon ions and it is significant for PIXE-based elemental analysis, encompassing archaeological samples, gas samples, environmental and planetary samples for geological and planetary research studies. It is also of relevance for any physics application, requiring the modelling of

particle induced atomic de-excitation or atomic de-excitation only.

6.2 Introduction

Particle Induced X-ray Emission (PIXE) is a very popular ion-beam technology. Thanks to its multi-elemental nature, it is suitable for geological, environmental, biological, art, and archaeological investigations. The PIXE technique is used to estimate the concentrations of high-Z elements in a given sample. The technique provides fast, non-destructive analysis of test materials in the form of solids, powders, gas, filter substrates, and liquids [21].

Monte Carlo simulation codes are perfectly suited to PIXE modelling in radiation physics for a number of reasons, one of which is that they are able to simulate the stochastic character of the X-ray fluorescence emission process. Ionisation of atoms by particle collisions is followed by de-excitation of the atoms, which provides the basis of modelling the PIXE process [14]. It is also applicable to any physics application that requires the modelling of particle-induced atomic de-excitation or atomic de-excitation on its own.

The Gryzinski theoretical model was used to implement the first PIXE process in Geant4. This model was subsequently improved according to the procedures outlined in Mantero et al. [84], and it was able to simulate PIXE from the ionisation of K-shells by incident protons [14].

There are already three different PIXE ionisation cross section data sets in Geant4 that may be used to simulate a vacancy in a shell: the *"Empirical"* [55–57], the *"Analytical"* [14] and the *"ECPSSR_FormFactor"* sets [58, 59]. The *"ECPSSR_ANSTO"* approach was recently introduced to model ionisation cross section data set of K, L and M shells and their sub-shells for incident protons (0 – 5 MeV) and α particles (0 - 20 MeV), based on the Australia's Nuclear Science and Technology Organisation's ANSTO calculations [16, 17]. This model has been released for the first time in Geant4 11.0.

It is possible to model PIXE with incident ions other than protons or α particles [46, 62]. The ionisation cross section $\sigma_h(E)$ of a generic ion is obtained by scaling the proton ionisation cross sections $\sigma_p(E)$ using the following scaling relation [46]:

$$\sigma_h(E) = Q^2 \cdot \sigma_p(E \cdot \frac{M_p}{Mh}) \tag{6.1}$$

Where E is the kinetic energy of the incident ion, M_h is the ion's mass, Q is the effec-

tive electric charge, and M_p is the mass of the proton [46].

For Geant4 applications that need atomic de-excitation modelling, the Atomic Relaxation Geant4 component handling the emission of X-rays and Auger/Coster-Kronig electrons [44, 46] is based on the Evaluated Atomic Data Library *"EADL"* [63] and provides the radiative (fluorescence) and non-radiative (Auger and Coster–Kronig electrons) transition probabilities. These tabulated data are used to compute the X-ray fluorescence lines [46]. This approach is applicable to elements with atomic numbers from 1 to 100 [14, 63].

EADL provides radiative transition probabilities derived using the Hartree-Slater (HS) method [66]), however, following Campbell et al.'s work [67, 68], Cohen et al. [2] recommended using the Hartree-Fock method instead [50], rather than the Hartree-Slater method [66].

Recently, Bakr et al. introduced an updated fluorescence data library, titled *fluor_ANSTO*, in Geant4 11.0, from the ANSTO calculations based on Hartree-Fock method [17]. The same binding energies as in the original *EADL* (as in G4EMLOW7.7) were adopted in the *fluor_ANSTO* library. These libraries have been added to G4EMLOW8.0. The new data libraries are applicable to targets with elements with atomic numbers ranging from 6 to 92 [14, 50]. Outside this range the default *EADL* data libraries are used.

This work aims to experimentally validate the PIXE modelling based on the *G4–ANSTO* model for the calculation of both the atomic ionisation cross sections [16] and X-ray fluorescence yields [17], which have been released in Geant4 11.0, and the existing *G4–default* model.

6.3 Materials and Methods

Eight target materials were selected (Si, Ti, Fe, Zn, Nb, Ru, Ce, Ta), to span the range from low to high atomic number Z. Carbon ion monochromatic beams (1.00, 1.67, 3.00 MeV/amu) were incident on targets 25 μm thick along the direction of the incident beam. The lateral dimensions were 50 μm. The secondary particle production threshold was ignored (this means that the full X-ray fluorescence cascade is modelled). Once produced in the target, the fluorescence X-rays were counted.

Two models were used for the Geant4 simulations; the *G4–ANSTO* model includes the *ECPSSR_ANSTO* ionisation cross sections data sets and the *fluor_ANSTO* data sets for the fluorescence X-ray emission rates. The second model is the *G4–default*, which includes the *ECPSSR_FormFactor* data sets for the ionisation cross sections and the default Geant4

Table 6.1: The target materials that were bombarded with the carbon ion beam.

Material	Thickness	On a layer of
silicon wafer	1 mm	-
TiN	50 nm	silicon
ZnO	50 nm	silicon
Ta_2O_3	25 nm	graphite
Ru oxide	25 nm	graphite
Nb oxide	45 nm	graphite
Fe_2O_3	embedded in boron oxide pellet	
CeO_2	embedded in boron oxide pellet	

atomic relaxation library, incorporating *EADL* [63] to calculate the emission rates of the fluorescence X-rays, once a vacancy has been generated. The Geant4 extended example *TestEm5* and *Geant4 10.05.p01* were used to execute the simulations. In order to attain a statistical uncertainty of less than $\sim 1\%$, the Geant4 simulation utilises 10^7 histories.

The results of the Geant4 simulations, using both models *G4–ANSTO* and *G4–default*, were subsequently compared to experimental measurements collected at ANSTO (Lucas Heights, NSW, Australia) using the 10 MV ANTARES tandem accelerator.

PIXE X-ray fluorescence spectra were obtained experimentally at the ANSTO heavy ion microprobe beamline utilising 1.00, 1.67, and 3.00 MeV/amu carbon ion beams with beam currents ranging from 0.5 to 2.5 nA. These precise energies were taken into account in the Geant4 simulations. A high purity Ge detector with a 100 mm^2 receiving area and a solid angle of 90 msr was utilised for X-ray detection. The detector is fitted with a Be window of 25 μm thickness. The data were obtained using the Melbourne University's Data Acquisition System mpsys4 and a Canberra Model 2060 digital signal processor. The irradiated samples are shown in table 6.1.

6.4 Results and Discussion

The simulation results obtained with both the *G4–ANSTO* and *G4–default* approaches are reproduced in figures 6.1 to 6.6. Note that the horizontal axis is energy (keV), and the vertical axis indicates X-ray frequency per incident carbon ion. The *G4–ANSTO* data were convolved with a Gaussian function to compare directly to the experimental spectra. The rationale for computing the Gaussian for the simulation results deriving from the adoption of *G4–ANSTO* is that several lines were adjacent, and so their contributions were complex for generating peaks comparable to the experimentally observed peaks.

For ease and meaningful comparison with the experimental data, I normalised the ex-

perimental spectrum and *G4–default* results to the highest peak of the *G4–ANSTO* results. Similarly, I computed the Gaussian of the *G4–ANSTO* and normalised it to the *G4–ANSTO* highest line as shown in the Figures below (The $K_{\alpha(I)}$ line was used for Si, Ti, Fe, Zn, Nb and Ru samples materials, and the $L_{\alpha(I)}$ line for Ce and Ta sample materials). If I did the same procedure for the *G4–default* approach and presentation of all the data and spectra on the same scale plots, the reader would be confused since the Gaussians of both *G4–ANSTO* and *G4–default* would look to be reasonably identical.

Then, I compared the predicted *G4–ANSTO* and *G4–default* X-ray fluorescence yields per incident carbon ion, in order to quantify differences between the two approaches. This is of relevance for any application of Geant4, not just the PIXE technique, in which the atomic de-excitation modelling is relevant.

6.4.1 1.00 MeV/amu Incident Carbon Ion Results

Figures 6.1 and 6.2 below provide comparisons of the X-ray fluorescence yields predicted by the *G4–default* and *G4–ANSTO* simulations, as well as experimentally measured results, for 1.00 MeV/amu carbon ion beams incident on the aforementioned Si, Ti, Fe, Zn, Nb, Ru, Ce and Ta targets.

Due to low energy background limitations, I couldn't experimentally produce the L shell X-ray emissions of Nb and Ru samples. It can be seen from figure 6.1 that the *G4–ANSTO* and *G4–default* simulations appear to be equivalent, except for the $K_{\alpha(II)}$ and $K_{\beta(I)}$ X-ray lines for Nb and Ru samples, where the *G4–default* simulation predicts slightly higher X-ray emission rates.

Figure 6.2 shows the ratios of X-ray emission yield per incident carbon ion, obtained with the two approaches, permitting easy quantification of the differences between the *G4–ANSTO* and the *G4–default* models.

In all investigated samples, the *G4–ANSTO* approach shows significantly higher X-ray emission rates for all X-ray lines than the *G4–default* approach, except for the Zn $L_{\beta(I)}$ X-ray line and L_l and $L_{\beta(I)}$ lines for Nb, Ru, Ce and Ta.

In figure 6.2, when comparing the X-ray fluorescence yield per incident carbon ion, for the $K_{\alpha(I)}$ line, the *G4–ANSTO* results were roughly $\sim 5\%$ higher than *G4–default* for Si, Ti, Fe and Zn materials, while it was around $\sim 50\%$ higher for Nb and Ru. This large discrepancy might be due to the difficulty in obtaining distinct K lines for medium Z materials in the experiments. For $L_{\alpha(I)}$ lines of Ce and Ta, it was found that *G4–ANSTO*

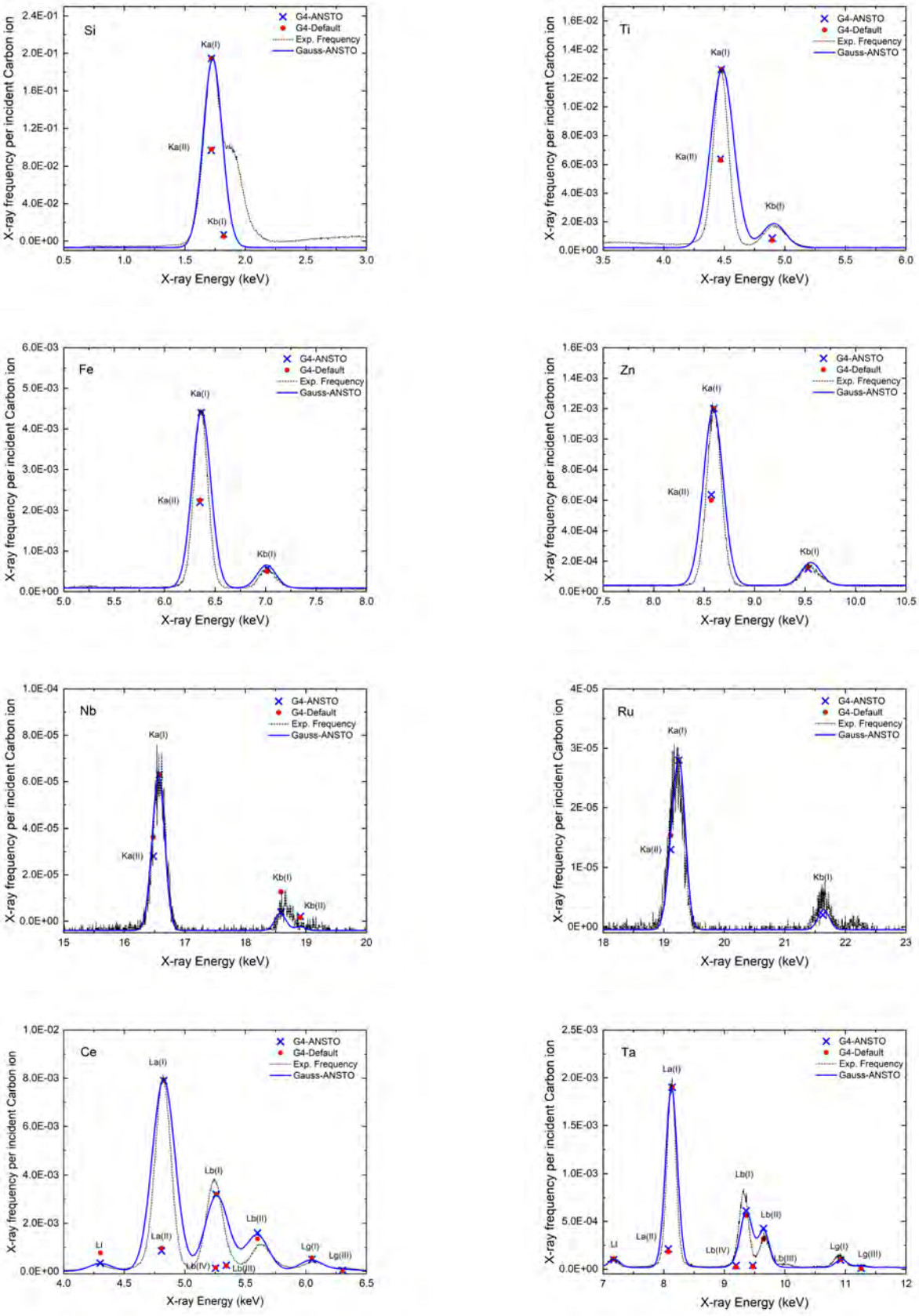

Figure 6.1: X-ray emission yields obtained with 1.00 MeV/amu incident carbon ions.

simulations were about 25% and 10% higher than *G4–default*. Furthermore, the ($L_{\beta(I)}$, $L_{\beta(III)}$, $L_{\beta(IV)}$) lines calculated using both the *G4–ANSTO* and *G4–default* approaches were lower than the experimental spectrum, which was due to the fact that these four lines were closely adjacent to each other and thus their contributions convolve to produce the higher peaks observed in the experimental data. Figure 6.2 shows the L_l line of Nb, Ru and Ce calculated by the *G4–default* approach was $\sim 60\%$ higher than that from the *G4–ANSTO* approach. To explain these changes in L_l X-ray yield, the X-ray fluorescence lines of the data libraries of *G4–default* and *G4–ANSTO* approaches were directly compared, and it was found that only the L_l X-ray line probability of transition was greater in *G4–default* when compared to the *G4–ANSTO* probability.

6.4.2 1.67 MeV/amu incident carbon ion results

The *G4–ANSTO* and *G4–default* calculated results and experimental data for 1.67 MeV incident beam energy are compared in figure 6.3 for Si, Ti, Fe, Zn, Nb, Ru, Ce and Ta targets.

The *G4–ANSTO* and *G4–default* approaches appear to provide identical results, with the exception of the $K_{\alpha(II)}$ X-ray line for Nb and Ru samples, as well as L_l X-ray line for Ce, where the *G4–default* calculates higher X-ray emission rates.

Moreover, the computed lines ($L_{\beta(I)}$, $L_{\beta(III)}$, $L_{\beta(IV)}$) using both the *G4–ANSTO* and *G4–default* approaches were slightly lower than the experimental spectrum. I observe that the *G4–ANSTO* approach gives slightly more realistic X-ray emission outcomes than the *G4–default* approach. The difference was particularly noticeable in the $L_{\alpha(I)}$ line. The ratio of X-ray emission rates per incident ion, calculated by *G4–ANSTO* and *G4–default*, are shown in figure 6.4 for Si, Ti, Fe, Zn, Nb, Ru, Ce and Ta samples.

In figure 6.4, the results of *G4–ANSTO* were approximately 5% higher than *G4–default* results for Si, Ti, Fe, and Zn in the case of $K_{\alpha(I)}$ X-ray line. For $L_{\alpha(I)}$ X-ray line, it was observed that *G4–ANSTO* results were about 45% higher than *G4–default* for Nb and Ru and around 25% higher for Ce and Ta.

The *G4–default* calculation for the L_l line of Nb, Ru, Ce and Ta was $\sim 60\%$ higher than that predicted by the *G4–ANSTO* approach, as illustrated in figure 6.4, since the probability of transition for the L_l X-ray line is higher in the *G4–default* approach.

6.4.3 3.00 MeV/amu incident carbon ion results

Figure 6.5 provides a comparison of calculated X-ray yields and the experimentally observed X-ray emission spectra of Si, Ti, Fe, Zn, Nb, Ru, Ce and Ta samples as a result of

incident 3.00 MeV/amu carbon ions.

The experimental spectra, *G4–default* and *G4–ANSTO* Gaussian, were normalised to the highest line of *G4–ANSTO* X-ray emissions ($K_{\alpha(I)}$ for Si, Ti, Fe, Zn, Nb, Ru and $L_{\alpha(I)}$ for Ce, Ta). Both the *G4–ANSTO* and *G4–default* approaches appear to make identical predictions. Figure 6.6 only shows the Geant4 simulation results, specifically the ratio of X-ray emission frequencies per incident ion calculated by the *G4–ANSTO* approach and the *G4–default* approach. Figure 6.6 demonstrates that the *G4–ANSTO* approach predicts roughly 3% greater $K_{\alpha(I)}$ X-ray frequency ratios than the *G4–default* for Si, Ti and Fe samples, and in the case of Zn the difference between the two models was about 20%.

For the $L_{\alpha(I)}$ lines, it was clear that *G4–ANSTO* values were around 40% higher than *G4–default* for Nb and Ru, and approximately 25% and 15% higher for Ce and Ta, respectively. Figure 6.6 shows that the L_l line of Nb and Ru calculated by the *G4–default* approach were 60% higher than those calculated by the *G4–ANSTO* approach, except in the case of Ce and Ta, where the differences were 50% and 25%, respectively.

6.5 Conclusion

Experimental results for incident carbon ions were compared with the *G4–ANSTO* approach, which combines the *ECPSSR_ANSTO* ionisation cross sections and *fluor_ANSTO* fluorescence yield libraries, and cross-compared with the *G4–default* approach. The *ECPSSR_FormFactor* ionisation cross sections and *EADL* fluorescence yield libraries are included in the *G4–default* approach. Carbon ion ionisation cross sections in Geant4 were derived by scaling proton ionisation cross sections.

Carbon ion monoenergetic beams of 1.00, 1.67, and 3.00 MeV/amu were used for these studies and fluorescence X-ray yields per incident particle were calculated with the *G4–ANSTO* and *G4–default* approaches for calculating X-ray emission spectra. Results were compared for low to high atomic number Z materials using eight different target materials (Si, Ti, Fe, Zn, Nb, Ru, Ce and Ta).

With the exception of the L_l line, which corresponds to the electron transition from the $M_{(I)}$ sub-shell to the $L_{(III)}$ sub-shell, most predicted values were higher when using the *G4–ANSTO* approach for all samples. When we look at the absolute values of the X-ray fluorescence yields per incident carbon ion, we usually found differences of about 5% between *G4–ANSTO* and *G4–default* approaches. However, for some specific target materials, X-ray lines and incident energies, the two methods occasionally diverged by larger

differences. In the case of $L_{\alpha(I)}$ for Ce and Ta the *G4–ANSTO* method predicted values about 25% higher than the *G4–default* approach. The only case in which agreement between the two methods was extremely poor and invites further study and refinement was $L_{\gamma(III)}$ for Ta where the calculated ratios differed by as much as 250%.

The investigation found that the *G4–ANSTO* calculated X-ray emission spectra and the ANSTO experimental measurements agreed reasonably well (see figures 6.1, 6.3 and 6.5). It is worth noting that differences between *G4–ANSTO* and *G4–default* codes using carbon ion are consistent with the results obtained previously by Bakr et al. [17] utilising protons and α particles.

It is generally assumed that collision ionisation cross sections for processes emitting X-rays involve single "hole" (vacancy) formation, but this is not the case for heavier ions such as carbon nuclei, because multiple vacancies reduce Coster-Kronig transition probabilities and increase fluorescence yields, particularly for L and higher shell vacancies. Using calculated carbon ion ionisation cross sections could address this issue and provide better predictions than scaled proton ionisation cross sections.

6.6 Acknowledgements

This research was funded by the *Australian Research Council* via the ARC DP 170100967 grant, for which we are most grateful. The authors would also like to thank the *Australian National Collaborative Research Infrastructure Strategy* (NCRIS) for funding the accelerators. We are also thankful for the staff at the *Centre for Accelerator Science* for providing access to the ion beam analysis facilities.

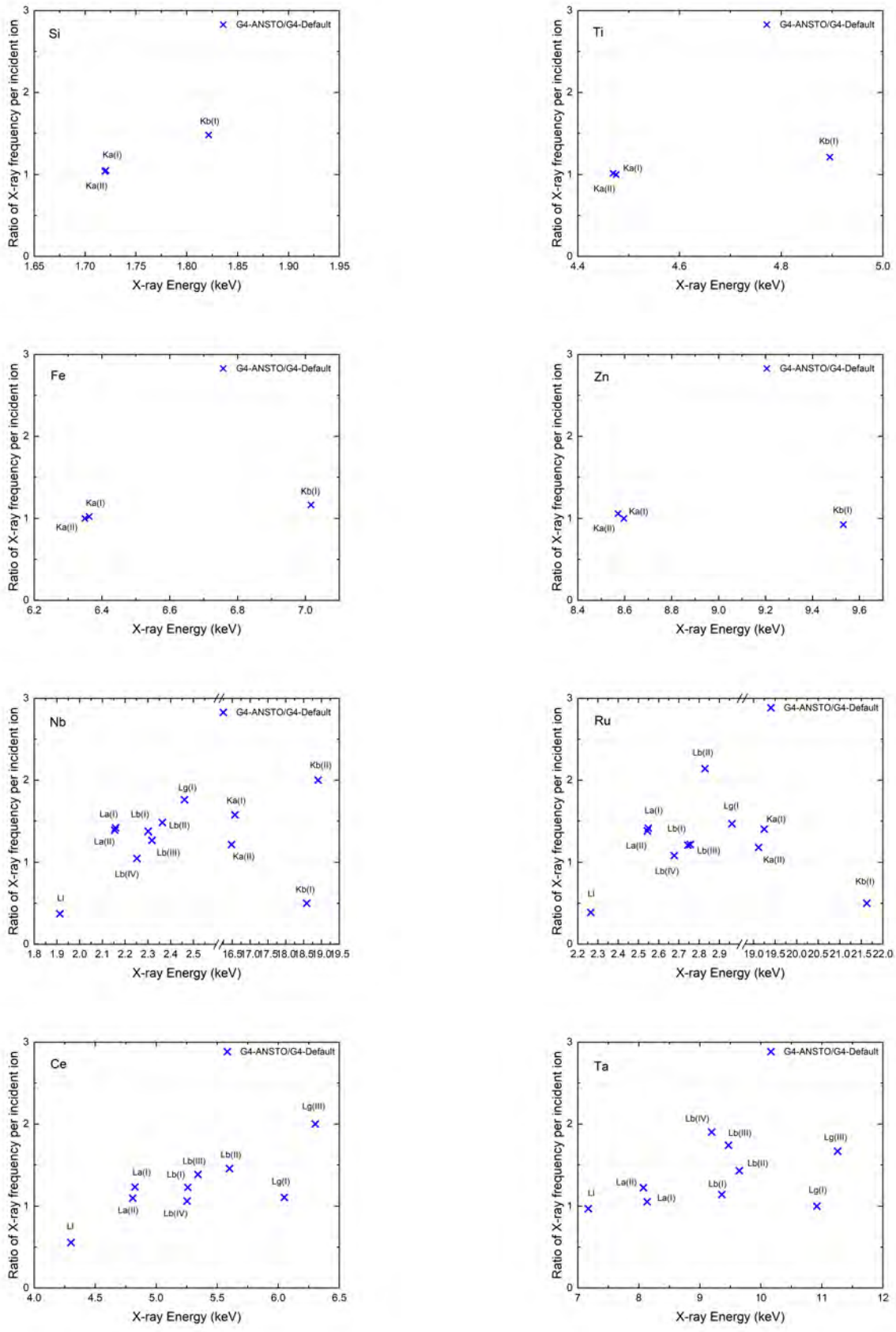

Figure 6.2: Ratio of X-ray emission yields for the case of 1.00 MeV/amu incident carbon ions.

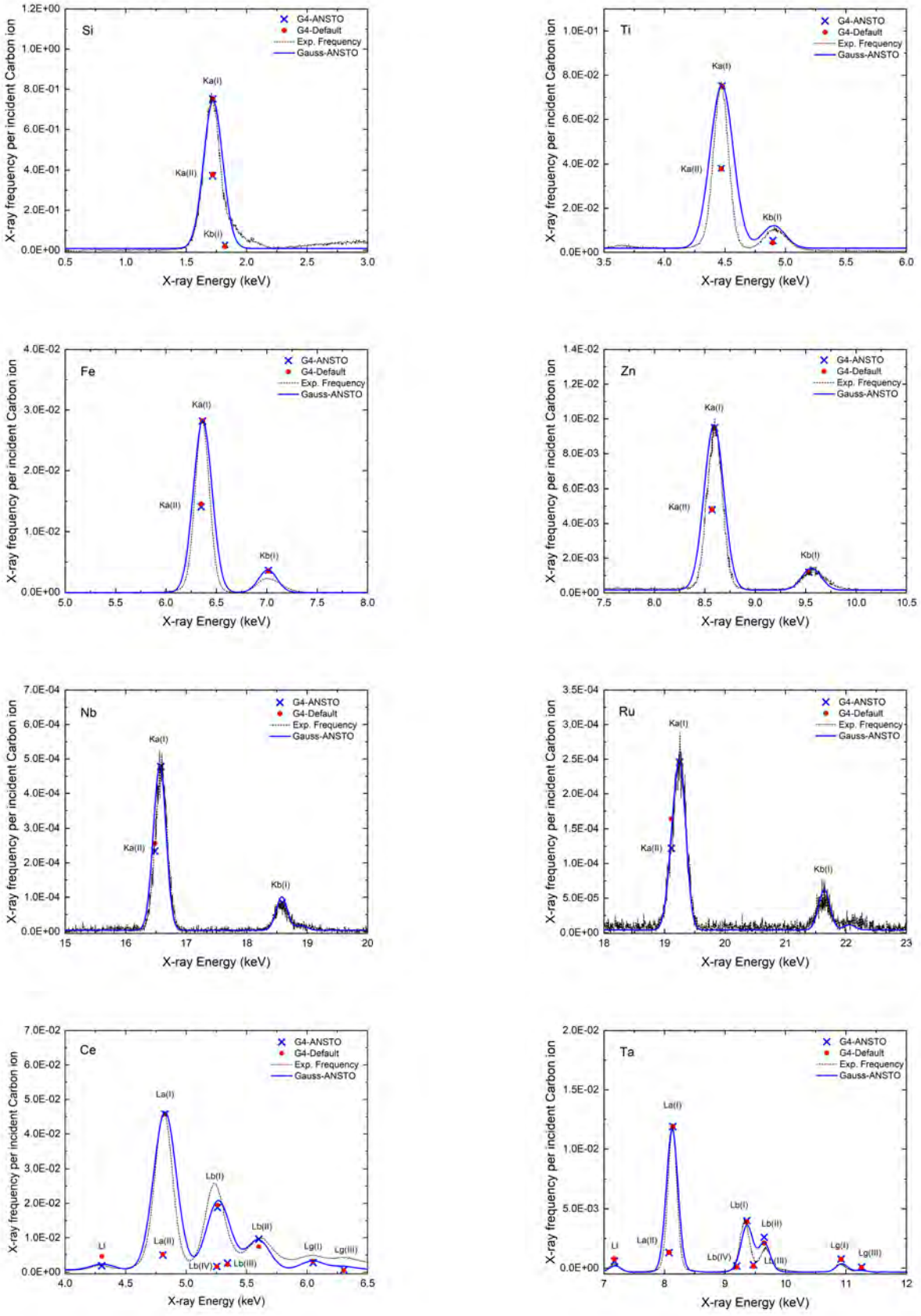

Figure 6.3: X-ray emission yields obtained with 1.67 MeV/amu incident carbon ions.

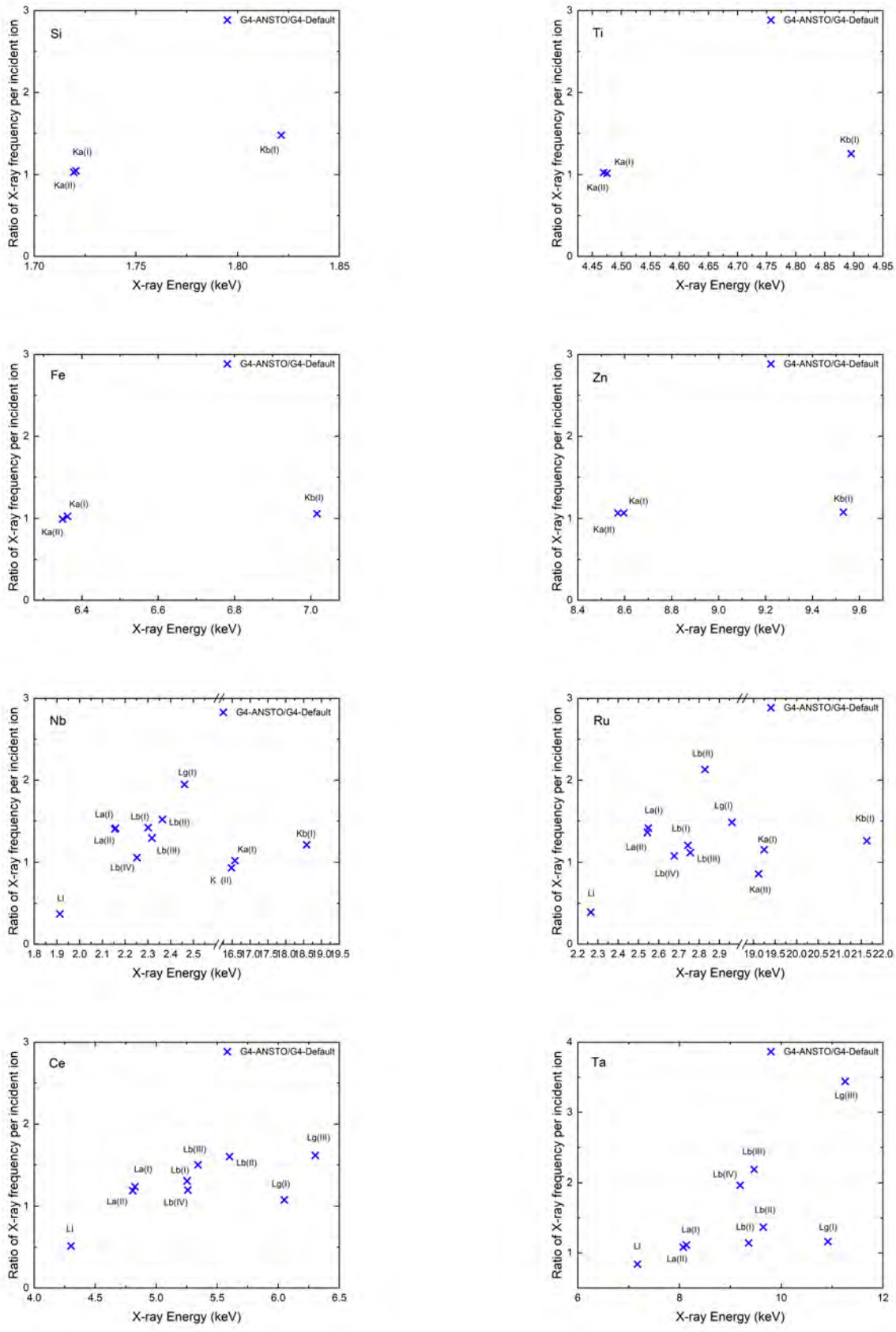

Figure 6.4: Ratio of X-ray emission yields for the case of 1.67 MeV/amu incident carbon ions.

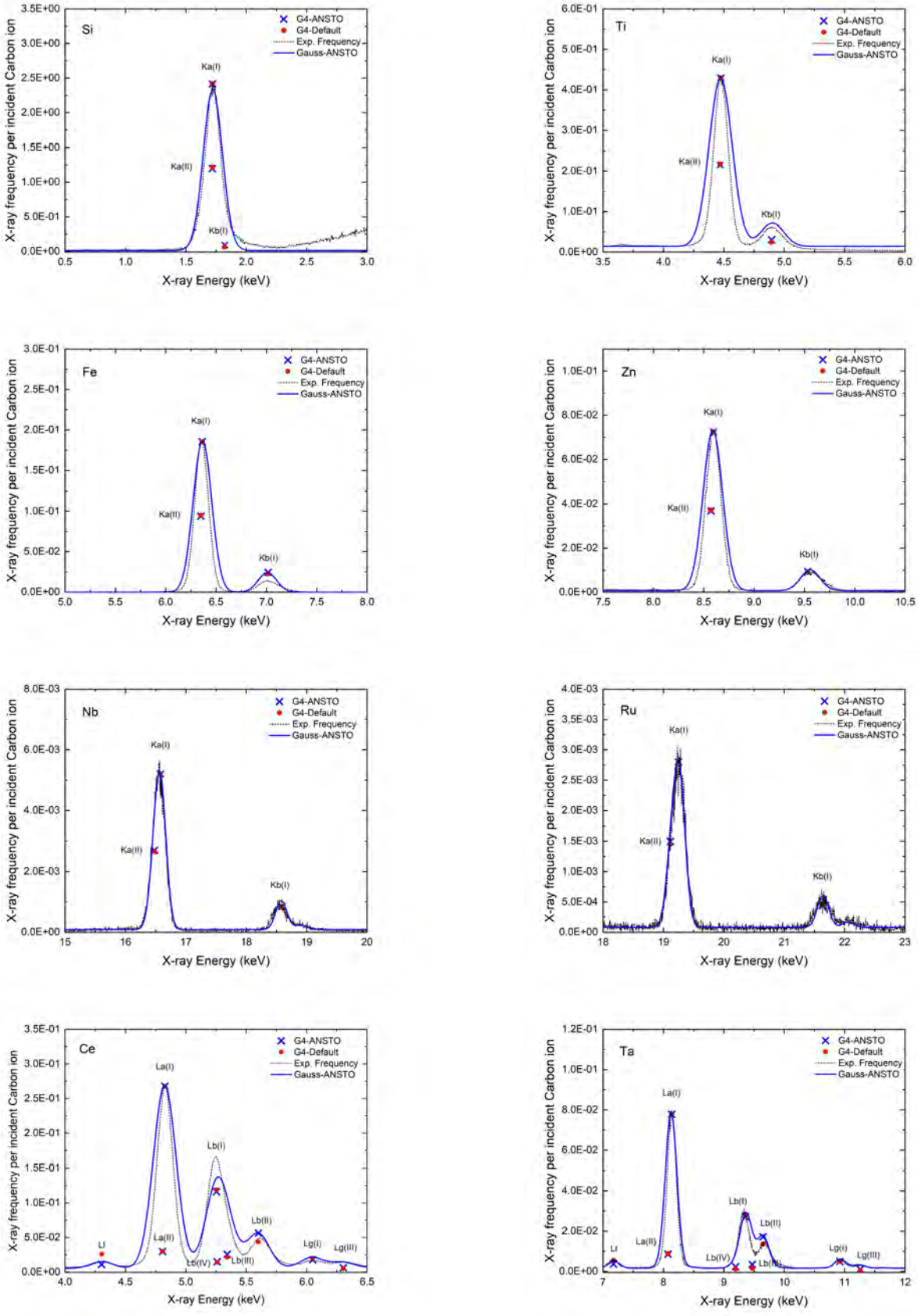

Figure 6.5: X-ray emission yields obtained with 3.00 MeV/amu incident carbon ions.

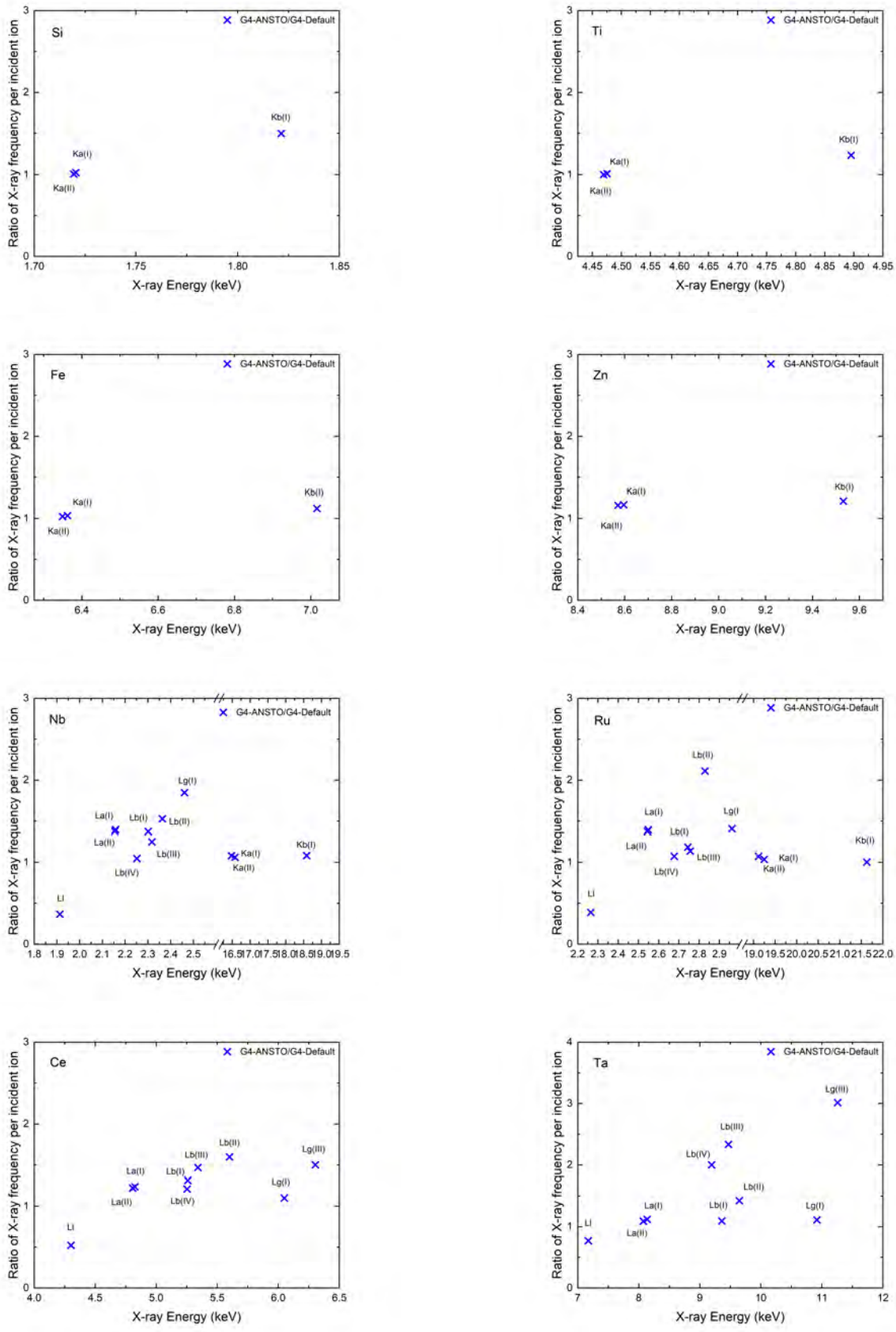

Figure 6.6: Ratio of X-ray emission yields for the case of 3.00 MeV/amu incident carbon ions.

Chapter 7

A Benchmarking Study of Geant4 Auger Electrons

In this chapter, I benchmarked for the first time the emission of Auger electrons derived from some medical radioisotope decays calculated using Geant4 against other theoretical approaches and experimental results.

This chapter is a modified version of the published work:
S. Bakr, T. Kibedi, B. Tee, D. Bolst, M. Vos, M. Alotiby, L. Desorgher, D. H. Wright, A. Mantero, A. Rosenfeld, V. Ivanchenko, S. Incerti, S. Guatelli, (2021) **"A benchmarking study of Geant4 for Auger electrons emitted by medical radioisotopes"**, *Journal of Applied Radiation and Isotopes* May 2021, 174.

`https://doi.org/10.1016/j.apradiso.2021.109777`

This work presented at the **26th Geant4 Collaboration** meeting 2021, (Online), **25th Geant4 Collaboration** meeting 2020, (Online).**24th Geant4 Collaboration** meeting 2019, (Jefferson Lab, New York, USA), **NSTLI seminars** 2019, (Australia's Nuclear Science and Technology Organization (ANSTO), Sydney, Australia), **Heavy Ion Accelerator** Symposium 2018, (Australian National University, Canberra, Australia), **Third Geant4 International User** conference 2018, (Bordeaux, France).

7.1 Abstract

Auger emitting radioisotopes are of great interest in targeted radiotherapy because, once internalised in the tumour cells, they can deliver dose locally to the radiation sensitive targets, while not affecting surrounding cells. Geant4 is a Monte Carlo code widely used

to characterise the physics mechanism at the basis of targeted radiotherapy. In this work, I benchmarked the modelling of the emission of Auger electrons in Geant4 deriving from the decay of ^{123}I, ^{124}I, ^{125}I radionuclides against existing theoretical approaches. I also compared Geant4 against reference data in the case of ^{131}Cs, which is of interest for brachytherapy. In the case of ^{125}I and ^{131}Cs, the simulation results are compared to experimental measurements as well. Good agreement was found between Geant4 and the reference data. As far as I know, this is the first study aimed to benchmark against experimental measurements the emission of Auger electrons in Geant4 for radiotherapy applications.

7.2 Introduction

The Auger effect involves the emission of atomic electrons as alternative channel to X-ray fluorescence in the atomic de-excitation, which follows the creation of a vacancy in an atomic shell [85, 86]. Auger electron emitting radionuclides are of great interest in targeted radiotherapy because Auger electrons have high Linear Energy Transfer (4–26 $keV/\mu m$) and short range [87–89].

The present chapter reports on the Auger electron emission following the radioactive decay of ^{123}I, ^{124}I, ^{125}I and ^{131}Cs. The iodine radioisotopes are widely used in nuclear medicine for the labelling of monoclonal antibodies, receptors and other radiopharmaceuticals, especially in diagnostic and therapeutic applications, where quantitative imaging over a period of several days is necessary [90, 91]. The optimal combination of half-life and energy of the emitted radiation makes ^{131}Cs an attractive radioisotope for brachytherapy of malignant tumours.

Geant4 [92] is a Monte Carlo code which is extensively used in medical physics applications, including micro- and nano-dosimetry [93, 94], brachytherapy and targeted radiotherapy [95, 96]. Therefore, it is important to benchmark the emission of Auger electrons in Geant4 against reference data.

The goal of this work is to benchmark, for the first time, Geant4 in terms of emission of Auger electrons. A Geant4 simulation was developed to calculate the emission yields and energy spectra of Auger electrons emitted from ^{123}I, ^{124}I, ^{125}I and ^{131}Cs radionuclides. The results were compared to other Monte Carlo based calculations available in the literature and experimental measurements performed at the *Australian National University* (ANU) and the *Joint Institute for Nuclear Research* (JINR) in the case of ^{125}I and ^{131}Cs, respectively.

7.3 Materials and Methods

7.3.1 Radioactive Decays Under Investigation

^{123}I (half-life $T_{1/2}$ = 13.224 hr) decays by electron capture (EC) (100% probability) to an excited state of ^{123}Te. The strongest transition at 159 keV carries 99% of the total intensity and 19% of the time will decay via internal conversion (IC) to ^{123}Te, which has a very long half-life ($T_{1/2} = 9.2 \times 10^{16}$ year) [97].

^{124}I ($T_{1/2}$ = 4.176 d) decays via either $\beta+$ (22.7% probability) or EC (77.3% probability) to either excited states (65% probability) or to the ground state (35% probability) of ^{124}Te [98].

^{125}I ($T_{1/2}$ = 59.49 d) decays by EC (100% probability) followed by either gamma ray emission (6.68% probability) or IC (93.32% probability), to the ground state of the stable ^{125}Te [99].

^{131}Cs decays directly via EC decay to the ground state of ^{131}Xe, hence, Auger electrons are only emitted from the atomic relaxation in ^{131}Xe from the vacancy created by EC. ^{131}Cs is one of the pure Auger emitters for nuclear medicine [100].

7.3.2 Atomic Relaxation in Geant4

Geant4 has the functionality of simulating both the radiative (X-ray) and non-radiative (Auger electron) atomic relaxation process of singly ionised atoms [44, 48]. Geant4 treats ionised atoms as isolated entities [63]. This means that an atom exists separately without bonding with any other atom. The creation of a vacancy is handled by the Geant4 electromagnetic physics package. The generation of the relaxation cascade is handled by the atomic relaxation component, which is used by all the primary processes generating a vacancy [44, 46, 48]. The simulation of atomic relaxation takes place in two stages:

1. determination of the shell (or sub-shell) where the vacancy is created by the primary process, radioactive decay in this case;

2. the relaxation cascade is then triggered, starting from the vacancy created by the primary process; secondary photons or electrons are generated through radiative and non-radiative transitions, based on the respective transition probabilities [44, 46, 48, 63].

In stage 1, the *G4RadioactiveDecay* module is used to simulate the decay, either at rest or in flight, of radioactive nuclei by electron capture (EC) and by α, $\beta-$ and $\beta+$ emission

or isomeric (IT) decay. If the daughter of a nuclear decay is an excited isomer, its prompt nuclear de-excitation is treated using the *G4PhotoEvaporation* class [92].

The sub-shell ratios for electron capture is calculated according to Bambynek [101]. In this model only electrons from the $s_{1/2}$ and $p_{1/2}$ sub-shells (K, L_1-L_2, M_1-M_2, N_1-N_2) are captured. Whereas, for internal conversion the probabilities are specified in Geant4 *PhotoEvaporation5.5* data library (version used in this work). These probabilities are computed with *BRICC* code [102], except if they are provided in the *ENSDF* files.

Geant4 uses the Livermore Evaluation Atomic Data Library *EADL* [63] in stage 2 to calculate the complete radiative and non-radiative emission of X-rays and Auger electrons as the atom relaxes [92]. The energy of the relaxation product is calculated as the difference of the sub-shell binding energies involved with the atomic de-excitation process [63]. It is assumed that the binding energy of all sub-shells are the same for neutral ground state atoms as for ionised atoms [63, 92]. The Geant4 Atomic Relaxation model does not distinguish between Auger and Coster-Kronig transitions [44], thus, the term Auger is used for both transitions.

7.3.3 Geant4 Simulation Setup

The Geant4 extended example *rdecay01* was used in this study and Geant4 10.05.p01 version has been adopted. A cube of 20 mm size of vacuum is modelled, with a point source of ^{123}I, ^{124}I, ^{125}I and ^{131}Cs in the centre of the box. The radioactive decay and the full atomic relaxation are modelled. The output of the simulation is the emission yield per radioactive decay and the energy spectra of the emitted Auger electrons. The number of histories in the Geant4 simulation is 10^7 to obtain a statistical uncertainty below 1%. Nevertheless, it should be noted that the uncertainty of *EADL* Auger electrons yields for an inner shell vacancy is less than 15% [63]. Only inner shell vacancies are considered in this work when comparing the simulation results to experimental data. The calculated Auger electron spectra were binned using 50 eV bin width. In the analysis of the results, the Auger electrons have been grouped according to the *IUPAC* notation, based on the atomic shells involved in the transition [103]. Following this notation, Auger *MXY*, M-shell Auger transition where neither of the two new vacancies is in the N-shell. Auger *LMX*, L-shell Auger transition where one of the vacancies is in the M-shell. Auger *LMM*, L-shell Auger transition where both new vacancies are in the M-shell. Auger *KLL*, K-shell Auger transition where both new vacancies are in the L-shell. Auger *KLX*, K-shell Auger transition where one of the two new vacancies is in the L-shell. And Auger *KXY*, K-shell Auger transition where neither of the two new vacancies is in the L-shell.

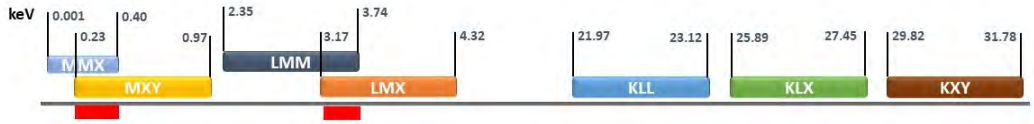

Figure 7.1: Energy ranges for Auger electron groups in tellurium according to *EADL* [63]. Overlapping energy ranges are indicated with red squares below the axis.

Each individual Auger electron energy line calculated by means of the Geant4 simulation needs to be associated to the specific transition producing it, as this information is not provided automatically in a Geant4 user application. This method has been adopted as currently it is not possible to directly retrieve the transition type in a Geant4 user application. In the analysis of the simulation results, Auger *KLL*, *KLX*, and *KXY* lines were grouped according to their energy ranges in *EADL* [63], as shown in figure 7.1 (e.g., the line 3.6185 keV matches with $L_2M_1O_3$ transition energy (*EADL* [63]), so it belongs to group *LMX*). To note, the Geant4 simulation results showed a slight energy broadening of the Auger lines due to momentum transfer to the daughter of the radioactive decay. When I find two transitions for the same energy in overlapping energy ranges as represented in figure 7.1, the difficulty to retrieve the transition shows up. This problem is due to the fact that the bin width in the simulation is 1 eV, which is greater than the difference between a few transition energies (e.g., the line $L_3M_5M_5$ 3.17422 keV and $L_3M_1N_1$ 3.17429 keV (*EADL* [63]). In these situations, I decided to choose the most probable transition for the specific line.

The mean energy, $\bar{E}$ of each Auger transition groups (*MXY, LMM, LMX, KLL, KLX* and *KXY*) was evaluated as:

$$\bar{E} = \frac{\sum_i (E_i \cdot Y_i)}{Y_{Total}} \tag{7.1}$$

where E_i is the energy and Y_i is the yield of an Auger line in the group. Y_{Total} is the total yield of the Auger group.

7.3.4 Theoretical Approaches Used to Benchmark Geant4 Atomic Relaxation

The theoretical approaches used to benchmark Geant4 are based on the Monte Carlo based calculations by Pomplun [104], Stepanek [105] and the BrIccEmis by Lee et al., developed at the Australian National University (ANU) [87, 106–108]. Table 7.1 summarises

Table 7.1: Atomic and nuclear data used in the calculations by Stepanek [105], Pomplun [104] and in BrIccEmis [106], as well as in Geant4.

	Stepanek [105]	**Pomplun [104]**	**BrIccEmis [106]**	**Geant4**
Nuclear decay data	ENSDF [109]	ICRP38 [110]	ENSDF [109]	ENSDF [109]
Electron capture probabilities	Gove et al. [111] Martin et al. [113]	Gove et al. [111]	Schönfeld [112]	Bambynek et al. [101]
Atomic shells	K-N	K-N	K-O	K-O
Atomic transition rates	Perkins et al. (EADL) [63]	Storm et al. [114] Chen et al. [51] McGuire et al. [115]	Perkins et al. (EADL) [63]	Perkins et al. (EADL) [63]
Atomic transition energies	Dirac-Hartree -Slater [50]	Dirac-Fock Deslaux [116]	Dirac-Fock Band et al. [117]	Perkins et al. (EADL) [63]

the models and data libraries used in the calculations. In the BrIccEmis calculations the so-called "isolated atom" approximation was used, namely once a vacancy reached the valence shell, it remained unfilled.

The yields of Auger electron emission have been calculated as described in section 7.3.3 and also computed analytically (called here Geant4Lib analytical code) by using directly the radioactive decay, nuclear de-excitation, and atomic relaxation data contained in the Geant4 data libraries. This approach allows to verify that the input data libraries are used correctly by the Geant4 kernel when performing simulations of radioactive decay.

In the Geant4lib analytical code, the yield of a given Auger electron line is obtained by the sum of the probabilities of the different disintegration branches leading to the emission of this specific line. Each disintegration branch consists in the succession of a radioactive disintegration of the parent nucleus to an excited state of the daughter, a cascade of nuclear de-excitation with at least one electron conversion emission, and an atomic relaxation cascade leading to the emission of the considered Auger line. The probability of a branch is obtained by the product of the probability of all steps involved in the branch. This code does not take into account the nuclear recoil broadening, which is instead considered in the full Geant4 simulation used in this work.

Table 7.2: List of reference published data used in this study. I compare only K-lines in the case of validation against experimental data.

	Calculations	**Experimental**
^{123}I	BrIccEmis [106] Pomplun [123]	-
^{124}I	BrIccEmis [106]	-
^{125}I	BrIccEmis [106] Stepanek [105] Pomplun (KLL spectrum) [104]	ANU (KLL spectrum) [118]
^{131}Cs	-	JINR (KLL spectrum) [121]

7.3.5 Reference Experimental Measurements

Two sets of experimental measurements of Auger electron spectra were used in this work. The first set derives from experimental measurement with an ^{125}I source performed at the ANU obtained with an electron momentum spectrometer (EMS) which can measure electrons from 2 keV to 40 keV (the energy resolution of the spectrometer is $\simeq$ 6 eV) [118]. The iodine source was prepared at ANSTO (Australia's Nuclear Science and Technology Organisation) with a NaI solution deposited on top of a 200 $\mu g/cm^2$ gold substrate, following the procedure described by Pronschinske et al [119]. The resulting source was a monolayer of ^{125}I on top of the gold substrate [120].

The second set of experimental measurements is documented in [121]. A $BaCO_3$ target was irradiated in the nuclear reactor IBR-2 of the JINR lab, Dubna, at the neutron flux of $\sim 2.5 \times 10^{12} \frac{n}{cm^2.s}$ for 10 days. The electron spectrum was measured using a combined electrostatic spectrometer [122], consisting of a retarding sphere followed by a double-pass cylindrical mirror energy analyser [121].

Table 7.2 summarises the radioisotopes under study and the reference theoretical and experimental data used to benchmark Geant4.

7.4 Results and Discussion

The first section shows the comparison of Geant4 results against the theoretical predictions by BrIccEmis [106, 108], Pomplun [104, 123] and Stepanek [105] for ^{123}I, ^{124}I and ^{125}I in terms of emission yields of Auger electrons. The second section is dedicated to the comparison against experimental measurements for ^{125}I and ^{131}Cs radioisotopes.

7.4.1 Comparison to Other Theoretical Approaches

Figures 7.2 to 7.4 present the generated energy spectra and yield of Auger electrons for ^{123}I, ^{124}I and ^{125}I decays, respectively, using the Geant4 simulation described in section 7.3.3 and BrIccEmis [106].

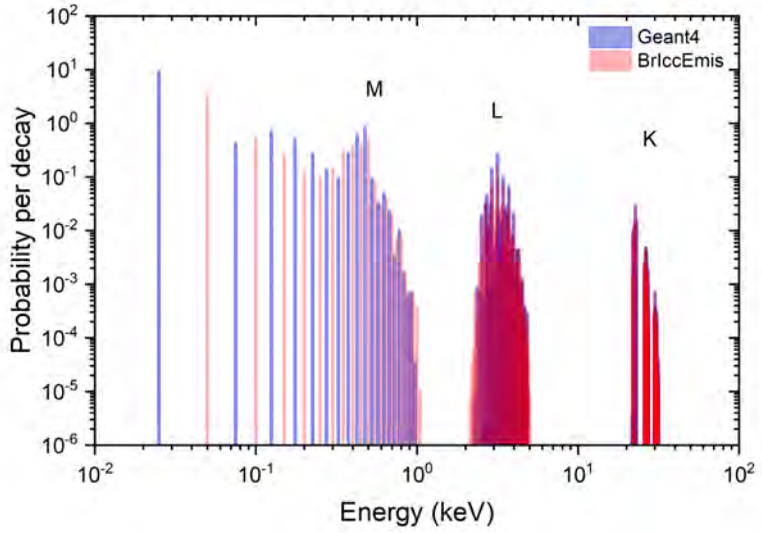

Figure 7.2: Calculated Auger electron spectrum following the radioactive decay of ^{123}I, normalized for 1 radioactive decay. K, L and M indicate the major Auger groups.

Tables 7.3 to 7.5 show the Auger electron energies and emission yields for ^{123}I, ^{124}I and ^{125}I decay, respectively, as calculated by means of the Geant4 simulation described in section 7.3.3, the Geant4Lib analytical code, BrIccEmis [106], Pomplun [123] and Stepanek [105].

In reference to figures 7.2 to 7.4, the Auger electron lines can be separated according to the atomic shell of the initial vacancy: above 20 keV for the K-shell, 2–5 keV for the L-shells, 0.2–1 keV for the M-shells, and below 0.2 keV for the remaining outer electron

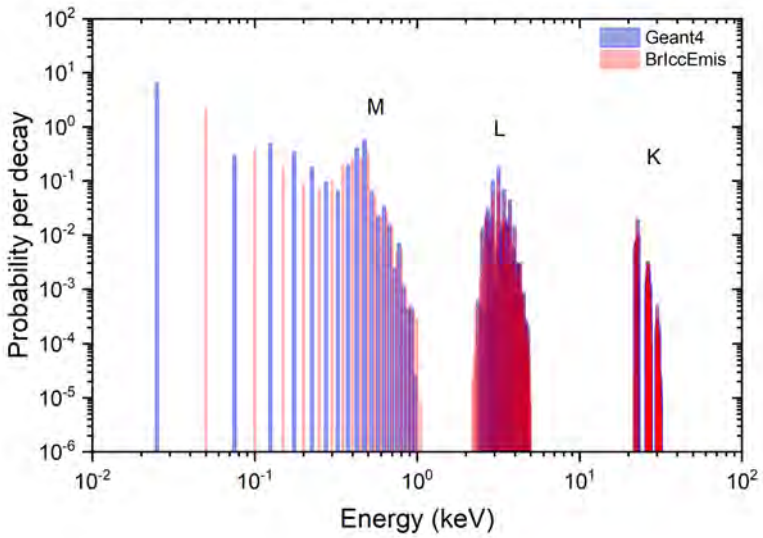

Figure 7.3: Calculated Auger electron spectrum following the radioactive decay of ^{124}I, normalized for 1 radioactive decay.

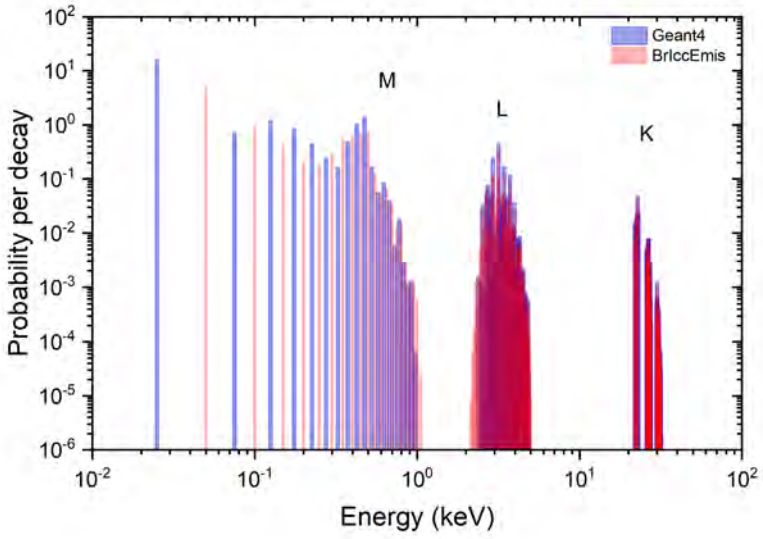

Figure 7.4: Calculated Auger electron spectrum following the radioactive decay of ^{125}I, normalized for 1 radioactive decay.

Table 7.3: Mean Auger electron energies and emission yields per decay calculated for ^{123}I. $\bar{E}$ is the mean energy of the transition as calculated in equation (7.1).

Line	Geant4 simulation		Geant4Lib Analytical Code		BrIccEmis [106]		Pomplun [123]	
	$\bar{E}$ (keV)	Yield	$\bar{E}$ (keV)	Yield	$\bar{E}$ (keV)	Yield	$\bar{E}$ (keV)	Yield
Auger MXY	0.435	2.286	0.453	1.946	0.411	1.94	0.394	1.93
Auger LMM	3.067	0.653	3.085	0.734	3.047	0.733	3.028	0.711
Auger LMX	3.565	0.305	3.679	0.208	3.675	0.206	3.656	0.200
Auger KLL	22.666	0.0807	22.665	0.0807	22.525	0.0805	22.52	0.0731
Auger KLX	26.505	0.0355	26.506	0.0355	26.456	0.0354	26.43	0.0328
Auger KXY	30.348	0.00375	30.346	0.00374	30.312	0.00362	30.30	0.00280
Auger total	0.499	14.89	0.529	13.67	0.933	7.39	-	7.3
Auger above 500 eV	-	1.30	-	1.29	-	1.27	-	-

Table 7.4: Mean Auger electron energies and emission yields per decay calculated for ^{124}I. $\bar{E}$ is the mean energy of the transition as calculated in equation (7.1).

Line	Geant4 simulation		Geant4Lib Analytical Code		BrIccEmis [106]	
	$\bar{E}$ (keV)	Yield	$\bar{E}$ (keV)	Yield	$\bar{E}$ (keV)	Yield
Auger MXY	0.435	1.533	0.453	1.306	0.413	1.30
Auger LMM	3.086	0.491	3.085	0.492	3.048	0.492
Auger LMX	3.680	0.135	3.679	0.139	3.676	0.138
Auger KLL	22.666	0.0538	22.665	0.0541	22.525	0.0539
Auger KLX	26.506	0.0239	26.506	0.0238	26.460	0.0240
Auger KXY	30.348	0.00250	30.346	0.00251	30.308	0.00256
Auger total	0.499	9.99	0.528	9.17	0.922	5.04
Auger above 500 eV	-	0.87	-	0.87	-	0.85

Table 7.5: Mean Auger electron energies and emission yields per decay calculated for ^{125}I. $\bar{E}$ is the mean energy of the transition as calculated in equation (7.1) and Yield is Y_{total} of equation (7.1).

Line	Geant4 simulation		Geant4Lib Analytical Code		BrIccEmis [106]		Stepanek [105]	
	$\bar{E}$ (keV)	Yield	$\bar{E}$ (keV)	Yield	$\bar{E}$ (keV)	Yield	$\bar{E}$ (keV)	Yield
Auger MXY	0.435	3.800	0.453	3.224	0.408	3.20	0.380	3.24
Auger LMM	3.093	1.228	3.090	1.218	3.047	1.21	3.01	1.22
Auger LMX	3.692	0.331	3.684	0.345	3.676	0.339	3.63	0.339
Auger KLL	22.666	0.1286	22.665	0.129	22.522	0.129	22.6	0.126
Auger KLX	26.506	0.0568	26.506	0.0566	26.454	0.0565	26.5	0.0580
Auger KXY	30.349	0.00604	30.346	0.00597	30.322	0.00595	30.3	0.00550
Auger total	0.490	24.85	0.519	22.81	0.953	11.8	-	8.92
Auger above 500 eV	-	2.15	-	2.14	-	2.08	-	-

shells. It can be observed that the Auger electrons spectra calculated with Geant4 and BrIccEmis are similar from 500 eV to higher energies. For lower energies, the two theoretical approaches show differences in the calculation of the yields. In particular, Geant4 calculates higher Auger yields than BrIccEmis for all the radionuclides considered. It was also noticed that the major contribution to Auger emissions with energy below ~ 500 eV derives from N shell transitions. These discrepancies between the two theoretical approaches should be compared with absolute N-shell Auger electron transition rates, however I am not aware of the existence of suitable experimental data.

Table 7.3 shows the Auger electron energies and emission yields for ^{123}I decay as calculated by means of BrIccEmis [106], Pomplun [123] and Geant4. Geant4 calculates by default the full decay chain, therefore the decay of ^{123}Te was switched off in the simulation, in order to compare the same physical quantity against the other data. The Geant4 simulation results agree with the Geant4Lib analytical code data in terms of Auger electron kinetic energies and in terms of radiation yields with 4%, apart from the case of the radiation yield of the *MXY, LMM* and *LMX* lines (17%, 11% and 46% of difference, respectively). This difference is ascribed to the difficulty to identify the yields of specific lines in the Geant4 simulation using the methodology described in section 7.3.3 because of the overlapping of some group lines (see figure 7.1). Apart from this discrepancy, the results show consistency between the Geant4 simulation output and the Geant4 data libraries used as input to describe Auger emission from radioactive decay, as expected.

In terms of both energy and radiation yield, BrIccEmis [106] within 1% with the Geant4 data libraries, apart from the case of Auger electron kinetic energies of *MXY* line where

an agreement within 9% has been observed and from the case of the radiation yield of the *KXY* line where a difference of 5% was found. For Pomplun [123], an agreement within 2% with Geant4 data libraries was found in terms of Auger electron kinetic energies, apart from 12% difference for *MXY* line. In terms of radiation yield, there is an agreement within 10% apart from the case of the *KXY* line where a difference of 25% was found. The total emission yield above 500 eV shows a very good agreement for Geant4Lib analytical code and Geant4 simulation (within 1%) and BrIccEmis [106] (within 2%).

Table 7.4 displays the Auger electron energies and emission yields for ^{124}I decay calculated by means of Geant4 and BrIccEmis [106]. The Geant4 simulation results agree with the Geant4Lib analytical code data in terms of Auger electron kinetic energies within 1% for all lines, apart from the case of *MXY* line where an agreement within 5% was found. In terms of emission yields, Geant4 simulation results are consistent with Geant4Lib analytical code, apart from a 17% difference for the *MXY* line. As in the case of ^{123}I, I ascribe the difference to the difficulty to determine the transition line (see section 7.3.3 and figure 7.1), complicated by the overlapping of the Auger emission energies. BrIccEmis [106] agrees with Geant4 data libraries within 1%, apart from the case of *MXY* line where an agreement within 8% has been observed. With regard to the total emission yield above 500 eV, there is excellent agreement between the Geant4 simulation and the Geant4Lib analytical code (within 0.5%), as expected. Agreement within 3% was found between the Geant4 data libraries and BrIccEmis [106].

Table 7.5 reports the Auger electron energies and emission yields for ^{125}I decay calculated by means of Geant4, BrIccEmis [106] and Stepanek [105]. In terms of Auger electron energy, Geant4 simulation results agree within 1% with the Geant4 data libraries, apart from the case of the *MXY* line (within 5%) and the total Auger electron emission. The differences are ascribed to the difficulty to identify some lines (see figure 7.1), which is further complicated by a slight broadening of the Auger electrons kinetic energies due to the momentum transfer to the nuclear recoil. The Geant4 data libraries agree with BrIccEmis within 1% apart from the *MXY* line (10%) and when considering the full spectrum of the Auger electrons. In terms of emission yields, Geant4 simulation results are consistent with the Geant4Lib analytical code apart from the case of *MXY* line, where differences up to 18% have been observed. This difference again should be due to the method to distinguish the transition lines in the Geant4 simulation. BrIccEmis [106] agrees with Geant4 data libraries within 2%. Besides, Stepanek [105] agrees within 3% with Geant4 data libraries, while 17% difference has been noticed in terms of Auger electron kinetic energies. In the matter of the total emission yield above 500 eV, there was an excellent agreement (within 0.5%) between the Geant4 data libraries and the Geant4 simulation. An agreement within 3% was found between the Geant4 data libraries and BrIccEmis

[106].

These results show, as expected, agreement between the Geant4 simulation and the Geant4Lib analytical code. Eventual disagreement is ascribed to the difficulty to identify the yields of specific lines in the Geant4 simulation. In addition, the results show an agreement within few percent between BrIccEmis [106], Stepanek [105] data and the Geant4Lib analytical code. Pomplun [123] data show less agreement with Geant4 and BrIccEmis [106].

7.4.2 Comparison With Experimental Data

Figure 7.5 shows the yield per ^{125}I decay for K Auger electrons using Geant4, BrIccEmis [106] and Pomplun [104] data compared with the experimental results performed at ANU [118]. Figure 7.6 shows the ratio of the Auger electron emission yield calculated by either Geant4 or BrIccEmis [106] and the experimental results [118]. Figure 7.7 shows the comparison of the Auger electron emission yield of ^{131}Cs decay calculated by means of Geant4, BrIccEmis [106] and the experimental data [121]. Figure 7.8 illustrates the ratio of the emission yields calculated by either Geant4 simulation or BrIccEmis [106] and the experimental results [121].

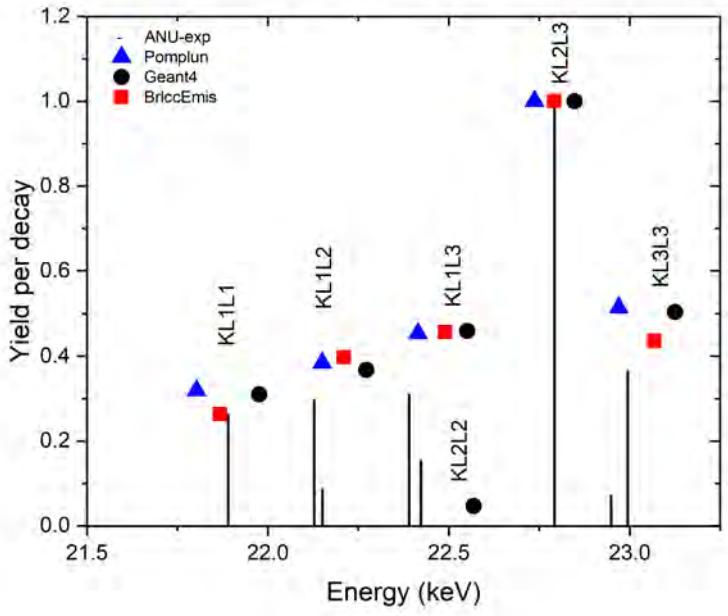

Figure 7.5: Comparison of the Auger electron yields calculated by means of Geant4, BrIccEmis [106], and Pomplun [104] with experimental data [118] for *KLL* peaks in the case of ^{125}I decay.

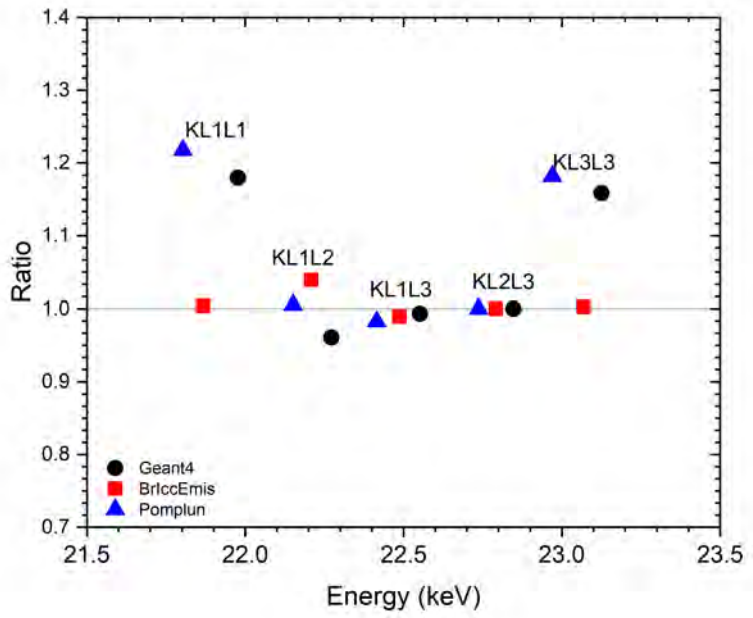

Figure 7.6: Ratio of the Auger emission yield calculated by means of either Geant4, BrIccEmis [106], and Pomplun [104] with experimental data [118]. The ratio has been calculated for *KLL* peaks in the case of ^{125}I decay.

Table 7.6: ^{125}I Auger electron yield calculated by means of Geant4, BrIccEmis [106, 118], Pomplun [104] and experimental data [118]. The experimental energy data have an uncertainty of around 10 eV. The intensities are normalised to the KL_2L_3 line.

Line	Geant4 simulation		Geant4Lib Analytical Code		BrIccEmis [106]		Pomplun [104]		Experimental [118]	
	$\bar{E}$ (keV)	Yield	$\bar{E}$ (keV)	Yield	$\bar{E}$ (keV)	Yield	$\bar{E}$ (keV)	Yield	$\bar{E}$ (keV)	Yield
$KL_1L_1(^1S_0)$	21.9765	0.309	21.9765	0.309	21.868	0.263	21.803	0.319	21.800(5)	0.262(5)
$KL_1L_2(^1P_1)$	22.2725	0.367	22.2725	0.367	22.210	0.397	22.151	0.384	22.128(5)	0.296(10)
$KL_1L_2(^3P_0)$									22.151(10)	0.086(6)
$KL_1L_3(^3P_1)$	22.5515	0.459	22.5515	0.460	22.490	0.457	22.415	0.454	22.390(5)	0.309(7)
$KL_1L_3(^3P_2)+$ $KL_2L_2(^1S_0)$	22.5685	0.047	22.5685	0.047					22.423(5)	0.153(6)
$KL_2L_3(^1D_2)$	22.8475	1.000	22.8475	1.000	22.792	1.000	22.737	1.000	22.702(3)	1.000
$KL_3L_3(^3P_0)$	23.1255	0.504	23.1255	0.504	23.068	0.436	22.970	0.514	22.948(10)	0.071(6)
$KL_3L_3(^3P_2)$									22.995(4)	0.364(7)

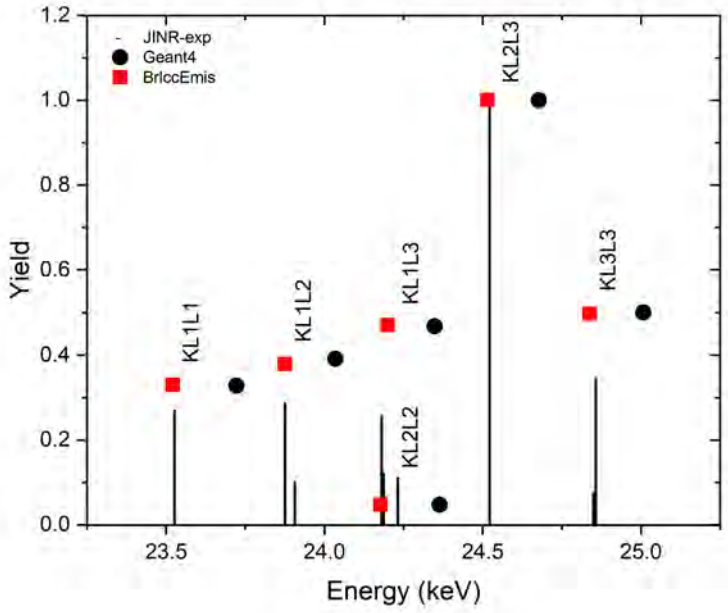

Figure 7.7: Comparison of the Auger electron yields calculated by means of Geant4, BrIccEmis [106], with experimental data [121] for Auger electron *KLL* peaks produced by ^{131}Cs decay.

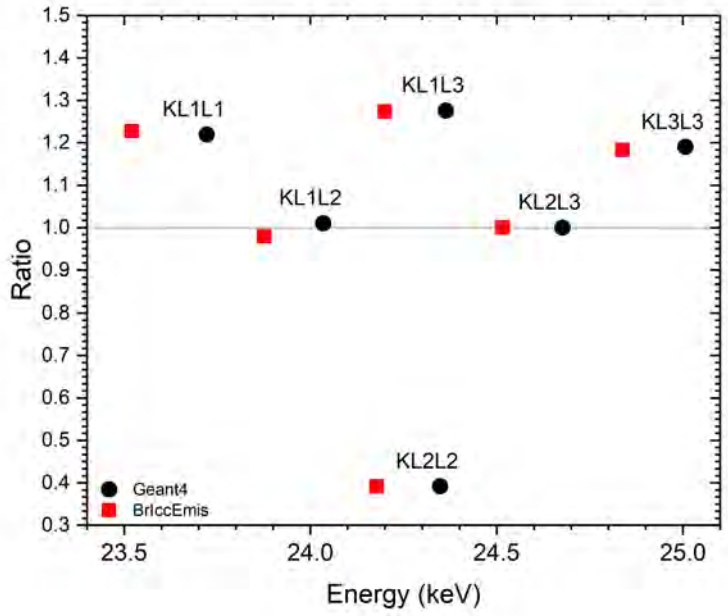

Figure 7.8: Emission yield's ratio calculated dividing the results obtained with either Geant4 or BrIccEmis [106], and the experimental data [121]. The ratios are shown for Auger electron *KLL* peaks produced by ^{131}Cs decay.

Table 7.7: ^{131}Cs Auger electron yield calculated by means of Geant4 and BrIccEmis [23], and experimental yield [121].

Line	Geant4 simulation		Geant4Lib Analytical Code		BrIccEmis [23]		Experimental [121]	
	$\bar{E}$ (keV)	Yield	$\bar{E}$ (keV)	Yield	$\bar{E}$ (keV)	Yield	$\bar{E}$ (keV)	Yield
$KL_1L_1(^1S_0)$	23.722	0.328	23.722	0.329	23.521	0.330	23.526(6)	0.269(5)
$KL_1L_2(^1P_1)$	24.035	0.391	24.035	0.390	23.876	0.379	23.875(8)	0.287(5)
$KL_1L_2(^3P_0)$							23.906(12)	0.100(5)
$KL_1L_3(^3P_1)$	24.364	0.472	24.364	0.470	24.200	0.471	24.181(14)	0.256(41)
$KL_1L_3(^3P_2)$	-	-	-	-	-	-	24.232(10)	0.110(5)
$KL_2L_2(^1S_0)$	24.348	0.047	24.348	0.048	24.178	0.047	24.187(18)	0.121(41)
$KL_2L_3(^1D_2)$	24.677	1.000	24.677	1.000	24.516	1.000	24.522(20)	1.000
$KL_3L_3(^3P_0)$	25.007	0.501	25.007	0.500	24.838	0.498	24.850(12)	0.074(5)
$KL_3L_3(^3P_2)$							24.857(6)	0.346(5)

Table 7.6 shows the ^{125}I Auger electron energies and yields obtained with Geant4 simulation, Geant4Lib analytical code, BrIccEmis [106] and Pomplun [104] models and the experimental data [118]. The experimental spectrum and theoretical peaks are scaled to match the intensity of the Geant4 KL_2L_3 Auger line. Good agreement in terms of Auger electron yield was found among Geant4, the experimental data and the other theoretical calculations. Geant4 simulations gave the same results of the Geant4Lib analytical code. Regarding to the emission yields of the experimental data [118] (see figures 7.5 and 7.6), an agreement within 15% (corresponding to the Geant4 model uncertainty) was found in comparison to Geant4 and 20% agreement with Pomplun [104]. In addition, a 5% agreement was found for BrIccEmis [106] in comparison to experimental data.

A comparison has been performed for the experimental *KLL* Auger energy spectrum deriving from the decay of ^{131}Cs, measured by Kovalik et al [121], with the theoretical one calculated using Geant4 simulation, Geant4Lib analytical code, and BrIccEmis [23]. The experimental spectrum and theoretical lines are scaled to match the intensity of the Geant4 KL_2L_3 Auger line. Table 7.7 displays the ^{131}Cs Auger electron energies and yields obtained with Geant4 and BrIccEmis [23] models and the experimental data. In terms of emission yields, good agreement (within 3%) was observed between Geant4 and BrIccEmis [23] theoretical calculations. Geant4 simulation results are consisted with the Geant4 data libraries. In figure 7.8, differences up to 25% were observed between Geant4 and BrlccEmis against the experimental data [121]. The only exception is the KL_2L_2 line, where a $\sim$ 250% discrepancy has been noticed in comparison to the reference data [121], for both Geant4 and BrlccEmis.

In both comparisons (see figures 7.5 and 7.7), a kinetic energy shift ($\sim$ 150 eV) of the

emission lines is observed for the Geant4 results. This most likely comes from the fact that Auger electron energies are derived from neutral binding energies (see section 7.3.3). Moreover, the existing physics models describing atomic de-excitation of Geant4 disregard the quantum electrodynamics (QED) and Breit magnetic electron interaction corrections which could cause energy shift of the emitted Auger electrons and X-rays [23]. The QED effect is due to the fact that an electron moving in the vacuum drags a cloud of virtual photons with it [124, 125]. BrIccEmis has semi-empirical correction for these effects.

Another difference in the model calculations is the atomic structure effect ($\sim$ 10 eV), which is only included in BrIccEmis and arises due to the fast vacancy cascade in the atom when it rearranges itself according to the atomic ground state of the daughter. This effect is important especially for transitions involving K and L shells where the vacancies have short lifetimes ($\sim 10^{-17}$ – 10^{-15} sec) [23].

7.5 Conclusion

In this work I benchmarked for the first time the emission of Auger electrons deriving from ^{123}I, ^{124}I, ^{125}I and ^{131}Cs decays calculated by means of Geant4 against other theoretical approaches (BrIccEmis [23, 106], Pomplun [104] and Stepanek [105]) and experimental results performed at the Australian National University (ANU) [118] and the Joint Institute for Nuclear Research (JINR) [121].

I verified the consistency between the Geant4 simulation results and the Geant4 data libraries, input to the Monte Carlo code, to calculate Auger electron kinetic energies and emission probabilities, deriving from atomic de-excitation after a radioactive decay. When comparing Geant4 to other theoretical approaches, an overall good agreement, usually within few percent in terms of Auger electron energies, was found between Geant4 and other theoretical approaches. In terms of emission yields, a good agreement (within 3%) was found for vacancies in the K shell. In the case of vacancies in the L and M shells, the level of agreement was worse (within 15%) because it was difficult to determine the associated transition lines in the Geant4 simulation. Overall, the total number of the Auger electron emitted per radioactive decay was found significantly higher in Geant4. However, it was noticed that the difference was mostly coming from the low energy range, below $\sim$ 500 eV, where the Auger electrons derive mainly from vacancies in N shell.

When comparing Geant4 simulation results to experimental data, a shift in the Auger kinetic energies was found. This may be caused to limitations of the theoretical approach, which considers the energy level of neutral atoms only and disregards quantum electrodynamics (QED) effects, Breit magnetic electron interaction corrections and atomic struc-

ture effects. These differences are not observed in the latest version of BrIccEmis [106], as it recently adopted a semi-empirical correction, which reduces the difference between the calculated and experimental Auger line energies below 10 eV [108].

In terms of Auger electron emission yields, once the results were normalised to KL_2L_3 line, an agreement within 15% for ^{125}I and 25% for ^{131}Cs radioactive decays, was found among Geant4, BrIccEmis [106] and the measured K Auger intensity.

For the future, I recommend extending the benchmarking to the conversion lines, other radioisotopes and to other sets of experimental measurements. As far as I know, this is the first time that the Geant4 Auger emission from radioactive decay of medical radioisotopes has been benchmarked against other theoretical approaches and validated against experimental measurements.

7.6 Acknowledgements

This work has been funded by the *Australian Research Council*, grant number ARC DP170100967 and DP140103317.

Chapter 8

Auger electron yields by means of the novel *fluo_ANSTO* library

In this chapter, the influence of the *fluo_ANSTO* X-ray fluorescence data library (described in chapter 4) on calculated Auger electron emission yields has been investigated. This work was presented at the **26th Geant4 Collaboration** meeting 2021 (Online: `https://indico.cern.ch/event/1052654/`).

8.1 Introduction

The Auger effect is characterised by the emission of atomic electrons as an alternative channel to X-ray fluorescence during atomic de-excitation (see section 2.2) [85, 86]. If the de-excitation channels from the excited atomic state are assumed to be independent, the radiative width Γ_R the Auger emission width, Γ_A and the Coster-Kronig width Γ_{CK} is based on the Evaluated Data Library *EADL* [63] and provides the radiative (fluorescence) and non-radiative (Auger and Coster–Kronig electrons) transition probabilities [23].

In this project, I developed a X-ray fluorescence data library, identified as *fluo_ANSTO*, which was derived from ANSTO calculations using the Hartree-Fock method (see chapter 4)[17]. Because the sum of X-ray fluorescence, Auger, and Coster-Kronig yields is equal to one, altering one would impact the others (see equation (2.6)), hence it is necessary to investigate the effect of using the new library, *fluo_ANSTO*, on Auger yields for software verification purposes.

The current chapter discusses the Auger electron emission that occurs as a result of ^{22}Al, ^{28}P, ^{38}Ca, ^{49}Fe, ^{61}Ga, ^{90}Ru, ^{123}I, ^{124}I, ^{125}I and ^{131}Cs radioactive decays. These radionuclides were chosen because they eject Auger electrons [126] to cover the entire range of Z. In addition, ^{123}I, ^{124}I, ^{125}I, ^{131}Cs are already known Auger emitters used

in nuclear medicine, hence the ^{123}I, ^{124}I, ^{125}I, ^{131}Cs results can provide a useful cross-reference against data already available. The particular purpose of this work is to examine the effect of using the *fluo_ANSTO* X-ray fluorescence library on the calculation of the yields of Auger electrons.

8.2 Materials and Methods

8.2.1 Geant4 Simulation Setup

In the Geant4 simulation study, two models were utilised; the first model uses *fluo_ANSTO* (see chapter 4) data sets for the fluorescence X-ray emission rates. The second model includes the *fluo_default* atomic relaxation library, based on *EADL* [63] to compute fluorescence X-ray emission rates once an electron shell vacancy has been created.

In this work, the Geant4 extended example *rdecay01* was used for guidance, and the Geant4 10.05.p01 version was used for calculations. A vacuum cube of 20 mm dimension was modelled, with a point source of the radionuclide in the centre of the box. The radioactive decay as well as the whole atomic relaxation were modelled by the software. The simulation produces a value of emission yield per radioactive decay and the energy spectrum of the emitted Auger electrons. The number of particle "histories" used in the Geant4 simulation is 10^7, in order to achieve a statistical uncertainty of less than 1%.

8.2.2 Radionuclides Under Investigation

The chosen range of radionuclides allows selection and study of materials with a range of both X-ray and Auger electron emission behaviours. This will allow fine-tuning of the energy-dependent characteristics stored in the libraries used by Geant4. The selected radionuclides have favourable properties as follows:

^{22}Al (half-life $T_{1/2}$ = 91.1 ms) decays by $\beta+$ and electron capture (EC, with accompanying Auger X-ray emission) to an excited state of ^{22}Mg [127].

^{28}P ($T_{1/2}$ = 270.3 ms) decays by $\beta+$ and EC to a stable state of ^{28}Si [128].

^{38}Ca ($T_{1/2}$ = 443.76 ms) decays by $\beta+$ and EC to an excited state of ^{38}K [129].

^{49}Fe ($T_{1/2}$ = 64.7 ms) decays by $\beta+$ and EC to an excited state of ^{49}Mn [130].

^{61}Ga ($T_{1/2}$ = 167 ms) decays by $\beta+$ and EC to an excited state of ^{61}Zn [131].

^{90}Ru ($T_{1/2}$ = 11.7 s) decays by $\beta+$ and EC to an excited state of ^{90}Tc [132].

^{123}I ($T_{1/2}$ = 13.224 hr) decays by EC to an excited state of ^{123}Te. The most probable transition at 159 keV carries 99% of the total intensity and 19% of the time will decay via internal conversion (IC) to ^{123}Te, which has a very long half-life ($T_{1/2} = 9.2 \times 10^{16}$ year) [97].

^{124}I ($T_{1/2}$ = 4.176 d) decays via either $\beta+$ (22.7% probability) or EC (77.3% probability) to either excited states (65% probability) or to the ground state (35% probability) of ^{124}Te [98].

^{125}I ($T_{1/2}$ = 59.49 d) decays by EC (100% probability) followed by either gamma ray emission (6.68% probability) or IC (93.32% probability), to the ground state of the stable ^{125}Te [99].

^{131}Cs ($T_{1/2}$ = 9.689 d) decays directly via EC decay to the ground state of ^{131}Xe [100].

8.2.3 Auger Electron Emission in Geant4

Geant4 calculates the total radiative and non-radiative emission of X-rays and Auger electrons when the atom relaxes, by using the Livermore *EADL* Data Library [63, 92]. The relaxation energy product is determined via the difference between the sub-shell binding energies involved in the atomic de-excitation process [63]. The binding energy of all sub-shells is considered to be the same for neutral ground state atoms as for ionised atoms [63, 92].

It is worth noting that Geant4 Atomic Relaxation model does not discriminate between Auger electrons and Coster-Kronig transitions; they are all treated as Auger electrons [44].

8.3 Results and Discussion

The figures below compare Geant4 Auger electron emission yields results utilising the X-ray *fluo_default* and *fluo_ANSTO* libraries. Figures 8.1a to 8.10a show the produced energy spectra and Auger electron yield for ^{22}Al, ^{28}P, ^{38}Ca, ^{49}Fe, ^{61}Ga, ^{90}Ru, ^{123}I, ^{124}I, ^{125}I and ^{131}Cs radioactive decays. The Auger electron lines can be distinguished according to the atomic shell level of the initial vacancy. Figures 8.1b to 8.10b illustrate the ratio

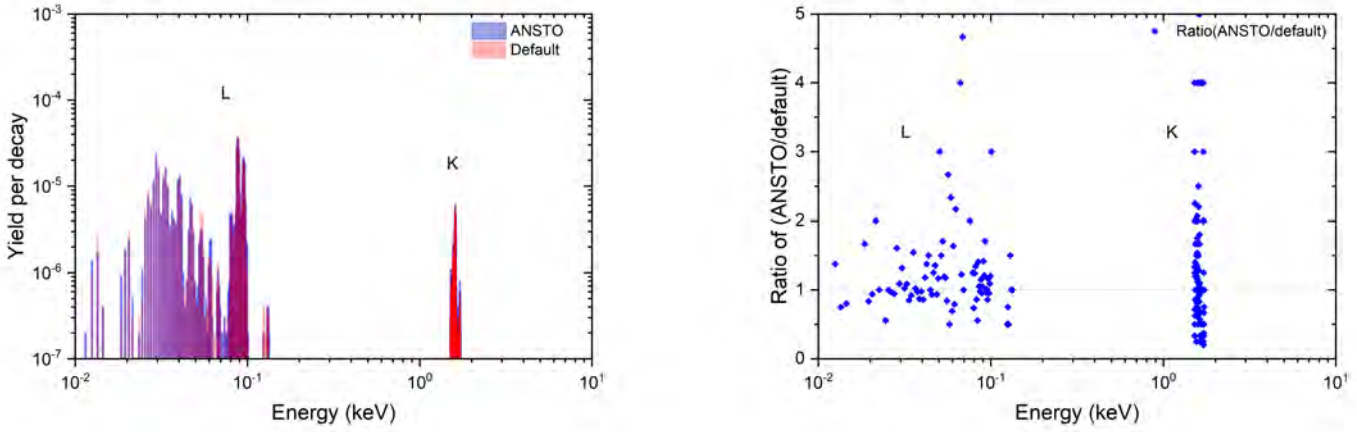

(a) **(b)**

Figure 8.2: (a) Calculated Auger electron spectrum following the radioactive decay of ^{28}P, normalised for 1 radioactive decay. (b) The ratio of Auger electrons emission (ANSTO/default) for ^{28}P.

of Auger electron yield values specified in the aforementioned two libraries.

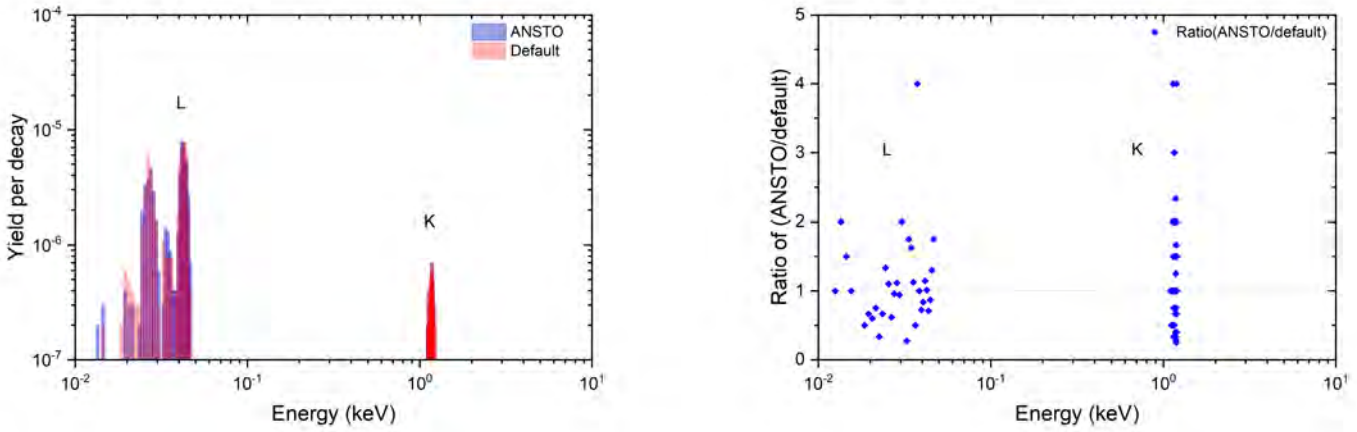

(a) **(b)**

Figure 8.1: (a) Calculated Auger electron spectrum following the radioactive decay of ^{22}Al, normalised for 1 radioactive decay. (b) The ratio of Auger electrons emission (ANSTO/default) for ^{22}Al.

The Auger electron emission yields for ^{22}Al, ^{28}P and ^{38}Ca are shown in figures 8.1a to 8.3a, respectively. In these figures, only K and L Auger electron emission yields are visible. The first Geant4 library is the *fluo_ANSTO* (in blue), while the second is the

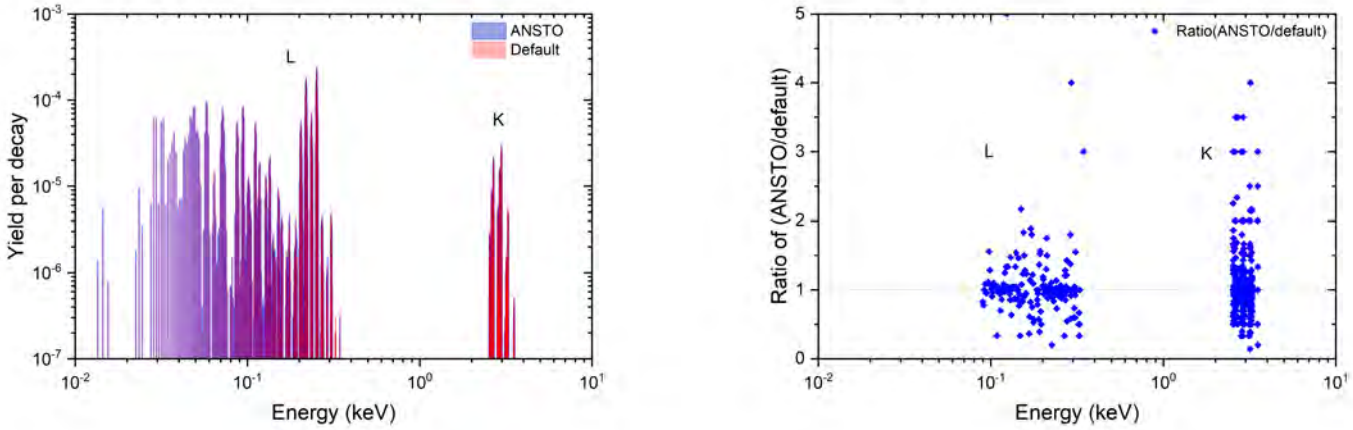

(a) **(b)**

Figure 8.3: (a) Calculated Auger electron spectrum following the radioactive decay of ^{38}Ca, normalised for 1 radioactive decay. (b) The ratio of Auger electrons emission (ANSTO/default) for ^{38}Ca.

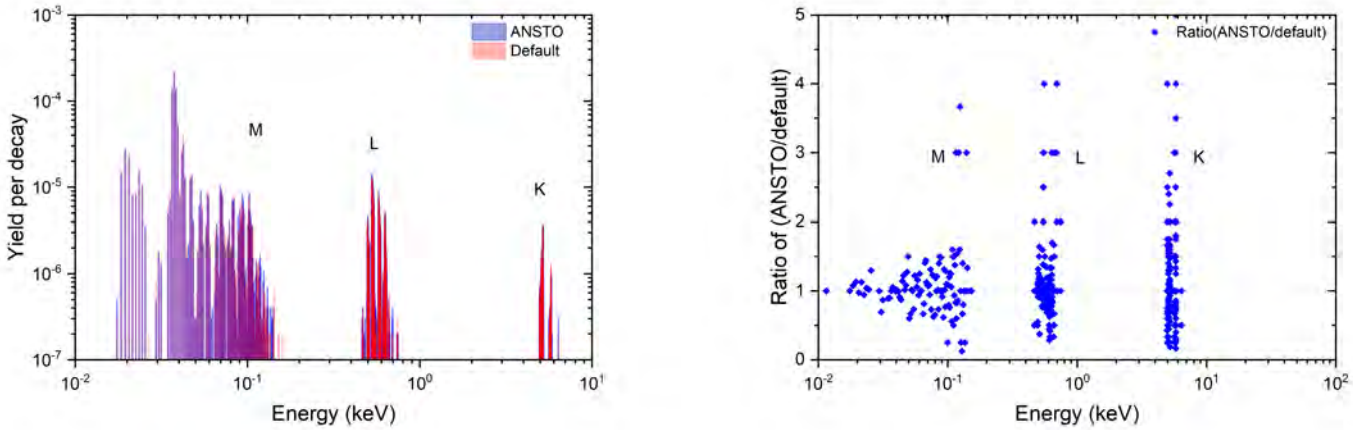

(a) **(b)**

Figure 8.4: (a) Calculated Auger electron spectrum following the radioactive decay of ^{49}Fe, normalised for 1 radioactive decay. (b) The ratio of Auger electrons emission (ANSTO/default) for ^{49}Fe.

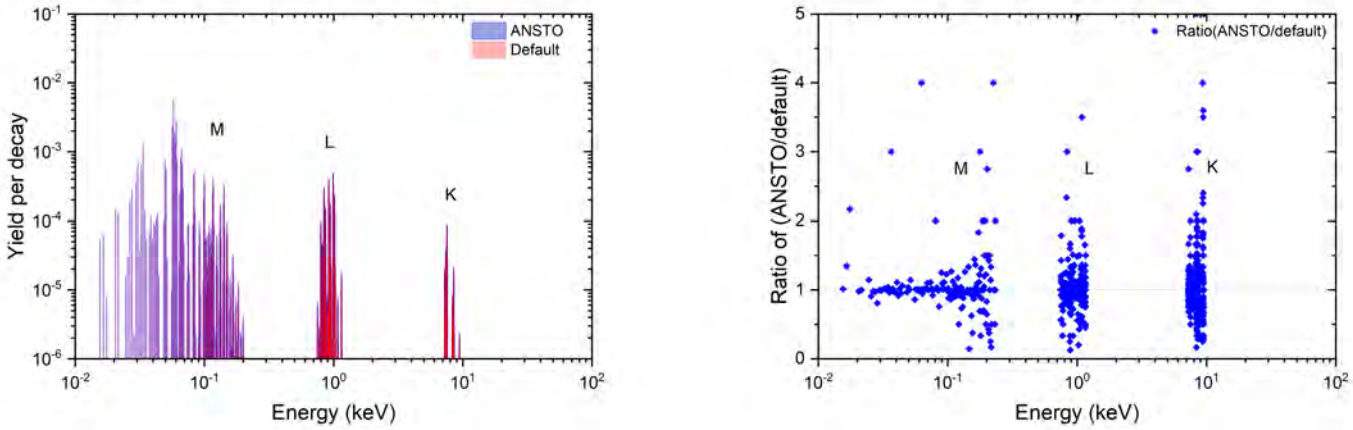

(a) **(b)**

Figure 8.5: (a) Calculated Auger electron spectrum following the radioactive decay of ^{61}Ga, normalised for 1 radioactive decay. (b) The ratio of Auger electrons emission (ANSTO/default) for ^{61}Ga.

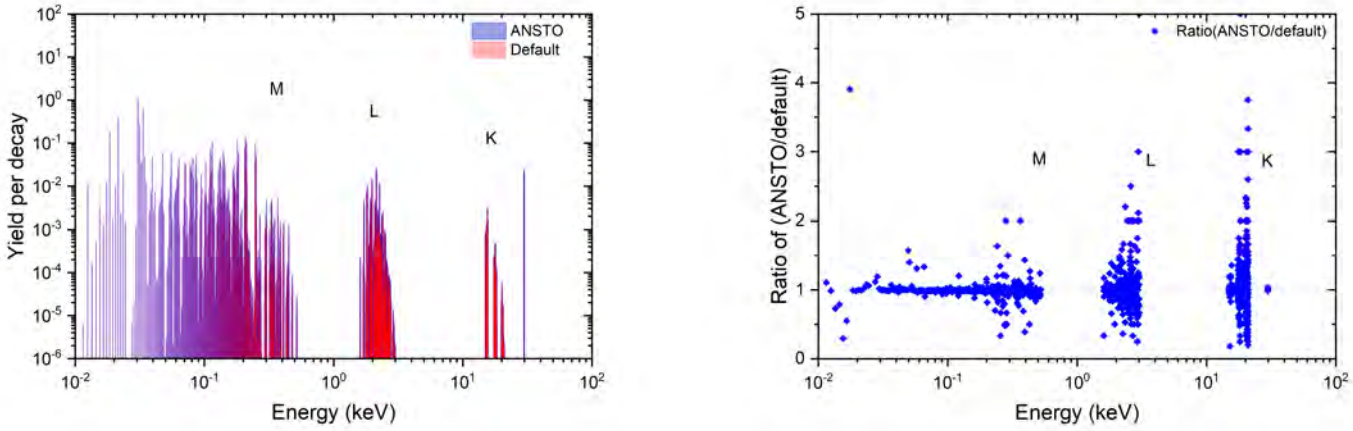

(a) **(b)**

Figure 8.6: (a) Calculated Auger electron spectrum following the radioactive decay of ^{90}Ru, normalised for 1 radioactive decay. (b) The ratio of Auger electrons emission (ANSTO/default) for ^{90}Ru.

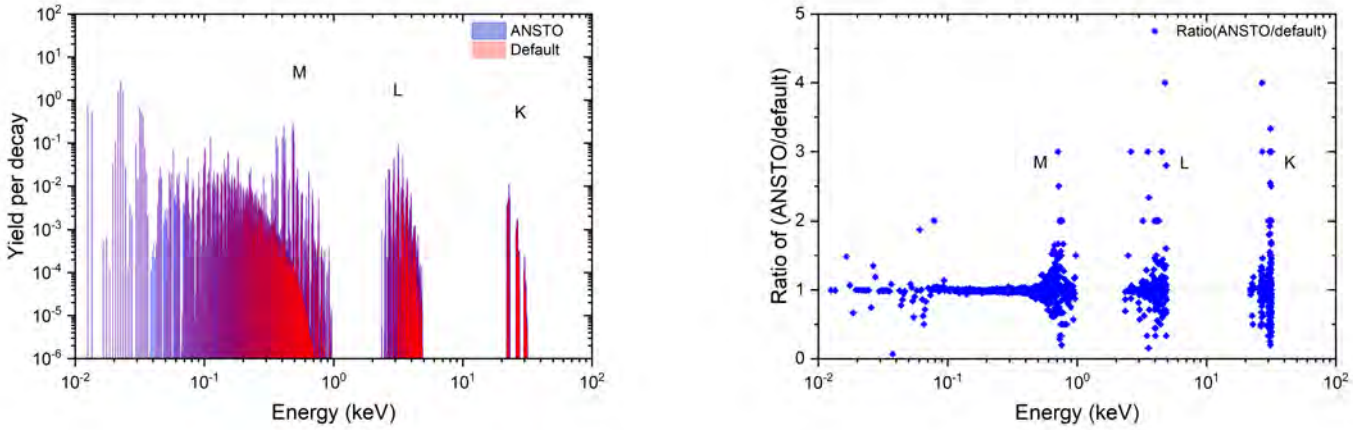

(a) **(b)**

Figure 8.7: (a) Calculated Auger electron spectrum following the radioactive decay of ^{123}I, normalised for 1 radioactive decay. (b) The ratio of Auger electrons emission (ANSTO/default) for ^{123}I.

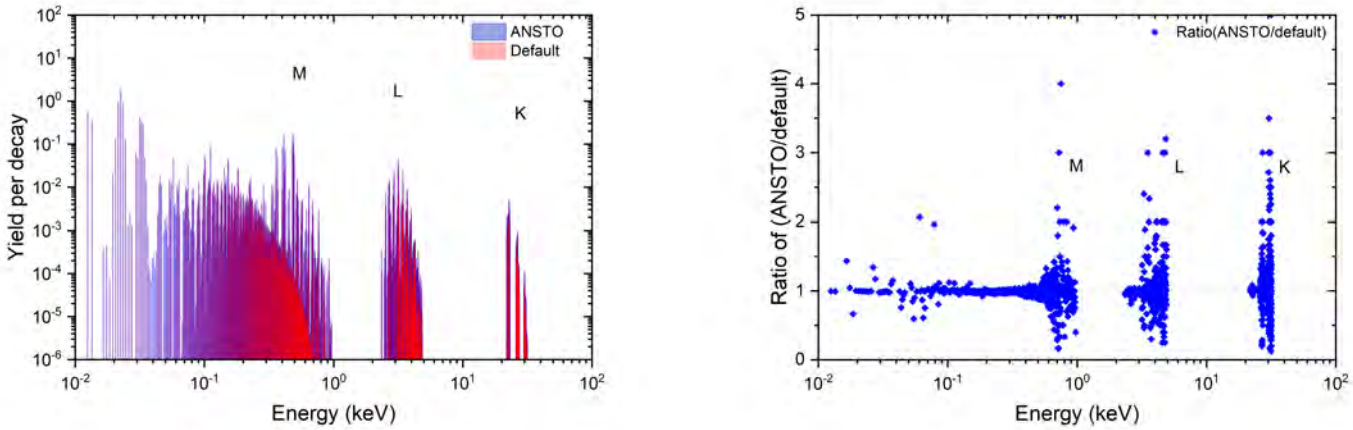

(a) **(b)**

Figure 8.8: (a) Calculated Auger electron spectrum following the radioactive decay of ^{124}I, normalised for 1 radioactive decay. (b) The ratio of Auger electrons emission (ANSTO/default) for ^{124}I.

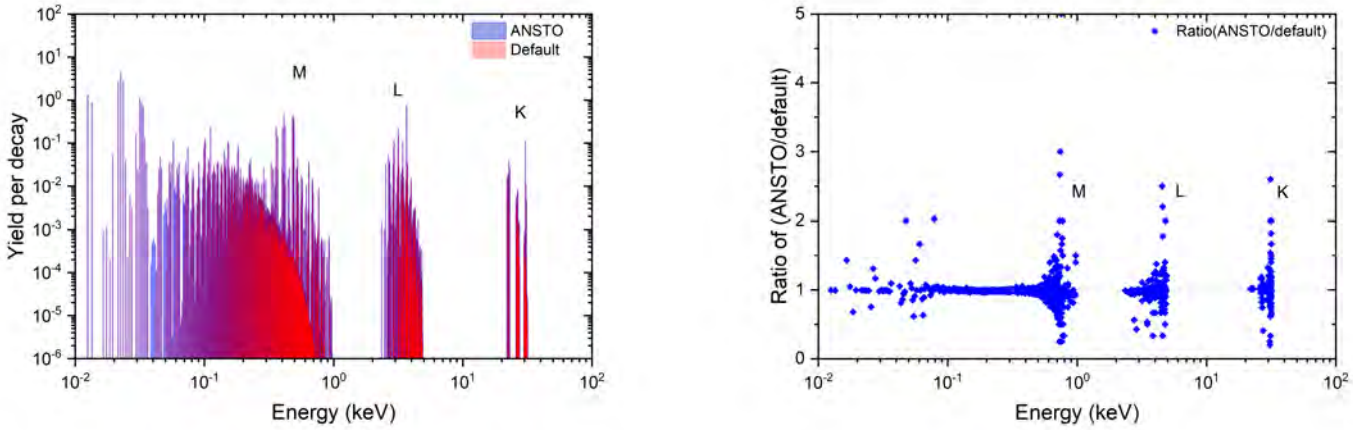

(a) **(b)**

Figure 8.9: (a) Calculated Auger electron spectrum following the radioactive decay of ^{125}I, normalised for 1 radioactive decay. (b) The ratio of Auger electrons emission (ANSTO/default) for ^{125}I.

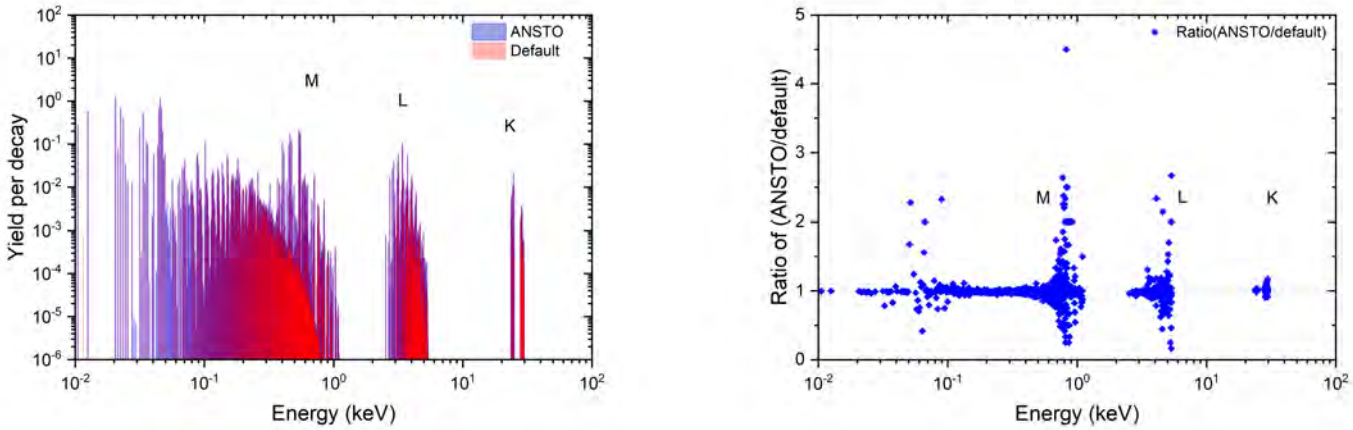

(a) **(b)**

Figure 8.10: (a) Calculated Auger electron spectrum following the radioactive decay of ^{131}Cs, normalised for 1 radioactive decay. (b) The ratio of Auger electrons emission (ANSTO/default) for ^{131}Cs.

Table 8.1: Total Auger electron emission yields per decay for radionuclides using *fluo_default* and *fluo_ANSTO* X-ray emission libraries.

radionuclide	**G4** ***fluo_ANSTO***	**G4** ***fluo_default***	**(*fluo_ANSTO*/*fluo_default*) ratio**
^{22}Al	0.000078	0.000083	0.944
^{28}P	0.0006	0.0006	0.994
^{38}Ca	0.0072	0.0072	0.998
^{49}Fe	0.0015	0.0016	0.959
^{61}Ga	0.049	0.049	0.998
^{90}Ru	6.39	6.43	0.994
^{123}I	14.79	14.89	0.993
^{124}I	9.92	9.99	0.993
^{125}I	25.58	25.75	0.993
^{131}Cs	11.8	11.9	0.992

fluo_default (in red); It can be observed that *fluo_default* and *fluo_ANSTO* both libraries produce fairly similar results. The discrepancies in results between these two libraries are seen in figures 8.1b to 8.3b.

Figures 8.4a to 8.10a illustrate the Geant4 Auger electron spectra for ^{49}Fe, ^{61}Ga, ^{90}Ru, ^{123}I, ^{124}I, ^{125}I and ^{131}Cs, respectively, using the two libraries under consideration. K , L , and M Auger electron emission yields are visible in these figures. The difference in the results of the studied libraries is hard to distinguish. Thus, figures 8.4b to 8.10b, show the ratio of Auger electron yields generated by the *fluo_ANSTO* library over those provided by the *fluo_default* library. However, it remains difficult to distinguish between the results of these two libraries.

Table 8.1 shows the total Auger electron emission yields for previously stated radionuclides, as calculated by means of the Geant4 using *fluo_default* and *fluo_ANSTO* X-ray fluorescence yield libraries (see section 8.2.1). Additionally, table 8.1 includes the ratio of *fluo_ANSTO* over *fluo_default*. It is clear from this table that the *fluo_default* library produces slightly higher results than the *fluo_ANSTO* library in all scenarios.

The findings of this investigation were expected since the X-ray fluorescence predicted by Geant4 *fluo_ANSTO* library is slightly greater than the prediction from the *fluo_default* library (as shown in chapter 4). The relationship between X-ray fluorescence and Auger electron yields is seen in equation (2.6). As a result, the greater the X-ray fluorescence yield, the lower the Auger electron yield.

8.4 Conclusion

The impact of the recently included X-ray fluorescence data library, titled *fluo_ANSTO*, on the calculation of the Auger electrons emission yield has been examined in this study. The Auger electron spectra and the total Auger electron yields for several radionuclides predicted by the *fluo_ANSTO* and *fluo_default* data libraries were compared to one another.

The comparison reveals that the results produced by both data libraries are up to 5% different. However, the *fluo_ANSTO* data libraries exhibit slightly lower Auger electron yields than the *fluo_default* data library, which is understandable given that the *fluo_ANSTO* data library predicts a greater X-ray fluorescence yield than the *fluo_default* data library does. Furthermore, because the X-ray fluorescence yield and the Auger electron emission yield collectively total to unity, the results are consistent with the underlying theory. These simulation results for Auger electron behaviour should be compared to many experimental measurements to understand which approach is more accurate. This was beyond the scope of this PhD thesis.

Chapter 9

General Conclusion

The purpose of the project is to develop a cutting-edge PIXE Package (*G4–ANSTO*) in the Geant4 simulation toolkit. This package will provide the most precise description of particle interactions at the micro- and nano-scale levels, not just with any PIXE-specific software tool, but also with any general-purpose Monte Carlo code used in radiation physics. This research will have an influence on fields ranging from environmental science and geology to space, materials, and life sciences.

To accomplish this, I revised the existing G4-PIXE in chapter 3 based on the recommendations of D. D. Cohen and R. Siegele, international leaders in experimental PIXE and associated theoretical modelling. Geant4 now includes the *ECPSSR_ANSTO* ionisation cross sections for proton and α particles for PIXE simulation. Only the *ECPSSR_ANSTO* and *ECPSSR_FormFactor* approaches are capable of handling M sub-shells relaxations.

To get a unique complete *G4–ANSTO* approach based on the ANSTO calculations and recommendations of D. D. Cohen and R. Siegele, in chapter 4, I integrated the *ANSTO HF* X-ray fluorescence yields, the second component of *G4–ANSTO* approach. The *G4–ANSTO* approach utilises both the *ECPSSR_ANSTO* ionisation cross sections and *ANSTO HF* fluorescence yield libraries. The *G4–default* approach includes the *ECPSSR_FormFactor* ionisation cross sections and the *EADL* fluorescence yield libraries. Geant4-calculated X-ray emission spectra were compared to those computed using the *G4–ANSTO* and *G4–default* approaches in terms of fluorescence X-ray yields per incident proton and α particles. Several target materials were investigated, ranging from low to high atomic number Z materials. Protons and α particles were employed as monoenergetic beams. The investigation found that the Geant4-calculated X-ray emission spectra and the ANSTO experimental results agreed pretty well.

Chapter 5 presents the additional experimental data that I obtained in order to conduct further validation tests for the new approach *G4–ANSTO*. The X-ray spectra were gener-

ated using a variety of materials at the ANSTO utilising ANTARES tandem accelerator. The spectra were obtained using the heavy ion microprobe beamline, which used carbon ions, and then were compared with the Geant4 in chapter 6. In terms of fluorescence X-ray yields, the *G4–ANSTO* and *G4–default* approaches were used to compare with the experimental results for incident carbon ion. Several target materials were studied, ranging from low to high atomic number Z. For all samples, the majority of lines were much greater when utilising the *G4–ANSTO* approach rather than the *G4–default* approach. Furthermore, the investigation discovered that the Geant4-calculated X-ray emission spectra and the ANSTO experimental measurements matched rather well. However, I am just looking at a few peaks with PIXE, but *G4–ANSTO* exhibits considerable variances with *G4–default* for other lines, which might be crucial in other application areas.

The emission of Auger electron benchmarking study had never been done before, so in chapter 7, I benchmarked for the first time the emission of Auger electrons derived from some medical radioisotope decays calculated using Geant4 against other theoretical approaches and experimental results performed at the *Australian National University* (ANU) [118] and the *Joint Institute for Nuclear Research* (JINR) [121]. I validated the compatibility of the Geant4 simulation results with the Geant4 data libraries to determine Auger electron kinetic energies and emission probabilities derived from atomic de-excitation following radioactive decay. When comparing Geant4 to other theoretical methods, it was discovered that there was an overall good agreement, generally within a few percent in terms of Auger electron energies.

Because the X-ray fluorescence yield and Auger electron yield should be equal to one, the *G4–ANSTO* approach, which includes the *ANSTO HF* X-ray fluorescence component, may have an effect on the Auger electron emissions. As a result, the influence of a recently included *ANSTO HF* X-ray fluorescence data library on the Auger electrons emission yield has been investigated in chapter 8. The Auger electron spectra and total Auger electron yield for various radionuclides were compared using the most recent and default data libraries. The Auger electron yields in the *ANSTO HF* data libraries are slightly lower than in the default data library, which is acceptable given that the *ANSTO HF* data library has a higher X-ray fluorescence yield than the default data library. Additionally, the results are rational and predictable since the X-ray fluorescence yield and the Auger electron emission yield are both equal to one.

The significance of obtaining accurate results from Geant4 and data that is as near to reality as possible comes from the requirement for such a simulation toolkit in medical applications for cancer treatment. This aim might be accomplished by examining dose enhancement of the treatment dose with the addition of nanoparticles made of high-Z ma-

terials and irradiation with X-rays. This will generate Auger electrons from these high Z materials, and because Auger electrons have a short range in tissue, they will increase the dosage to malignant cells while having negligible effect on normal tissue.

The Geant4 users will be able to use our novel *G4–ANSTO* libraries and models, which provide a unique, self-consistent, and stable recommended approach, for the first time in Geant4 11.0. My motivation for future research is to include the ANSTO ionisation cross section for carbon, oxygen, and any recommended ion, in PIXE domain, directly into Geant4, avoiding the scaling of proton ionisation cross section, to achieve better results. Additionally, I recommend extending the Auger electron benchmarking to the conversion lines, other radioisotopes and to other sets of experimental measurements.

Bibliography

(1) S. Agostinelli, J. Allison, K. a. Amako, J. Apostolakis, H. Araujo, P. Arce, M. Asai, D. Axen, S. Banerjee, G. 2. Barrand et al., "GEANT4—a simulation toolkit", *Nuclear instruments and methods in physics research section A: Accelerators, Spectrometers, Detectors and Associated Equipment*, 2003, **506**, 250–303.

(2) D. D. Cohen, J. Crawford and R. Siegele, "K, L, and M shell datasets for PIXE spectrum fitting and analysis", *Nuclear Instruments and Methods in Physics Research Section B: Beam Interactions with Materials and Atoms*, 2015, **363**, 7–18.

(3) S. McKinnon, E. Engels, M. Tehei, K. Konstantinov, S. Corde, S. Oktaria, S. Incerti, M. Lerch, A. Rosenfeld and S. Guatelli, "Study of the effect of ceramic Ta2O5 nanoparticle distribution on cellular dose enhancement in a kilovoltage photon field", *Physica Medica*, 2016, **32**, 1216–1224.

(4) D. D. Cohen, "Particle induced x-ray emission.", 1991.

(5) S. A. Johansson and J. L. Campbell, "PIXE: A novel technique for elemental analysis", 1988.

(6) I. Mitchell and K. Barfoot, "Particle induced X-ray emission analysis application to analytical problems", *Nucl. Sci. Appl., Sect. B*, 1981, **1**, 99–162.

(7) J. R. Bird, P. Duerden and D. J. Wilson, "Ion beam techniques in archaeology and the arts", *Nucl. Sci. Appl.;(United States)*, 1983, **1**.

(8) D. D. Cohen and E. Clayton, in Elsevier, 1990, ch. 5, Ion Induced X-ray Emission.

(9) S. A. Johansson, J. L. Campbell and F. Adams, *PIXE: A novel technique for elemental analysis: Wiley, New York, 1988 (ISBN 0-471-92011-8). xii+ 347 pp. Price£ 42.50*, 1989.

(10) F. Watt and G. W. Grime, "Principles and applications of high-energy ion microbeams", 1987.

(11) `https://www.ansto.gov.au`.

(12) S. A. Johansson and T. B. Johansson, "Analytical application of particle induced X-ray emission", *Nuclear Instruments and Methods*, 1976, **137**, 473–516.

(13) T. Johansson and R. Akselsson, "SAE Johansson X-ray analysis: elemental trace analysis at the 10–12g level Nucl", *Instr. Meth*, 1970, **84**, 141–143.

(14) H. B. Abdelouahed, S. Incerti and A. Mantero, "New Geant4 cross section models for PIXE simulation", *Nuclear Instruments and Methods in Physics Research Section B: Beam Interactions with Materials and Atoms*, 2009, **267**, 37–44.

(15) R. Zeisler and V. P. Guinn, *Nuclear Analytical Methods in the Life Sciences*, Springer Science & Business Media, 2012.

(16) S. Bakr, D. D. Cohen, R. Siegele, S. Incerti, V. Ivanchenko, A. Mantero, A. Rosenfeld and S. Guatelli, "Latest Geant4 developments for PIXE applications", *Nuclear Instruments and Methods in Physics Research Section B: Beam Interactions with Materials and Atoms*, 2018, **436**, 285–291.

(17) S. Bakr, D. D. Cohen, R. Siegele, J. W. Archer, S. Incerti, V. Ivanchenko, A. Mantero, A. Rosenfeld and S. Guatelli, "Geant4 X-ray fluorescence with updated libraries", *Nuclear Instruments and Methods in Physics Research Section B: Beam Interactions with Materials and Atoms*, 2021, **507**, 11–19.

(18) M. H. Kabir, "Particle Induced X-ray Emission (PIXE) Setup and Quantitative Elemental Analysis", 2007.

(19) R. K. Hobbie and B. J. Roth, *Intermediate physics for medicine and biology*, Springer, 2007.

(20) E. B. Podgoršak et al., *Radiation physics for medical physicists*, Springer, 2006, vol. 1.

(21) P. A. Mandò and W. J. Przybyłowicz, "Particle-Induced X-Ray Emission (PIXE)", *Encyclopedia of Analytical Chemistry: Applications, Theory and Instrumentation*, 2006.

(22) H. R. Verma, *Atomic and nuclear analytical methods*, Springer, 2007.

(23) B. Q. Lee et al., "A Numerical Model of Atomic Relaxation and its Applications", 2017.

(24) W. Bambynek, "Reorganization of atomic shells after radioactive decay", *Low-Level Measurements of Man-Made Radionuclides in the Environment-Proceedings of the 2nd International Summer School. Edited by GARCIA-LEON M & MADURGA G. Published by World Scientific Publishing Co. Pte. Ltd*, 1991, 156–175.

(25) Toshiyouri, *Auger xray efficiency comparison*, `https://commons.wikimedia.org/wiki/File:Auger_xray_efficiency_comparison.svg`, [Online; accessed 19-July-2021], 2015.

(26) J. Hubbell, P. Trehan, N. Singh, B. Chand, D. Mehta, M. Garg, R. Garg, S. Singh and S. Puri, "A review, bibliography, and tabulation of K, L, and higher atomic shell x-ray fluorescence yields", *Journal of Physical and Chemical Reference Data*, 1994, **23**, 339–364.

(27) J. R. Bird and J. S. Williams, *Ion Beams for Materials Analysis*, 1989.

(28) W. Bambynek, B. Crasemann, R. Fink, H.-U. Freund, H. Mark, C. Swift, R. Price and P. V. Rao, "X-ray fluorescence yields, Auger, and Coster-Kronig transition probabilities", *Reviews of modern physics*, 1972, **44**, 716.

(29) M. O. Krause, "Atomic radiative and radiationless yields for K and L shells", *Journal of physical and chemical reference data*, 1979, **8**, 307–327.

(30) I. Govil, "Proton Induced X-ray Emission–A tool for non-destructive trace element analysis", *Current Science*, 2001, 1542–1549.

(31) R. Gellert, R. Rieder, J. Brückner, B. Clark, G. Dreibus, G. Klingelhöfer, G. Lugmair, D. Ming, H. Wänke, A. Yen et al., "Alpha Particle X-ray Spectrometer (APXS): Results from Gusev crater and calibration report", *Journal of Geophysical Research: Planets*, 2006, **111**.

(32) J. L. Campbell, C. M. Heirwegh and B. Ganly, "Non-linearity issues and multiple ionization satellites in the PIXE portion of spectra from the Mars alpha particle X-ray spectrometer", *Nuclear Instruments and Methods in Physics Research Section B: Beam Interactions with Materials and Atoms*, 2016, **383**, 143–151.

(33) P. A. Mandò and W. J. Przybyłowicz, "Particle-Induced X-Ray Emission (PIXE)", *Encyclopedia of Analytical Chemistry*, 2009.

(34) M. Zaider, B. H. H. Rossi and M. Zaider, *Microdosimetry and its Applications*, Springer, 1996.

(35) H. Paganetti, *Proton Beam Therapy*, IOP Publishing, 2017.

(36) G. Biasi, "Design of a solid-state array detector prototype for small-field dosimetry in megavoltage photon beams", 2019.

(37) J. Allison, K. Amako, J. Apostolakis, H. Araujo, P. A. Dubois, M. Asai, G. Barrand, R. Capra, S. Chauvie, R. Chytracek et al., "Geant4 developments and applications", *IEEE Transactions on nuclear science*, 2006, **53**, 270–278.

(38) J. Allison, K. Amako, J. Apostolakis, P. Arce, M. Asai, T. Aso, E. Bagli, A. Bagulya, S. Banerjee, G. Barrand et al., "Recent developments in Geant4", *Nuclear instruments and methods in physics research section A: Accelerators, Spectrometers, Detectors and Associated Equipment*, 2016, **835**, 186–225.

(39) R. Brun, R. Hagelberg and M. Hansroul, *Geant, Simulation Program for Particle Physics Experiments; User Guide and Reference Manual*, CERN. Data Handling Division, 1978.

(40) G. Battistoni, J. Bauer, T. T. Boehlen, F. Cerutti, M. P. Chin, R. Dos Santos Augusto, A. Ferrari, P. G. Ortega, W. Kozłowska, G. Magro et al., "The FLUKA code: an accurate simulation tool for particle therapy", *Frontiers in oncology*, 2016, **6**, 116.

(41) T. Goorley, M. James, T. Booth, F. Brown, J. Bull, L. Cox, J. Durkee, J. Elson, M. Fensin, R. Forster et al., "Initial MCNP6 release overview", *Nuclear technology*, 2012, **180**, 298–315.

(42) T. Sato, Y. Iwamoto, S. Hashimoto, T. Ogawa, T. Furuta, S.-i. Abe, T. Kai, P.-E. Tsai, N. Matsuda, H. Iwase et al., "Features of particle and heavy ion transport code system (PHITS) version 3.02", *Journal of Nuclear Science and Technology*, 2018, **55**, 684–690.

(43) D. Bolst, "Silicon microdosimetry in hadron therapy using Geant4", 2019.

(44) S. Guatelli, A. Mantero, B. Mascialino, P. Nieminen and M. G. Pia, "Geant4 atomic relaxation", *IEEE Transactions on Nuclear Science*, 2007, **54**, 585–593.

(45) S. Guatelli, A. Mantero, B. Mascialino, M. Pia and V. Zampichelli, 2006 IEEE Nuclear Science Symposium Conference Record, 2007, vol. 3, pp. 1516–1518.

(46) A. Mantero, H. Ben Abdelouahed, C. Champion, Z. El Bitar, Z. Francis, P. Guèye, S. Incerti, V. Ivanchenko and M. Maire, "PIXE simulation in Geant4", *X-Ray Spectrometry*, 2011, **40**, 135–140.

(47) V. Ivanchenko, J. Apostolakis, A. Bagulya, H. B. Abdelouahed, R. Black, A. Bogdanov, H. Burkhard, S. Chauvie, G. A. P. Cirrone, G. Cuttone et al., "Recent improvements in geant4 electromagnetic physics models and interfaces", *Progress in nuclear science and technology*, 2011, **2**, 898–903.

(48) S. Incerti, B. Suerfu, J. Xu, V. Ivantchenko, A. Mantero, J. Brown, M. Bernal, Z. Francis, M. Karamitros and H. Tran, "Simulation of Auger electron emission from nanometer-size gold targets using the Geant4 Monte Carlo simulation toolkit", *Nuclear Instruments and Methods in Physics Research Section B: Beam Interactions with Materials and Atoms*, 2016, **372**, 91–101.

(49) S. Incerti, P. Barberet, G. Deves, C. Michelet, Z. Francis, V. Ivantchenko, A. Mantero, Z. El Bitar, M. Bernal, H. Tran et al., "Comparison of experimental proton-induced fluorescence spectra for a selection of thin high-Z samples with Geant4 Monte Carlo simulations", *Nuclear Instruments and Methods in Physics Research Section B: Beam Interactions with Materials and Atoms*, 2015, **358**, 210–222.

(50) J. H. Scofield, "Relativistic Hartree-Slater values for K and L X-ray emission rates", *Atomic Data and Nuclear Data Tables*, 1974, **14**, 121–137.

(51) M. H. Chen, B. Crasemann and H. Mark, "Relativistic radiationless transition probabilities for atomic K-and L-shells", *Atomic Data and Nuclear Data Tables*, 1979, **24**, 13–37.

(52) J. Hubbell, "National institute of Standards and Technology Report NISTIR 89-4144", *US Department of Commerce, Gaithersburg, MD*, 1989.

(53) A. Mantero, Ph.D. Thesis, PhD Thesis, Univ. of Genova, 2008.

(54) S. Guatelli, A. Mantero, B. Mascialino, P. Nieminen, M. G. Pia and S. Saliceti, IEEE Symposium Conference Record Nuclear Science 2004. 2004, vol. 4, pp. 2178–2181.

(55) H. Paul and J. Sacher, "Fitted empirical reference cross sections for K-shell ionization by protons", *Atomic Data and Nuclear Data Tables*, 1989, **42**, 105–156.

(56) H. Paul and O. Bolik, "Fitted empirical reference cross sections for K-shell ionization by alpha particles", *Atomic data and nuclear data tables*, 1993, **54**, 75–131.

(57) I. Orlic, C. Sow and S. Tang, "Experimental L-shell X-ray production and ionization cross sections for proton impact", *Atomic data and nuclear data tables*, 1994, **56**, 159–210.

(58) A. Taborda, P. Chaves and M. Reis, "Polynomial approximation to universal ionisation cross-sections of K and L shells induced by H and He ion beams", *X-ray Spectrometry*, 2011, **40**, 127–134.

(59) A. Taborda, P. Chaves, M. Carvalho and M. Reis, "Polynomial approximation to universal M-shell ionisation cross-sections induced by H+ and He2+ ions", *X-Ray Spectrometry*, 2013, **42**, 177–182.

(60) D. Cohen and M. Harrigan, "L shell line intensities for light ion induced X-ray emission", *Nuclear Instruments and Methods in Physics Research Section B: Beam Interactions with Materials and Atoms*, 1986, **15**, 576–580.

(61) W. Brandt and G. Lapicki, "Energy-loss effect in inner-shell Coulomb ionization by heavy charged particles", *Physical Review A*, 1981, **23**, 1717.

(62) A. Bagulya, M. Vladimirov, V. Ivanchenko and N. Starkov, "Heavy-particle energy loss simulation using the Geant4 toolkit", *Bulletin of the Lebedev Physics Institute*, 2009, **36**, 127–134.

(63) S. Perkins, D. Cullen, M. Chen, J. Rathkopf, J. Scofield and J. Hubbell, "Tables and graphs of atomic subshell and relaxation data derived from the LLNL Evaluated Atomic Data Library (EADL), Z= 1–100", 1991.

(64) M. G. Pia, H. Seo, M. Batic, M. Begalli, C. H. Kim, L. Quintieri and P. Saracco, "Evaluation of atomic electron binding energies for Monte Carlo particle transport", *IEEE Transactions on Nuclear Science*, 2011, **58**, 3246–3268.

(65) R. D. Deslattes, E. G. Kessler Jr, P. Indelicato, L. De Billy, E. Lindroth and J. Anton, "X-ray transition energies: new approach to a comprehensive evaluation", *Reviews of Modern Physics*, 2003, **75**, 35.

(66) D. Walters and C. Bhalla, "Z Dependence of the K- LL Auger Rates", *Physical Review A*, 1971, **3**, 519.

(67) J. Campbell, "Fluorescence yields and Coster–Kronig probabilities for the atomic L subshells", *Atomic Data and Nuclear Data Tables*, 2003, **85**, 291–315.

(68) J. Campbell, "Fluorescence yields and Coster–Kronig probabilities for the atomic L subshells. Part II: the L1 subshell revisited", *Atomic Data and Nuclear Data Tables*, 2009, **95**, 115–124.

(69) D. Cohen and M. Harrigan, "K-and L-shell ionization cross sections for protons and helium ions calculated in the ecpssr theory", *Atomic Data and Nuclear Data Tables*, 1985, **33**, 255–343.

(70) D. D. Cohen, "K-and L-shell ionization cross sections for deuterons calculated in the ECPSSR theory", *Atomic data and nuclear data tables*, 1989, **41**, 287–338.

(71) T. Schlathölter, P. Eustache, E. Porcel, D. Salado, L. Stefancikova, O. Tillement, F. Lux, P. Mowat, A. K. Biegun, M.-J. van Goethem et al., "Improving proton therapy by metal-containing nanoparticles: nanoscale insights", *International journal of nanomedicine*, 2016, **11**, 1549.

(72) E. Porcel, O. Tillement, F. Lux, P. Mowat, N. Usami, K. Kobayashi, Y. Furusawa, C. Le Sech, S. Li and S. Lacombe, "Gadolinium-based nanoparticles to improve the hadrontherapy performances", *Nanomedicine: Nanotechnology, Biology and Medicine*, 2014, **10**, 1601–1608.

(73) E. Porcel, S. Li, N. Usami, H. Remita, Y. Furusawa, K. Kobayashi, C. Le Sech and S. Lacombe, Journal of Physics: Conference Series, 2012, vol. 373, p. 012006.

(74) S. McKinnon, S. Guatelli, S. Incerti, V. Ivanchenko, K. Konstantinov, S. Corde, M. Lerch, M. Tehei and A. Rosenfeld, "Local dose enhancement of proton therapy by ceramic oxide nanoparticles investigated with Geant4 simulations", *Physica Medica*, 2016, **32**, 1584–1593.

(75) E. Engels, S. Corde, S. McKinnon, S. Incerti, K. Konstantinov, A. Rosenfeld, M. Tehei, M. Lerch and S. Guatelli, "Optimizing dose enhancement with Ta2O5 nanoparticles for synchrotron microbeam activated radiation therapy", *Physica Medica*, 2016, **32**, 1852–1861.

(76) D. Cohen, E. Stelcer, J. Crawford, A. Atanacio, G. Doherty and G. Lapicki, "Comparison of proton and helium induced M subshell X-ray production cross sections with the ECUSAR theory", *Nuclear Instruments and Methods in Physics Research Section B: Beam Interactions with Materials and Atoms*, 2014, **318**, 11–14.

(77) H. Verma, "X-ray fluorescence (XRF) and particle-induced X-ray emission (PIXE)", *Atomic and Nuclear Analytical Methods: XRF, Mössbauer, XPS, NAA and B63Ion-Beam Spectroscopic Techniques*, 2007, 1–90.

(78) E. Clayton, P. Duerden and D. D. Cohen, "A discussion of PIXAN and PIXANPC: The AAEC PIXE analysis computer packages", *Nuclear Instruments and Methods in Physics Research Section B: Beam Interactions with Materials and Atoms*, 1987, **22**, 64–67.

(79) Z. Pastuovic, D. Button, D. Cohen, D. Fink, D. Garton, M. Hotchkis, M. Ionescu, S. Long, V. Levchenko, M. Mann et al., "SIRIUS–A new 6 MV accelerator system for IBA and AMS at ANSTO", *Nuclear Instruments and Methods in Physics Research Section B: Beam Interactions with Materials and Atoms*, 2016, **371**, 142–147.

(80) T. D. Malouff, A. Mahajan, S. Krishnan, C. Beltran, D. S. Seneviratne and D. M. Trifiletti, "Carbon ion therapy: a modern review of an emerging technology", *Frontiers in oncology*, 2020, **10**, 82.

(81) `https://www.ansto.gov.au/our-facilities/centre-for-accelerator-science/antares-accelerator`.

(82) Z. Pastuovic, R. Siegele, D. Cohen, M. Mann, M. Ionescu, D. Button and S. Long, "The new confocal heavy ion microprobe beamline at ANSTO: The first microprobe resolution tests and applications for elemental imaging and analysis", *Nuclear Instruments and Methods in Physics Research Section B: Beam Interactions with Materials and Atoms*, 2017, **404**, 1–8.

(83) R. Siegele, A. Kachenko, M. Ionescu and D. Cohen, "Improved resolution and sensitivity on the ANSTO microprobe and it's application to μ-PIXE", *Nuclear Instruments and Methods in Physics Research Section B: Beam Interactions with Materials and Atoms*, 2009, **267**, 2054–2059.

(84) A. Mantero, B. Mascialino, M. Pia, S. Saliceti and P. Nieminen, "Geant4 atomic relaxation models", *The Monte Carlo Method: Versatility Unbounded in a Dynamic Computing World, on CD-ROM, American Nuclear Society, LaGrange Park, IL*, 2005.

(85) B. Cornelissen and K. A Vallis, "Targeting the nucleus: an overview of Auger-electron radionuclide therapy", *Current drug discovery technologies*, 2010, **7**, 263–279.

(86) R. W. Howell, "Auger processes in the 21st century", *International journal of radiation biology*, 2008, **84**, 959–975.

(87) B. Q. Lee, T. Kibédi and A. E. Stuchbery, EPJ Web of Conferences, 2015, vol. 91, p. 00007.

(88) B. M. Bavelaar, B. Q. Lee, M. R. Gill, N. Falzone and K. A. Vallis, "Subcellular targeting of theranostic radionuclides", *Frontiers in pharmacology*, 2018, **9**, 996.

(89) A. I. Kassis, "The amazing world of auger electrons", *International journal of radiation biology*, 2004, **80**, 789–803.

(90) A. M. S. Braghirolli, W. Waissmann, J. B. da Silva and G. R. dos Santos, "Production of iodine-124 and its applications in nuclear medicine", *Applied Radiation and Isotopes*, 2014, **90**, 138–148.

(91) P. Balagurumoorthy, X. Xu, K. Wang, S. J. Adelstein and A. I. Kassis, "Effect of distance between decaying 125I and DNA on Auger-electron induced double-strand break yield", *International journal of radiation biology*, 2012, **88**, 998–1008.

(92) GEANT4-Collaboration, "Physics Reference Manual", *GEANT4 A simulation toolkit - Manual*, 2019, **1**, 1–554.

(93) P. Arce, D. Bolst, M.-C. Bordage, J. Brown, P. Cirrone, M. A. Cortés-Giraldo, D. Cutajar, G. Cuttone, L. Desorgher, P. Dondero et al., "Report on G4-Med, a Geant4 benchmarking system for medical physics applications developed by the Geant4 Medical Simulation Benchmarking Group", *Medical physics*, 2021, **48**, 19–56.

(94) S. Incerti, M. Douglass, S. Penfold, S. Guatelli and E. Bezak, "Review of Geant4-DNA applications for micro and nanoscale simulations", *Physica Medica*, 2016, **32**, 1187–1200.

(95) C.-Y. Huang, S. Guatelli, B. M. Oborn and B. J. Allen, "Microdosimetry for targeted alpha therapy of cancer", *Computational and mathematical methods in medicine*, 2012, **2012**.

(96) C.-Y. Huang, B. M. Oborn, S. Guatelli and B. J. Allen, "Monte Carlo calculation of the maximum therapeutic gain of tumor antivascular alpha therapy", *Medical physics*, 2012, **39**, 1282–1288.

(97) S. Ohya, "Nuclear data sheets for A= 123", *Nuclear Data Sheets*, 2004, **102**, 547–718.

(98) J. Katakura and Z. Wu, "Nuclear data sheets for A= 124", *Nuclear Data Sheets*, 2008, **109**, 1655–1877.

(99) J. Katakura, "Nuclear data sheets for A= 125", *Nuclear Data Sheets*, 2011, **112**, 495–705.

(100) Y. Khazov, I. Mitropolsky and A. Rodionov, "Nuclear data sheets for A= 131", *Nuclear Data Sheets*, 2006, **107**, 2715–2930.

(101) W. Bambynek, H. Behrens, M. Chen, B. Crasemann, M. Fitzpatrick, K. Ledingham, H. Genz, M. Mutterer and R. Intemann, "Orbital electron capture by the nucleus", *Reviews of Modern Physics*, 1977, **49**, 77.

(102) T. Kibedi, T. Burrows, M. B. Trzhaskovskaya, P. M. Davidson and C. W. Nestor Jr, "Evaluation of theoretical conversion coefficients using BrIcc", *Nuclear Instruments and Methods in Physics Research Section A: Accelerators, Spectrometers, Detectors and Associated Equipment*, 2008, **589**, 202–229.

(103) R. Jenkins, R. Manne, R. Robin and C. Senemaud, "IUPAC—nomenclature system for x-ray spectroscopy", *X-Ray Spectrometry*, 1991, **20**, 149–155.

(104) E. Pomplun, "Auger electron spectra-the basic data for understanding the Auger effect", *Acta Oncologica*, 2000, **39**, 673–679.

(105) J. Stepanek, "Methods to determine the fluorescence and Auger spectra due to decay of radionuclides or due to a single atomic-subshell ionization and comparisons with experiments", *Medical Physics*, 2000, **27**, 1544–1554.

(106) B. Q. Lee, H. Nikjoo, J. Ekman, P. Jönsson, A. E. Stuchbery and T. Kibédi, "A stochastic cascade model for Auger-electron emitting radionuclides", *International journal of radiation biology*, 2016, **92**, 641–653.

(107) B. Q. Lee, T. Kibédi, A. E. Stuchbery and K. A. Robertson, "Atomic radiations in the decay of medical radioisotopes: a physics perspective", *Computational and mathematical methods in medicine*, 2012, **2012**.

(108) B. Tee, T. Kibédi, B. Lee, M. Vos, R. du Rietz and A. Stuchbery, EPJ Web of Conferences, 2020, vol. 232, p. 01006.

(109) *Evaluated nuclear structure data file*, `https://www.nndc.bnl.gov/ensdf/`.

(110) A. Endo, Y. Yamaguchi and K. F. Eckerman, *Nuclear decay data for dosimetry calculation. Revised data of ICRP Publication 38*, tech. rep., Japan Atomic Energy Research Inst., 2005.

(111) N. Gove and M. Martin, "Log-f tables for beta decay", *Atomic Data and Nuclear Data Tables*, 1971, **10**, 205–219.

(112) E. Schönfeld, "Calculation of fractional electron capture probabilities", *Applied radiation and isotopes*, 1998, **49**, 1353–1357.

(113) B.-T. MartinMJ, "Radioactiveatoms, Auger electron, a-,@-,@ y-, and x-ray data", *Nuci Data TablesA8: 1â*, 1970, **198**.

(114) L. Storm and H. I. Israel, "Photon cross sections from 1 keV to 100 MeV for elements Z= 1 to Z= 100", *Atomic Data and Nuclear Data Tables*, 1970, **7**, 565–681.

(115) E. J. McGuire, "K-shell Auger transition rates and fluorescence yields for elements Be-Ar", *Physical Review*, 1969, **185**, 1.

(116) J. Desclaux, "Relativistic Dirac-Fock expectation values for atoms with Z= 1 to Z= 120", *Atomic data and nuclear data tables*, 1973, **12**, 311–406.

(117) I. Band, M. Trzhaskovskaya, C. Nestor Jr, P. Tikkanen and S. Raman, "Dirac–Fock internal conversion coefficients", *Atomic Data and Nuclear Data Tables*, 2002, **81**, 1–334.

(118) M. Alotiby, I. Greguric, T. Kibedi, B. Lee, M. Roberts, A. Stuchbery, P. Tee, T. Tornyi and M. Vos, "Measurement of the intensity ratio of Auger and conversion electrons for the electron capture decay of 125I", *Physics in Medicine & Biology*, 2018, **63**, 06NT04.

(119) A. Pronschinske, P. Pedevilla, C. J. Murphy, E. A. Lewis, F. R. Lucci, G. Brown, G. Pappas, A. Michaelides and E. C. H. Sykes, "Enhancement of low-energy electron emission in 2D radioactive films", *Nature materials*, 2015, **14**, 904–907.

(120) M. Alotiby, I. Greguric, T. Kibedi, B. Tee and M. Vos, "Quantitative electron spectroscopy of 125I over an extended energy range", *Journal of Electron Spectroscopy and Related Phenomena*, 2019, **232**, 73–82.

(121) A. Kovalık, V. Gorozhankin, A. Novgorodov, M. Mahmoud, N. Coursol, E. Yakushev and V. Tsupko-Sitnikov, "The electron spectrum from the atomic deexcitation of 13154Xe", *Journal of electron spectroscopy and related phenomena*, 1998, **95**, 231–254.

(122) C. Briançon, B. Legrand, R. Walen, T. Vylov, A. Minkova and A. Inoyatov, "A new combined electrostatic electron spectrometer", *Nuclear Instruments and Methods in Physics Research*, 1984, **221**, 547–557.

(123) E. Pomplun, "Monte Carlo-simulated auger electron spectra for nuclides of radiobiological and medical interest–a validation with noble gas ionization data", *International journal of radiation biology*, 2012, **88**, 108–114.

(124) P. W. Milonni, *The quantum vacuum: an introduction to quantum electrodynamics*, Academic press, 2013.

(125) T. Rentrop, A. Trautmann, F. Olivares, F. Jendrzejewski, A. Komnik and M. K. Oberthaler, "Observation of the phononic Lamb shift with a synthetic vacuum", *Physical Review X*, 2016, **6**, 041041.

(126) *IAEA Live Chart of Nuclides*, `https://www-nds.iaea.org/relnsd/vcharthtml/VChartHTML.html`.

(127) M. S. Basunia, "Nuclear data sheets for A= 22", *Nuclear Data Sheets*, 2015, **127**, 69–190.

(128) M. S. Basunia, "Nuclear data sheets for a= 28", *Nuclear Data Sheets*, 2013, **114**, 1189–1291.

(129) J. Chen, "Nuclear data sheets for A= 39", *Nuclear Data Sheets*, 2018, **149**, 1–251.

(130) T. Burrows, "Nuclear data sheets for A= 49", *Nuclear Data Sheets*, 2008, **109**, 1879–2032.

(131) K. Zuber and B. Singh, "Nuclear data sheets for A= 61", *Nuclear Data Sheets*, 2015, **125**, 1–200.

(132) S. Basu and E. A. Mccutchan, "Nuclear Data Sheets for A= 90", *Nuclear Data Sheets*, 2020, **165**, 1–329.

(133) B. D. Chithrani, J. Stewart, C. Allen and D. A. Jaffray, "Intracellular uptake, transport, and processing of nanostructures in cancer cells", *Nanomedicine: Nanotechnology, Biology and Medicine*, 2009, **5**, 118–127.

(134) S. Jain, D. Hirst and J. O'Sullivan, "Gold nanoparticles as novel agents for cancer therapy", *The British journal of radiology*, 2012, **85**, 101–113.

(135) E. Engels, M. Lerch, M. Tehei, K. Konstantinov, S. Guatelli, A. Rosenfeld and S. Corde, Journal of Physics: Conference Series, 2017, vol. 777, p. 012011.

(136) E. Engels, M. Westlake, N. Li, S. Vogel, Q. Gobert, N. Thorpe, A. Rosenfeld, M. Lerch, S. Corde and M. Tehei, "Thulium Oxide Nanoparticles: A new candidate for image-guided radiotherapy", *Biomedical Physics & Engineering Express*, 2018, **4**, 044001.

(137) S. Her, D. A. Jaffray and C. Allen, "Gold nanoparticles for applications in cancer radiotherapy: Mechanisms and recent advancements", *Advanced drug delivery reviews*, 2017, **109**, 84–101.

(138) H. Tran, M. Karamitros, V. Ivanchenko, S. Guatelli, S. McKinnon, K. Murakami, T. Sasaki, S. Okada, M.-C. Bordage, Z. Francis et al., "Geant4 Monte Carlo simulation of absorbed dose and radiolysis yields enhancement from a gold nanoparticle under MeV proton irradiation", *Nuclear Instruments and Methods in Physics Research Section B: Beam Interactions with Materials and Atoms*, 2016, **373**, 126–139.

(139) P. Zygmanski and E. Sajo, "Nanoscale radiation transport and clinical beam modeling for gold nanoparticle dose enhanced radiotherapy (GNPT) using X-rays", *The British journal of radiology*, 2016, **89**, 20150200.

(140) R. Liu, T. Zhao, X. Zhao and F. J. Reynoso, "Modeling gold nanoparticle radiosensitization using a clustering algorithm to quantitate DNA double-strand breaks with mixed-physics Monte Carlo simulation", *Medical physics*, 2019, **46**, 5314–5325.

(141) Y. Lin, S. J. McMahon, M. Scarpelli, H. Paganetti and J. Schuemann, "Comparing gold nano-particle enhanced radiotherapy with protons, megavoltage photons and kilovoltage photons: a Monte Carlo simulation", *Physics in Medicine & Biology*, 2014, **59**, 7675.

(142) M. McDonald, S. Oktaria, K. Konstantinov, A. Rosenfeld, M. Lerch, S. Corde and M. Tehei, "Radiosensitisation enhancement effect of BrUdR and Ta2O5 NSPs in combination with 5-Fluorouracil antimetabolite in kilovoltage and megavoltage radiation", *Biomedical Physics & Engineering Express*, 2018, **4**, 034001.

(143) J. F. Hainfeld, F. A. Dilmanian, D. N. Slatkin and H. M. Smilowitz, "Radiotherapy enhancement with gold nanoparticles", *Journal of pharmacy and pharmacology*, 2008, **60**, 977–985.

(144) J. F. Hainfeld, H. M. Smilowitz, M. J. O'Connor, F. A. Dilmanian and D. N. Slatkin, "Gold nanoparticle imaging and radiotherapy of brain tumors in mice", *Nanomedicine*, 2013, **8**, 1601–1609.

(145) A. Mesbahi, "A review on gold nanoparticles radiosensitization effect in radiation therapy of cancer", *Reports of Practical Oncology & Radiotherapy*, 2010, **15**, 176–180.

(146) S.-R. Kim and E.-H. Kim, "Gold nanoparticles as dose-enhancement agent for kilovoltage X-ray therapy of melanoma", *International journal of radiation biology*, 2017, **93**, 517–526.

(147) S.-R. Kim and E.-H. Kim, "Feasibility study on the use of gold nanoparticles in fractionated kilovoltage X-ray treatment of melanoma", *International journal of radiation biology*, 2018, **94**, 8–16.

(148) D. Y. Joh, L. Sun, M. Stangl, A. Al Zaki, S. Murty, P. P. Santoiemma, J. J. Davis, B. C. Baumann, M. Alonso-Basanta, D. Bhang et al., "Selective targeting of brain tumors with gold nanoparticle-induced radiosensitization", *PloS one*, 2013, **8**, e62425.

(149) M. Grotzer, E. Schültke, E. Bräuer-Krisch and J. Laissue, "Microbeam radiation therapy: Clinical perspectives", *Physica Medica*, 2015, **31**, 564–567.

(150) C. Boudou, J. Balosso, F. Estève and H. Elleaume, "Monte Carlo dosimetry for synchrotron stereotactic radiotherapy of brain tumours", *Physics in Medicine & Biology*, 2005, **50**, 4841.

(151) S. H. Cho, "Estimation of tumour dose enhancement due to gold nanoparticles during typical radiation treatments: a preliminary Monte Carlo study", *Physics in Medicine & Biology*, 2005, **50**, N163.

(152) B. L. Jones, S. Krishnan and S. H. Cho, "Estimation of microscopic dose enhancement factor around gold nanoparticles by Monte Carlo calculations", *Medical physics*, 2010, **37**, 3809–3816.

(153) W. R. Nelson, H. Hirayama and D. W. Rogers, *EGS4 code system*, tech. rep., Stanford Linear Accelerator Center, Menlo Park, CA (USA), 1985.

(154) J. Baro, J. Sempau, J. Fernández-Varea and F. Salvat, "PENELOPE: an algorithm for Monte Carlo simulation of the penetration and energy loss of electrons and positrons in matter", *Nuclear Instruments and Methods in Physics Research Section B: Beam Interactions with Materials and Atoms*, 1995, **100**, 31–46.

(155) X. MCNP, "Monte Carlo Team, 2003", *MCNP da General Monte Carlo N-Particle Transport Code, Version*, 2005, **5**.

(156) B. Grosswendt, "Formation of ionization clusters in nanometric structures of propane-based tissue-equivalent gas or liquid water by electrons and α-particles", *Radiation and environmental biophysics*, 2002, **41**, 103–112.

(157) W. Friedland, M. Dingfelder, P. Kundrát and P. Jacob, "Track structures, DNA targets and radiation effects in the biophysical Monte Carlo simulation code PARTRAC", *Mutation Research/Fundamental and Molecular Mechanisms of Mutagenesis*, 2011, **711**, 28–40.

(158) H. Nikjoo, D. Emfietzoglou, T. Liamsuwan, R. Taleei, D. Liljequist and S. Uehara, "Radiation track, DNA damage and response—a review", *Reports on Progress in Physics*, 2016, **79**, 116601.

(159) V. Semenenko, J. Turner and T. Borak, "NOREC, a Monte Carlo code for simulating electron tracks in liquid water", *Radiation and environmental biophysics*, 2003, **42**, 213–217.

(160) G. Cirrone, G. Cuttone, F. Di Rosa, L. Pandola, F. Romano and Q. Zhang, "Validation of the Geant4 electromagnetic photon cross-sections for elements and compounds", *Nuclear Instruments and Methods in Physics Research Section A: Accelerators, Spectrometers, Detectors and Associated Equipment*, 2010, **618**, 315–322.

(161) D. E. Cullen, J. H. Hubbell and L. Kissel, *EPDL97: the evaluated photo data library97 version*, tech. rep., Lawrence Livermore National Lab., CA (United States), 1997.

(162) J. M. Fernández-Varea, G. González-Muñoz, M. E. Galassi, K. Wiklund, B. K. Lind, A. Ahnesjö and N. Tilly, "Limitations (and merits) of PENELOPE as a track-structure code", *International journal of radiation biology*, 2012, **88**, 66–70.

(163) P. Lazarakis, S. Incerti, V. Ivanchenko, I. Kyriakou, D. Emfietzoglou, S. Corde, A. B. Rosenfeld, M. Lerch, M. Tehei and S. Guatelli, "Investigation of track structure and condensed history physics models for applications in radiation dosimetry on a micro and nano scale in Geant4", *Biomedical Physics & Engineering Express*, 2018, **4**, 024001.

(164) I. Kyriakou, V. Ivanchenko, D. Sakata, M. Bordage, S. Guatelli, S. Incerti and D. Emfietzoglou, "Influence of track structure and condensed history physics models of Geant4 to nanoscale electron transport in liquid water", *Physica Medica*, 2019, **58**, 149–154.

(165) M. Bernal, M. Bordage, J. Brown, M. Davidkova, E. Delage, Z. El Bitar, S. Enger, Z. Francis, S. Guatelli, V. Ivanchenko et al., "Track structure modeling in liquid water: A review of the Geant4-DNA very low energy extension of the Geant4 Monte Carlo simulation toolkit", *Physica Medica*, 2015, **31**, 861–874.

(166) D. Bernard, "A 5D, polarised, Bethe–Heitler event generator for $\gamma\rightarrow$ e+ e- conversion", *Nuclear Instruments and Methods in Physics Research Section A: Accelerators, Spectrometers, Detectors and Associated Equipment*, 2018, **899**, 85–93.

(167) D. Sakata, S. Incerti, M. Bordage, N. Lampe, S. Okada, D. Emfietzoglou, I. Kyriakou, K. Murakami, T. Sasaki, H. Tran et al., "An implementation of discrete electron transport models for gold in the Geant4 simulation toolkit", *Journal of Applied Physics*, 2016, **120**, 244901.

(168) D. Sakata, I. Kyriakou, S. Okada, H. N. Tran, N. Lampe, S. Guatelli, M.-C. Bordage, V. Ivanchenko, K. Murakami, T. Sasaki et al., "Geant4-DNA track-structure simulations for gold nanoparticles: The importance of electron discrete models in nanometer volumes", *Medical physics*, 2018, **45**, 2230–2242.

(169) D. Sakata, I. Kyriakou, H. N. Tran, M.-C. Bordage, A. Rosenfeld, V. Ivanchenko, S. Incerti, D. Emfietzoglou and S. Guatelli, "Electron track structure simulations in a gold nanoparticle using Geant4-DNA", *Physica Medica*, 2019, **63**, 98–104.

(170) E. Lechtman, S. Mashouf, N. Chattopadhyay, B. Keller, P. Lai, Z. Cai, R. Reilly and J. Pignol, "A Monte Carlo-based model of gold nanoparticle radiosensitization accounting for increased radiobiological effectiveness", *Physics in Medicine & Biology*, 2013, **58**, 3075.

(171) S. J. McMahon, "The linear quadratic model: usage, interpretation and challenges", *Physics in Medicine & Biology*, 2018, **64**, 01TR01.

(172) M. Scholz and G. Kraft, "Calculation of heavy ion inactivation probabilities based on track structure, x ray sensitivity and target size", *Radiation Protection Dosimetry*, 1994, **52**, 29–33.

(173) M. Scholz and G. Kraft, "Track structure and the calculation of biological effects of heavy charged particles", *Advances in Space Research*, 1996, **18**, 5–14.

(174) M. Scholz and G. Kraft, "The physical and radiobiological basis of the local effect model: a response to the commentary by R. Katz", *Radiation research*, 2004, **161**, 612–620.

(175) S. J. McMahon, W. B. Hyland, M. F. Muir, J. A. Coulter, S. Jain, K. T. Butterworth, G. Schettino, G. R. Dickson, A. R. Hounsell, J. M. O'sullivan et al., "Biological consequences of nanoscale energy deposition near irradiated heavy atom nanoparticles", *Scientific reports*, 2011, **1**, 1–10.

(176) V. Ferrero, G. Visonà, F. Dalmasso, A. Gobbato, P. Cerello, L. Strigari, S. Visentin and A. Attili, "Targeted dose enhancement in radiotherapy for breast cancer using gold nanoparticles, part 1: A radiobiological model study", *Medical physics*, 2017, **44**, 1983–1992.

(177) H. N. McQuaid, M. F. Muir, L. E. Taggart, S. J. McMahon, J. A. Coulter, W. B. Hyland, S. Jain, K. T. Butterworth, G. Schettino, K. M. Prise et al., "Imaging and radiation effects of gold nanoparticles in tumour cells", *Scientific reports*, 2016, **6**, 1–10.

(178) L. Bobyk, M. Edouard, P. Deman, M. Vautrin, K. Pernet-Gallay, J. Delaroche, J.-F. Adam, F. Estève, J.-L. Ravanat and H. Elleaume, "Photoactivation of gold nanoparticles for glioma treatment", *Nanomedicine: Nanotechnology, Biology and Medicine*, 2013, **9**, 1089–1097.

(179) J. Domey, U. Teichgräber and I. Hilger, "Gold nanoparticles allow detection of early-stage edema in mice via computed tomography imaging", *International journal of nanomedicine*, 2015, **10**, 3803.

(180) C. S. Kim, X. Li, Y. Jiang, B. Yan, G. Y. Tonga, M. Ray, D. J. Solfiell and V. M. Rotello, "Cellular imaging of endosome entrapped small gold nanoparticles", *MethodsX*, 2015, **2**, 306–315.

(181) G. Poludniowski, G. Landry, F. Deblois, P. Evans and F. Verhaegen, "SpekCalc: a program to calculate photon spectra from tungsten anode x-ray tubes", *Physics in Medicine & Biology*, 2009, **54**, N433.

(182) M. J. Berger, J. S. Coursey, M. A. Zucker et al., "ESTAR, PSTAR, and ASTAR: computer programs for calculating stopping-power and range tables for electrons, protons, and helium ions (version 1.21)", 1999.

(183) J. Coulter, K. Butterworth and S. Jain, "Prostate cancer radiotherapy: potential applications of metal nanoparticles for imaging and therapy", *The British journal of radiology*, 2015, **88**, 20150256.

(184) J. M. Brown and F. J. Currell, "A local effect model-based interpolation framework for experimental nanoparticle radiosensitisation data", *Cancer nanotechnology*, 2017, **8**, 1–10.

(185) G. Garty, R. Schulte, S. Shchemelinin, C. Leloup, G. Assaf, A. Breskin, R. Chechik, V. Bashkirov, J. Milligan and B. Grosswendt, "A nanodosimetric model of radiation-induced clustered DNA damage yields", *Physics in Medicine & Biology*, 2010, **55**, 761.

(186) J. Apostolakis, M. Asai, A. Bogdanov, H. Burkhardt, G. Cosmo, S. Elles, G. Folger, V. Grichine, P. Gumplinger, A. Heikkinen et al., "Geometry and physics of the geant4 toolkit for high and medium energy applications", *Radiation Physics and Chemistry*, 2009, **78**, 859–873.

(187) A. Bagulya, J. Brown, H. Burkhardt, V. Grichine, S. Guatelli, S. Incerti, V. N. Ivanchenko, O. Kadri, M. Karamitros, M. Maire et al., Journal of Physics: Conference Series, 2017, vol. 898, p. 042032.

(188) S. Incerti, V. Ivanchenko and M. Novak, "Recent progress of Geant4 electromagnetic physics for calorimeter simulation", *Journal of Instrumentation*, 2018, **13**, C02054.

(189) V. Ivanchenko and S. Incerti, EPJ Web of Conferences, 2017, vol. 142, p. 01016.

(190) I. Kawrakow and A. F. Bielajew, "On the representation of electron multiple elastic-scattering distributions for Monte Carlo calculations", *Nuclear Instruments and Methods in Physics Research Section B: Beam Interactions with Materials and Atoms*, 1998, **134**, 325–336.

(191) S. Goudsmit and J. Saunderson, "Multiple scattering of electrons", *Physical review*, 1940, **57**, 24.

(192) N. F. Mott, "The scattering of fast electrons by atomic nuclei", *Proceedings of the Royal Society of London. Series A, Containing Papers of a Mathematical and Physical Character*, 1929, **124**, 425–442.

(193) I. Kawrakow, "Electron transport: lateral and longitudinal correlation algorithm", *Nuclear Instruments and Methods in Physics Research Section B: Beam Interactions with Materials and Atoms*, 1996, **114**, 307–326.

(194) I. Kawrakow and A. F. Bielajew, "On the condensed history technique for electron transport", *Nuclear Instruments and Methods in Physics Research Section B: Beam Interactions with Materials and Atoms*, 1998, **142**, 253–280.

(195) G. J. Lockwood et al., "Calorimetric Measurement of Electron, Energy Deposition in Extended Media–Theory vs. Experiment, SANDIA REPORT SAND79-0414", *UC-34a, February*, 1987.

(196) V. Ivanchenko, O. Kadri, M. Maire and L. Urban, Journal of Physics: Conference Series, 2010, vol. 219, p. 032045.

(197) G. Wentzel, "Zwei bemerkungen über die zerstreuung korpuskularer strahlen als beugungserscheinung", *Zeitschrift für Physik*, 1926, **40**, 590–593.

(198) H. Bethe and W. Heitler, "On the stopping of fast particles and on the creation of positive electrons", *Proceedings of the Royal Society of London. Series A, Containing Papers of a Mathematical and Physical Character*, 1934, **146**, 83–112.

(199) P. Gros and D. Bernard, "γ-ray telescopes using conversions to e+ e- pairs: event generators, angular resolution and polarimetry", *Astroparticle Physics*, 2017, **88**, 60–67.

(200) I. Semeniouk and D. Bernard, "C++ implementation of Bethe–Heitler, 5D, polarized, $\gamma\rightarrow$ e+ e- pair conversion event generator", *Nuclear Instruments and Methods in Physics Research Section A: Accelerators, Spectrometers, Detectors and Associated Equipment*, 2019, **936**, 290–291.

(201) R. Jost, J. Luttinger and M. Slotnick, "Distribution of recoil nucleus in pair production by photons", *Physical Review*, 1950, **80**, 189.

(202) V. Boldyshev and Y. P. Peresun'ko, *ELECTRON–POSITRON PAIR PHOTOPRODUCTION ON ELECTRONS AND ANALYSIS OF PHOTON BEAM POLARIZATION*. Tech. rep., Physical-Technical Inst., Kazan, 1971.

(203) D. Cullen, "IAEA-NDS-218, IAEA Nuc", *Data Section*, 2014.

(204) M. Gavrila, "Relativistic k-shell photoeffect", *Physical Review*, 1959, **113**, 514.

(205) G. Blair, H. Burkhardt and H. Schreiber, *Background simulation for the CLIC beam delivery system with Geant*, tech. rep., 2002.

(206) `http://www.wolfram.com/mathematica/`.

(207) S. J. Brodsky and R. F. Lebed, "Production of the smallest QED atom: true muonium ($\mu+\ \mu$-)", *Physical review letters*, 2009, **102**, 213401.

(208) M. Boscolo, M. Antonelli, O. Blanco-Garcia, S. Guiducci, S. Liuzzo, P. Raimondi and F. Collamati, "Low emittance muon accelerator studies with production from positrons on target", *Physical Review Accelerators and Beams*, 2018, **21**, 061005.

(209) `http://geant4-dna.org/`.

(210) S. Incerti, G. Baldacchino, M. Bernal, R. Capra, C. Champion, Z. Francis, P. Gueye, A. Mantero, B. Mascialino, P. Moretto et al., "The geant4-dna project", *International Journal of Modeling, Simulation, and Scientific Computing*, 2010, **1**, 157–178.

(211) S. Incerti, A. Ivanchenko, M. Karamitros, A. Mantero, P. Moretto, H. Tran, B. Mascialino, C. Champion, V. Ivanchenko, M. Bernal et al., "Comparison of GEANT4 very low energy cross section models with experimental data in water", *Medical physics*, 2010, **37**, 4692–4708.

(212) S. Incerti, I. Kyriakou, M. Bernal, M.-C. Bordage, Z. Francis, S. Guatelli, V. Ivanchenko, M. Karamitros, N. Lampe, S. B. Lee et al., "Geant4-DNA example applications for track structure simulations in liquid water: A report from the Geant4-DNA Project", *Medical physics*, 2018, **45**, e722–e739.

(213) I. Kyriakou, S. Incerti and Z. Francis, "Improvements in geant4 energy-loss model and the effect on low-energy electron transport in liquid water", *Medical physics*, 2015, **42**, 3870–3876.

(214) V. Ivanchenko, A. Bagulya, S. Bakr, M. Bandieramonte, D. Bernard, M.-C. Bordage, J. Brown, H. Burkhardt, P. Dondero, S. Elles et al., EPJ Web of Conferences, 2019, vol. 214, p. 02046.

(215) J. Lindhard, A. H. So et al., "Relativistic theory of stopping for heavy ions", *Physical Review A*, 1996, **53**, 2443.

(216) A. Bogdanov, H. Burkhardt, V. Ivanchenko, S. Kelner, R. Kokoulin, M. Maire, A. Rybin and L. Urban, "Geant4 simulation of production and interaction of muons", *IEEE Transactions on nuclear science*, 2006, **53**, 513–519.

(217) `https://indico.cern.ch/event/845054/`.

(218) `https://indico.cern.ch/event/769192/`.

(219) S. Incerti, I. Kyriakou, M.-C. Bordage, S. Guatelli, V. Ivanchenko and D. Emfietzoglou, "Track structure simulations of proximity functions in liquid water using the Geant4-DNA toolkit", *Journal of Applied Physics*, 2019, **125**, 104301.

Appendix A

Dose Enhancement Using Nano-particles

In this appendix the dose enhancement of the treatment dose with the addition of nanoparticles made of high-Z materials and irradiation with X-rays has been examined.

This chapter is a modified version of the published work:
E.Engels, **S. Bakr**, D. Bolst, D. Sakata, N. Li, P. Lazarakis, S. J. McMahon, V. Ivanchenko, A. Rosenfeld, S. Incerti, I. Kyriakou, D. Emfietzoglou, M. L. F. Lerch, M. Tehei, S. Corde and S. Guatelli, (2020) **"Advances in modelling gold nanoparticle radiosensitization using new Geant4-DNA physics models"**, *Physics in Medicine and Biology*, November 2020, 174.

`https://doi.org/10.1088/1361-6560/abb7c2`

My participation percentage in this work is roughly 5%. In this work, I have used Geant4 10.4.p01 version to run the application using only Livermore physics models through all geometrical set-up.

A.1 Abstract

Gold nanoparticles have demonstrated significant radiosensitization of cancer treatment with X-ray radiotherapy. To understand the mechanisms at the basis of nanoparticle radiosensitization, Monte Carlo simulations are used to investigate the dose enhancement, given a certain nanoparticle concentration and distribution in the biological medium. Earlier studies have ordinarily used condensed history physics models to predict nanoscale dose enhancement with nanoparticles. This study uses Geant4-DNA complemented with

novel track structure physics models to accurately describe electron interactions in gold and to calculate the dose surrounding gold nanoparticle structures at nanoscale level. The computed dose *in silico* due to a clinical kilovoltage beam and the presence of gold nanoparticles was related to *in vitro* brain cancer cell survival using the local effect model. The comparison of the simulation results with radiobiological experimental measurements shows that Geant4-DNA and local effect model can be used to predict cell survival *in silico* in the case of X-ray kilovoltage beams.

A.2 Introduction

High atomic number (Z) nanoparticles (NPs), such as gold, platinum and ceramic metal oxide particles are sub-cellular in size and are ideally suited to internalize within cells [133–136]. When exposed to X-rays used in radiotherapy, NPs enhance local radiation doses and increase cancerous cell destruction [137]. This is due to an excess of low energy electrons produced from the NPs, which deposit energy locally in the surrounding biological medium [134].

With inert properties and high Z of 79, gold NPs (GNPs) are among the most researched candidates for NP-enhanced cancer treatment using methods such as Monte Carlo simulations [3, 138–140], and both *in vitro* [141, 142] and *in vivo* studies [143, 144]. The enhanced photoelectron production, emission of low energy Auger electrons and fluorescence X-rays associated with the high-Z of gold cause significant localized damage to cancer cells, particularly in kilovoltage (kV) radiation fields [141, 145]. Currently, kV radiotherapy is used to treat skin cancer [146, 147], but could be used to treat brain and central nervous system cancers (CNS), [75, 148, 149].

Where normal tissue sparing remains a concern with standalone radiation treatments, GNPs offer a means to better target cancerous cells, maintaining tumor control, while reducing the normal tissue radiation dose [145]. Optimal energies for dose enhancement effects with GNPs is estimated to be 60–90 keV using monochromatic beams due to the comparatively smaller X-ray absorption of tissues (or water) at these energies [150].

A.2.1 Monte Carlo Simulation and GNP-enhanced Radiotherapy

Monte Carlo (MC) simulations describe particle transport in matter and interactions, and are widely used to investigate the energy deposition around GNPs in the biological medium when irradiated by a radiotherapeutic field. Simulations determine the effect of varying the size, distribution and shape of the GNPs [151, 152].

The physics models, included in the "general purpose" MC codes such as EGS [153], PENELOPE [154], Geant4 [1], and MCNP [155] adopt a condensed history (CH) approach, where a large number of collision processes are grouped together ("condensed"), producing an artificial mean free path called a "step". This approach has made MC simulations a highly useful investigation tool, but inherently inadequate to describe detailed particle interactions at nanometer scale and low energy (<keV).

Specialized MC codes, such as PTra [156] PARTRAC [157], KURBUC [158], NOREC [156], and TRAX [159] usually known as "track structure codes" (TS codes), have been developed to calculate the energy deposition at nanometer scale, modelling particle tracks according to each physics process occurring, typically in gaseous medium or liquid water, to approximate biological systems [158].

The Geant4 electromagnetic physics classes adopt the CH approach and contain models addressed to medical physics applications [93]. One is based on the Livermore evaluated data library [160] with a recommended low-energy limit of 250 eV [63, 161]. The second one is based on the Penelope MC code, valid down to approximately 100 eV [162–164].

Geant4 is the only general-purpose radiation transport MC code which offers TS physics models to describe particle interactions in liquid water at nanometer level, through the Geant4-DNA Package (G4DNA), [48, 94, 165, 166]. This package currently provides a complete set of models describing process by process the electromagnetic interactions of particles (including electrons, protons, α particles and ions) with liquid water [165].

Sakata et al (2016) developed the first TS-based physics models within G4DNA capable of describing electron interactions in GNPs [167, 168]. Such models have been refined in a second iteration, where the Energy Loss Function formalism has been adopted to describe the ionization and excitation processes in gold down to $\sim$ 10 eV [169]. The new gold models adopt the ELSEPA code to calculate elastic scattering cross section [167].

A.2.2 Modelling Cell Survival

Translation from Monte Carlo simulations to in vitro experimental results is still sought after, particularly concerning the nanoscale dose inhomogeneity produced by GNPs. The linear quadratic model (LQM) is based on the linear quadratic nature of the cell survival curve, [170, 171]. The LQM relates the average dose, D, delivered to the cell population with X-rays, to the cell surviving fraction, S_X, according to equation (A.1)

$$S_X = exp(-(\alpha D + \beta D^2)) \tag{A.1}$$

The parameters α and β relate D to S_X and can be evaluated experimentally *in vitro*. The LQM, in its simplicity, is ideally suited to describe the effect of averaged and uniform radiation field doses on cell survival. Due to this, the LQM is not well-suited to spatially fractionated or non-uniform dose fields such as microbeam radiation therapy [149] and particle therapy [138, 172]. This has led to the development of other radiobiological models including the local effect model (LEM), [172–174].

The LEM, described in equations (A.2) and (A.3), is a more sophisticated approach to dose non-uniformity than the LQM and was originally developed to determine the radiobiological effectiveness of heavy ion radiation field for hadron therapy applications [172]. LEM relates energy depositions on the nanoscale to the cell survival S, determined from in vitro experiments. S can be expressed as function of the number of lethal events, N, following Poisson statistics, equivalent to equation equation (A.2)

$$S = exp(-N) \tag{A.2}$$

N is calculated by means of equation (A.3) where the local dose in the biological medium, $D(x,y,z)$, due to the incident X-ray field is used to compute a spatially dependent $S(D(x,y,z))$, obtained using equation (A.2), which is evaluated at nanoscale volumes (dV) within a sensitive volume, V_S

$$N = -\int_{V_S} \frac{ln(S(D(x,y,z)))}{V_S} dV \tag{A.3}$$

The average number of lethal events due to a non-uniform radiation field, such as the one obtained with NPs internalized in the cell (N_{NP}), can also be evaluated using this approach. Implementation of the LEM for this purpose is described further in the method for our study.

Many correlations to *in vitro* studies with GNPs have been made using LEM [170, 171, 175, 176], however, this is the first study to investigate the impact of new specialized G4DNA gold physics models [167, 168] in GNP radio-enhancement and how this is related to cell survival *in vitro* for a more realistic GNP distribution. This work calculates the dose enhancement on the nanoscale with a single GNP and a simplistic model of the clustering GNPs around the cell nucleus. G4DNA, with the novel specialized gold TS physics models was compared to the case with the CH Livermore Package to describe particle interactions in the medium. The cell surviving fraction with GNPs was then calculated *in silico* by applying the LEM to 9 l gliosarcoma cancer cells irradiated with kV X-rays. Direct correlation was made between the computed cancer cell survival and the in vitro results with GNPs.

A.3 Method

A.3.1 Cell Experiment Design

Cell experiments were carried out with 9 l gliosarcoma (9LGS), rat glioma cells derived from an N-nitroso-N-methylurea (NMU)-induced tumor and were purchased from the European Collection of Cell Cultures (ECACC). Cell cultures were maintained at 37 $^{\circ}C$ and 5% (v/v) CO_2 in a T75 cm^2 tissue culture flask containing complete-DMEM (Dulbecco's Modified Eagle Medium, *Gibco*®, Life Sciences), supplemented with 10% (v/v) FBS (Fetal Bovine Serum, Invitrogen) and 1% (v/v) PS (penicillin/streptomycin, *Gibco*®, Life Sciences)). GNPs with a diameter of 15 nm are studied in many radiosensitization studies [137, 177]. They are commonly used *in vitro* and *in vivo* experiments as they have low toxicity [178], and show more lingering internalization and efficient localization at tumor site through the vasculature supply [179]. *AuroVist*^{TM} 15 nm diameter NPs are commercially available for preclinical use (Nanoprobes Inc. NY). To prepare the GNPs, a portion of the original 200 mg ml^{-1} GNP stock was diluted in phosphate buffered saline (PBS, *Gibco*®) to a final concentration of 10 mg ml^{-1}.

Cell Imaging for Simulation Set Up

Confocal imaging was performed to determine the distribution of GNPs in 9LGS, adapting a similar method outlined by Kim et al [180].

9LGS cells were incubated with or without GNPs in an *ibidi*® μ-slide, 8 well, chambered coverslip (ibidi GmbH, Lochhamer Schlag 11, 82 166 Grafelfing). GNPs were added to 9LGS cell medium 24 h before imaging, at a final concentration of 500 $\mu g ml^{-1}$. Images were acquired with a Leica TCS SP5 confocal microscope (Leica Microsystems Pty Ltd, Macquarie Park, 2113 Australia). After 24 h incubation, the μ-slide was placed directly in the confocal microscope (without washing) on a movable stage and a 40x oil immersion lens used to image cells once immersion oil was applied to the slide. An argon laser with wavelength 488 nm was used to expose the cells and GNPs, in order to produce fluorescence or light scatter from the sample. Light was detected using a photomultiplier tube in the range of 510–600 nm. Bright field (BF) images were also collected. Images were obtained at multiple depths within the cell.

Figure A.1 shows a confocal microscopic image of GNPs inside the 9LGS cells, with pixel size of 0.48 μm by 0.48 μm. The green light scatter indicates the presence of GNPs by exploiting the surface plasmon resonance of gold above 10 nm [180] and shows that the GNPs tend to congregate around the cell nucleus of the 9LGS. This motivated the use of a simplistic geometrical model of the GNP configuration for the evaluation of the LEM.

When using BF imaging alone (no laser, as shown in figure A.1, top-left), there is no visible evidence of GNPs. The accumulations of GNPs therefore are of a size much less than the BF visible resolution of 0.48 μm, and only appear present with laser light. These experimental findings have prompted the use of a GNP upper size limit of 100 nm diameter in the simulation study to mimic the order of magnitude of the largest possible GNP clusters, as well as the original single GNPs that are 15 nm diameter.

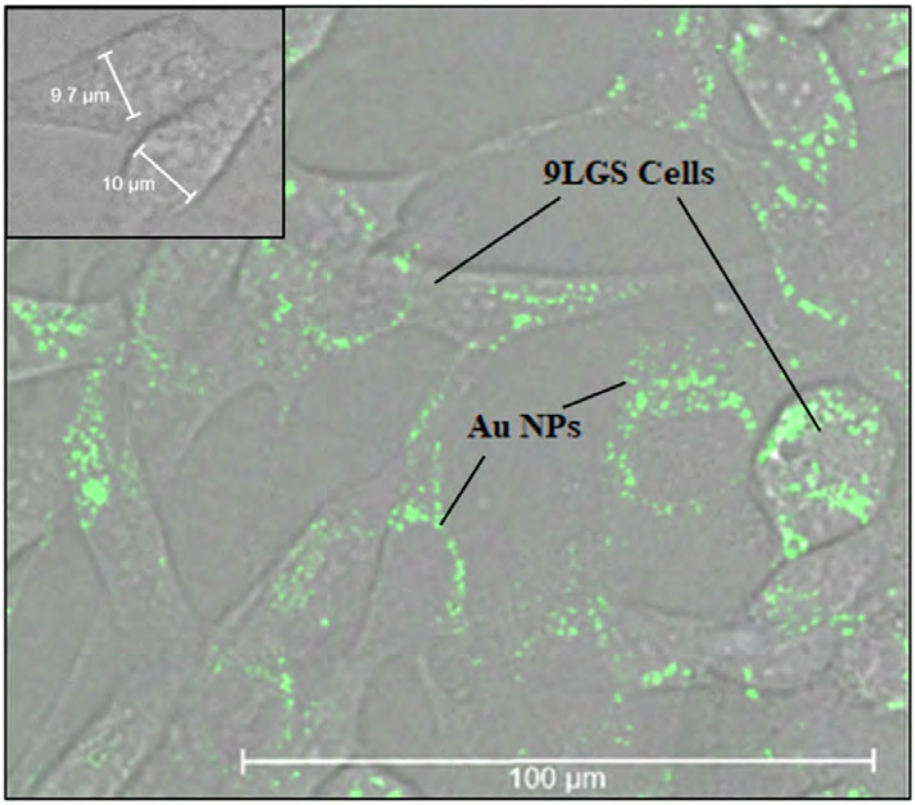

Figure A.1: Confocal microscopy of GNPs (shown in green) incubated in 9LGS for 24 h at a concentration of 500 $\mu g ml^{-1}$. Insert (top-left), shows image of 9LGS cells without argon laser illumination. Dimensions of cell nuclei are shown.

In biological experiments multiple GNPs and GNP clusters often develop into larger structures which affect the dose enhancement of the GNPs to the cell [3, 140]. For the LEM method, the GNP-shell geometry resembling the realistic GNP distribution was therefore considered by recording the positions of the GNPs over the entire volume of the 9LGS cell. On average, a shell-like distribution was seen, as shown in figure A.1, which was estimated in 3 dimensions to be 1 GNP thick throughout the shell. It was also found that the GNPs were less likely to be on the top of the nucleus or on the bottom against the flask. Therefore, a GNP shell distribution was modelled 2 μm from the top of the 9LGS nucleus, 6 μm deep, and surrounding the 9LGS nucleus of 10 μm diameter (see figure A.4).

Cell Irradiation

24 hrs prior to irradiation, 500 μgml^{-1} GNPs were added to 9LGS cells that were sub-cultured into T12.5 cm^2 flasks (BD FalconTM) containing c-DMEM. The irradiation of 9 l cells with and without GNPs was performed at the Prince of Wales Hospital (Randwick, New South Wales, Australia 2031) using a Nucletron Oldelft Therapax DXT 300 Series 3 Orthovoltage X-ray machine (Nucletron B.V., Veenendaal, The Netherlands). T12.5 cm^2 flasks containing a monolayer of 9 l cells under 6 mm medium were positioned at a distance of 50 cm from the X-ray tube. Flasks rested on a 10 cm solid water phantom and were surrounded by 6 mm of solid water to ensure full particle equilibrium. X-rays were generated at 150 kVp with a beam current of 20 mA using inherent filtration of 3 mm beryllium with additional 0.35 mm of copper and 1.5 mm of aluminum (HVL = 0.68 mm Cu). Cells were irradiated with a dose rate of 0.754 Gy min^{-1} for doses ranging from 1 to 8 Gy at 6 mm depth. Figure A.2 shows the 150 kVp spectra. Following the X-ray irradiation, cells were seeded at low density into 100 mm petri dishes containing 10 ml of c-DMEM. Each independent flask was seeded in triplicate sets corresponding to each radiation dose including an unirradiated control sets with and without GNPs to determine any toxicity due to GNPs. After 14 doubling times (necessary to obtain an adequate number of colonies), each dish was washed with 5 ml PBS (calcium and magnesium positive) and stained with a solution of 25% crystal violet solution (2.3% crystal violet, 0.1% ammonium oxalate, 20% ethyl alcohol, from Sigma-*Aldrich*®, Australia) and 75% ethanol (v/v).

Surviving colonies of 50 cells or more were counted and divided by the original seeding number to determine the plating efficiency (PE). For each treatment group, the PE was averaged, and standard deviation of the mean calculated. The surviving fraction S_X was evaluated by taking the ratio of the PE of the treated cells and the PE of the non-irradiated control.

A.3.2 Simulation Methods

Characterization of Single GNP Dose Enhancement

To compare G4DNA TS physics models with the CH Livermore models, a single GNP was simulated using Geant4 10.4 patch01 and placed at 6 mm depth in a liquid water phantom with dimensions of $12 \times 12 \times 12\ mm^3$ to replicate the setup of the experimental study. A schematic of the simulation geometry is shown in figure A.3.

The incident radiation field modelled in the Geant4 simulation was the 150 kVp ortho-

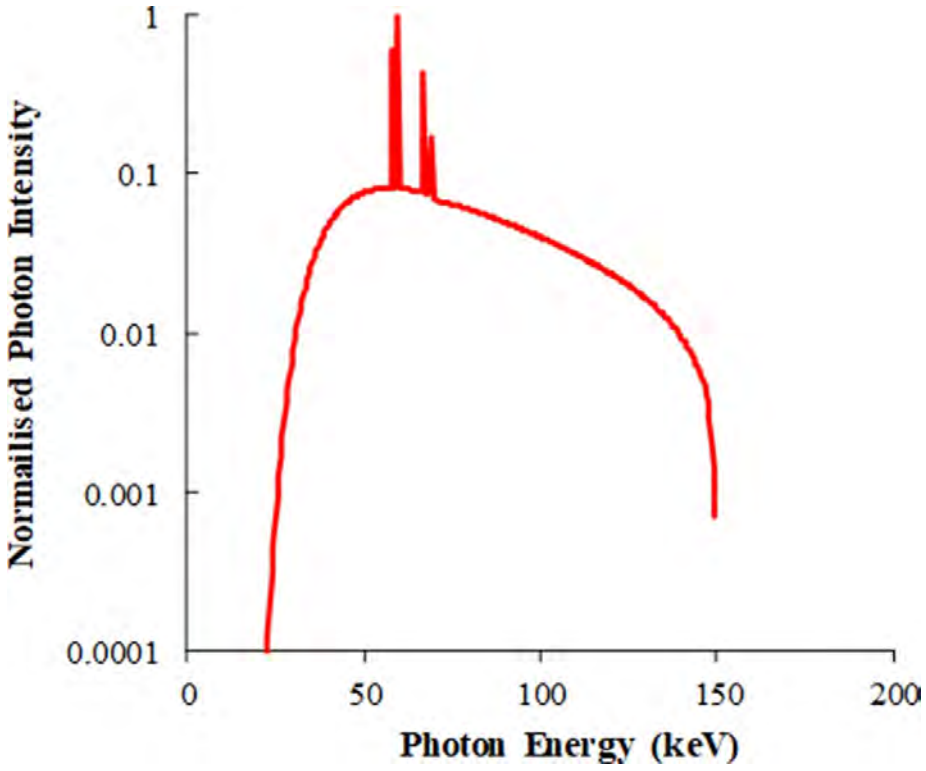

Figure A.2: 150 kVp orthovoltage X-ray spectra (generated using SpekCalc, Poludniowski et al [181]) used to irradiate 9LGS cells experimentally and used in the simulation.

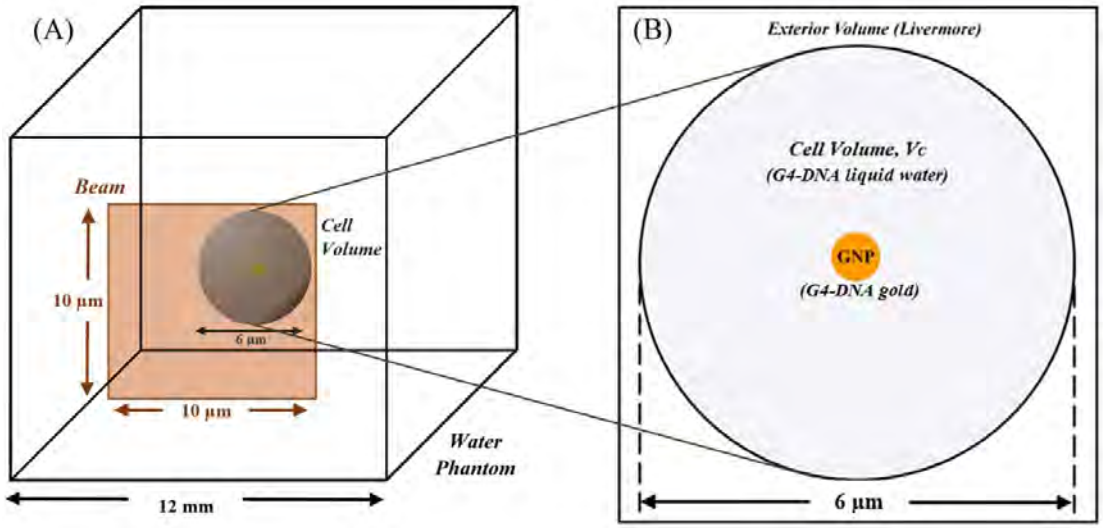

Figure A.3: Geometry of the Monte Carlo simulation (sizes not to scale). The X-ray beam is incident normally on the water phantom (A). The orange box shows the lateral dimensions of the incident beam. A single GNP is set at 6 mm depth in the phantom. The G4DNA is active within V_C (6 μm diameter sphere), with Livermore physics in the surrounding water volume, as shown in the magnified view (B).

voltage X-ray beam used in the experiment (figure A.2). A maximum of 10^{11} histories were simulated to obtain each set of results. The beam was incident normally to the water phantom with a lateral size of 10 μm. Two GNP radii were considered; a GNP radius of 7.5 nm, corresponding to the real dimension of individual GNPs, and 50 nm, to mimic a GNP aggregate, as observed with confocal imaging (figure A.1). A cell volume (V_C) was added to encompass the GNP with dimensions shown in figure A.3(B).

The following situations were considered when modelling the physics processes in the simulation:

- G4DNA in the GNP (gold material) and V_C (liquid water material). A cut of 10 eV was adopted. The newly developed G4DNA models specialized for gold targets (described in Sakata et al [168]) were used to model electron interactions in the GNP. The Livermore physics models were used to describe particle interactions in the water phantom surrounding the V_C, up to a distance of 6 mm, to reduce simulation execution times.
- Livermore physics models were used throughout all the geometrical set-up (that is within the GNP, within V_C and in the water phantom surrounding V_C).

Atomic de-excitation was also modelled. Auger electrons and fluorescence photons were simulated, including the full relaxation cascade.

The Livermore physics models were adopted for the CH approach because Lazarakis et al [163] and Kyriakou et al [164] showed that such models could begin to approximate G4DNA better than the other available CH approaches of Geant4 when using a 10 eV secondary electron production lower energy limit, while a limit of 250 eV has been recommended by the authors of the Livermore models [44].

The low electron energy (LEE) limit controls the cut of the secondary electron production in the CH models. The LEE limits of 10 eV and 250 eV were investigated in this study of the case of a 50 nm radius GNP radioenhancement.

The simulation calculated the radial absorbed dose distribution from the surface of the GNP per incident photon and the Dose Enhancement Ratio (DER). The DER is the ratio of the absorbed dose with and without the GNP in water.

Dose Enhancement of a GNP in a Partial Shell Configuration

A GNP shell-like configuration was considered to match experimental observations (figure A.1) and is similar to the distribution previously described in McKinnon et al [3] and

Liu et al [140]. This design was considered as there were some initial discrepancies with LEM using single GNPs (not shown) that we estimated were due to incorrect extrapolation of realistic GNP geometry in 9LGS.

V_C, originally 3 μm in radius, was increased to 10 μm in radius to encompass the 9LGS cell nucleus which has a radius of 5 μm, based on experimental observations (figure A.1). The beam dimensions were increased to 24×24 μm^2 accordingly.

In this geometrical cell configuration, the cell "nucleus" with radius 5 μm, was partially surrounded with a 15 nm thick GNP shell. The confocal imaging showed that the GNPs were only visible using light scatter from the 20 mW Argon laser, and have sizes smaller than the visible resolution. The GNP shells were sometimes incomplete or had regions of thicker deposits of GNPs. On average, the coverage of the GNPs around the nucleus of 9LGS was approximated to be 1 GNP thick (15 nm) with the top and bottom of the nucleus uncovered by GNPs. This geometry in a simplistic sense mimics the average GNP distribution surrounding the 9LGS nucleus using confocal imaging, and is shown in figure A.4.

Figure A.4 represents the geometrical set-up in Geant4, including dimensions of the GNP shell and position of the incident beam. The inner radius of the GNP shell was set equal to 5 μm based on the 9LGS nucleus size in the confocal images. The energy deposited within the cell nucleus was scored as well as 5 μm outside the shell. G4DNA and Livermore physics models were activated for this simulation as described in the next section.

A.3.3 Analysis Using LEM-based Radiobiological Models

To determine the effect of the average dose enhancement due to the GNP shell congregation, a LEM approach was considered which adapts equations (A.2) and (A.3). The dose $D(x,y,z)$ is calculated in terms of radial distance r, as $D(r)$, and ranges from the origin at the center of V_C to the interior surface of the GNP shell in 1 nm steps ($\triangle r = 1nm$), denoted by the total radius of V_C (R_C).

Equation (A.3) can then be used to compute the lethal events due to the GNP alone ($D(r)$), after subtracting the dose calculated without GNPs in water ($D(r) = D_{GNP}(r) - D_{water}(r)$). The lethal events due to the GNP alone are shown in equation (A.4)

$$N_{NP} = \frac{1}{R_C^3} \sum_{r=0}^{R_C} (\alpha D(r) + \beta D(r)^2)((r+\triangle r)^3 - r^3) \tag{A.4}$$

Characteristic parameters α and β were obtained from the experimental cell survival

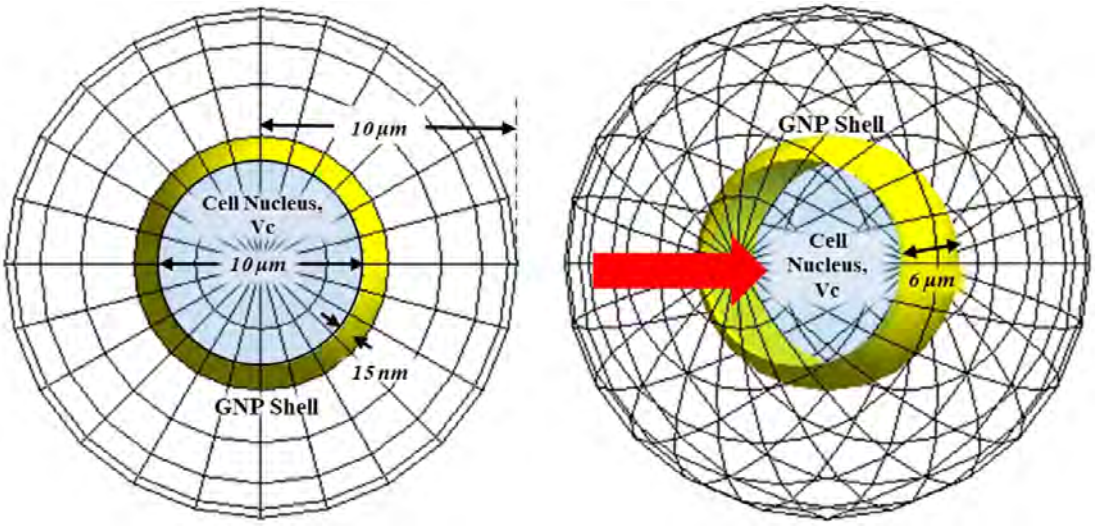

Figure A.4: The partial GNP shell (yellow) modelled in the Geant4 simulation, shown from a beam view and 30° perspective. The red arrow shows the direction of the incident beam. The 6 μm-wide GNP shell surrounds V_C and begins at 2 μm depth from the surface of V_C, and was constructed to surround 60% of the cell as estimated from confocal imaging.

obtained in absence of GNPs. For this study, the lethal events were considered to be inside the nucleus of 9LGS. Therefore $D(r)$ was calculated from the inside of the GNP shell.

The complete cell survival due to the GNPs (S_{NP}) and X-rays was then evaluated with the number of lethal events created by X-ray interaction with the GNP alone (N_{NP}) and without the GNP (N_X), described in equation (A.5)

$$S_{NP} = exp(-(N_{NP} + N_X)) \tag{A.5}$$

S_{NP} was evaluated for each dose delivered to water (D in equation (A.1)), ranging from 1 to 10 Gy. The additional dose predicted by LEM due to the GNPs in V_C can also be recorded. The effective dose D_{eff} following treatment with 1 Gy of X-rays in the presence of GNPs was calculated by substituting S for S_{NP} in equation (A.1) and solving for D. This substitution is shown in equation (A.6)

$$-ln(S_{NP}) = \alpha D_{eff} + \beta D_{eff}^2 \tag{A.6}$$

D_{eff} is the effective dose due to the GNPs and X-rays as calculated by the LEM, S_{NP} is calculated using equation (A.5), and the α and β parameters are due to X-ray irradiation of 9LGS only (no GNPs). The effective dose was calculated using the quadratic formula. The effective dose enhancement DE_{eff} in V_C was then derived as D$DE_{eff} = D_{eff}/1$ Gy. For comparison, the average dose enhancement (DE_{av}) in V_C was also calculated.

Table A.1: Summary of the radiobiological parameters (α and β) due the radiation treatment of 9LGS cells with (500 μgml^{-1} GNPs) and without (0 μgml^{-1}) GNPs. LQM fits were performed in *MATLAB*® R2018b using the Curve Fitting *Tool*^{TM} (MATLAB 2018). Errors are within a 95% confidence interval.

Treatment	$\alpha\ Gy^{-1}$	$\beta\ Gy^{-2}$
Control (0 μgml^{-1} GNPs)	0.135 ± 0.052	0.011 ± 0.008
500 μgml^{-1} GNPs	0.334 ± 0.027	0

A.4 Results

A.4.1 Experimental Results

To characterize the effect of the *AuroVist*^{TM} GNPs on 9LGS cells, a clonogenic assay was performed and confirmed that the GNPs did not produce any intrinsic toxicity towards 9LGS cells, with a surviving fraction of (1 ± 0.1). Figure A.5 shows the clonogenic surviving fraction of 9LGS cells following irradiation with 150 kVp orthovoltage X-rays with and without GNPs at a nominal concentration of 500 μgml^{-1}.

The addition of GNPs with increasing X-ray radiation dose, causes radiosensitization of the 9LGS cells, as expected. As a result, the GNPs produce a reduction in the cell surviving fraction (shown by S_{NP}) across all doses compared to X-rays alone (S_X). The 500 μgml^{-1} concentration of GNPs and corresponding enhancement is comparable to other radiosensitization studies with kilovoltage X-rays at similar concentrations [170, 175]. The α and β parameters, obtained by fitting the SF curves with the LQM model, are shown in table A.1.

The primary effect of the addition of GNPs to 9LGS was on the α parameter, which produces significantly more linearity to the surviving fraction S_{NP} and is often related to unrepairable double strand DNA breaks [171].

These parameters will be used in the LEM in the final section.

A.4.2 Characterization of Physics Models for Gold Nanoparticles in Geant4

Radial Dose Calculation Using Different Geant4 Physics Models

GNP dose enhancement due exposure with an X-ray beam was investigated initially on single GNPs to understand the differences between TS and CH physics models. The radial dose distribution and DER produced around a single GNP of two sizes (7.5 or 50 nm) due to 150 kVp X-rays was compared in figure A.6 using Livermore low energy limit cut (LEE) of 10 eV and G4DNA.

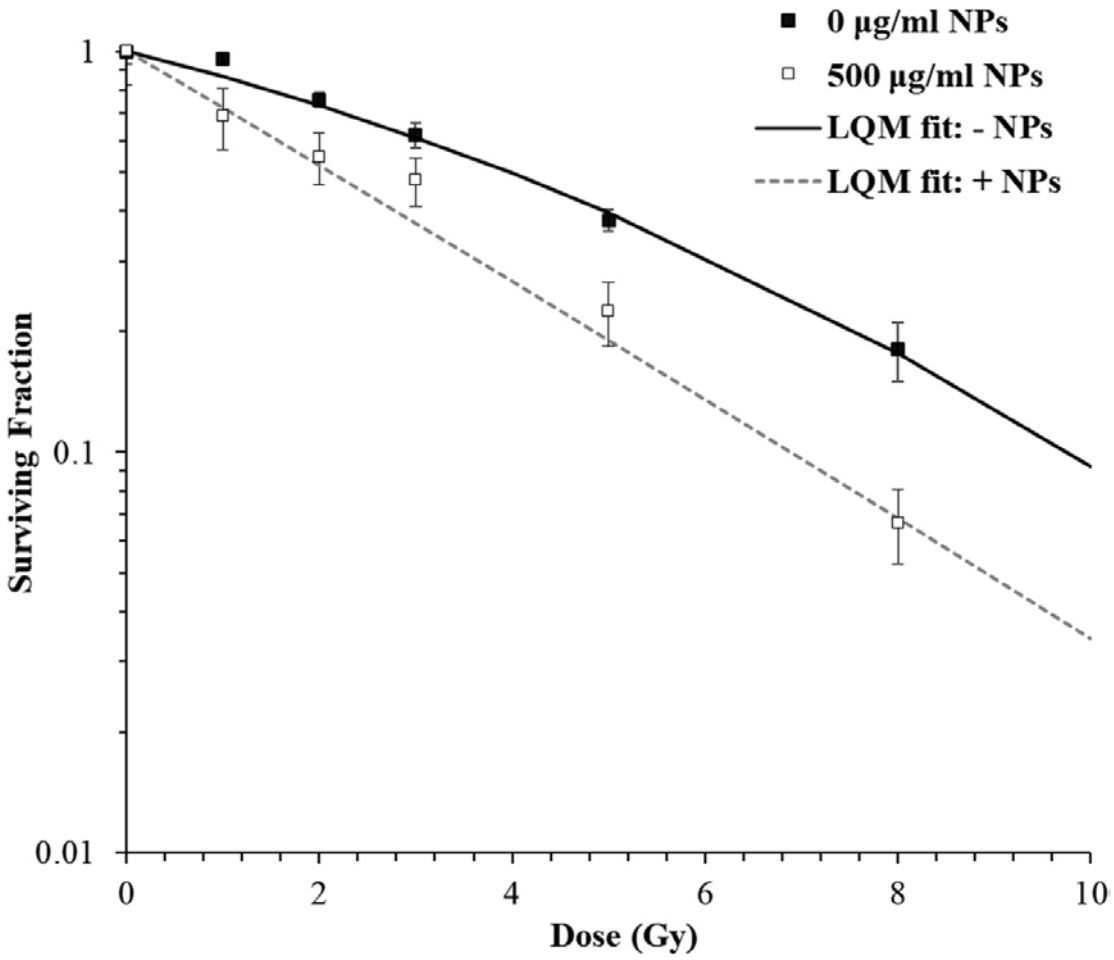

Figure A.5: Clonogenic surviving fraction of 9LGS following 150 kVp orthovoltage X-ray irradiation, showing the surviving fraction without GNPs, 0 μgml^{-1} (S_X), and with 500 μgml^{-1} GNPs (S_{NP}), and the corresponding linear quadtric model (LQM) fitted lines. The continous and dashed black lines are the LQM fits to the radiobiological experimental data with without NPs (-NPs) and with (+NPs), respectively.

CH Livermore physics produced more dose near the GNP than the G4DNA TS models. With a low energy limit of 10 eV (below the recommended 250 eV), the results obtained with Livermore show a DER of (22.2 $\pm$ 3.9) and (47.5 $\pm$ 2.6) within 1 nm of the GNP for the 7.5 nm and 50 nm GNP radius, respectively. G4DNA produced DERs of (18.7 $\pm$ 3.6) and (37.5 $\pm$ 1.9) at the GNP surface with 7.5 nm and 50 nm GNPs, respectively, due to an overall greater electron stopping power in gold with the TS approach, as noted by Sakata et al [168]. DER decreases with distance as low-energy secondary electrons originating in the GNP deposit energy locally in the surrounding biological medium. Sakata et al [168] likewise shows additional absorbed dose produced with Livermore (but with LEE = 250 eV) compared to TS models up to 1 μm from the center of a GNP with radius 30 nm.

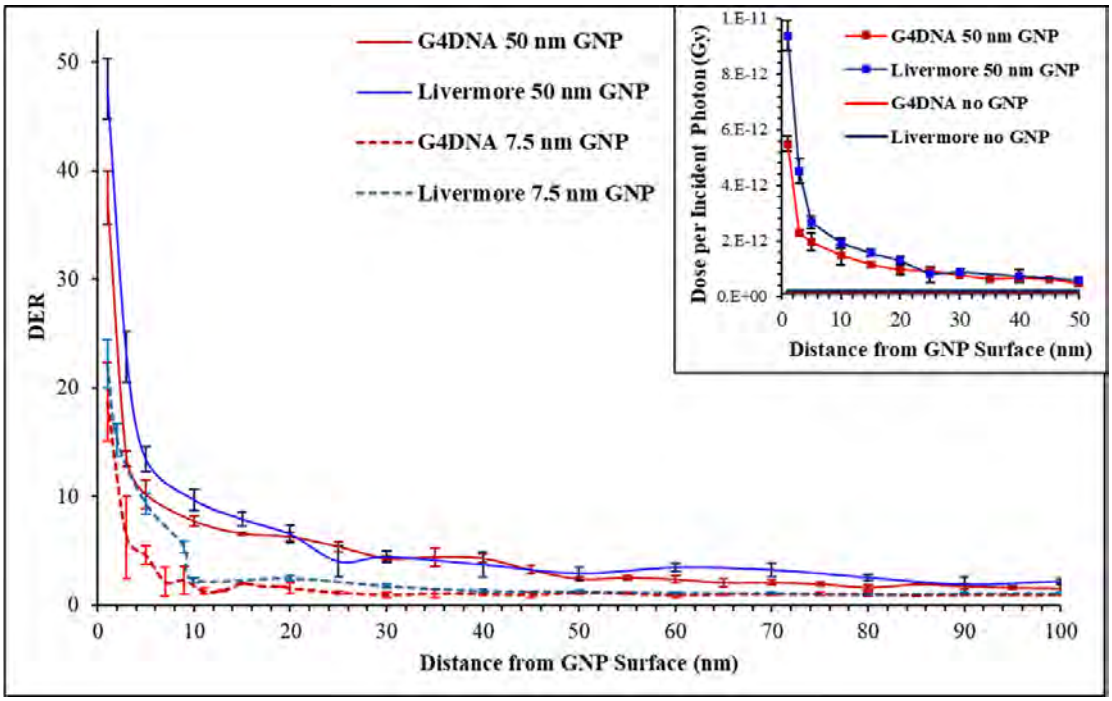

Figure A.6: Dose enhancement ratio (DER) with respect to the distance from the edge of the GNP, for 7.5 nm and 50 nm radius GNPs, using the specialized TS gold physics models (G4DNA in the legend) and the Livermore models (Livermore in the legend). Inserted graph shows the radial dose per incident photon using each physics model for a 50 nm radius GNP.

The DER becomes equal to 1 at a radial distance of 250 nm using the 50 nm radius GNP for both TS and Livermore models in our case. After this, the statistical fluctuation of DER lies within 3% of 1 (equivalent to water) within 95% confidence level. However, some secondary electrons created by the GNP can travel to micrometer distances away from the GNP, but these do not produce a significant change to the DER produced by a single GNP.

Effect of Auger Electrons on the Radial Dose Distribution

The Auger electrons are suspected to be responsible for significant dose enhancement near GNPs [175]. Auger generation was switched off in the GNP region only and compared to complete Auger activation throughout all volumes between Livermore (LEE = 10 eV) and G4DNA models in figure A.7.

Our results confirm that Auger electrons have a significant impact on the energy deposited near the GNP, as noted in previous studies [175]. The additional dose produced by the Auger electrons emitted by the 50 nm GNP is (43. $\pm$ 1.)% and (53. $\pm$ 2.) % when considering distances up to 500 nm from the GNP surface, using the G4DNA and Livermore physics models (LEE = 10 eV), respectively.

Effect of the Low Electron Energy Limit Cut

The kinetic energy of the secondary electrons leaving the GNP was scored for both the Livermore approach and the G4DNA models to compare the effect of changing the Livermore LEE with G4DNA. Figure A.8 shows the kinetic energy spectra and number of electrons per incident photon emerging from a 50 nm radius GNP.

The spectra calculated with the two physics approaches are similar for energies above $\sim$ 1 keV. For lower energies Livermore tends to produce more electrons, on average (1.4 $\pm$ 0.3) times for electrons below 5 keV, which is expected due to the higher stopping power of the G4DNA models for gold and accurate modelling of the production and transport of low energy electrons [168]. Overall, G4DNA produces fewer electrons from the GNP than Livermore.

The Livermore LEE = 250 eV spectra shows that there are no electrons with energy below 250 eV, as expected. The LEE of 250 eV results in more energy deposition near the GNP due to the lost energy being deposited locally rather than converted into δ-electrons.

The average kinetic energy of electrons emerging from the GNP is (18 $\pm$ 1) keV, (21 $\pm$ 1) keV and (24 $\pm$ 1) keV, when using the G4DNA and Livermore LEE = 10 eV and 250 eV, respectively. These energies correspond to ranges between 7 μm to 9.5 μm in water, and 1 μm and 1.45 μm in gold [182]. Therefore, the average electron will traverse a single GNP without self-absorption for both 7.5 nm and 50 nm radius GNPs.

Figure A.9 shows the effect of changing the Livermore LEE from 10 eV to 250 eV in terms of radial dose distribution and DER, in the case of a GNP with a 50 nm diameter.

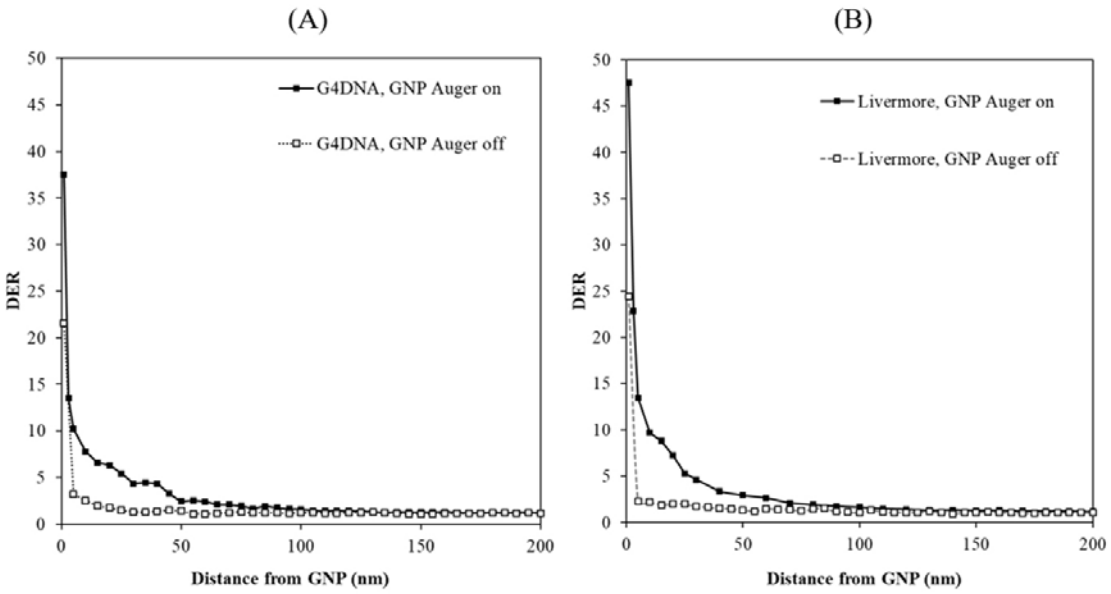

Figure A.7: A comparison of the effect on the DER due to Auger electrons produced by the GNP using G4DNA (A) and Livermore physics models (LEE = 10 eV) (B). For each physics model, Auger electron production in the GNP was switched off (white boxes) and compared with the case with GNP Auger electrons switched on (black boxes).

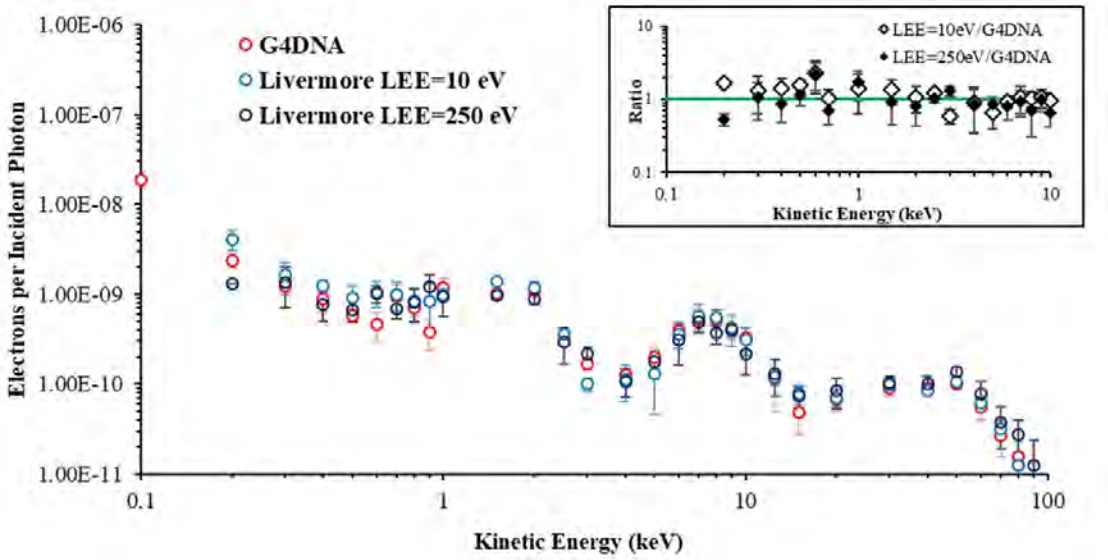

Figure A.8: Kinetic energy spectra of electrons leaving the GNP using G4DNA and Livermore physics models (LEE = 10 eV and LEE = 250 eV). The main plot shows the kinetic energy of electrons per incident photon for G4DNA (red), Livermore LEE = 10 eV (light blue) and LEE = 250 eV (dark blue). The inserted graph shows the ratio of the number of electrons emitted when activating Livermore and G4DNA. Minimum bin size is 0.1 keV.

10 eV LEE provides a much better agreement with G4DNA than the 250 eV limit, confirming the results of Lazarakis et al [163] and Kyriakou et al [164]. When using LEE = 250 eV, Livermore produces larger doses that diverges from G4DNA by 37% within 10 nm from the GNP surface. The LEE = 250 eV Livermore produces a large dose deposition near the GNP due to the higher electron production cut leading to a higher local energy deposition. These results show that the Livermore physics models, with a LEE of 10 eV, could be used when calculating the dose at sub-μm scale if TS codes are not available. This should be done with care, given that the authors of the Livermore models recommend its use down to 250 eV.

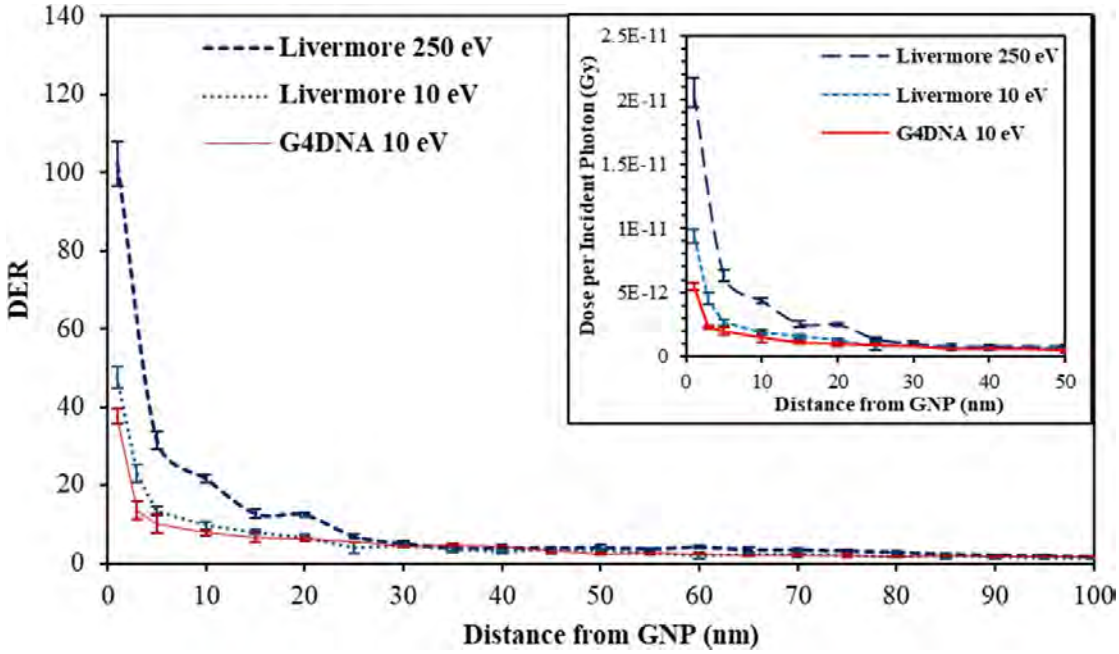

Figure A.9: Radial dose distribution obtained with LEE equal to 10 eV and to 250 eV in the case of the Livermore physics. DER is shown on main plot and radial dose per incident photon on inserted graph.

Thus far, differences between G4DNA with TS-based code and CH Livermore have been identified for GNP simulations involving radial dose on the nanoscale in a kV field. The next section will compare models for more "realistic" GNP geometry which will be used for the LEM comparison.

A.4.3 Partial Shell GNP Configuration and *in silico* Cell Survival

Rarely GNPs accumulate homogeneously within cells, instead GNPs aggregate into new configurations, such as the "shell"-like structures in 9LGS (see figure A.1). We simulated the shell to be 1 GNP (15 nm) thick based on confocal imaging and constructed to

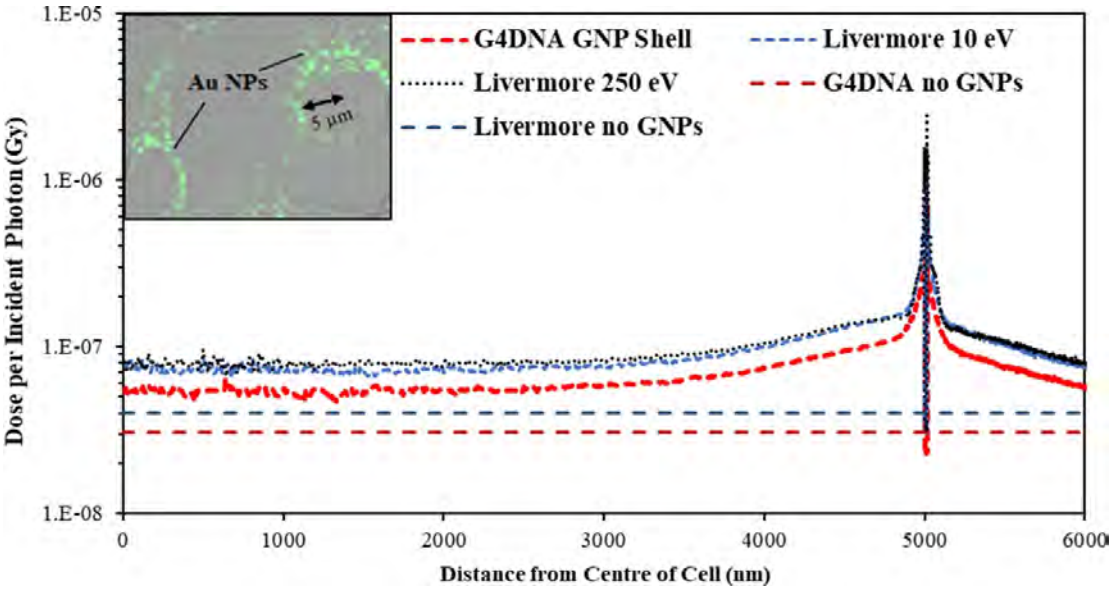

Figure A.10: Dose per incident photon due to the GNP shell with Livermore LEE = 10 eV (blue) and LEE = 250 eV (black), compared to G4DNA (red). The inserted image shows a 9LGS cell including the radius of the cell nucleus.

surround 60% of the 9LGS nucleus volume with radius 5 μm, shown in the insert on figure A.10. The entire radial dose on the nanoscale was recorded inside V_C, in figure A.10, and extending 1 μm beyond.

The dose per incident photon between Livermore and G4DNA is significantly different both in water and when the GNP shell is present. Livermore produces $(30 \pm 4)\%$ more dose than G4DNA in water alone. Using the data presented in figures A.10 and A.11 shows the resulting radial DER for each physics model due to the GNP shell, including an insert showing more detail within 200 nm of the GNP surface. In this case the significant dose discrepancy between Livermore and G4DNA is eliminated by normalizing to water in the DER calculation. However, there is still significant differences in the absorbed dose near the GNP.

The DER inside V_C never approaches 1 in contrast to the case of a single GNP where DER = 1 from ~ 70 nm from the edge of the NP. This occurs due to the greater number of high energy electrons that have been produced from the greater likelihood of X-ray interaction with gold (the shell is made of thousands of single GNPs). This highlights the benefit of the GNP-shell formation in largely increasing the dose to the nucleus of cancer cells without having to be internalized into the nucleus, as mentioned in previous studies as an ideal case to produce Auger electrons near DNA [3, 135].

Comparing directly between CH Livermore with LEE = 10 eV and LEE = 250 eV and G4DNA for the GNP shell, Livermore consistently produces greater radial dose and DER

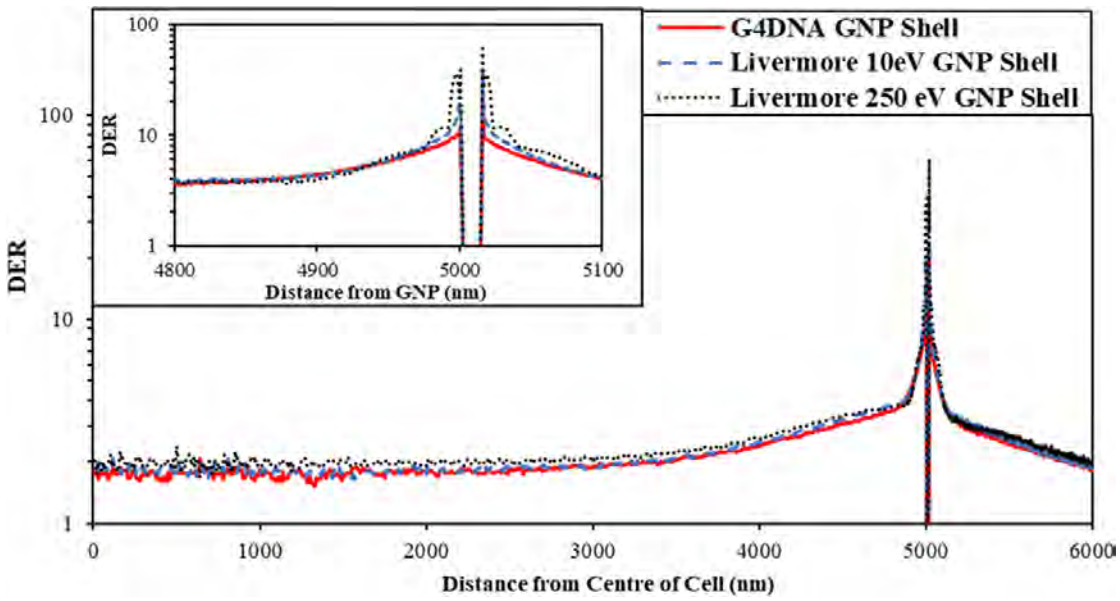

Figure A.11: "Realistic" GNP distribution radial DER using G4DNA (red) and Livermore physics with a 10 eV (blue) and 250 eV LEE (black). The DER near the GNP shell is zoomed in the top insert.

near the GNP surface, as noted in the previous section. The Livermore (LEE = 10 eV) DER converges to the G4DNA DER after 800 nm from the GNP surface, whereas the LEE = 250 eV never completely converges to G4DNA.

A.4.4 Evaluating LEM-based Radiobiological Models for Clustered Shell GNP Configurations

The expected surviving fraction of 9LGS with GNPs (S_{NP}) using the LEM was calculated from the radial dose profiles presented in figures A.10 and A.11, for CH Livermore (LEE = 10 eV and LEE = 250 eV) and G4DNA TS codes. The resulting S_{NP} for the models is shown in figure A.12, compared to the experimental data for S_{NP} and S_X (no GNPs).

Using the "realistic" GNP distribution, the LEM method agrees with the experimental results. The large changes in the DER gradient from the surface of the GNP shell are evaluated through calculation of the lethal events at each 1 nm step from the shell using LEM.

This allows an effective dose due to the inhomogeneous dose field of the GNPs to be calculated inside V_C.

Table A.2 shows a comparison of the effective dose enhancement due to the GNP shell in V_C using the LEM (DE_{eff}) as calculated using equation (A.6), with the average dose

enhancement in V_C (DE_{av}) for each of the physics models considered.

The DE_{eff} is smaller than the average dose enhancement in V_C for each physics approach considered. This is due to the calculation of the cell survival with GNPs at each radial dose step from the GNP shell minimizing the impact of the large dose near the GNP shell. In contrast, DE_{av} is affected by this initial large radial dose near the GNP surface (as seen in figure A.11). This is a result of the assumption that there is no interaction between GNP-related dose and water-only related dose (equation (A.5)), which reduces the impact of the added dose from the NPs. As a result, the average dose enhancement provides over 2.2 times the dose in water alone for each physics model and would cause a significant divergence in the predicted LQM cell survival. For this study, the DE_{av} was therefore not appropriate for GNP modelling of cell survival with our GNP distribution.

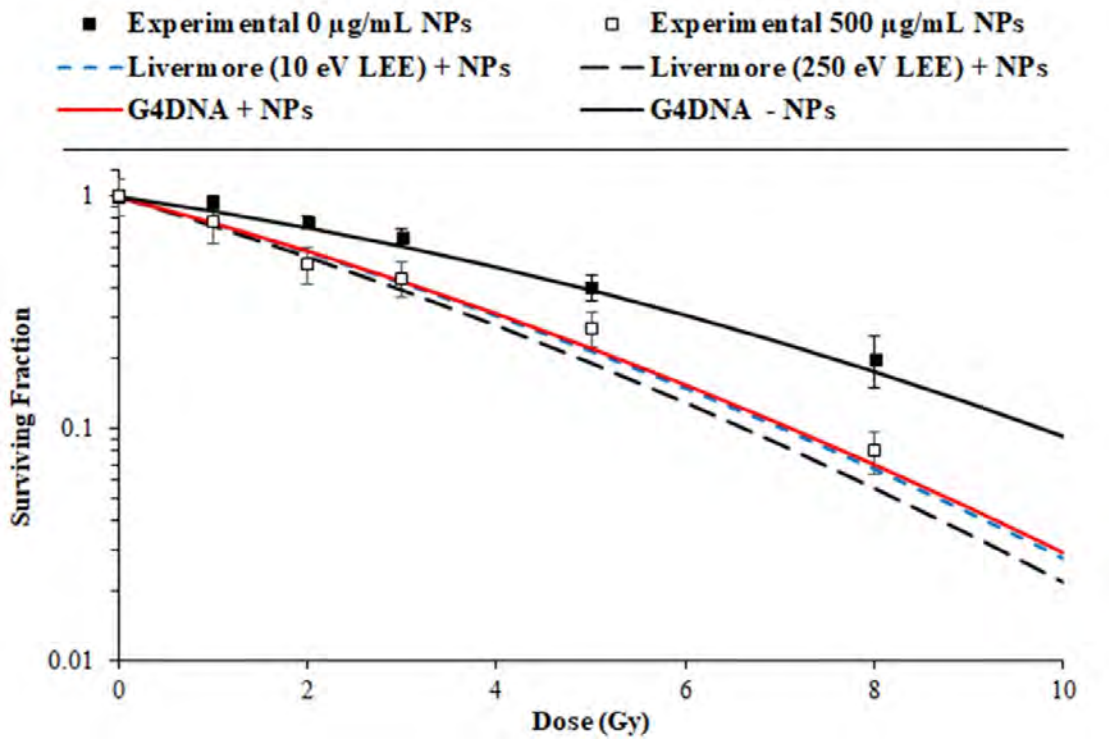

Figure A.12: Predicted cell surviving fraction using the LEM for the "realistic" GNP shell distribution modelled with G4DNA (red line), Livermore physics with LEE = 10 eV (blue line) and LEE = 250 eV (black line). The LEM-computed survival without GNPs is shown for G4DNA. Experimental data with (S_{NP}) and without (S_X) GNPs, (white and black squares, respectively) is overlaid. In the legends, (+NP and -NP) indicate with and without the NP in the biological medium.

Instead, the similar DE_{eff} produced by G4DNA and 10 eV LEE Livermore produced a good agreement with the experimental data. The higher effective dose enhancement using the 250 eV LEE Livermore model increased the predicted cell killing of the S_{NP}, as seen in figure A.12.

Table A.2: Effective dose enhancement in V_C using LEM, compared to the average DER in V_C , determined using G4DNA and Livermore physics with LEE = 10 eV and 250 eV.

	G4DNA	Livermore LEE 10 eV	Livermore LEE 250 eV
DE_{eff}	1.72	1.75	1.89
DE_{av}	2.28 ± 0.03	2.44 ± 0.04	2.22 ± 0.03

A.5 Discussion

This study has characterized the variations in absorbed dose to water produced by single GNPs in an X-ray field due to TS and CH physics models in Geant4. We applied these findings to simplistically model a GNP distribution in Geant4 confocal imaging of GNPs in 9LGS cells, and calculate the corresponding cell survival using the LEM. Our results show that the new TS-based G4DNA models for gold can produce a good correlation to experimental GNP radiosensitization, if considering the nanoscale dose and a partial-shell GNP structure.

Livermore CH models with an LEE of 10 eV provided a dose enhancement result that was more consistent with the TS model than when using the recommended LEE of 250 eV.

Livermore physics produced 30% more dose in water than G4DNA. The greatest difference between G4DNA and Livermore was the larger DER at the GNP surface regardless GNP size, and further increased when increasing the cut threshold from 10 eV to 250 eV.

Livermore at LEE = 10 eV overall produced good agreement to G4DNA, in agreement with Lazarakis et al [163] and Kyriakou et al [164]. However, Livermore is not recommended to be used below 250 eV, [63, 161] with significant differences in terms of spectra of low energy secondary electrons and calculation of energy deposition around GNPs with respect to G4DNA [167, 168].

When using TS and CH models, Auger electrons are predominantly contributing to single GNP dose enhancement. For small radii, this happens when the GNPs are situated near or inside the cell nucleus to maximize the DNA damage. With larger GNP distributions, where multiple GNPs interact to enhance the dose to the cell, the higher energy electrons, and not the Auger electrons, enhance significantly the dose distribution over micrometer distances [3, 183].

Previous studies have scarcely considered the effect of a more realistic GNP distribution in the LEM when translating Monte Carlo results to radiobiological experiments. Instead, single GNPs are often used [175, 176] with one study randomizing GNP positions within the cell before applying the LEM using PENELOPE CH models [170].

The distribution of GNPs must be considered carefully as it is known to differ between cell lines [175, 184]. More homogeneously distributed GNPs in cells can produce good agreement between using a single GNP and the LEM, as the GNP systems are more isolated and significant dose enhancements occur within 10–100 nm. However, in some cell lines (such as 9LGS), the clustering of NPs causes superimposing and shielding effects on the dose enhancement [3]. Brown and Currel [184] include components accounting for dose saturation when NP shells form around 9LGS, and other cell lines in the LEM calculation. In our study, electrons with energies between 10–100 keV (figure A.8) have a larger role in the dose enhancement in the cell when the GNPs are configured in a "shell-like" distribution. This was also noted by McKinnon et al [3] and in other kV applications with NPs [75]. Our GNP layer around 9LGS cells can be thicker than 1 GNP realistically (see figure A.1) and can be partially incomplete around the cell nucleus. This in turn affects the dose to the nucleus and nearby cells, and may be of interest in future simulations.

Modelling multiple GNPs with accurate physics models and including real GNP distributions is an important step to advance the modelling of NP radioenhancement by means of the LEM and Monte Carlo simulations. Future studies should also consider the effect of indirect radiation damage by modelling radiochemistry [165] and other radiobiological models besides LEM which incorporate DNA damage on the nanoscale [185].

A.6 Conclusion

This research marks the first use of the new Geant4 TS-based models for gold to predict GNP dose enhancement in a cancerous cell line. This study has investigated simulation physics models (CH and TS) and parameters (LEE) to describe GNP radioenhancement in kV beam when considering a distribution of GNPs that more resembles the configuration of GNPs seen in an *in vitro* cell population.

We have demonstrated a noticeable difference in physics models in Geant4 on the nanoscale dose around a gold nanoparticle. Overall, (CH) Livermore physics overestimated the dose and dose enhancement with GNPs compared to Geant4-DNA models. The advantage of the TS-models in this study was an accurate secondary electron production and tracking, which led to significant differences in terms of dose calculation to the Livermore close to the GNP surface. Accurate low-energy electron tracking will become more important for further studies investigating GNP radioenhancement considering realistic distributions of the gold nanoparticles and when including the chemical stage modelling (radiolysis). When the TS models are not available for modelling NP dose, using Liver-

more with a 10 eV LEE appears to be an alternative for NP dose calculations. In addition, we underlined the necessity of simulating fully Auger emission, which directly impacts DER.

The local effect model (LEM) was used to calculate the cancer cell survival according to an approximation of a more realistic GNP distribution. A good agreement was found between the simulation results and the experimental measurements. To our knowledge, this is the first study to use a shell-like geometric model of GNPs in the translation of Monte Carlo to experimental data with the LEM. In future, simulations should consider more realistic conditions, and we will be considering an alternative model which instead calculates the direct and indirect (chemical) damage of radiation in a GNP configuration that is based in individual particle positions in the cell.

This work contributes to the translation of Monte Carlo based studies in GNP dose enhancement to experimental GNP radiosensitization. This study highlights the benefits of combining state of the art Monte Carlo simulation with biological imaging, radiobiological models and *in vitro* studies.

A.7 Acknowledgements

We would like to acknowledge the University of Wollongong (UOW) Information Technology Services (ITS), the Centre for Medical Radiation Physics, and the Australian National Computational Infrastructure (NCI) for computing time and resources. We acknowledge the access facilities at the Illawarra Health and Medical Research Institute, and Prince of Wales Hospital, Randwick, NSW, Australia. We acknowledge the financial support of the Australian Government Research Training Program Scholarship, Australian Research Council (DP170100967) and Australian National Health and Medical Research Council (APP1084994).

Appendix B

Progress of Geant4 Electromagnetic Physics

This appendix is a modified version of the published work:

V. Ivanchenko, A. Bagulya, **S. Bakr**, M. Bandieramonte, D. Bernard, M. Bordage, J. Brown, H. Burkhardt, P. Dondero, S. Elles, V. Grichine, S. Guatelli, F. Hariri, A. Howard, S. Incerti, S. Yung Jun, O. Kadri, I. Kyriakou, M. Maire, A. Mantero, M. Novak, D. Sawkey, I. Semeniouk, A. Sokolov, and L. Urban on behalf of the Geant4 Collaboration, (2019), **"Progress of Geant4 electromagnetic physics developments and applications"**, *EPJ Web of Conferences*.

`https://doi.org/10.1051/epjconf/202024502009`

B.1 Abstract

We report on developments of the Geant4 electromagnetic physics sub-libraries of Geant4 release 10.4 and beyond. Modifications are introduced to the models of photoelectric effect, bremsstrahlung, gamma conversion, single and multiple scattering. The theory-based Goudsmit-Saunderson model of electron/positron multiple scattering has been recently reviewed and a new improved version, providing the most accurate results for scattering of electrons and positrons, was made available. The updated interfaces, models and configurations have already been integrated into LHC applications and may be useful for any type of simulations.

B.2 Introduction

The Geant4 electromagnetic (EM) physics sub-libraries [47, 186] are an important component of the Geant4 toolkit [1, 37, 38]. In this work, we report on recent progress in EM model developments and on updates of user interfaces, which are included in the Geant4 versions 10.4 and 10.5beta. In our previous reports [187, 188], earlier Geant4 versions were described.

Important modifications were made in the material, EM physics, and physics list Geant4 sub-libraries. The goal was to make the most advanced EM theoretical models available to the groups performing LHC and other HEP experiment simulations. In Run-3 at LHC, higher statistics are expected than in Run-2. To provide adequate accuracy of simulations, EM physics models are under continuous review and the next-to-leading-order corrections are taken into account. This reduces systematic uncertainties in simulation predictions and provides simulation of second order effects which are important for very high energies (LHC and FCC programs), and in simulation of backgrounds in the dark matter searches [189]. Although focused on HEP experiments, these upgrades are at the same time useful for many other applications including those in medical physics and space science.

B.3 EM Model Developments

In Geant4 10.4, substantial improvements were introduced in the models of photoelectric effect, gamma conversion, multiple, and single scattering. Corrections to scattering of positrons and to sampling of displacement have been recently added to the Geant4 default Urban model. In Geant4 10.5beta, some minor fixes were added and code clean-up was performed for these models as well as for bremsstrahlung models. Additionally a new alternative model for gamma conversion to e^+ e^- pair was introduced. In what follows we describe the most important modifications of EM models.

B.3.1 The Goudsmit-Saunderson Multiple Scattering Model

The Geant4 Goudsmit-Saunderson (GS) model for multiple Coulomb scattering of $e^\pm$ is based on the "any-angle" multiple scattering model developed by Kawrakow and Bielajew [190]. The exact Goudsmit-Saunderson [191] angular distributions, computed by utilising the screened Rutherford differential cross section (DCS) for elastic scattering, can be represented in a compact numerical form suitable for fast run-time sampling of the corresponding angular deflections. The accuracy of the GS model is already appropriate for many HEP applications. However, starting from Geant4 version 10.4, the GS model provides an option of using a more accurate description of the scattering problem

through the introduction of higher order corrections. The most important among these is the correction to the GS angular distributions, computed by using the screened Rutherford DCS, based on the more accurate Mott elastic DCS (spin effects) [192]. Besides the accurate multiple scattering angular distributions, the GS model provides the possibility to use the Lateral and Longitudinal Correlation Algorithm (LLCA) [193, 194], that can produce lateral and longitudinal condensed history end-point distributions that are very close to those obtained by using the corresponding single scattering model. Moreover, the algorithm makes sure that the boundary is always crossed in the single scattering mode, which makes this stepping algorithm free from stepping artefacts.

As a result of these improvements, the Geant4 version 10.4 of the GS model can provide highly accurate $e^{\pm}$ transport simulations even in the case of extreme geometrical conditions (e.g. high granularity calorimeters) or low energies, independently from the target atomic number as illustrated in figure B.1 (see more details in [188]).

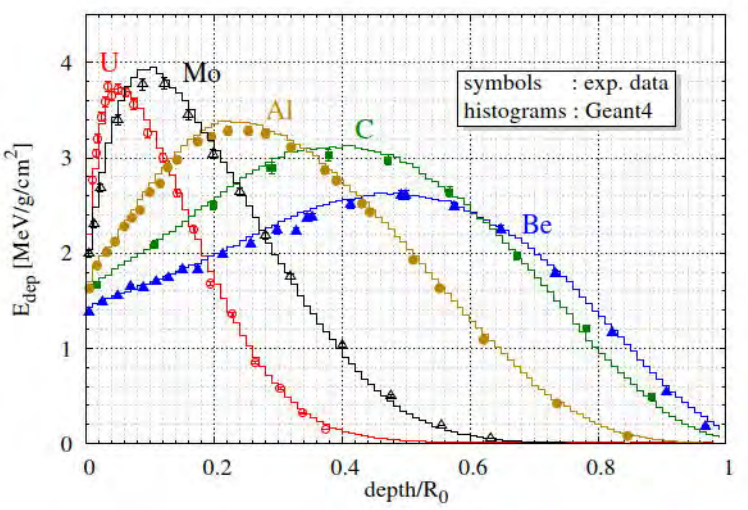

Figure B.1: Comparison of experimental (symbols [195]) and simulated (histograms Geant4 10.4. EM Opt4) electron energy deposition profiles in semi-infinite U, Mo, Al, C media with primary electron energy of 1.0 MeV and in Be with 1.033 MeV. Coordinates are normalized to the CSDA (continuous-slowingdown-approximation) range of electrons in corresponding materials.

B.3.2 WentzelVI Combined Scattering Model

The WentzelVI multiple scattering model combined with the single elastic scattering (SS) model [196] is the current Geant4 default approach for $e^{\pm}$ above 100 MeV and for all other charged particles at any energy [38]. The limited scattering angle between multiple and single scattering is selected dynamically depending of step size and particle momentum. In Geant4 version 10.4, both models use the same Wentzel cross section [197],

which does not take into account Mott corrections. For Geant4 10.5beta the SS model has been updated for $e^{\pm}$ to use an alternative single scattering model which takes into account the Mott corrections. The model was developed for the $e^{\pm}$ non-ionising energy loss computations [187]. Both GS and SS models implement Mott corrections now and the results of the simulations of scattering off thin foils become very similar for these models.

B.3.3 5D Gamma Conversion to e^+ e^- Pair Model

The differential cross section of the conversion of a γ ray to an e^+ e^- pair in the field of the nucleus ("nuclear conversion") or of an electron ("triplet conversion") of an atom was first computed by Bethe and Heitler [198]. The phase space consists of five variables that can be chosen to be the azimuthal and the polar angles of the electron and of the positron and the fraction of the photon energy taken away by the positron.

The existing Geant4 γ-conversion models are appropriate for the simulation of EM showers, but are not accurate enough for a precise simulation of the high-performance γ-ray telescopes [199]. This is due to their sampling the polar angles of the two leptons independently and due to performing the decay in a plane containing the directions of the photon, of the electron and of the positron, without any allowance for a transverse out-of-plane recoil momentum. The class *G4BetheHeitler5DModel* [166, 200] samples the full, 5D, Bethe-Heitler differential cross section, energy-momentum is strictly conserved and this model samples realistic correlations between the variables.

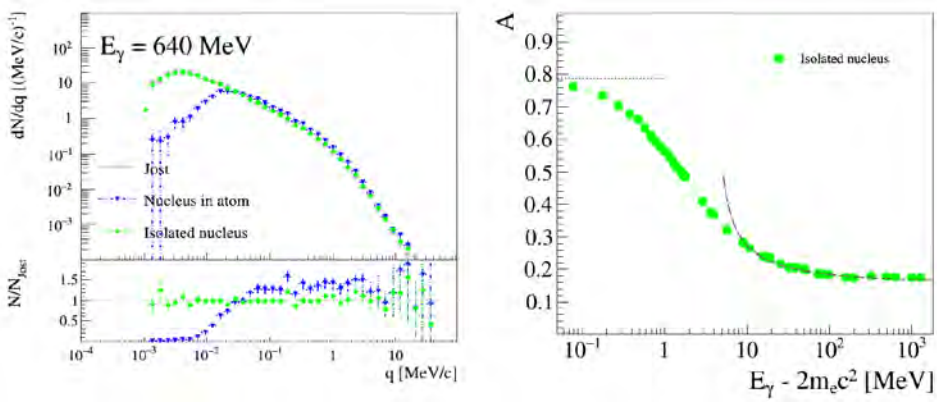

Figure B.2: Performance of the 5D gamma conversion model. Left: recoil momentum distribution compared to the analytical high-energy expression from [201]. For isolated targets, the simulation (bullets) matches nicely a distribution obtained from [201]. For nuclei inside an atom (triangles), the suppression of lowrecoil-momentum events is visible below a few 10^{-2} MeV/c. The ratio plot is relative to [201]. Right: polarization asymmetry as a function of available energy, compared to published asymptotic expressions (dotted line – low energy from [199], dashed line – high energy from [202]).

The distribution of the magnitude of the recoil momentum is found (figure B.2 left and [166, 200]) to be compatible with the analytical expression computed in the high-energy approximation [201]. The nuclear or triplet conversion of linearly polarized or non-polarized γ rays on isolated or atomic targets is simulated. For linearly-polarized γ rays, the polarization asymmetry is found (figure B.2 right and [166, 200]) to be compatible with the known asymptotic expressions [199, 202]. Because of 5D sampling, the new model is significantly slower than the default Bethe-Heitler model, so the 5D model is included only in the two EM physics constructors *G4EmLivermorePhysics* and *G4EmLowEPPhysics*.

B.3.4 Livermore Photoeffect Model

A revised Livermore model of the photoelectric effect is provided with Geant4 10.4. The total photoelectric and single shell cross sections are based on the evaluated cross section data from the EPICS2014 (Electron Photon Interaction Cross Sections) data library [203]. This updated library has been reported to be more accurate with respect to the previous version EPDL97 [161], previously used. Depending on the energy of the incident γ, the model provides cross sections based either on the interpolation (linear or spline) of tabulated cross sections or on the parameterisation of cross sections data. The parameterisation over γ energy E was obtained through two fits in two different energy ranges, with six parameters each, as follows:

$$\sigma(E) = \frac{a_1}{E} + \frac{a_2}{E^2} + \frac{a_3}{E^3} + \frac{a_4}{E^4} + \frac{a_5}{E^5} + \frac{a_6}{E^6} \tag{B.1}$$

The intervals ranges are set dynamically and they depend on the atomic number of the element and the corresponding K-shell binding energy.

These improvements allowed the reduction of the threshold for the parameterisation from 600 keV to 5 keV, resulting in a measured speedup of about 20% for the final state generation sampling. In figure B.3 the results of speedup of the updated Livermore model for different elements are shown. The simulations used 10^6 γ with energy 0.4 MeV, and 20 repetitions for each element.

The angular distribution of the emitted e^- follows the Sauter-Gavrila distribution [204] initially proposed for the K-shell. It is based on a new and optimised implementation (similarly to the model of Penelope 2014). This implementation is faster and gives a 4% to 20% speedup. The updated Livermore model has been tested and verified against other Geant4 photo-electric models and the observed cross sections have a maximum variation of 5% with respect to the Penelope cross section. For the majority of atoms and energy ranges cross sections agree within 1%. Since Geant4 10.4, the new Livermore model is

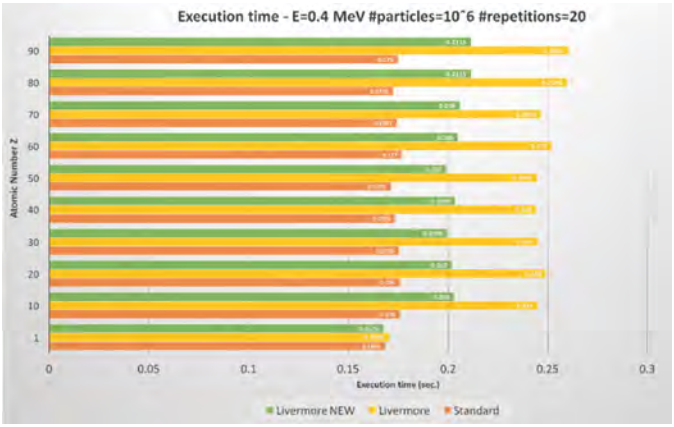

Figure B.3: Comparison of execution times between the updated Livermore model (green), the old Livermore (yellow) and the standard model (orange) as a function of the atomic number.

the default in all EM physics lists except Penelope.

B.3.5 Gamma Conversion to Muon Pair Model

The total cross section and the angular distribution of muons in Geant4 gamma conversion model is based on the multi-differential cross section [205] (*G4GammaConversionToMuons* class). For Geant4 10.4 we validated the total cross section of the process using direct integration of the Williams-Weizsacker differential cross section using Wolfram Mathematica 11.0 [206]. The obtained values for several targets agree within a few percent with the current parameterisation [205]. The model used for the final state generation was improved. The dependence of the angular distribution on the momentum transfer to the recoiling nucleus was taken into account, which slightly reduced scattering to the backward hemisphere. This update was inspired by the dark matter search experiment SHiP study on muon background and other projects in this area [189].

B.3.6 Improved Threshold for Positron Annihilation to $\mu^+ \mu^-$

The threshold positron energy in the laboratory system for the positron annihilation with atomic electrons into $\mu^+ \mu^-$ pair is $E_{th} = 43.69$ GeV. Taking into account that the electron is much lighter than the muon, the lowest order cross section can be written as

$$\sigma = \frac{\pi r_\mu^2}{3} \varepsilon (1 + \frac{\varepsilon}{2}) \sqrt{1 - \varepsilon} \tag{B.2}$$

where $r_\mu = r_e m_e / m_\mu$ is the classical muon radius, m_e and m_μ are electron and muon masses, r_e is the classical electron radius, $\varepsilon = E_{th}/E_{lab}$, where E_lab is the total positron

energy in the laboratory frame. We now take into account the increase in cross section by the Sommerfeld-Schwinger-Sakharov (SSS) threshold Coulomb re-summation factor [207]

$$S(\beta) = \frac{X(\beta)}{1 - e^{-X(\beta)}}, \; X(\beta) = \frac{\pi\alpha}{\beta\gamma} = \pi\alpha\frac{\sqrt{1-(\beta)^2}}{\beta} \tag{B.3}$$

where α is the fine structure constant, β and γ are kinematic variables of muons in the centre of mass frame. The SSS-corrected cross section can be written at all energies as

$$\sigma_{SSS} = \frac{\pi r_\mu^2}{3}\varepsilon(1+\frac{\varepsilon}{2})\frac{\pi\alpha\sqrt{\varepsilon}}{1 - e^{-\frac{\pi\alpha\sqrt{\varepsilon}}{\sqrt{1-\varepsilon}}}} \tag{B.4}$$

These expressions are used in the simulation of this process since Geant4 10.5beta. The final factor in the expression is replaced by its asymptotic value of unity close to threshold to avoid numerical instabilities. The cross section with and without the correction is shown in figure B.4. The noticeable increase of the cross section close to threshold by the SSS-factor is of practical interest for the low emittance production of muons, as proposed in [208].

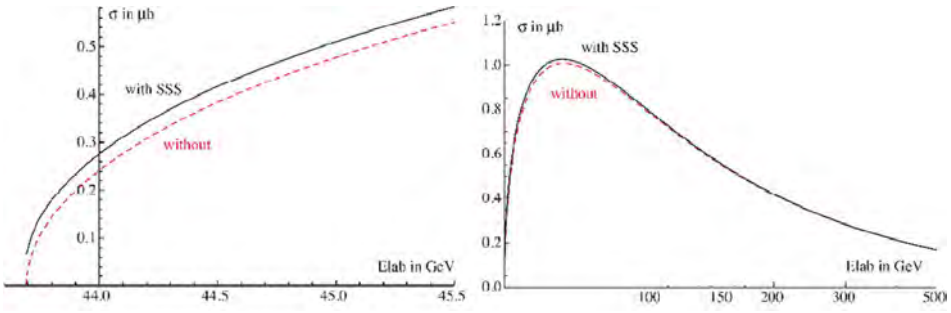

Figure B.4: Total cross section for $e^+e^- \longrightarrow \mu^+\mu^-$ as a function of the e^+ energy in the laboratory system. With (solid line) and without (dashed red line) SSS Coulomb re-summation factor, zoomed close to the threshold (left), and using a wider energy range (right).

B.4 Updates to EM Physics Infrastructure

Interfaces to material properties and density effect parameterisation for compounds were improved. Additional C++ interfaces to EM parameters and corresponding UI commands were introduced. The method of automatic documentation for EM models, processes and physics list constructors has been developed. The web documentation for EM physics was reviewed and re-structured. Some of these developments will be described below.

B.4.1 Geant4 Material Properties

The interface for material properties defined in user code have been improved to allow significant speed-up, particularly in transport of optical photons. These properties are stored in a C++ standard template library map. The keys for this map are now elements of an enumeration, replacing the char pointers used previously. The user still defines the material property vectors and constants in user code with *AddProperty(const char* key, ...)* or *AddConstProperty(const char* key, ...)*. Here "key" is, for example, "RINDEX" for the refractive index. Corresponding physics process classes in the Geant4 distribution have been updated to retrieve the material property vectors and constants with *GetProperty(G4int)* and *GetConstProperty(G4int)* methods. The parameter is the enumerator, for example, *kRINDEX* for the refractive index.

In the user code, the material property vectors and constants may be retrieved using either the enumerator or the string label. Internally, a vector of string names is used to determine the integer corresponding to the string. In the case of a custom property (those not pre-defined in Geant4), an integer key is assigned automatically when the property is defined. In order to retrieve a custom property by index, the integer key may be first obtained using the methods *GetPropertyIndex(G4String key)* or *GetConstPropertyIndex(G4String key)*.

B.4.2 EM physics configuration

In recent versions of Geant4, explicit EM model parameters were introduced [187, 188]. Each EM physics list has a set of specific parameters which users may modify using User Interface (UI) commands or the C++ interface. In Geant4 10.4 we extended the list of parameters and improve the visibility of the list in the output. In addition, we add extra methods to stream out model and process descriptions enabling automatic documentation generation for each EM configuration.

The default EM physics list (Opt0) is used in the majority of Geant4 Physics Lists. The Urban multiple scattering model is used for $e^{\pm}$ below 100 MeV [38]. In the Opt4 EM physics list the GS model of multiple scattering with Mott corrections enabled is used below 100 MeV instead of the Urban model. The Opt4 physics list uses the most accurate models for each process, as well as stricter configuration parameters for tracking of charged particles. The alternative EM physics list Opt3 may be considered as an intermediate variant between Opt0 and Opt4.

For testing purposes of novel calorimeters, we provide a configuration of electron scat-

tering based on the GS model or on the SS model. In addition, the GS model with Mott corrections enabled is included in the Livermore and Penelope EM physics constructors. To improve usability, a new set of UI commands and corresponding C++ interfaces have been added. In particular, the photo-absorption ionisation model may be enabled per detector region using the corresponding UI command.

Since version 10.4, three new EM physics constructors (G4EmDNAPhysics_optionX, where X=2, 4 or 6) are available. They allow a discrete simulation of particle interactions in liquid water, the main component of biological media, down to a few tens of eV. These constructors are developed in the context of the Geant4-DNA project [209, 210]. The processes they include: ionisation, electronic excitation, elastic scattering, vibrational excitation and molecular attachment for electrons. For protons, neutral hydrogen atoms, α particles and their charge states, the ionisation, electronic excitation, elastic scattering, and charge exchange processes are available. These processes have been recently described in detail in [165, 211] and the performance of these three physics constructors has been evaluated for nano- and micro-dosimetry simulations, notably through the usage of Geant4 extended examples [212, 213]. A variety of their applications is described in [94].

B.5 Summary

Goudsmit-Sounderson model, which is the most accurate one for $e^{\pm}$ transport, was improved in Geant4 10.4. The model may be recommended for a wide variety of simulation applications. Improvements in modelling of other processes, as well as in EM code infrastructure were introduced. Mott corrections were added to the WentzelVI model used for simulation of high energy scattering. In Geant4 10.5beta the new 5D gamma conversion model was added. More effective handling of the material properties is provided, the interface to EM parameters is extended, and the set of EM physics list components is improved. We continue reviewing EM models in order to take into account various next-to-leading-order corrections to the cross sections and to the final state generation.

B.6 Acknowledgements

We acknowledge the support of the French National Research Agency (ANR-13-BS05-0002); Fermi Research Alliance, LLC under Contract No. DE-AC02-07CH11359 with the United States Department of Energy.

Appendix C

Geant4 Electromagnetic Physics Progress

This appendix is a modified version of the published work:

V. Ivanchenko, A. Bagulya, **S. Bakr**, M. Bandieramonte, D. Bernard, M. Bordage, J. Brown, H. Burkhardt, P. Dondero, V. Grichine, S. Guatelli, I. Hrivnacova, S. Incerti, O. Kadri, D. Konstantinov, I. Kyriakou, M. Maire, A. Mantero, J. Ramos-Mendez, M. Novak, L. Pandola, D. Sakata, D. Sawkey, I. Semeniouk, W. G. Shin,N. H. Tran, and L. Urban on behalf of the Geant4 Collaboration, (2020), **"Geant4 electromagnetic physics progress"**, *EPJ Web of Conferences*.

https://doi.org/10.1051/epjconf/202024502009

C.1 Abstract

The Geant4 electromagnetic (EM) physics sub-packages are a component of LHC experiment simulations. During long shutdown 2 for LHC, these packages are under intensive development and we report progress of EM physics in Geant4 versions 10.5 and 10.6, which includes faster computation, more accurate EM models, and extensions to the validation suite. New approaches are developed to simulate radiation damage for silicon vertex detectors and for configuration of multiple scattering per detector region. Improvements in user interfaces developed for low-energy and the Geant4-DNA project are used also for LHC simulation optimisation.

C.2 Introduction

EM physics sub-libraries [47, 186] are an important component of the Geant4 toolkit [1, 37, 38], which affects both Monte Carlo (MC) simulation accuracy and CPU performance of LHC detector simulations. In this work, we report on recent progress in EM model developments and on updates of user interfaces, which are included in the Geant4 versions 10.5 and 10.6. In our previous reports [38, 187, 188, 214], earlier Geant4 versions were described. Combined configurations of Geant4-DNA and standard models were described in Refs. [47, 138, 168]. Common validation efforts for high and low-energy use-cases allow improving quality of EM simulation in general.

C.3 EM Physics Progress

Two recent Geant4 versions, 10.5 and 10.6, were released during the large shutdown of LHC between data taking periods Run-2 and Run-3. In these Geant4 versions, all EM physics developments are included into the toolkit without any restriction. EM physics updates are focused on improving of accuracy and speed of MC simulations.

C.3.1 Updates for Geant4 10.5

The Geant4 default model *G4UrbanMscModel* [38] for electron and positron multiple scattering (MSC) was tuned to backscattering data at low energies from different targets (full set of references in [188]). Above 100 MeV, a combination of the *G4eCoulombScatteringModel* single scattering model and the *G4WentzelVIModel* multiple scattering model was used [38]. For these models Mott corrections were added using a pre-existing data class, which was also optimized for more effective usage of precomputed data.

For gamma conversion and bremsstrahlung, the default angular generator was updated to *G4ModifiedTsai*. For gamma conversion, the main models (*G4BetheHeitlerModel* and *G4PairProductionRelModel*) were reviewed. Several improvements were introduced for the screening function approximation, Landau-Pomeranchuk-Migdal function approximation, and selection of elements in compounds. A new option was added to *G4SeltzerBergerModel* for bremsstrahlung: a mechanism of sampling of final state using a sampling table instead of differential cross section table.

New EM model classes were added:

- *G4BetheHeitler5DModel* (5D) - sampling of final state for gamma conversion con-

sidering nuclear recoil and linear polarisation of primary gamma [214], which is used in gamma-ray astronomy and may be applied for LHC simulations. This model is more accurate but is slower than the default model.

- Optional ICRU90 data for stopping powers of protons and α particles, requested for simulation of proton/ion therapy.

- *G4LindhardSorensenModel* – parametrized ion ionisation model above 10 MeV/u based on Lindhard-Sorensen theory [215], also alternative models *G4AtimaEnergyLossModel* and *G4AtimaFluctuations*, which are C++ implementations of the ATIMA code. Both new models are used for relativistic ion transport simulations.

- *G4eplusTo2GammaOKVIModel* and *G4eplusTo3GammaOKVIModel* classes implement 2-gamma and 3-gamma positron annihilation in flight and at rest, essential for positron tomography simulations.

These models are not included in the default EM configuration (Opt0) but are available in the alternative EM physics configuration (Opt4) prepared for accurate simulations including medical and space applications of Geant4, it is also called EMZ in reference Physics Lists.

C.3.2 Updates for Geant4 10.6

In this version of Geant4, previously introduced models were updated and substantial effort went to speed up computations in EM physics. Kernel classes used for handling of data tables were reviewed, and several optimizations were introduced into the toolkit. The most critical is the reduction of the number of calls to the logarithm function. This improvement was possible because EM tables are logarithmic over particle kinetic energy. At every step of every track, energy loss, ranges, and cross sections are recomputed using internal tables. The main optimisation was to only compute the logarithm once, unless the particle energy changes. Also, the interpolation code was optimized such that number of lines of code at each call was reduced nearly a factor of 10. Benchmark results for speed up of simulation for CMS geometry without hit creation:

- $\sim$ 8% faster for Mac Book Pro (Mac OS 10.13.2) 2.8 GHz i7;

- $\sim$ 5% faster for AMD (SLC6 gcc8.2.0) 3.5 GHz.

Another optimisation was implemented as “general” process for gamma (figure C.1). This approach means that Geant4 kernel sees the transportation process and only one physical process, which combines all 6 different gamma interactions implemented in

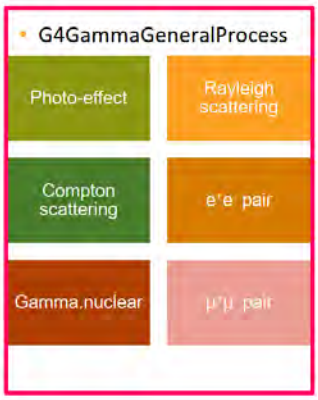

Figure C.1: General process for gamma includes 6 different Geant4 processes.

Geant4. In this case, only one integral interaction length is calculated at a step of a gamma. At the interaction point, the concrete process is selected randomly according to partial cross sections. The CPU advantage of this approach depends on the concrete geometry and may be estimated on level of 5% for HEP applications.

It is expected that similar EM results will be obtained with Geant4 10.5 and 10.6. This may be illustrated using ATLAS type simplified calorimeter response (figure C.2). For Geant4 10.4 visible energy was lower for $\sim 1\%$ and the resolution was wider for $\sim 2\%$.

The process class *G4GammaConversionToMuons* has been available for a long time, but was recommended only for the ultra-relativistic case [216]. Due to the request of the Gamma Factory design group [217], the applicability area of this process was extended down to the muon pair production threshold (figure C.3). For that, recently introduced 5D-model has been extended for the case of the muon pair production, which required a revision of sampling algorithm to increase its efficiency.

For radiation damage studies [218] a new helper class *G4NIELCalculator* has been introduced for computation of non-ionising energy loss (NIEL). This class may be used in user classes at each step of a particle in silicon detector. The advantage of this method is in independence of computations of crystal displacement on Geant4 cuts and stepping algorithm. Also, the model of displacement probability may be customized by users.

C.4 Low-Energy EM Physics

Geant4-DNA example applications relevant for the simulation of track structures (TS) in liquid water were reviewed [212]. These examples serve for evaluating Geant4-DNA physics models performance. We have also undertaken calculations on the influence of

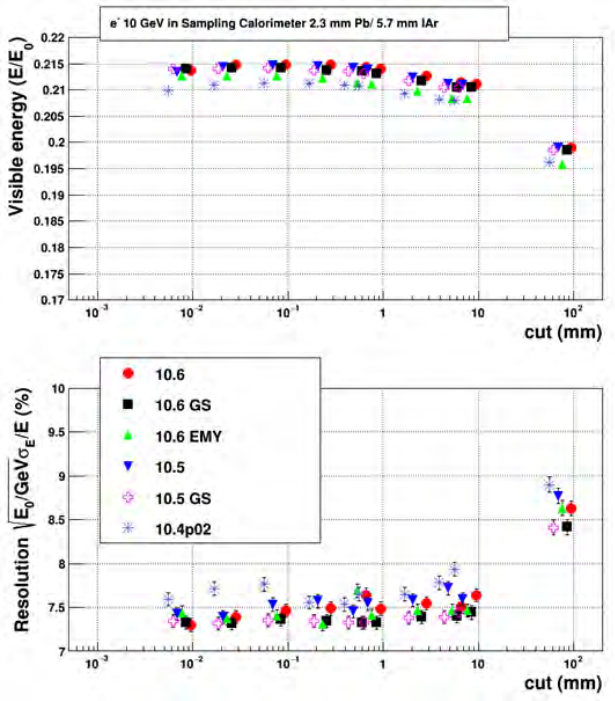

Figure C.2: Simulation of the response of simplified ATLAS type EM calorimeter for 10 GeV gamma as a function of *cut in range* (Geant4 tracking parameter, see description in [1, 186]) for different Geant4 versions from 10.4 to 10.6: top - visible energy, bottom – resolution. GS is the EM physics configuration where the default MSC model for $e^{\pm}$ is substituted by the Goudsmit-Saunderson model [188]. EMY is the EM physics configuration used for medical and other low-energy applications. For this type of calorimeter for cut value 1 mm, in Geant4 10.5 and 10.6 compared to 10.4 visible energy increases by 1.5% and resolution decreases by 1.5%.

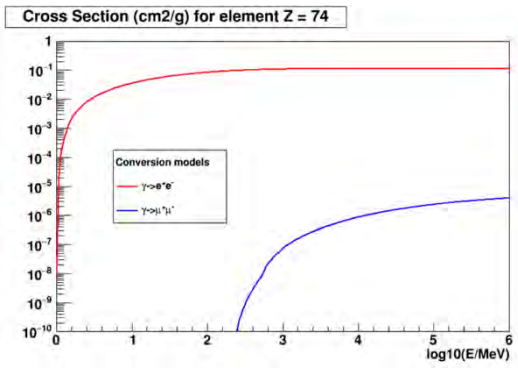

Figure C.3: Geant4 10.6 cross sections of lepton pair production in a tungsten target as a function of gamma energy. The arrow shows approximate working point for the Gamma Factory [217].

some user-defined simulation parameters (tracking and production cuts and maximum step size) in liquid water medium using some of the condensed history (CH) and TS models of Geant4 [164]. Using the TS models as reference, it was shown that Livermore inelastic models offer the best performance among the CH models for nanoscale electron transport.

Apart from lineal and specific energy simulated in Geant4 with the extended example "microyz", another fundamental description of the energy deposition pattern is obtained through the differential proximity function of tracks [219]. These functions are defined as the mean energy deposited to a spherical shell of given radius and thickness centred at a randomly chosen energy-transfer point in the shower of tracks induced by a primary particle and all its secondaries. In Geant4 version 10.6 a new Geant4-DNA application is implemented dedicated to the simulation of proximity functions in liquid water.

C.5 Validation of EM Physics

Validation of EM physics is carried out permanently for each reference development version and each release using the EM testing suite [38, 187, 188, 214]. The response and resolution for various calorimeter setups, response of tracking devices, backscattering of electrons and transmission via absorbers are controls. For Geant4 10.6 EM physics tests become a part of the geant4-val tool [219], which allows a significant improvement in the statistics of these tests and in the number of variants of EM calorimeter configurations.

C.6 Customisation of EM Physics

Geant4 distributions include a sub-library of Physics Lists components. The recommended physics list for HEP applications is FTFP_BERT, which includes the default EM physics constructor. In order to reach desired optimum between simulation accuracy and CPU speed, the user may customise EM physics by varying values of *cuts in range* (figure C.2), changing the EM physics constructor, defining alternative EM physics models per detector region, and changing EM parameters [5-8].

In Geant4 10.6, modifications in the default EM physics compared to 10.5 are the lateral displacement algorithm in Urban multiple scattering model and the angular generator for bremsstrahlung and pair production. For applications which require high simulation accuracy, it is recommended to use the Opt4 (EMZ) EM physics configuration, which

includes more strong step limitations, the Goudsmit-Saunderson (GS) model of MSC for electrons and positrons below 100 MeV, 5D-model of gamma conversion, and a more accurate model for the Compton scattering. A significant CPU penalty compared with the default EM physics is expected depending on geometry and primary energies. It may be more than factor 2 for LHC experiment simulations. However, this EM configuration is recommended as an alternative to the default for estimation of systematic uncertainty of the simulation.

For simulations where CPU efficiency is essential, there are more options which can be applied on top of the default EM physics. First, Opt1 (EMV) and Opt2 (EMY) EM physics constructors include simplified step limitations for MSC. This may be recommended for simulation of crystal calorimeters but not for sampling calorimeters, for which several parameters of electron multiple scattering are available:

- RangeFactor – defines step size in vicinity of geometry boundary.
- GeomFactor – defines number of steps in thin layers for the Urban model.
- Stepping algorithm – type of step limitation.
- LateralDisplacement flag enabling lateral displacement of an end point at each step.
- SafetyFactor – additional step limitation factor for the Urban model.
- LambdaLimit – parameter for the Urban model sensitive to material density.

These parameters are different for the default, EMY, and EMZ configurations. They may be changed via C++ interface or by Geant4 UI commands. This should be done before Geant4 initializes physics models.

For the case where a detector consists of several different calorimeters, it is possible to configure electron MSC for each calorimeter separately. For that, a new instance of the MSC model object should be created and desired parameters should be set only for this object and this object should be locked from further changes of parameters. This method should be implemented in custom EM physics constructor, for example, as is implemented for the CMS simulation [214]. Note, that such customisations may be performed both to speed-up simulation and to improve its accuracy.

C.7 Summary

The Geant4 version 10.6 includes several new EM models and helper classes which allow extend Geant4 capabilities for LHC experiments simulations. Geant4 10.6 is faster than

previous Geant4 versions. New instruments are also available for customisation of MSC parameters per calorimeter region, which allows further increases in speed.

C.8 Acknowledgements

IK acknowledges financial support from the European Space Agency (ESA) under contract No. 4000126645/19/NL/BW.